

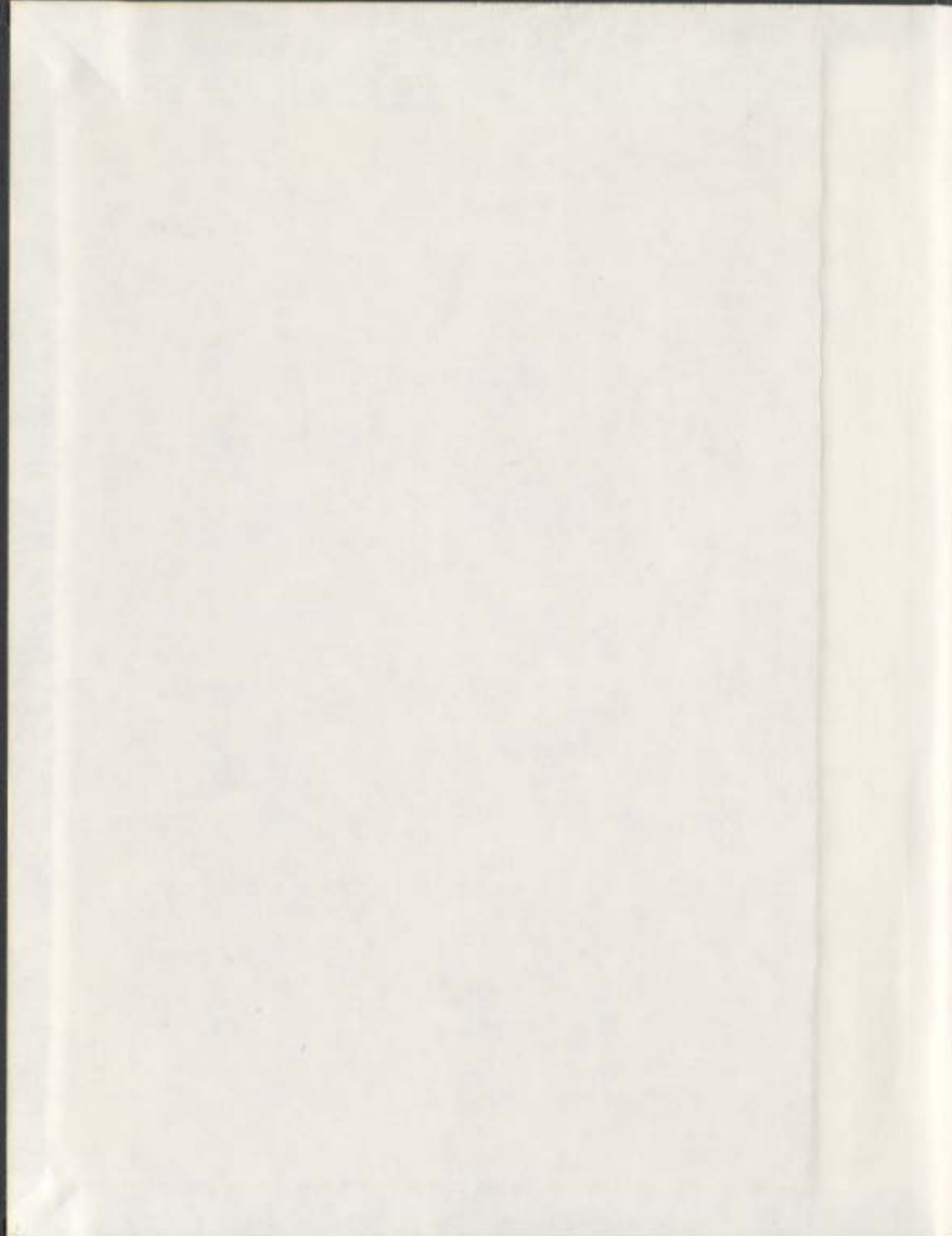
MAGNETIC ANISOTROPY AND CORRECTION OF
PALEOMAGNETIC INCLINATION SHALLOWING
IN DEEP-SEA SEDIMENTS

CENTRE FOR NEWFOUNDLAND STUDIES

**TOTAL OF 10 PAGES ONLY
MAY BE XEROXED**

(Without Author's Permission)

SATRIA BIJAKSANA



**MAGNETIC ANISOTROPY AND CORRECTION OF PALEOMAGNETIC
INCLINATION SHALLOWING IN DEEP-SEA SEDIMENTS**

by

Satria Bijaksana, B.Sc. Hon., M.Sc.

A Thesis submitted to the School of Graduate
Studies in partial fulfilment of the
requirements for the degree of
Doctor of Philosophy

Department of Earth Sciences
Memorial University of Newfoundland

February 1996

St. John's

Newfoundland



National Library
of Canada

Acquisitions and
Bibliographic Services

395 Wellington Street
Ottawa ON K1A 0N4
Canada

Bibliothèque nationale
du Canada

Acquisitions et
services bibliographiques

395, rue Wellington
Ottawa ON K1A 0N4
Canada

Your file *Votre référence*

Our file *Notre référence*

The author has granted a non-exclusive licence allowing the National Library of Canada to reproduce, loan, distribute or sell copies of this thesis in microform, paper or electronic formats.

The author retains ownership of the copyright in this thesis. Neither the thesis nor substantial extracts from it may be printed or otherwise reproduced without the author's permission.

L'auteur a accordé une licence non exclusive permettant à la Bibliothèque nationale du Canada de reproduire, prêter, distribuer ou vendre des copies de cette thèse sous la forme de microfiche/film, de reproduction sur papier ou sur format électronique.

L'auteur conserve la propriété du droit d'auteur qui protège cette thèse. Ni la thèse ni des extraits substantiels de celle-ci ne doivent être imprimés ou autrement reproduits sans son autorisation.

0-612-25768-1

Canada

ABSTRACT

The inclination (I_{obs}) of natural remanent magnetization (NRM) in sediment may be shallower than the inclination (I_H) of the Earth's field in which it is acquired. This thesis investigates whether such inclination shallowing can be detected and corrected for by measuring the magnetic anisotropy of the sediment. Paleomagnetism and magnetic anisotropy were measured for 79 turbidite specimens from 3 cores on the Scotian Rise, 87 pelagic clay specimens from DSDP site 578, and 90 pelagic lime-mud specimens from DSDP site 606.

For the turbidites, I_{obs} is on average 12° shallower than the 61° expected from the geocentric axial dipole (GAD) model. The turbidites are also highly anisotropic with the ratio of anhysteretic remanence (ARM) along the hard axis (ARM_{min}) to that along the easy axis (ARM_{max}) averaging 0.82. A significant correlation between $\tan I_{obs}$ and ARM_{min}/ARM_{max} exists as *Hodych and Bijaksana* [1993] showed was expected from the theory of *Jackson et al.* [1991]. The correlation line's estimate of $\tan I_{obs}$ when $ARM_{min}/ARM_{max} = 1$ predicts $I_H = 69^\circ (+5^\circ/-10^\circ)$ with 95% confidence agreeing with the expected 61° .

The turbidites show a significant correlation between $\tan I_{obs}$ and the degree of compaction ΔV . The correlation line's estimate of $\tan I_{obs}$ when $\Delta V = 0$ predicts $I_H = 71^\circ (+6^\circ/-12^\circ)$ agreeing with the 61° and suggesting that the inclination shallowing is compaction-induced. A significant correlation between ARM_{min}/ARM_{max} and ΔV suggests the ARM anisotropy is also compaction-induced. Compaction experiments on a few

specimens further support a compaction origin for the ARM anisotropy and the inclination shallowing.

For the turbidites, the susceptibility anisotropy was similar to but smaller than the ARM anisotropy. The ratio of susceptibility along the hard axis (χ_{min}) to susceptibility along the easy axis (χ_{max}) averaged 0.90. A significant correlation was found between χ_{min}/χ_{max} and ARM_{min}/ARM_{max} and hence between $\tan I_{obs}$ and χ_{min}/χ_{max} . The latter correlation line's estimate of $\tan I_{obs}$ when $\chi_{min}/\chi_{max} = 1$ predicts $I_H = 67^\circ (+6^\circ/-13^\circ)$. This prediction is as successful as that using ARM_{min}/ARM_{max} and is much faster to measure.

An attempt was made to study the pelagic clays and pelagic lime-muds in a similar fashion. However, inclination shallowing only averaged 1° for the pelagic clays and 4° for the pelagic lime-muds and ARM anisotropy was also very low. The low inclination shallowing and anisotropy in these pelagic sediments are probably due to relatively low compaction.

Key words: paleomagnetism, deep-sea sediments, turbidites, pelagic sediments, magnetic inclination shallowing, magnetic anisotropy, sediment compaction.

To my parents

Siti Amsah Nataprawira and Supardan Martaadisubrata

ACKNOWLEDGEMENTS

I would like to express my appreciation to my supervisor, Joseph Hodych, for his constant encouragement and guidance in carrying out this research. Joe showed me the importance of perseverance and willpower in conducting research. He is also a great person to work with. I know many graduate students in the department of Earth Sciences who are envious of me for having such a wonderful supervisor.

I also like to thank Ali Aksu and Garry Quinlan who have served on my thesis committee. Ali showed me a lot about sampling and handling the sediments. Thanks are also due to Ernie Deutsch and G. S. Murthy for introducing me to the ideas and methods in paleomagnetism and rock magnetism.

I am indebted to Ray Pätzold for all the assistance he gave in the paleomagnetic laboratory, including proof-reading this thesis. I am also indebted to Helen Gillespie for her help in using the X-radiograph, to Maggie Piranian for her help in using the electron microprobe, and to Carolyn Emerson for her help in using the scanning electron microscope.

Over the years, a number of undergraduate students as well as participants of the WISE (women in science and engineering) program have helped me with the tedious tasks of demagnetizing the samples and measuring their magnetic anisotropy. I thank Kevin Dunphy, Phil McCausland, Christine White, Tanja Dwyer, Alison Gollop, Paul Spurvey and Jenny Slade for their help.

Some measurements were conducted at the Institute for Rock Magnetism (IRM) at the University of Minnesota, Minneapolis. I thank the scientists and staff at the IRM for their assistance, support and hospitality. Chris Hunt and Jim Marvin, in particular, helped me with the instruments. Also, I learned a lot from discussions with Subir Banerjee, Bruce Moskowitz, and Weiwei Sun. The IRM is funded by the W. M. Keck Foundation, the National Science Foundation, and the University of Minnesota.

I thank the Ocean Drilling Program and the Atlantic Geoscience Center at the Bedford Institute of Oceanography for allowing me to use samples from their repositories. The assistance and hospitality of the curators (Gerry Bode and Steve Prinz at ODP West-Coast Repository, Paula Weiss at ODP East-Coast Repository and Jean Pansford at Bedford) are acknowledged.

Living in a place far away from home is not always easy. Fortunately, there are many people who helped me and my family feel at home here. Dave and Sonja Curnew adopted me through the host family program and over the years we had become very good friends. I thank Joe and Carolyn Hodych, Ernie and Gladys Deutsch, Ray and Linda Pätzold as well as Mike and Camilla Tubrett for their hospitality. I also like to thank the graduate students in the department of Earth Sciences for their friendship. Special thank to Simon O'Brien, my office mate for years for being a real friend. Also special thank to the Muslim community of St. John's who have enriched our stay here.

Finally, I thank my wife, Tintin, for her patience and understanding and my children, Tizar and Afifah, for the joy and happiness they gave me.

This research was supported by a research grant to Joseph Hodych from the Natural Sciences and Engineering Research Council of Canada and by a scholarship from the Ministry of Education and Culture of the Republic of Indonesia. Additional financial support in the form of travel allowance was also received from the IRM.

TABLE OF CONTENTS

	Page
ABSTRACT	ii
ACKNOWLEDGEMENTS	v
TABLE OF CONTENTS	viii
LIST OF TABLES	xii
LIST OF FIGURES	xiii
LIST OF ABBREVIATIONS AND SYMBOLS USED	xix
CHAPTER 1 INTRODUCTION	
1.1 Marine Sediments and Paleomagnetism	1
1.2 Magnetization of Marine Sediments	2
1.3 Paleomagnetic Inclination Shallowing	4
1.4 Detecting and Correcting Inclination Shallowing in Marine Sediments ..	8
1.5 The Objectives of this Study	16
CHAPTER 2 DESCRIPTION OF THE SPECIMENS	
2.1 Introduction	18
2.2 Clay-rich Turbidite Muds from the Scotian Rise	19
2.3 Pelagic Clay-rich Muds of DSDP Site 578	21
2.4 Pelagic Lime-Muds of DSDP Site 606	24

	Page
2.5 Sampling of the Specimens	26
CHAPTER 3 ROCK MAGNETIC AND SCANNING ELECTRON MICROSCOPY (SEM) INVESTIGATIONS	
3.1 Introduction	29
3.2 Methods	30
3.3 Results	
3.3.1 Clay-rich Turbidite Muds from the Scotian Rise	34
3.3.2 Pelagic Clay-rich Muds of DSDP Site 578	39
3.3.3 Pelagic Lime-Muds of DSDP Site 606	43
CHAPTER 4 PALEOMAGNETIC MEASUREMENTS	
4.1 Methods	52
4.2 Results	
4.2.1 Clay-rich Turbidite Muds from the Scotian Rise	53
4.2.2 Pelagic Clay-rich Muds of DSDP Site 578	56
4.2.3 Pelagic Lime-Muds of DSDP Site 606	61
CHAPTER 5 MAGNETIC ANISOTROPY MEASUREMENTS	
5.1 Introduction	66

	Page
5.2	Methods of Magnetic Anisotropy Measurements 67
5.3	Results
5.3.1	Clay-rich Turbidite Muds from the Scotian Rise 70
5.3.2	Pelagic Clay-rich Muds of DSDP Site 578 71
5.3.3	Pelagic Lime-Muds of DSDP Site 606 79
5.4	Magnetic Anisotropy of the Turbidites and the Pelagic Sediments Compared 82
5.5	Comparing ARM Anisotropy and Susceptibility Anisotropy 83
CHAPTER 6 CORRELATING REMANENCE INCLINATION AND MAGNETIC ANISOTROPY AND PREDICTING PALEOMAGNETIC INCLINATION SHALLOWING	
6.1	Correlation between Remanence Inclination and ARM Anisotropy..... 90
6.2	Predicting Paleomagnetic Inclination Shallowing using the Correlation between Remanence Inclination and ARM Anisotropy 97
6.3	Correlation between Remanence Inclination and Susceptibility Anisotropy 103
CHAPTER 7 PARTICLE ARM ANISOTROPY	
7.1	Particle ARM Anisotropy Measurement 108

	Page
7.2 Grain Elongation and the Origin of Magnetic Anisotropy in the Turbidites	116
7.3 Estimating Particle ARM Anisotropy from Particle Shape	122
CHAPTER 8 ARE THE OBSERVED INCLINATION SHALLOWING AND ARM ANISOTROPY COMPACTION INDUCED?	
8.1 Correlating the Degree of Compaction with Remanence Inclination and ARM Anisotropy in the Turbidites	124
8.2 Compaction Experiments	130
8.3 Difficulties in Measuring Parameter <i>b</i>	137
8.4 Low Inclination Shallowing in the Pelagic Sediments	141
CHAPTER 9 CONCLUSIONS	144
REFERENCES	150
APPENDICES	
Appendix A Detailed Paleomagnetic Data	157
Appendix B Detailed ARM Anisotropy Data	167
Appendix C Detailed AMS Data	174

LIST OF TABLES

		Page
Table 2.1	Turbidite cores data	19
Table 3.1	Selected oxide concentrations from SEM semi-quantitative analysis	38
Table 5.1	Parameters p_o and s for the turbidite specimens	87

LIST OF FIGURES

	Page
Figure 1.1	The relation between $\tan I_{obs} / \tan I_H$ and ARM_{min} / ARM_{max} as predicted by Eq. (1.12) for various values of ARM_{\perp} / ARM_H 15
Figure 2.1	Location map of AGC sites from which the turbidites specimens came 20
Figure 2.2	Location map of DSDP site 578 22
Figure 2.3	Location map of DSDP site 606 25
Figure 2.4	Schematic of sampling technique 28
Figure 3.1	Example of typical hysteresis loops before and after paramagnetic correction showing all parameters obtained from the loops 33
Figure 3.2	SEM micrographs of magnetically extracted grains from core 28 35
Figure 3.3	SEM micrographs of magnetically extracted grains from core 24 36
Figure 3.4	SEM micrographs of magnetically extracted grains from core 13 37
Figure 3.5	Normalized susceptibility as a function of high temperature (a) and SIRM as a function of low temperature (b) for a typical turbidite specimen from the Scotian Rise 40
Figure 3.6	Parameters J/J_s and H_c/H_c from analysis of hysteresis loops for turbidite specimens from cores 28 (a), 24 (b) and 13 (c) 41
Figure 3.7	SEM micrographs of magnetically extracted grains from site 578 44

	Page
Figure 3.8	Normalized susceptibility as a function of high temperature (a) and SIRM as a function of low temperature (b) for a typical pelagic clay specimen from site 578 45
Figure 3.9	Parameters J/J_s and H_c/H_c from analysis of hysteresis loops for pelagic clay specimens of DSDP site 578 46
Figure 3.10	SEM micrographs of magnetically extracted grains from site 606 47
Figure 3.11	Normalized susceptibility as a function of high temperature (a) and SIRM as a function of low temperature (b) for a typical pelagic lime-mud specimen of DSDP site 606 50
Figure 3.12	Parameters J/J_s and H_c/H_c from analysis of hysteresis loops for lime-mud specimens of DSDP site 606 51
Figure 4.1	Typical intensity decay curves and the components of NRM during AF demagnetization for turbidite specimens from the Scotian Rise 54
Figure 4.2	The summary of paleomagnetic measurements on turbidite specimens from the Scotian Rise 57
Figure 4.3	Typical intensity decay curves and the components of NRM during AF demagnetization for pelagic clay specimens of DSDP site 578 58
Figure 4.4	The summary of paleomagnetic measurements on pelagic clay specimens of DSDP site 578 60

	Page
Figure 4.5	Typical intensity decay curves and the components of NRM during AF demagnetization for pelagic lime-mud specimens of DSDP site 606 62
Figure 4.6	Summary of paleomagnetic measurements on pelagic lime-mud specimens of DSDP site 606 65
Figure 5.1	The summary of ARM anisotropy measurements for turbidite specimens of cores 28, 24 and 13 72
Figure 5.2	The summary of AMS measurements for turbidite specimens of cores 28, 24 and 13 73
Figure 5.3	Equal area projection of directions of ARM_{max} and ARM_{min} axes in specimens of cores 28, 24 and 13 74
Figure 5.4	Equal area projection of directions of maximum and minimum susceptibility axes in specimens of cores 28, 24 and 13 ... 75
Figure 5.5	The absolute value of the primary inclination for specimen whose MAD values are less than 10° and the summary of ARM anisotropy measurements for DSDP site 578 76
Figure 5.6	The summary of AMS measurements for pelagic clay specimens of DSDP site 578 77
Figure 5.7	Equal area projection of directions of maximum and minimum axes of ARM anisotropy (a) and AMS (b) in pelagic clay specimens of DSDP site 578 78

Figure 5.8	The absolute value of the primary inclination for specimen whose MAD values are less than 10° and the summary of ARM anisotropy measurements for DSDP site 606	80
Figure 5.9	Equal area projection of directions of ARM_{max} and ARM_{min} axes in pelagic lime-mud specimens of DSDP site 606	81
Figure 5.10	The normalized principle axes of the susceptibility ellipsoid (p_i) and ARM ellipsoid (q_i) for turbidite specimens of cores 28, 24 and 13	85
Figure 5.11	The relation between ARM_{min}/ARM_{max} and χ_{min}/χ_{max} predicted by Eq. (5.6) for various values of p_o in the observed range of χ_{min}/χ_{max} (a) and the plots for the turbidite specimens (b)	89
Figure 6.1	Tangent of the observed inclination $\tan I_{obr}$ and the inverse ARM anisotropy ARM_{min}/ARM_{max} for the three turbidite cores	92
Figure 6.2	The inclination of the ARM_{max} axis and the ARM_{min} axis of specimens as a function of depth in core 28	94
Figure 6.3	The X-radiographs of 28-0459 (a) and 28-0877 (b) that represent typical disturbed and undisturbed turbidite specimens respectively	95
Figure 6.4	Tangent of the observed inclination I_{obr} and the inverse ARM anisotropy ARM_{min}/ARM_{max} for cores 28 and 24 after the exclusion of the specimens whose ARM_{min} axis is more than 15° from vertical	96

Figure 6.5	The correlation observed between $\tan I_{obs}$ and the ARM_{min}/ARM_{max} for the turbidite cores 28 (a), 24 (b), 13 (c) and the combined data (d)	99
Figure 6.6	Plots of $\tan I_{obs}/\tan I_H$ versus ARM_{min}/ARM_{max} for a given predicted I_H in cores 28 (a), 24 (b), 13 (c) and the combined data (d)	101
Figure 6.7	Tangent of the observed inclination $\tan I_{obs}$ and the ratio χ_{min}/χ_{max} for the three turbidite cores	104
Figure 6.8	The correlation observed between $\tan I_{obs}$ and the χ_{min}/χ_{max} for the turbidite cores 28 (a), 24 (b), 13 (c) and the combined data (d)	106
Figure 7.1	Results of particle ARM anisotropy measurement, in which magnetic grains from each composite sample for each core were aligned using a DC field	113
Figure 7.2	Results of particle ARM anisotropy measurement, in which magnetic grains from each composite sample for each core were aligned using an alternating field	117
Figure 7.3	The relation between the particle ARM anisotropy γ and the grain axial ratio predicted by Eq. (7.5)	123
Figure 8.1	The relation between ARM_{min}/ARM_{max} and ΔV predicted by Eq. (8.3) for various values of b	127
Figure 8.2	Tangent of the observed inclination $\tan I_{obs}$, the degree of compaction	

	ΔV and the inverse ARM anisotropy ARM_{min}/ARM_{max} for cores 28 and 24	128
Figure 8.3	The correlation between $\tan I_{obs}$ and the degree of compaction ΔV for the turbidite cores 28 (a) and 24 (b)	131
Figure 8.4	The correlation between ARM_{min}/ARM_{max} and the degree of compaction ΔV for the turbidite cores 28 (a) and 24 (b)	133
Figure 8.5	Schematic of compaction apparatus used in this study	138
Figure 8.6	Results of compaction experiment in the turbidite samples.....	139

LIST OF ABBREVIATIONS AND SYMBOLS USED

Abbreviations

AF	Alternating Field
AGC	Atlantic Geoscience Centre
AMS	Anisotropy of Magnetic Susceptibility
ARM	Anhyseretic Remanent Magnetization
CRM	Chemical Remanent Magnetization
DC	Direct Current
DRM	Detrital Remanent Magnetization
DSDP	Deep Sea Drilling Project
GAD	Geocentric Axial Dipole
HPC	Hydraulic Piston Corer
IRM	Isothermal Remanent Magnetization
MAD	Maximum Angular Deviation
MD	Multi-domain
MPTS	Magnetic Polarity Time Scale
NRM	Natural Remanent Magnetization
ODP	Ocean Drilling Program
pDRM	Post-depositional DRM
PSD	Pseudo-single-domain

SD	Single-domain
SEM	Scanning Electron Microscope
SIRM	Saturation Isothermal Remanent Magnetization

Symbols

α	Particle susceptibility anisotropy
ARM_{hor}	Intensity of ARM given along the horizontal axis
ARM_{ver}	Intensity of ARM given along the vertical axis
ARM_{max}	Eigen-value of ARM anisotropy tensor along the maximum axis
ARM_{int}	Eigen-value of ARM anisotropy tensor along the intermediate axis
ARM_{min}	Eigen-value of ARM anisotropy tensor along the minimum axis
ARM_x	Intensity of ARM given along the x axis
ARM_y	Intensity of ARM given along the y axis
ARM_z	Intensity of ARM given along the z axis
ARM_{\perp}	ARM susceptibility of the particle perpendicular to its long axis
ARM_{\parallel}	ARM susceptibility of the particle parallel to its long axis
B	Magnetic Induction
b	A constant that relates inclination shallowing to compaction
χ	Intensity of specific (mass) susceptibility
χ_a	Susceptibility of the particle measured parallel to the long axis
χ_b	Susceptibility of the particle measured perpendicular to the long axis

χ_{max}	Eigen-value of AMS tensor along the maximum axis
χ_{int}	Eigen-value of AMS tensor along the intermediate axis
χ_{min}	Eigen-value of AMS tensor along the minimum axis
χ_o	Intrinsic susceptibility
χ_x	Susceptibility along the x axis
χ_y	Susceptibility along the y axis
χ_z	Susceptibility along the z axis
χ_{\perp}	Susceptibility of the particle perpendicular to its long axis
$\chi_{//}$	Susceptibility of the particle parallel to its long axis
DRM_x	DRM given along the x axis
DRM_y	DRM given along the y axis
DRM_z	DRM given along the z axis
ΔV	Degree of compaction
F	Magnetic foliation
f	Flattening factor
f_g	Flattening factor as a function of rolling angle
f_k	Flattening factor as a function of fraction of disc-shaped grains
ϕ	Porosity
ϕ_o	Initial porosity
γ	ARM particle anisotropy

h_A	Percent ARM anisotropy
H_c	Coercive force
H_{cr}	Coercivity of remanence
h_x	Percent susceptibility anisotropy
I_H	Inclination of the ambient field
I_{obs}	Inclination of observed remanence
J	Magnetization
J_r	Saturation remanence
J_s	Saturation magnetization
K_{ARM}	Anhyseretic susceptibility indicating the intensity of ARM
L	Magnetic lineation
λ	Paleolatitude
M/Mo	Ratio of NRM intensity to its original value
N	Number of observations
N_a	Demagnetizing factor parallel to the long axis
N_b	Demagnetizing factor perpendicular to the long axis
p_{max}	Normalized susceptibility along the maximum axis
p_{int}	Normalized susceptibility along the intermediate axis
p_{min}	Normalized susceptibility along the minimum axis
p_o	Parameter connecting susceptibility and remanence ellipsoids
p_x	Normalized susceptibility along the x direction

p_y	Normalized susceptibility along the y direction
p_z	Normalized susceptibility along the z direction
q_{max}	Normalized ARM along the maximum axis
q_{int}	Normalized ARM along the intermediate axis
q_{min}	Normalized ARM along the minimum axis
q_x	Normalized ARM along the x direction
q_y	Normalized ARM along the y direction
q_z	Normalized ARM along the z direction
R	Correlation coefficient
ρ	Bulk density of sample
ρ_w	Pore fluid density
s	$(1 - 3 p_o)$
T	Shape parameter
T_c	Curie point
T_V	Verwey transition temperature
v_f	Volume fraction of ilmenite lamellae
w	Volume fraction of water in the sample
x	Fraction of Fe_2TiO_4 in magnetite-ulvöspinel solid solution series
y	Fraction of Cr in chromian spinel series

CHAPTER 1

INTRODUCTION

1.1 Marine Sediments and Paleomagnetism

Long cores of marine sediments such as those of the DSDP (Deep Sea Drilling Project) and ODP (Ocean Drilling Program) are paleomagnetically valuable because they provide a continuous geomagnetic record that can encompass a large time interval. Moreover, the presence of fossils in these sediments provides accurate age information required for stratigraphic correlation. For these reasons, paleomagnetic study has been used as a standard procedure for nearly each leg of DSDP/ODP since the first legs in 1968 (*Opdyke and Phillips, 1969*). Although the cores are not oriented in azimuth, changes in sign of inclination or changes of 180° in declination allow measurement of the polarity changes used in magnetic stratigraphy. This marine polarity record extends back to 10 Ma or more (*Opdyke et al., 1974*) and agrees with the pattern of magnetic anomalies produced by sea-floor spreading (*Foster and Opdyke, 1970*).

Advances in paleomagnetic instrumentation now enable scientists to extract even more information from the core. For example, push-through cryogenic magnetometers give almost continuous readings of remanence direction and intensity along the core, facilitating paleointensity studies of the Earth's field. Push-through susceptibility meters give continuous readings of magnetic susceptibility along the core, facilitating correlation between cores and detection of paleoclimate signals. For example, magnetic susceptibility

of marine sediments has recently been shown to record climate changes driven by Milankovich cycles (e.g., *Bloemendal and deMenocal*, 1989; *Rea*, 1994; *Verosub and Roberts*, 1995).

However, one question remains about the use of marine sediments in paleomagnetism. Do these sediments record the magnetic inclination of the ambient field accurately? Although some observations show that this is the case, some recent observations show that the magnetic inclination recorded in marine sediment is shallower than predicted from other paleomagnetic data.

1.2 Magnetization of Marine Sediments

The presence of ferromagnetic grains enables sediments to acquire a remanent magnetization. Among the magnetic minerals normally present in marine sediments, magnetite is the most important since it is most abundant and has a high saturation magnetization of 4.8×10^5 A/m (*Butler*, 1992, p.29). In the marine environment, magnetite may be of organic as well as inorganic origin (*Chang and Kirschvink*, 1989; *Stolz et al.*, 1990).

In most cases, marine sediments carry detrital remanent magnetism (DRM). The acquisition of DRM can be complicated because of the many processes that may occur during sediment formation (*Verosub*, 1977; *Butler*, 1992). However, DRM acquisition is often simplified and divided into two phases. The first one occurs when fine-grained magnetized particles align with the Earth's magnetic field as they settle to the sea floor.

This magnetization acquired at the sediment-water interface is termed a depositional DRM. Fine magnetic grains within water filled voids in the sediments remain able to rotate and do not yet contribute to the remanence. However, further sedimentation increases the overburden load and compacts the sediments, preventing these fine magnetic grains from rotating freely. The remanence resulting from these fine magnetic grains is termed post-depositional DRM (pDRM). Bioturbation (mixing of near-surface sediments by organisms) frequently occurs in marine sediments, destroying depositional DRM and leaving only a pDRM (*Verosub, 1977*).

The orientation of coarser-grained magnetic particles, however, may be less affected by the Earth's magnetic field than by mechanical forces such as those due to gravity and water current (see *Tarling and Hrouda, 1993*). Although these grains are not the carriers of stable remanence, they are important in defining magnetic fabric, which often reflects sedimentological fabric.

After DRM is acquired, it may be affected by chemical alteration of the magnetic minerals (as reviewed by *Henshaw and Merrill, 1980*). For example DRM intensity may be lowered in the upper few metres of hemipelagic sediments if reducing conditions convert magnetite into pyrite (*Karlin and Levi, 1985*). Chemical remanent magnetization (CRM) may mask DRM if enough hematite forms from goethite, an oxyhydroxide produced by alteration of Fe-bearing silicates. However, the organic matter in fossil-bearing pelagic sediments may prevent such oxidation (*Butler, 1992, p. 129*).

1.3 Paleomagnetic Inclination Shallowing

Early paleomagnetic studies using conventional and giant (25-30 m) piston cores suggested that marine sediments could record the magnetic inclination of the ambient field accurately (e.g., *Opdyke and Henry, 1969*). In fact, the paleolatitude data derived from magnetic inclination records of marine sediments had been used to estimate the latitudinal component of the absolute motion of the drilling sites and to reconstruct the motion of the oceanic plates (*Sclater and Cox, 1970*).

However, with the advance of drilling techniques (hydraulic piston and rotary coring) that enable one to obtain cores from greater depth, recent observations (e.g., *Kent and Spairosu, 1982; Celaya and Clement, 1988; Arason and Levi, 1990a; Gordon, 1990; Tarduno, 1990*) show that the magnetic inclination recorded in marine sediment is sometimes shallower than predicted from other paleomagnetic data. This phenomenon is termed magnetic inclination shallowing and is also observed in non-marine sediments as well as in laboratory experiments (*Johnson et al., 1948; King, 1955; Griffith et al., 1960*). Inclination shallowing occurs when the inclination of the observed remanence I_{obs} is less than the inclination of the ambient field I_H and is often expressed as

$$f = \frac{\tan I_{obs}}{\tan I_H} \quad (1.1),$$

where $f (< 1)$ is called the flattening factor. Inclination shallowing leads to underestimation of paleolatitude λ , since following the geocentric axial dipole (GAD) model, we expect

$$\lambda = \tan^{-1}\left(\frac{1}{2} \tan I_{obs}\right) \quad (1.2),$$

assuming that $I_{obs} = I_H$.

Various mechanisms have been proposed as the cause of magnetic inclination shallowing. Early experimental studies (*e.g.*, *King*, 1955; *Griffith et al.*, 1960) showed that although the way the magnetic grains were aligned at the sediment/water interface did not affect the declination of the acquired DRM, it might deflect the inclination toward the horizontal. *King* [1955] measured inclination shallowing in laboratory redeposition of glacial varved sediments. *King* assumed that there were two types of magnetic carriers, namely spherical and disc-shaped grains whose magnetic moment is in the disc plane. The spherical grains should record the inclination of the ambient field accurately. However, the disc-shaped grains would be deposited with the disc plane horizontal at the sediment interface giving a shallower inclination. *King* suggested that the inclination shallowing would be the following function of f_k , the fraction of disc-shaped grains.

$$\frac{\tan I_{obs}}{\tan I_H} = 1 - f_k \quad (1.3).$$

For the varved sediments he used, *King* found that $f_k \approx 0.4$ fit the experimental data.

Like *King* [1955], *Griffith et al.* [1960] also redeposited the glacial varved sediments in the laboratory and measured their remanence inclination. They found that the

inclination shallowing was independent of particle size. They also noted that the division between spherical and disc-shaped grains in sediment as required by King's model was not obvious. *Griffith et al.* [1960] proposed an alternate model, in which inclination shallowing results from random rolling of magnetized spherical grains into adjacent holes at the sediment-water interface. For an assemblage of grains, this random rolling will not affect declination but will give inclination shallowing. *Griffith et al.* solved the problem of averaging over particles that roll in all directions analytically and found that

$$\frac{\tan I_{obs}}{\tan I_H} = 1 - f_g \quad (1.4),$$

where $f_g = (1 - \cos \Delta\theta) / (1 + \cos \Delta\theta)$ and $\Delta\theta$ is the rolling angle.

More recent experimental studies (*Blow and Hamilton, 1978; Anson and Kodama, 1987; Deamer and Kodama, 1990; Lu et al., 1990*), however, showed that compaction is a more likely cause for magnetic inclination shallowing observed in deep-sea sediments. *Blow and Hamilton* [1978] redeposited deep-sea sediment of the silty clay grade in the laboratory. Assuming that the remanence acts like a passive line element, they found that compaction induces magnetic inclination shallowing which fits the following relation

$$\frac{\tan I_{obs}}{\tan I_H} = 1 - \Delta V \quad (1.5),$$

where ΔV is the degree of compaction.

Anson and Kodama [1987] compacted synthetic sediments (equidimensional or acicular magnetite in a slurry of kaolinite and distilled water) and found that their data fit the above equation of *Blow and Hamilton* if it were modified by a constant factor b giving

$$\frac{\tan I_{obs}}{\tan I_H} = 1 - b \Delta V \quad (1.6).$$

They found that the value of b depends on the shape of the magnetic grains. Their results yielded $b = 0.54 \pm 0.18$ for equidimensional magnetite grains and $b = 0.63 \pm 0.18$ for acicular magnetite grains. They went further by proposing that the positively charged magnetite grains are electrostatically attached to the negatively charged clay flakes. Compaction rearranges the clay flakes more horizontally and consequently induces inclination shallowing. Although this electrostatic model was later discredited by *Deamer and Kodama* [1990] and *Lu et al.* [1990], who proposed Van der Waals forces instead, the governing Eq. (1.6) should still be valid. Furthermore, *Arason and Levi* [1990b] theoretically derived the inclination shallowing expected for various microscopic models of compacting sediment and suggested a similar expression to Eq. (1.6), where b is a constant whose value depends on the specific model. *Arason and Levi* [1990b] recommended choosing b to fit the inclination shallowing data from laboratory experiments and natural sediments.

A relation between compaction and inclination shallowing has also been observed in natural sediments. *Celaya and Clement* [1988] showed that the inclination shallowing

observed in deep-sea carbonate muds from DSDP sites in the North Atlantic correlates with a downhole decrease in water content, presumably due to compaction. *Arason and Levi* [1990a] showed that the downhole inclination shallowing observed in the clay-rich muds of DSDP Pacific site 578 correlates with the downhole decrease in average porosity suggesting a compaction-induced inclination shallowing. *Gordon* [1990] showed that the Cretaceous paleolatitudes estimated paleomagnetically using deep-sea sedimentary rock cores at nine DSDP sites from the Pacific were mostly shallower than predicted from other paleolatitude indicators. Later, *Tarduno* [1990] re-examined these paleomagnetic data and showed that the only likely mechanism for this remanence shallowing is compaction of sediments after deposition.

1.4 Detecting and Correcting Inclination Shallowing in Marine Sediments

The presence of inclination shallowing in marine sediments has usually been detected indirectly, *e.g.* by comparing the observed inclination with paleoinclination predicted from the paleomagnetism of igneous rocks (*Gordon*, 1990). Recently, several workers (*Arason*, 1991; *Collombat et al.*, 1993; *Hodych and Bijaksana*, 1993) have attempted to detect inclination shallowing from the magnetic properties of the sediments themselves and to correct for it. In principle, correcting for inclination shallowing requires determining the flattening factor $f = \tan I_{obs} / \tan I_H$.

Theoretically, there are two ways to approach this problem. One way is to assume that magnetic inclination shallowing is induced solely by compaction as described in Eq.

(1.6). *Arason and Levi* [1990a] suggested that the value of ΔV can be calculated from porosity data using

$$\Delta V = \frac{\phi_0 - \phi}{1 - \phi} \quad (1.7),$$

where ϕ is porosity and ϕ_0 is the initial porosity. Values of ϕ_0 for various types of marine sediments are given in *Hamilton* [1976]. Once the value of ΔV is known, one can find the corrected paleoinclination I_H from Eq. (1.6) if one can determine b . The parameter b can be estimated from experiments like those of *Anson and Kodama* [1987] in which sediments were given a pDRM and then were compacted in a consolidometer.

The other way to approach this problem is by measuring the anhysteretic remanent magnetization (ARM) anisotropy of the sediments. The association between magnetic inclination shallowing and ARM anisotropy has been confirmed by earlier studies *e.g.*, *Kodama and Sun* [1990] and *Hodych and Bijaksana* [1993]. *Kodama and Sun* [1990] found that laboratory compaction produced ARM anisotropy as well as inclination shallowing in their artificial clay-rich sediments. For their samples containing magnetite needles with a length of 0.45 μm and an elongation of 6:1, the percent ARM anisotropy (see Chap.5 for its definition) increased from 13.0% at an initial pressure of 18.4 kPa to 32.9% at 188.4 kPa, while remanence inclination decreased from 45° to 35°. Studying Cretaceous deep-sea limestones taken from five DSDP sites in the Pacific, *Hodych and Bijaksana* [1993] found that the primary inclination of their samples was on average 17°

shallower than the average 44° expected paleofield inclination and the average ARM anisotropy was 13%. In both studies, the samples were magnetically foliated with the maximum ARM axes parallel to bedding and the minimum axes perpendicular to bedding.

The association of ARM anisotropy with inclination shallowing suggests that ARM anisotropy can be used to detect and perhaps correct for magnetic inclination shallowing. Assuming that DRM acquisition is an anisotropic process and that the ARM tensor is a good estimate for the DRM tensor, *Jackson et al.* [1991] derived the following relation between inclination shallowing and ARM anisotropy for samples containing elongated single-domain particles

$$f = \frac{ARM_z}{ARM_x} \quad (1.8).$$

Here ARM_x and ARM_z are the maximum (x) and the minimum (z) principal components of the ARM tensor. The observed DRM vector consists of the vertical component (DRM_z) and the horizontal component, which for simplicity is denoted DRM_x ($DRM_y = 0$). Equation (1.8) and $\tan I_{obs} = DRM_z/DRM_x$ give the paleofield inclination I_H as

$$I_H = \tan^{-1} \left(\frac{DRM_z}{DRM_x} \frac{ARM_x}{ARM_z} \right) \quad (1.9).$$

Jackson et al. [1991] argued that the above approach is also physically justified for pDRM, if the rotation of magnetic particles is due to magnetic or non-magnetic alignment

and if the particles have uniaxial prolate shape anisotropy. Magnetic alignment is a rotation of magnetic particles due to an external magnetic field. This produces an errorless pDRM and an almost isotropic assemblage. Non-magnetic alignment is a mechanism (such as compaction and the attachment of magnetite to platy clay particles) that rotates the particle long axes into the horizontal plane. Unlike magnetic alignment, non-magnetic alignment produces both inclination shallowing of pDRM and a magnetically anisotropic assemblage.

Jackson et al. also recognized that there is another set of processes during pDRM acquisition termed randomization that can rotate the magnetic particles randomly. These processes produce a weaker pDRM intensity and although they do not change the direction of pDRM, they do reduce magnetic anisotropy. Hence, if randomization is significant in sediments, magnetic anisotropy will undercorrect for the inclination shallowing.

Jackson et al. modified Eq. (1.8) to take account of grains other than the elongated single-domain ones. Using a long-axis distribution function of *Stephenson et al.* [1986] and assuming that the grains have a uniform uniaxial prolate shape anisotropy, *Jackson et al.* derived

$$f = \frac{q_z \left(\frac{ARM_{\parallel}}{ARM_{\perp}} + 2 \right) - 1}{q_x \left(\frac{ARM_{\parallel}}{ARM_{\perp}} + 2 \right) - 1} \quad (1.10).$$

Here q_z (q_x) is the normalized ARM along the z (x) direction and is given by $q_z = ARM_z / (ARM_x + ARM_y + ARM_z)$ [$q_x = ARM_x / (ARM_x + ARM_y + ARM_z)$] and ARM_{\parallel} and ARM_{\perp} are ARM susceptibilities of the particle parallel and normal to its long axis. For simplicity, the quantity $ARM_{\parallel} / ARM_{\perp}$ is termed ARM particle anisotropy γ . Consequently, Eq. (1.10) becomes

$$I_H = \tan^{-1} \left(\frac{DRM_z (q_x(\gamma + 2) - 1)}{DRM_x (q_z(\gamma + 2) - 1)} \right) \quad (1.11).$$

For $\gamma \rightarrow \infty$ (as in the case of single-domain grains), the above equation reduces to Eq. (1.9).

Applying Eq. (1.11) requires two kinds of ARM anisotropy measurements. The first is the measurement of the specimen's bulk ARM anisotropy, from which q_x , q_z , and the ARM anisotropy tensor are obtained (McCabe *et al.*, 1985). The second is the measurement of ARM particle anisotropy, *i.e.* the average ARM anisotropy of the individual magnetic particles in the specimen (γ). While the measurement of the ARM anisotropy tensor for bulk specimens has been done widely and is accepted as a standard procedure, measurement of γ is difficult. Discussion of γ measurement will be deferred to Chapter 7.

The Jackson *et al.* model has been tested by Kodama and Sun [1992] and by Hodych and Bijaksana [1993]. Experimentally redepositing natural and artificial clay-rich samples, Kodama and Sun argued that this model is acceptable for the later stages of

compaction but not for the early stage. They found (see also *Sun and Kodama, 1992*) that during the early stage of compaction, there was a large decrease in inclination and magnetic intensity without the development of magnetic anisotropy. They suggested that this was caused by directional disturbance or randomization of magnetite grains with subvertical easy axes as the clay particles and clay domains move closer together during compaction at very low pressures. As the pressure increases, in the later stages of compaction, they suggest that the magnetite particles become attached to clay particles and follow the development of the clay fabric. This process induces both inclination shallowing and magnetic anisotropy. *Kodama and Sun [1992]* recommended that the correction for inclination shallowing be done separately for the two stages. While the model of *Jackson et al.* could be used for the later stages, early stage compaction would require compaction experiments to find the relationship between magnetic anisotropy and inclination shallowing developed during compaction.

If the ARM anisotropy is foliated in the bedding plane (ARM_{min} is perpendicular to bedding and $ARM_{int} \approx ARM_{max}$), Eq. (1.10) can be modified as follows

$$\frac{\tan I_{obs}}{\tan I_H} = \frac{(ARM_{min}/ARM_{max})(1 + ARM_{\perp}/ARM_{\parallel}) - 2 (ARM_{\perp}/ARM_{\parallel})}{1 - (ARM_{min}/ARM_{max})(ARM_{\perp}/ARM_{\parallel})} \quad (1.12)$$

(*Hodych and Bijaksana, 1993*). This equation predicts a relation between $\tan I_{obs}/\tan I_H$ and ARM_{min}/ARM_{max} that depends on the magnetic particle anisotropy parameter $ARM_{\perp}/ARM_{\parallel}$ ($= 1/\gamma$). Figure 1.1 (after *Hodych and Bijaksana, 1993*) shows this relation

for the observed range of ARM_{min}/ARM_{max} . For $ARM_{\perp}/ARM_{//} = 0$ (that is, for very elongated single-domain grains), the relation is linear. *Hodych and Bijaksana* [1993] used Fig. 1.1 to show that the predicted relation remains approximately linear, with the line continuing to pass through (1.0,1.0) provided that $ARM_{\perp}/ARM_{//}$ remains small compared to 1.0. They showed that this theoretical relationship agrees with the experimental results of *Kodama and Sun* [1992] on how $\tan I_{obs}/\tan I_H$ and ARM_{min}/ARM_{max} changed during the later stages of laboratory compaction of two clay-rich marine sediments containing magnetite of probable pseudo single-domain grain size. The data of *Kodama and Sun* [1992], shown by open and solid circles in Fig. 1.1, are in reasonable agreement with Eq. (1.12). The equation predicts that $ARM_{\perp}/ARM_{//}$ is ~ 0.25 and ~ 0.55 for the two specimens. Unfortunately $ARM_{\perp}/ARM_{//}$ measurements are not available to test this prediction. The data fit reasonably well to straight lines passing close to (1.0,1.0).

Hodych and Bijaksana [1993] also suggested that finding a significant linear correlation between $\tan I_{obs}$ and ARM_{min}/ARM_{max} is evidence of inclination shallowing and can be used to correct the inclination shallowing in a suite of sediments deposited together in a field of unknown inclination I_H . If the ARM anisotropy is foliated in the bedding plane and $\tan I_{obs}$ correlates significantly with ARM_{min}/ARM_{max} , then the correlation line's prediction of I_{obs} when $ARM_{min}/ARM_{max} = 1$ will be an estimate of I_H . They showed that this method is successful for the data of *Collombat et al.* [1990] on clay-rich Holocene marine sediments. They estimated I_H to be $58^{\circ} \pm 6^{\circ}$ compared to the 61° expected for the sampling site.

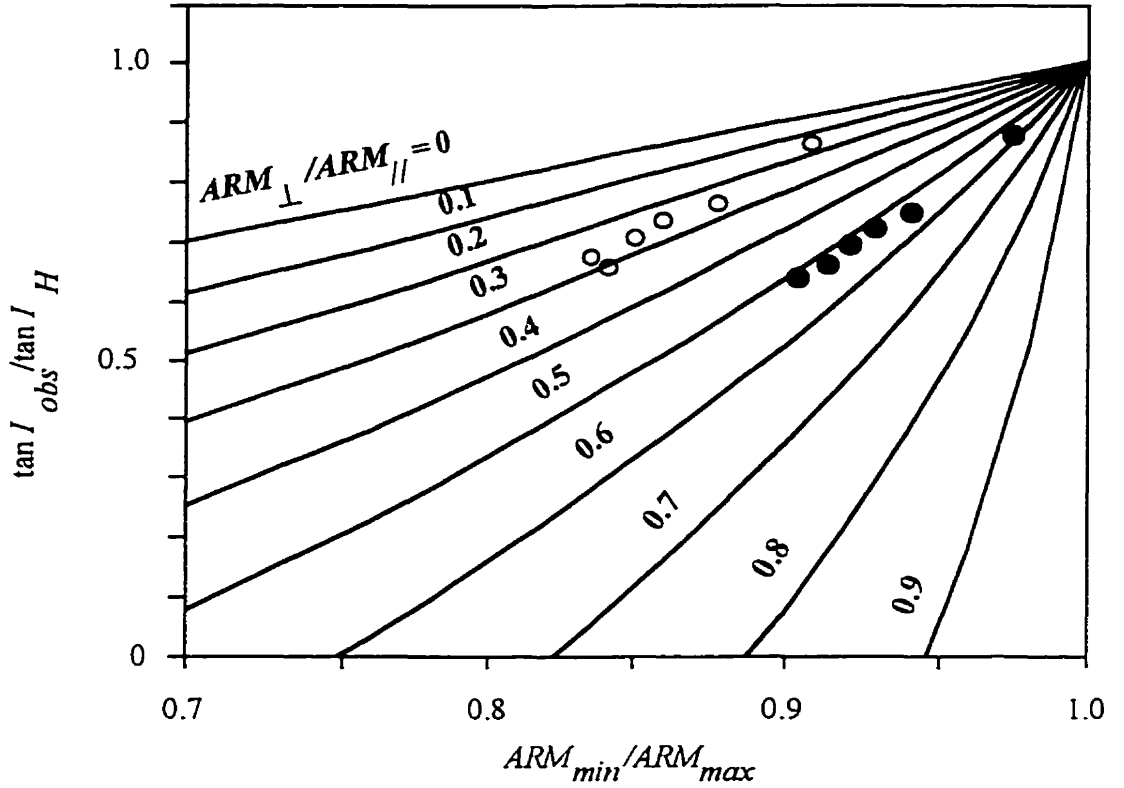


Figure 1.1 The relation between $\tan I_{obs} / \tan I_H$ and ARM_{min} / ARM_{max} predicted by Eq. (1.12) for various values of particle ARM anisotropy $ARM_{\perp} / ARM_{\parallel}$. The open and solid circles indicate observations by *Kodama and Sun* [1992] on the two clay-rich marine sediments that they progressively compacted in the laboratory.

Meanwhile, *Collombat et al.* [1990, 1993] using the same data showed empirically that

$$f = \frac{1}{P_A^3} \quad (1.13),$$

where $P_A = ARM_{hor}/ARM_{ver}$ and ARM_{hor} and ARM_{ver} are the ARM components along the horizontal and vertical respectively. However, using this relation to detect inclination shallowing is not recommended because it lacks theoretical justification and because, as shown by *Hodych and Bijaksana* (1993), the data of *Collombat et al.* show an equally good correlation between $\tan I_{obs}$ and ARM_{min}/ARM_{max} .

I.5 The Objectives of this Study

The primary objective of this study is to establish a method for detecting and possibly correcting magnetic inclination shallowing in deep-sea sediments. The main method developed uses magnetic anisotropy measurements. A reliable and well-tested method would improve the accuracy of the magnetic inclination record in deep-sea sediments so that wishfully they can be used for tectonic reconstructions. The other objective is to improve our understanding on how compaction of sediments affects their remanence inclination and magnetic anisotropy.

To achieve these objectives, specimens of different sedimentary types were studied. They are described in Chapter 2. The magnetic properties of these specimens

were studied by observing the extracted magnetic grains under a scanning electron microscope (SEM) and by using several rock magnetic methods to identify the magnetic minerals (Chapter 3). The natural remanence of the specimens was measured and the results are described in Chapter 4. The ARM anisotropy as well as the anisotropy of magnetic susceptibility (AMS) of most specimens were measured and the results are described in Chapter 5. This chapter also discusses the probable cause of magnetic anisotropy in the sediments including why some of the sediments are more anisotropic than others. The ARM anisotropy of anisotropic specimens was compared with the susceptibility anisotropy and the relation between the two was investigated.

Correlation between remanence inclination and magnetic anisotropy was tested, as described in Chapter 6, and used to detect and to correct for the inclination shallowing. Several methods for measuring particle ARM anisotropy γ , which is crucial in modelling inclination shallowing, were attempted and are discussed in Chapter 7. In Chapter 8 the role of compaction in inducing magnetic anisotropy and inclination shallowing in the sediments was tested using both compaction data from the cores and the results of our laboratory compaction experiments. Chapter 9 summarizes the conclusions of this study.

CHAPTER 2

DESCRIPTION OF THE SPECIMENS

2.1 Introduction

The marine sediments used in this study were chosen based on the following criteria. Firstly, they have to be deposited in mid-latitudes where inclination shallowing should be most pronounced. Secondly, it helps if the sedimentary record is continuous and relatively young in age. Inclination shallowing in older sedimentary rocks is more difficult to prove since it is more difficult to obtain a reliable estimate of the paleolatitude of deposition. Also, older sediments often display hiatuses that complicate the determination of their age and sedimentation rate. Older sediments are likely to be more lithified making redeposition and compaction experiments harder. Thirdly, it is important to study different types of marine sediments since the mechanisms for magnetization acquisition and inclination shallowing depend on factors such as lithology and sedimentation rate as well as magnetic mineralogy. This study selected pelagic clay-rich muds, pelagic lime-muds, and clay-rich turbidite muds since they represent the most common types of deep-sea sediments.

Clay-rich turbidite muds were sampled from several AGC (Atlantic Geoscience Centre) cores which had never been measured paleomagnetically, but which were collected near sites at which inclination shallowing had been reported by *Collombat et al.* [1990, 1993]. Pelagic clay-rich muds were sampled from cores from DSDP sites 578 at

which magnetic inclination shallowing had been reported by *Arason and Levi* [1990a]. Pelagic lime muds were sampled from cores from DSDP site 606 at which *Celaya and Clement* [1988] reported inclination shallowing.

2.2 Clay-rich Turbidite Muds from the Scotian Rise

AGC cores HUD88010 no. 24 and 28 and HUD91020 no. 13 were located (Fig. 2.1) in the levee of a 130 km wide channelized debris flow system on the Scotian Rise (*Berry, 1992*). The cores were obtained using a large piston corer system called the Long Core Facility. Table 2.1 summarizes the core data. For simplicity, these cores will be identified throughout this study as cores 24, 28 and 13.

Based on radiocarbon dating of foraminifera, the sediment in core 13 is determined to be 20 ka in age at 6.8 m depth . Although the age of sediments in the other two cores is less well constrained, the presence of certain marker such as the Albatross Debris Flow suggests that their age is comparable to that of core 13 (*Berry and Piper, 1993*).

Table 2.1 Turbidite core data (from *Berry, 1992*)

Cruise/ Core Number	Location	Water depth (m)	Total length (m)
HUD88010-24	42°10.25'N 62°36.14'W	2,613	8.4
HUD88010-28	41°32.65'N 62°15.04'W	3,825	11.3
HUD91020-13	41°49.76'N 62°19.81'W	3,450	7.7

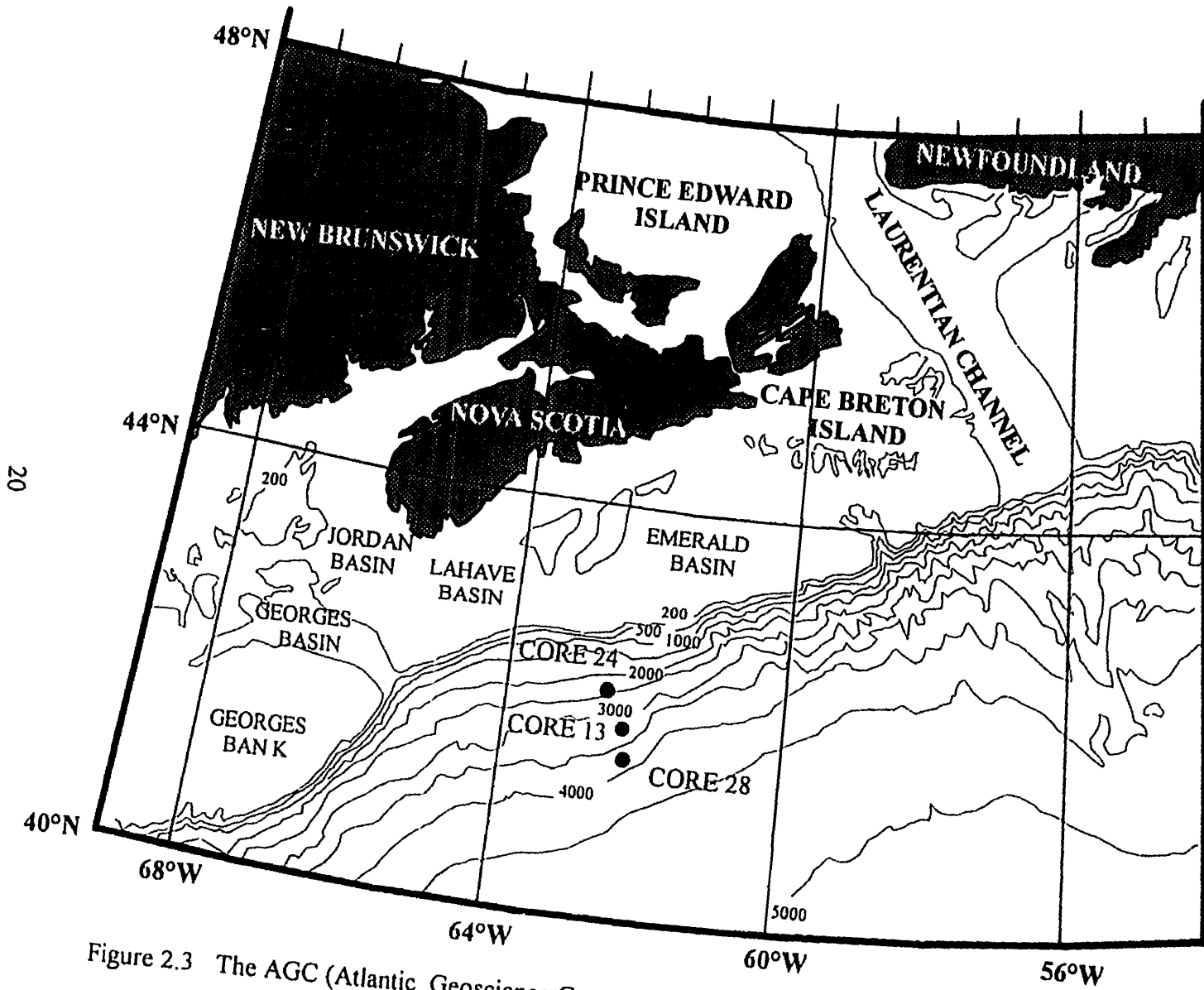


Figure 2.3 The AGC (Atlantic Geoscience Centre) sites from which the turbidite specimens came. ● CORE SITES

All specimens were taken from a depth of 4 m or greater where the cores are classified as laminated mud, based on the facies analysis of *Berry* [1992]. The mud consists of clay size particles and is brown to reddish brown in colour. Laminations are indicated by variation in silt content and/or colour changes. There is no sign of bioturbation. This mud is interpreted to be a fine-grained turbidite (*Berry*, 1992). Towards the bottom of core 28, there are intervals of unordered mud conglomerate interpreted as debris flow deposits (*Berry*, 1992).

The density of sediments increases with depth from about 1.5 g cm^{-3} at the top of the core to about 1.8 g cm^{-3} at the bottom. The water content (weight of salt water/weight of solid) decreases abruptly from 120% at about 60-80 cm to about 70-80% at 100-150 cm and then decreases steadily to about 50% at the bottom (*Berry*, 1992). Density and water content data are not available for core 13.

2.3 Pelagic Clay-rich Muds of DSDP Site 578

DSDP site 578 ($33^{\circ}55.56'N$; $151^{\circ}37.74'E$) is located on the west side of Shatsky Rise about 1000 km off Japan (Fig. 2.2). The cores, 176.8 m in total length, were obtained using a hydraulic piston corer (HPC) at a water depth of 6,010 m. The core recovery was high (98%) while the drilling disturbance was minimal (*Shipboard Scientific Party*, 1985). A combination of microfossils and paleomagnetic stratigraphy showed that the sediment accumulation rate changed dramatically from 40 mm/ka to 25 mm/ka during the Pleistocene to 8 mm/ka during the Miocene (*Shipboard Scientific Party*, 1985). This

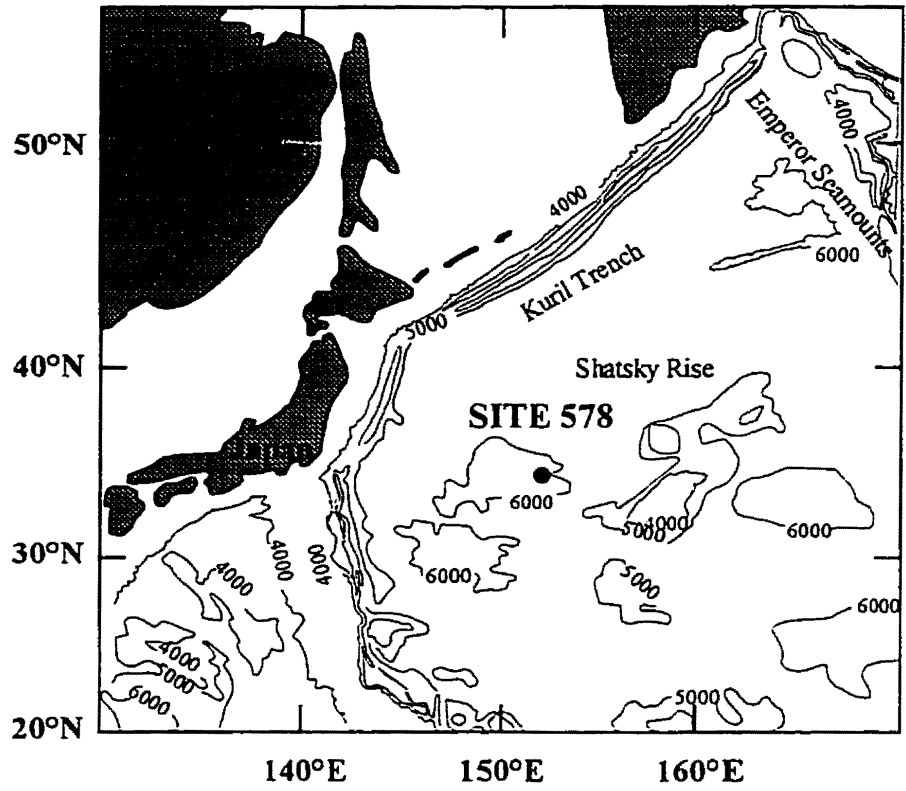


Figure 2.2 Location map of DSDP site 578.

change occurs at a depth of about 120 m. The quality of paleomagnetic data deteriorates at this level (*Heath et al.*,1985; *Arason and Levi* 1990a). For these reasons, only specimens from the upper 120 m of sediments (the Pleistocene to the late Miocene) were used in this study.

Based on macroscopic core description and smear slide analyses, the *Shipboard Scientific Party* (1985) divided these 120 m of sediments into 2 units. Unit 1 (0 m to 76.60 m) is gray to olive gray siliceous-clay while unit 2 (76.60 m to 124.50 m) is yellowish brown to brown siliceous-clay. The clay content is as high as 93% in some specimens (*Lenôtre et al.*,1985), whereas the calcium carbonate content is < 0.6% throughout the core (*Ku et al.*, 1985). More than 80% of the sediments total mass were eolian in origin (*Janecek*, 1985).

Using X-Ray diffraction to study the clay stratigraphy, *Lenôtre et al.* [1985] showed that these sediments contain comparable amount of illite and smectite (25 to 40%) and lesser amounts of chlorite, kaolinite and mixed layers. In contrast, the sediments below 120 m contain up to 80% smectite. Ash layers are common except between 29.7 and 39.5 m (*Shipboard Scientific Party*, 1985). These sediments also seem to be bioturbated at various places (*Shipboard Scientific Party*, 1985). The bulk density increases downward from 1.319 g cm⁻³ at 9.68-9.75 m to 1.364 g cm⁻³ at 110.08-110.15 m, probably due to compaction accompanying burial (*Schoonmaker et al.*, 1985).

2.4 Pelagic Lime-Muds of DSDP Site 606

DSDP site 606 (37°20.32'N; 35°29.99'W) is located on the western flank of the Mid-Atlantic Ridge (Fig. 2.3). The cores, 165.75 m in total length, were obtained using the advanced piston corer at a water depth of 3,007 m. The oldest sediment cored is early Pliocene. The core recovery was high (93%), while the drilling disturbance was minimal (*Shipboard Scientific Party*, 1987).

Using paleomagnetic stratigraphy, *Baldauf et al.* [1987] calculated the sedimentation rates at this site and showed that they average 30 m/m.y. for the Pleistocene (0 to 54 m). They vary from about 25 m/m.y. in the upper 25 m to about 42 m/m.y. in the interval from 25 to 54 m. From 54 to 107 m (the upper Pliocene) the average sedimentation rate increases to 34 m/m.y. From 107 m to the bottom of the hole (the upper to lower Pliocene) the sedimentation rate jumps to 62 m/m.y.

The major lithologic unit is foraminiferal-nannofossil ooze. The first 100 m contains green and purple laminae (subunit A). The lamination disappears gradually at a depth of 100 m giving way to a white and homogeneous sediment (subunit B). The calcium carbonate content is high throughout the cored section ranging from 80 to 90% in the top 25 m to more than 90% in the remainder of the core. Pyrite-rich patches and stringers are abundant. Bioturbation is noted in only very few spots. The water content and porosity decrease almost linearly with depth. The bulk density increases from about 1.6 g cm⁻³ in the first few meters to about 1.8 g cm⁻³ at the bottom of the core (*Shipboard Scientific Party*, 1987).

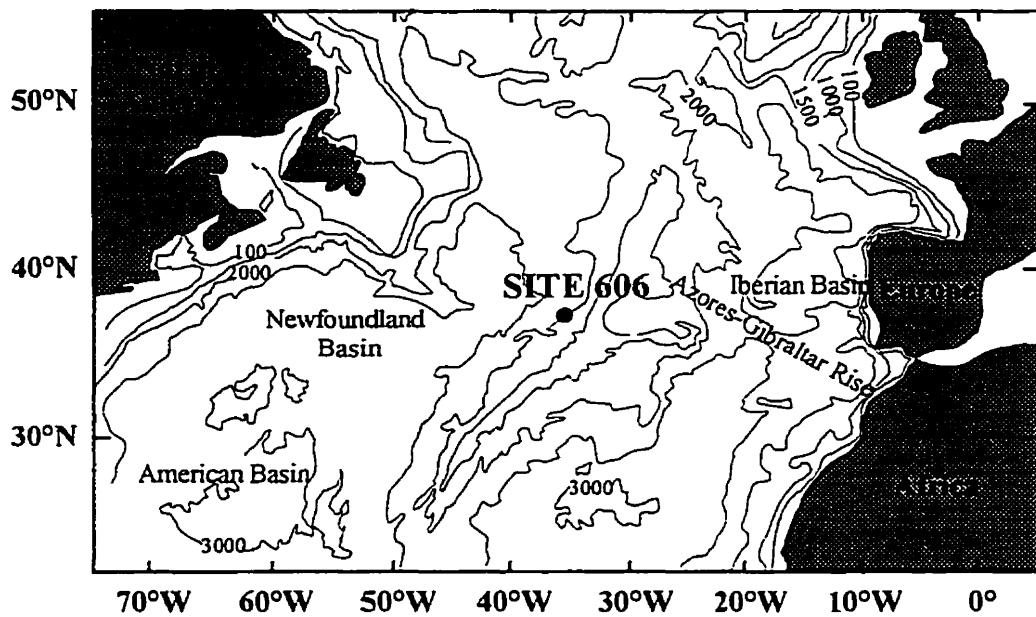


Figure 2.3 Location map of DSDP site 606.

2.5 Sampling of the Specimens

The turbidites were sampled at the repository workshop of the AGC in Dartmouth, Nova Scotia. The DSDP specimens were sampled at the DSDP/ODP repository workshops at Scripps Institution of Oceanography in La Jolla, California (for site 578) and at Lamont-Doherty Earth Observatory in Palisades, New York (for site 606).

The specimens were taken by pushing a 25.4 mm cylindrical plastic holder (22 mm internal diameter \times 19 mm length and tapered at the bottom rim) into a section of the split core which looks undisturbed. Assuming that the cores were drilled vertically, the proposed specimen was marked for up-down and horizontal orientations (Fig. 2.4.a). The holder was then pushed into the core (Fig. 2.4.b). To prevent it from rotating during penetration, the holder was held by an aluminium tube connected to a mechanical press. Excess specimen at the bottom of the holder was then trimmed (Fig. 2.4.c). The orientation perpendicular to the up-down axis is nominally called "east-west" axis, while the orientation along the cylindrical axis of the holder is called "north-south" axis. To prevent the specimens from drying, they were sealed with plastic caps and cello tape and then individually housed in small plastic vials along with a piece of wet foam. The whole collection was then stored in a cold-storage chamber (2 to 4°C).

Each DSDP specimen was taken at intervals of 1 to 1.5 m along the core and is assigned a number such as 578-1-1-47, which indicates that the specimen was taken 47 cm below the top of section 1 of core 1 from the hole drilled at site 578. This labelling is followed occasionally by another label such as 0.47 mbsf for specimen 578-1-1-47, which

means that the specimen was at 0.47 meter below sea floor (mbsf). The turbidites were taken at an interval of 20 cm. To avoid "soupy" sections, only specimens from the depth of about 4 m or greater were collected. Each turbidite specimen was assigned a number such as 28-0645 indicating that the specimen was taken 645 cm below the top of core HU88010-28.

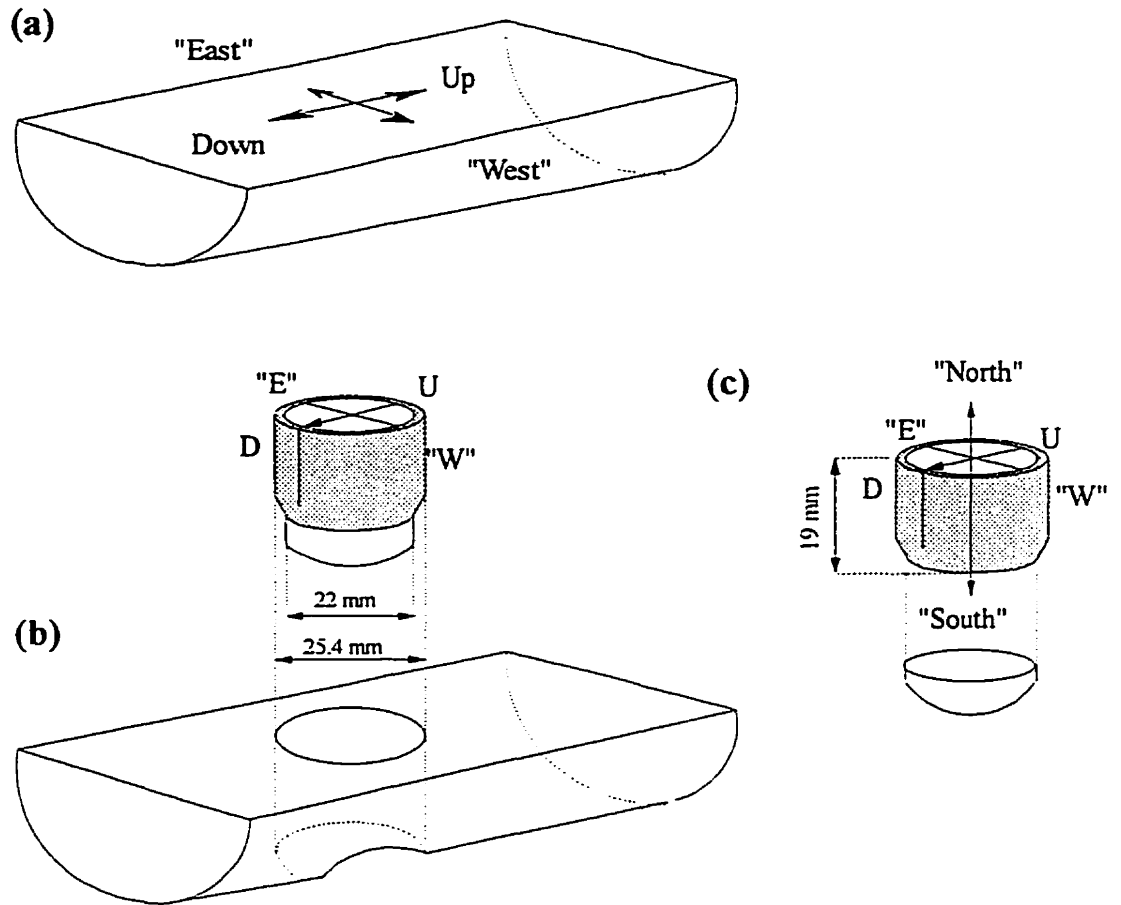


Figure 2.4 Schematic of sampling technique. (a) The vertical and horizontal orientations are marked on the split core sample. (b) A tapered cylindrical plastic holder is then pushed into the core using a mechanical press (not drawn) that was designed to prevent the holder from rotating during penetration. The holder is also marked for down and up orientations. (c) The specimen is then trimmed to fit the holder. Note that the 'east-west' and the 'north-south' axes are arbitrary.

CHAPTER 3
ROCK MAGNETIC AND SCANNING ELECTRON MICROSCOPE (SEM)
INVESTIGATIONS

3.1 Introduction

Magnetic properties of natural sediments depend not only on what magnetic minerals they contain but also on their concentration and the size and shape of their grains. The concentration of magnetic grains affects the intensity of magnetization and the magnetostatic interactions between the grains. Differences in grain size can produce differences in domain state and hence great differences in magnetic properties. The shape of the magnetic grains affects how anisotropic the sediment is.

The aim of rock magnetic and scanning electron microscope (SEM) investigations in this study is to determine the above properties of the magnetic minerals in the studied samples. The rock magnetic and SEM methods complement each other.

SEM provides direct observation of the size and shape of magnetic grains extracted from the sediments. Equipped with an energy-dispersive X-ray analysis system, SEM also provides semi-quantitative estimates of the percentages of elements (other than oxygen) in the magnetic grains. However, due to their resolution limit of $\sim 0.1 \mu\text{m}$, commercially available SEMs cannot resolve single-domain magnetite grains that are smaller than $0.1 \mu\text{m}$ (Freeman, 1986) which can be important carriers of stable remanence. Indeed, in the energy-dispersive mode, resolution is even poorer. The SEM

investigation also depends on the success of the magnetic extraction, which tends to separate larger and more magnetic grains.

Rock magnetic methods, on the other hand, help identify magnetic minerals and help measure their concentrations even when grains are less than 0.1 μm . All rock magnetic measurements were performed at the Institute for Rock Magnetism at the University of Minnesota, Minneapolis, whereas the SEM studies were performed at Memorial University of Newfoundland, St. John's.

3.2 Methods

For SEM observation, the magnetic grains have to be extracted and concentrated because their concentration in natural sediments is very low. The larger magnetic grains are more likely to be extracted, but we assume that their shape and mineralogy are similar to those of the smaller grains. The extraction was performed by inserting a rod magnet, covered by a thin plastic sheet (Saran Wrap), into a thin slurry made by mixing small samples (1 g), taken from four representative specimens within one core or hole, with deionized water. After stirring for about 10 minutes, the magnet was taken out of the slurry and its plastic cover was removed. The particles that clung to the plastic were then washed off with alcohol onto a glass slide, which was then placed in an alternating magnetic field of about 200 mT to align the grains. Soon after the alcohol dried out (it took only a minute or so), the field was removed and the slide was then carbon coated.

The carbon-coated slides were then examined in a Hitachi S570 Scanning Electron Microscope at an accelerating voltage of 20 kV. This microscope is also capable of backscattered electron imaging and is equipped with an energy-dispersive X-ray analysis system which allows semi-quantitative analysis of element or oxide concentrations. Tracor Northern's software package called SSQ was used. It models and subtracts background, measures peak intensities and then provides analyses of samples without a standard to calculate element or oxide percentage. It uses a ZAF program that automatically corrects for atomic number (Z), absorption (A), and fluorescence (F). The TiO_2/FeO ratios obtained with the SEM seem quite reliable; titanomagnetite grains extracted from a dolerite sample yielded 0.260 ± 0.068 (averaging 8 analysed grains) by SEM and 0.225 ± 0.026 (averaging 6 analysed grains) with a polished thin section and quantitative analysis with a Cameca SX50 electron microprobe. The backscattered and secondary electron images were recorded on Polaroid Type 650 Positive/Negative film.

In this study, measurements of magnetic susceptibility versus high temperature and saturation remanence versus low temperature were used to infer the type of magnetic mineral present. Hysteresis loops were also measured to infer domain state.

Magnetic susceptibility was measured as a function of high temperature using a KLY-2 Kappabridge susceptibility meter with a CS-2 furnace (Geofizika Brno). The heating was carried out in air. The curve of magnetic susceptibility versus temperature can provide the Curie point (T_c) which is, for example, about 580°C for pure magnetite and about 680°C for hematite (*Butler*, 1992, pp.29-31).

Saturation isothermal remanent magnetization (SIRM) was measured as a function of low temperature using the Magnetic Property Measurement System (MPMS, Quantum Design). In this measurement, a small sample (about 20-30 mg) was cooled to liquid helium temperature and was given a SIRM. Remanence was measured as temperature was increased in small steps until room temperature was reached. For magnetite-bearing samples, one can expect a large drop in intensity at about 120K close to the Verwey transition temperature, T_v (Hodoch, 1991). This drop is due to magnetite's crystallographic phase transition from orthorhombic to cubic. However, oxidation of the magnetite (Özdemir *et al.*, 1993) or the presence of other elements such as titanium (Syono, 1965) or chromium (Schmidbauer, 1971) may suppress the Verwey transition.

The domain state of magnetic grains in the specimens was inferred by measuring their hysteresis loops which yielded the coercive force (H_c), saturation magnetization (J_s) and saturation remanence (J_r). Saturation magnetization was determined from the loops after they had been corrected for paramagnetism as shown in Fig. 3.1.a. The coercivity of remanence (H_{cr}) was measured by determining the size of DC field required to reduce SIRM to zero (Fig. 3.1.b). The measurements were performed using an alternating gradient force magnetometer (MicroMag, Princeton Measurements) which requires only a tiny specimen of about 10-20 mg. The instrument calculated all the parameters automatically. A plot of J/J_s vs H_{cr}/H_c was then used as suggested by Day *et al.* [1977] to infer the domain state of the specimen's magnetic grains.

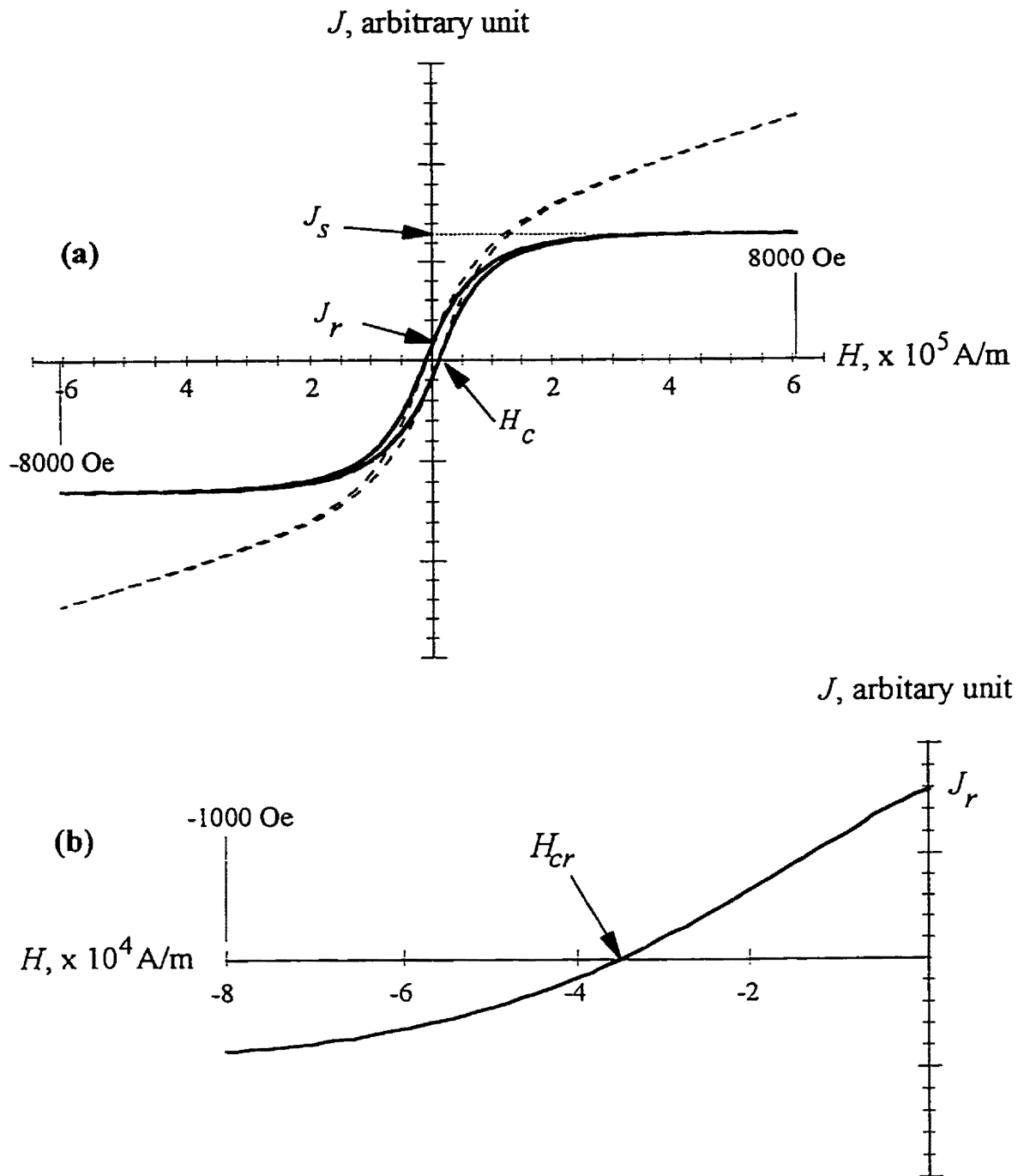


Figure 3.1 (a) Example of typical hysteresis loops before (dashed) and after (solid) paramagnetic correction showing all parameters obtained from the loops. (b) The coercivity of remanence H_{cr} was determined by demagnetizing SIRM with a DC field. All parameters were calculated automatically by the same software that controls the MicroMag. Data are for specimen 28-0945.

3.3 Results

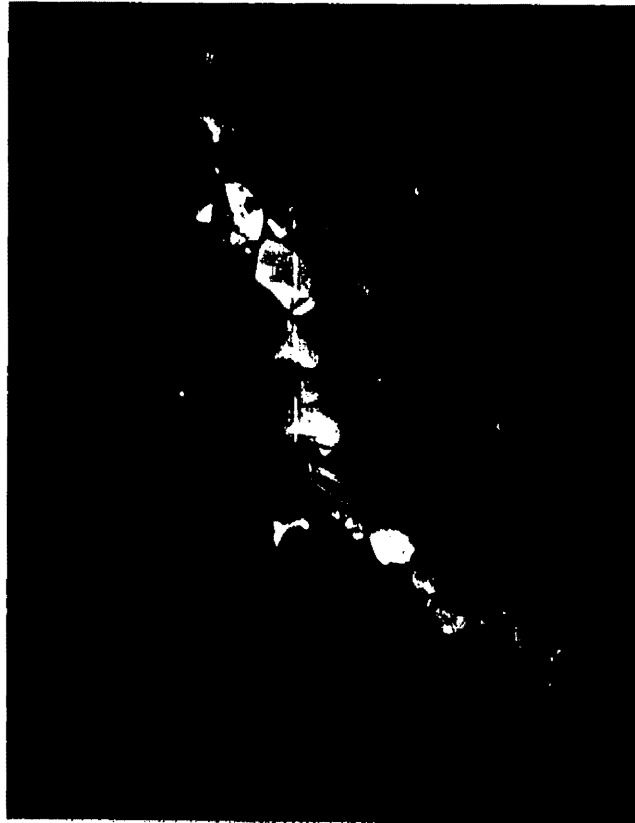
3.3.1 Clay-rich Turbidite Muds from the Scotian Rise

Three slides of the grains extracted from composite samples representing the turbidites of cores 28, 24 and 13 respectively, were examined with the SEM. Figures 3.2 to 3.4 show typical SEM images for the three turbidite slides in both backscattered and secondary electron modes. Iron-rich magnetic grains are identified readily from their bright appearance in the backscattered electron images. Some non-magnetic minerals, such as quartz, are also present and are identified by their dull appearance in backscattered electron images. In all slides, the magnetic grains are irregular in size and shape but most are roughly equidimensional and seem to be fragments of once larger particles.

Energy-dispersive X-ray analyses were obtained for 21 or 22 iron oxide grains from each slide and the normalized weights of selected oxides were calculated. Titanium was the only element, other than iron, detected in significant amount in the magnetite grains and even the titanium content was very low. The weight ratio of TiO_2/FeO is listed in Table 3.1 and averages 0.01 ± 0.02 for cores 28 and 13 and 0.01 ± 0.01 for core 24. That is, the magnetite is essentially pure suggesting it originated from a felsic rather than a mafic source rock (*Freeman, 1986*).

Nine turbidite specimens (5 from core 28 and 2 each from cores 24 and 13) were measured for magnetic susceptibility and SIRM as a function of temperature. Figure 3.5.a shows magnetic susceptibility as a function of temperature on heating to 700°C and cooling, for specimen 28-0714, which is typical of all nine specimens. A rise of

(a)



(b)



Figure 3.2 SEM micrographs of magnetically extracted grains from a composite sample made of four of the turbidite specimens from core 28 in backscattered (a) and secondary (b) electron images.

(a)**(b)**

Figure 3.3 SEM micrographs of magnetically extracted grains from a composite sample made of four of the turbidite specimens from core 24 in backscattered (a) and secondary (b) electron images.

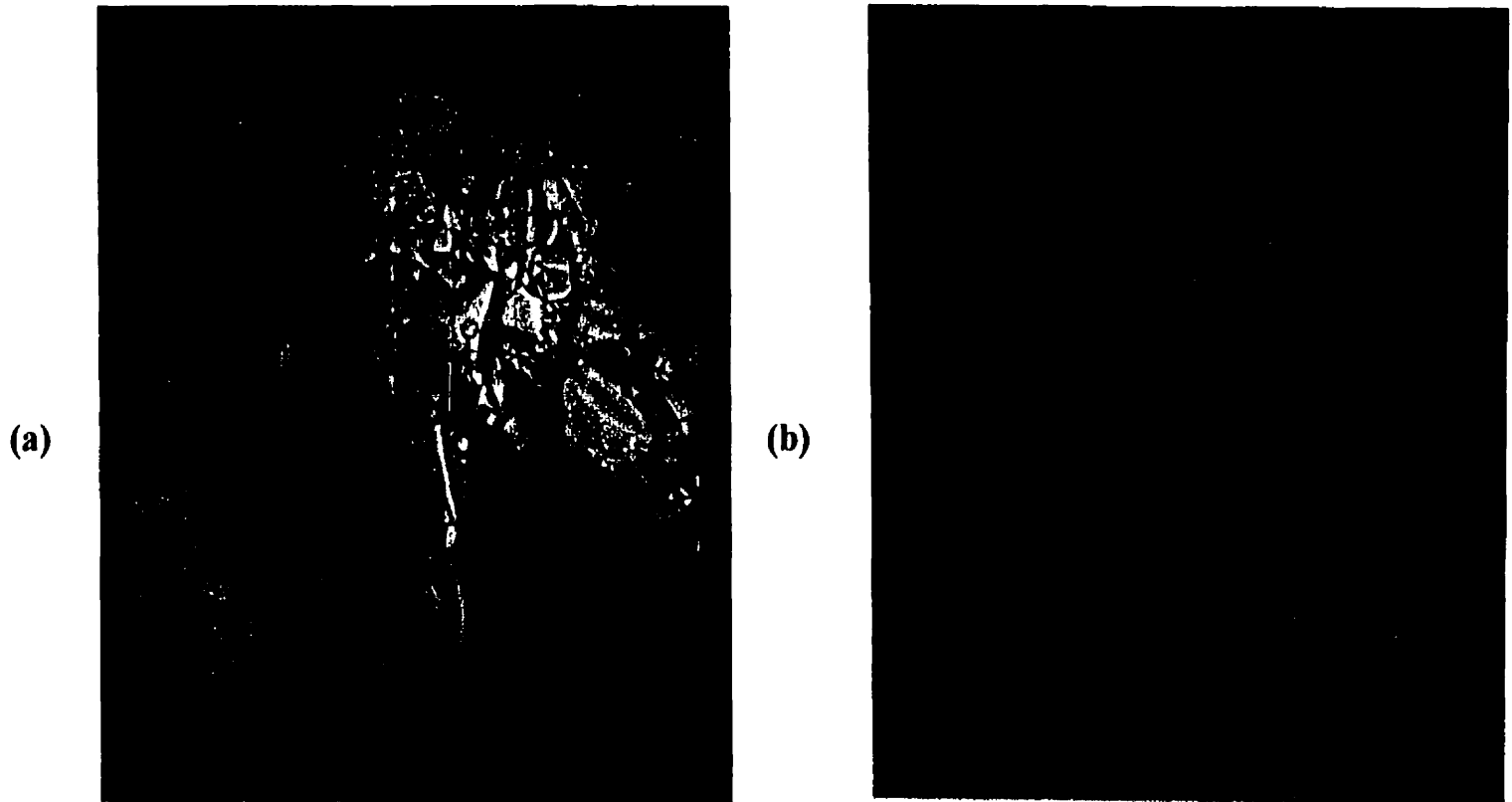


Figure 3.4 SEM micrographs of magnetically extracted grains from a composite sample made of four of the turbidite specimens from core 13 in backscattered (a) and secondary (b) electron images.

Table 3.1 Selected oxide concentrations from SEM semi-quantitative analysis

Core/Site	28	24	13	578		606				
grain #	$\frac{\text{TiO}_2}{\text{FeO}}$	$\frac{\text{TiO}_2}{\text{FeO}}$	$\frac{\text{TiO}_2}{\text{FeO}}$	$\frac{\text{TiO}_2}{\text{FeO}}$	x	$\frac{\text{TiO}_2}{\text{FeO}}$	x	$\frac{\text{Cr}_2\text{O}_3}{\text{FeO}}$	y	$\frac{\text{NiO}}{\text{FeO}}$
1	0.096	0.003	0.001	0.106	0.261	0.000				
2	0.008	0.001	0.000	0.128	0.311	0.000				
3	0.035	0.001	0.004	0.058	0.148	0.004				
4	0.002	0.000	0.000	0.101	0.251	0.000				
5	0.015	0.003	0.034	0.087	0.217	0.001				
6	0.002	0.000	0.000	0.218	0.491	0.125	0.303			
7	0.000	0.025	0.000	0.085	0.213	0.193	0.443			
8	0.000	0.021	0.003	0.359	0.731	0.237	0.527			
9	0.014	0.003	0.000	0.008	0.023	0.292	0.624			
10	0.004	0.014	0.001	0.216	0.488	0.490	0.917			
11	0.000	0.002	0.000	0.084	0.212	0.290	0.621			
12	0.001	0.000	0.000	0.077	0.194	0.312	0.656			
13	0.005	0.015	0.001	0.094	0.235			0.260	0.362	0.107
14	0.001	0.001	0.000	0.145	0.346			0.262	0.365	0.096
15	0.000	0.000	0.073	0.087	0.218			0.269	0.373	0.098
16	0.003	0.002	0.000	0.120	0.293			0.265	0.369	0.099
17	0.000	0.001	0.003	0.131	0.315			0.262	0.365	0.112
18	0.000	0.006	0.000	0.678	1.136			0.271	0.375	0.108
19	0.000	0.007	0.003	0.521	0.956			0.264	0.367	0.113
20	0.004	0.013	0.004	0.137	0.329			0.180	0.261	0.000
21	0.000	0.002	0.000	0.128	0.309			0.262	0.365	0.104
22		0.000						0.262	0.364	0.113
average	0.009	0.005	0.006	0.170	0.366	0.277	0.585	0.256	0.357	0.095
s.deviation	0.021	0.007	0.017	0.157	0.263	0.106	0.178	0.025	0.032	0.032

Parameters x and y are defined in Eqs. (3.1) and (3.2) respectively.

susceptibility on approaching the Curie point indicates the Hopkinson effect (Nagata, 1961). The Curie point itself is not obvious. A decline of susceptibility at 520°C might be interpreted as a Curie point of Ti-poor magnetite; however, it seems more likely to be just a spurious result of the Hopkinson effect. Another decline of susceptibility at 580°C suggests the presence of pure magnetite in agreement with the SEM analyses. The cooling curve shows that susceptibility has been enhanced by the heating in air.

Figure 3.5.b shows SIRM as a function of low temperature for specimen 28-0714 which was typical of all nine turbidite specimens measured. The curve shows a clear Verwey transition in the SIRM curve at about 120K confirming the presence of pure magnetite.

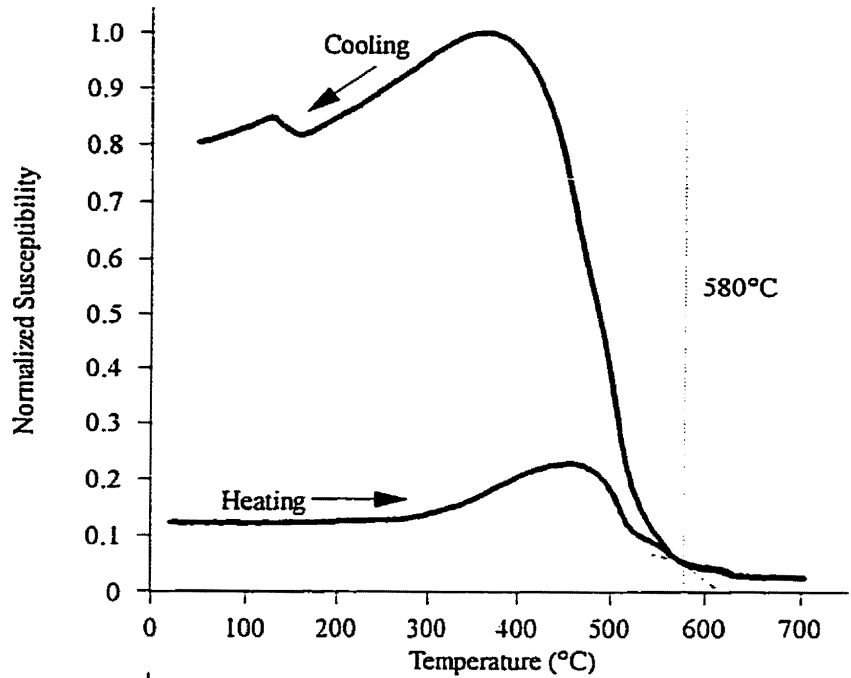
Figure 3.6 shows the results of hysteresis loop analysis for all specimens from each turbidite core. The plots of J/J_s vs H_c/H_c show that all specimens from each core plot closely together in the pseudo-single-domain region (with the exception of specimen 28-0765).

3.3.2 Pelagic Clay-rich Muds of DSDP Site 578

Figure 3.7 shows typical SEM images for the magnetic grains extracted from a composite sample of pelagic clay specimens of DSDP site 578. Like those extracted from the turbidites, most of magnetic grains from site 578 are roughly equidimensional and seem to be fragments of once larger particles. However, unlike those from the turbidites, they have high Ti content (Table 3.1). Magnetite likely crystallized as a magnetite-

28-0714
7.14 mbsf

(a)



(b)

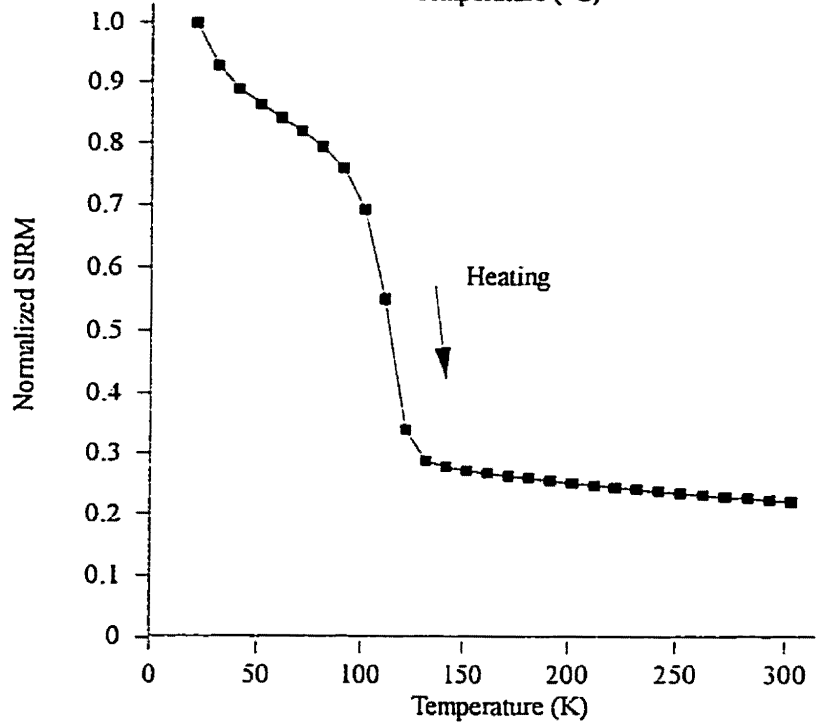
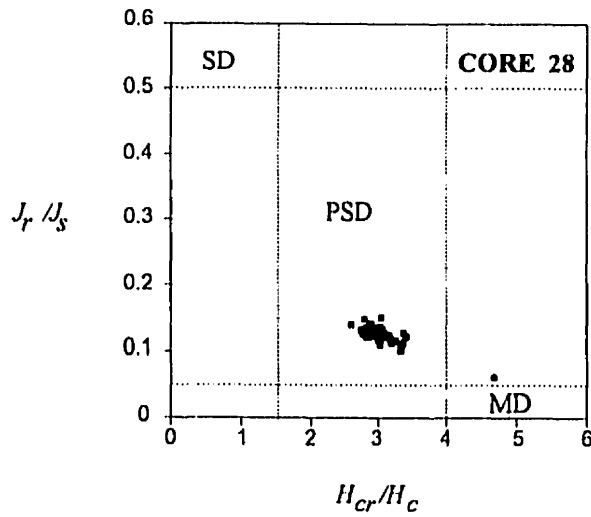
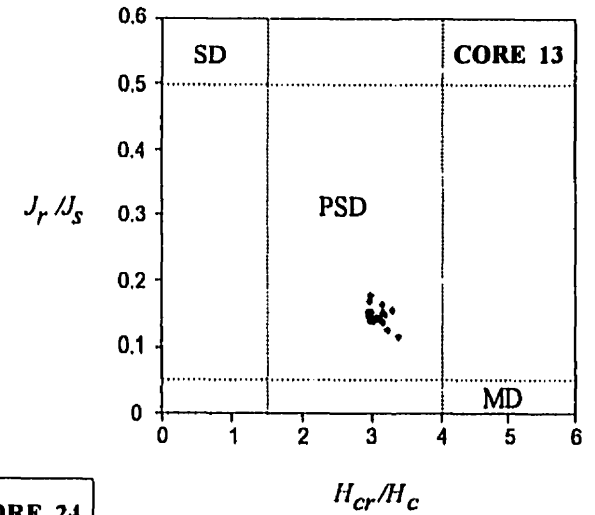


Figure 3.5 (a) Normalized susceptibility of a typical turbidite specimen from the Scotian Rise as a function of temperature. A rise of susceptibility as the Curie point is approached indicates the Hopkinson effect. The decline of susceptibility at 580°C suggests the presence of pure magnetite. (b) Normalized SIRM as a function of low temperature (20 to 300K). A drop in SIRM at about 120K indicates the Verwey transition of pure magnetite.



(a)



(c)

(b)

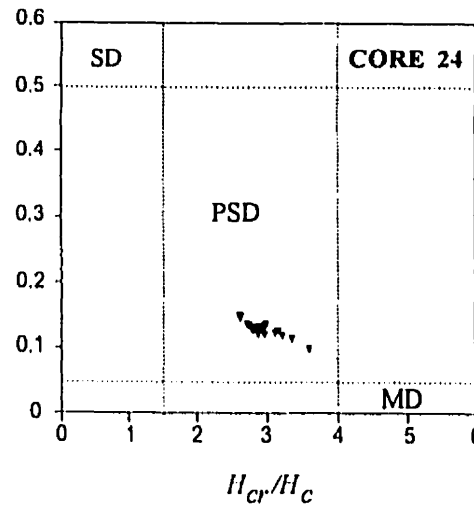


Figure 3.6 Parameters J_r/J_s and H_{cr}/H_c from analysis of hysteresis loops for all turbidite specimens from cores 28 (a), 24 (b) and 13 (c). They are plotted on the diagram of *Day et al.* [1977]. The points for all specimens except 28-0765 fall in the pseudo-single-domain (PSD) region.

ulvöspinel solid solution series with the general formula of $(1 - x) \text{Fe}_3\text{O}_4 \cdot x \text{Fe}_2\text{TiO}_4$. Oxidation-exsolution on cooling likely produced an intergrowth of nearly pure magnetite with ilmenite lamellae along [111] planes in magnetite (*Buddington and Lindsley, 1964; Strangway et al., 1968*). This explains the observed Curie points being near that of pure magnetite (see below) despite the high Ti content of the magnetic grains. The value of x can be calculated from the weight ratio of TiO_2/FeO . Using 55.8, 47.9 and 16.0 as the atomic weights for Fe, Ti and O respectively, it can be shown that

$$x = \frac{215.4 \frac{\text{TiO}_2}{\text{FeO}}}{79.9 + 71.8 \frac{\text{TiO}_2}{\text{FeO}}} \quad (3.1).$$

The values of x for the grains that were analyzed are listed in Table 3.1. The average x for site 578 is 0.37 ± 0.26 which suggests a source rock of intermediate (*e.g.*, andesitic) composition (*Buddington and Lindsley, 1964*).

For five specimens from site 578, magnetic susceptibility and SIRM were measured as a function of temperature. Figure 3.8.a shows magnetic susceptibility change on heating to 700°C and cooling for specimen 578-5-2-112 (35.92 mbsf), which is typical of all five specimens. On heating, the main magnetic mineral shows a Curie point of about 510°C suggesting $x \sim 0.1$ (*Nagata, 1961*). The SEM analysis, on the other hand, gives $x \sim 0.4$, which suggests that the grains contain ilmenite exsolution lamellae. A smaller amount of pure magnetite also seems to be present as shown by its Curie point of about 580°C. As

in specimen 28-0714, the cooling curve shows that susceptibility was enhanced by the heating in air.

The curve of SIRM as a function of low temperature for specimen 578-5-2-112 in Fig. 3.8.b is typical of all five specimens measured. It is very similar to that of surface oxidized magnetite (Özdemir *et al.*, 1993). Oxidation creates a layer of maghemite (γ Fe_2O_3) around the unoxidized magnetite core which suppresses the Verwey transition. However, the presence of unoxidized magnetite can still be detected by a little peak on the dSIRM/dT curve (B. Moskowitz, personal discussion, 1994) as seen at about 120K in Fig. 3.8.b.

Figure 3.9 shows the result of hysteresis loop analysis for 33 specimens of site 578. Points plot close together in the pseudo-single-domain (PSD) region.

3.3.3 Pelagic Lime-Muds of DSDP Site 606

For site 606, magnetic grains could be extracted only from specimens in the first 60 m of core. The lower half of the core was much more weakly magnetized and yielded almost no magnetic grains. Even the upper 60 m yielded fewer grains than the other cores. Figure 3.10 shows typical SEM images for these grains. They are irregular in size and shape. The elemental composition of these grains is more complicated than in the other cores. The grains basically fall into three groups. The first group (grains nos. 1 to 5 in Table 3.1) is simply pure magnetite ($\text{TiO}_2/\text{FeO} \sim 0$) as in the turbidites. The second group (nos. 6 to 12) has high Ti content with x averaging 0.6, suggesting a mafic source rock

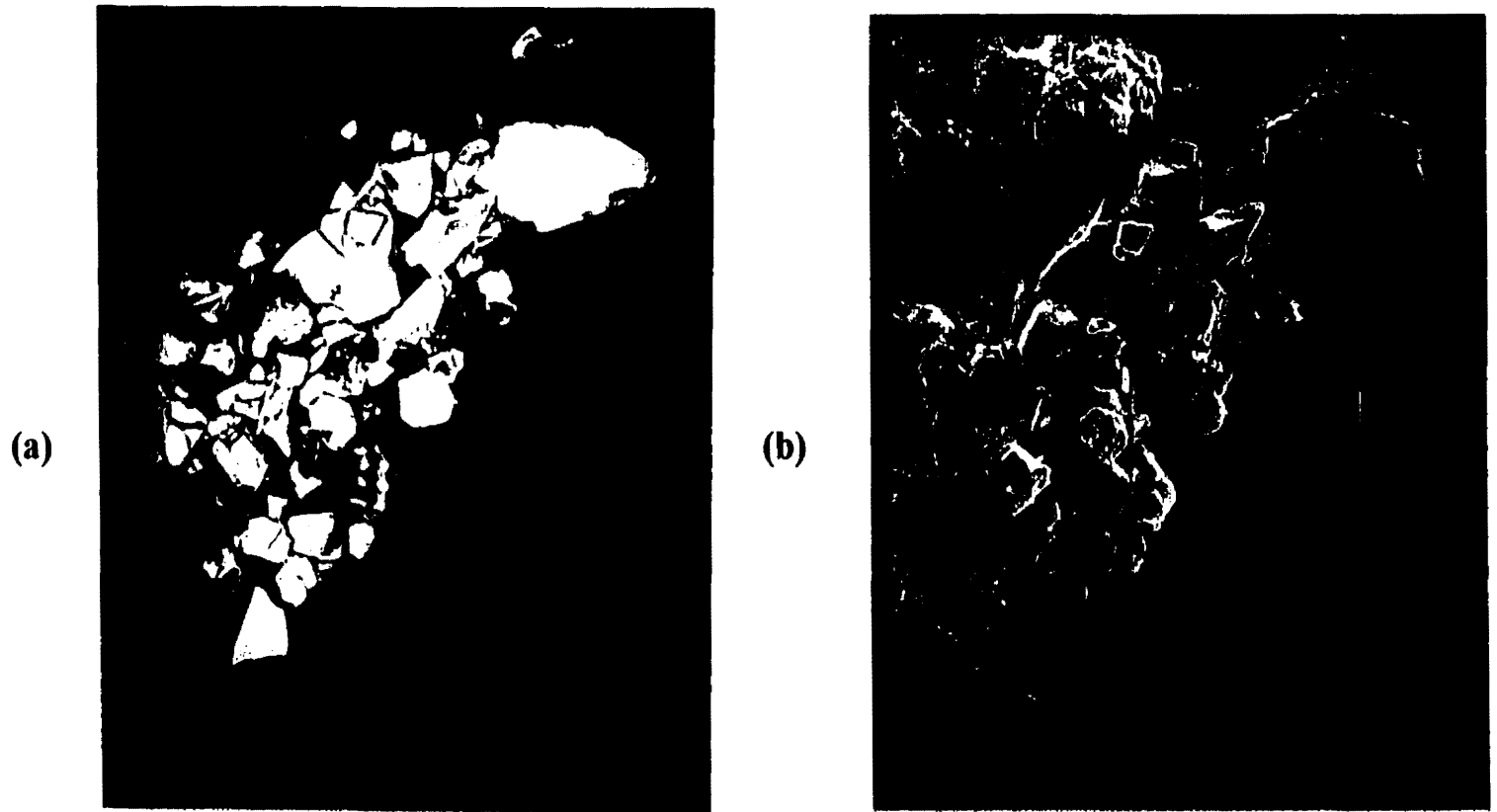
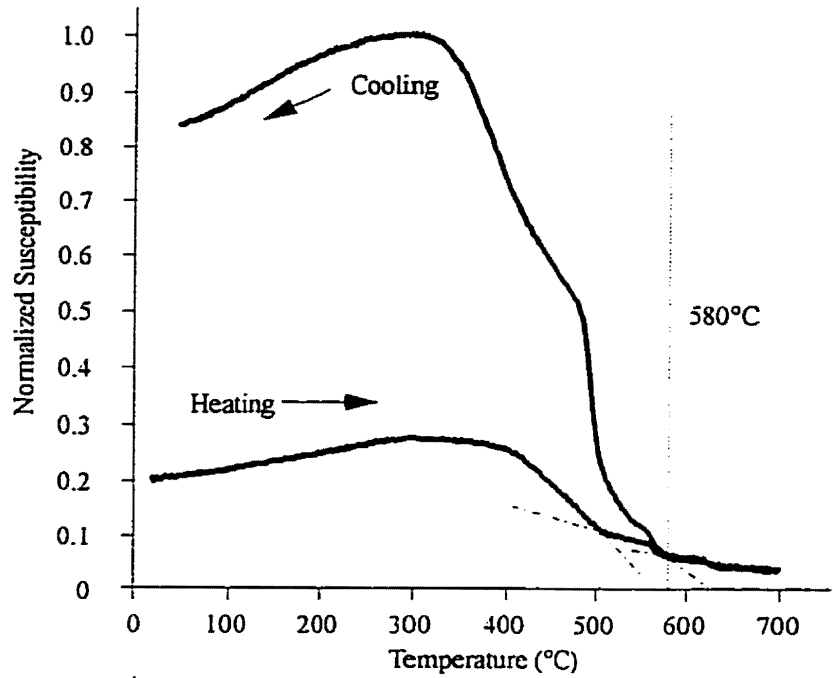


Figure 3.7 SEM micrographs of magnetically extracted grains from a composite sample made of four of the pelagic clay specimens from site 578 in backscattered (a) and secondary (b) electron images.

578-5-2-112
35.92 mbsf

(a)



(b)

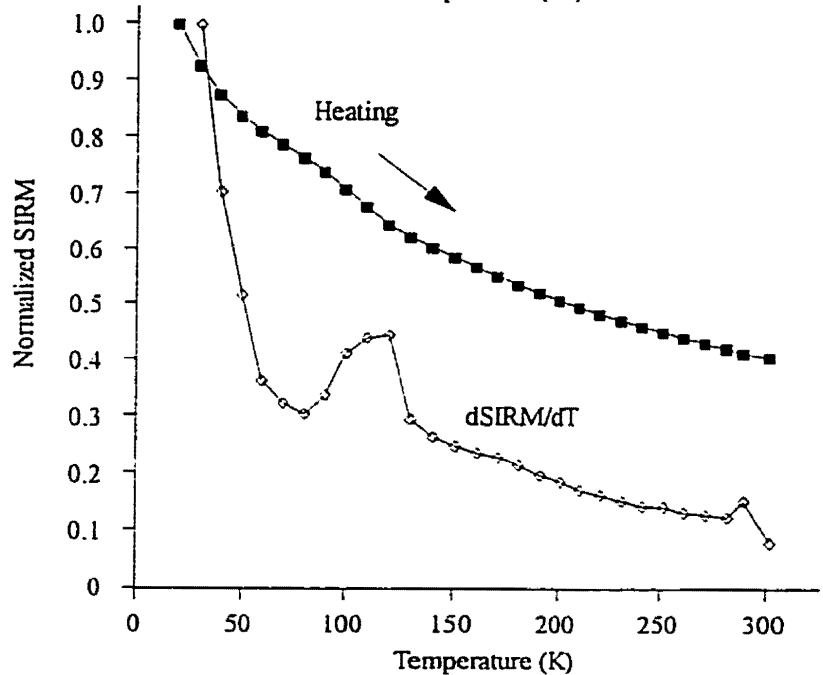


Figure 3.8 (a) Normalized susceptibility of a typical pelagic clay specimen from site 578 as a function of temperature. On heating, the main magnetic mineral shows a Curie point of about 510°C suggesting magnetite with a small Ti content. A smaller amount of pure magnetite also seems to be present as indicated by its Curie point of about 580°C. (b) Normalized SIRM (solid squares) as a function of low temperature (20 to 300K). The Verwey transition is suppressed probably due to surface oxidation but appears as a peak on the dSIRM/dT curve (hollow diamonds).

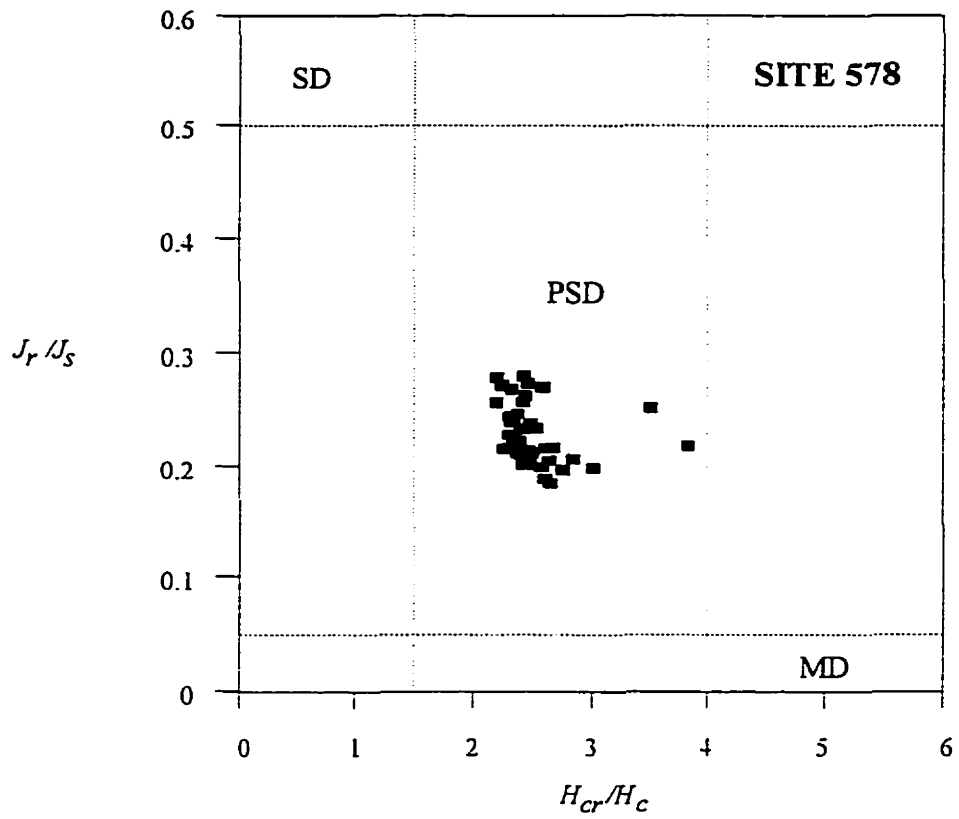


Figure 3.9 Parameters J_r/J_s vs H_{cr}/H_c from analysis of hysteresis loops for pelagic clay specimens of DSDP site 578. They are plotted on the diagram of *Day et al.* [1977]. The values for all specimens fall in the pseudo-single-domain (PSD) area.

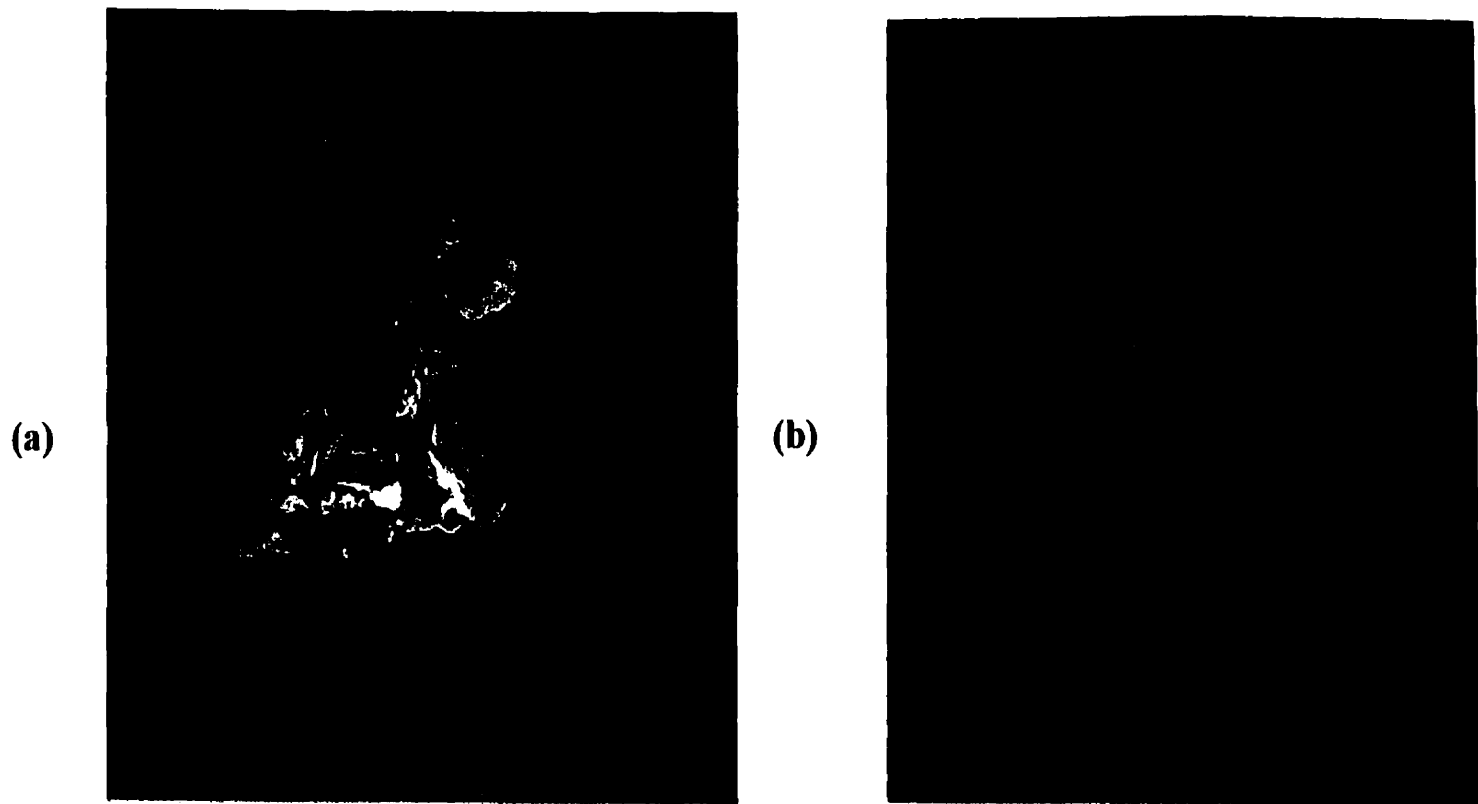


Figure 3.10 SEM micrographs of magnetically extracted grains from a composite sample made of four of the pelagic lime-mud specimens from site 606 (0-60 m) in backscattered (a) and secondary (b) electron images.

(*Buddington and Lindsley, 1964*). The last group (nos. 13 to 22) has a high content of Cr and Ni along with Ti and Fe indicating iron-rich chromian spinels. These chromian spinels can be considered a solid solution series between chromite and titanomagnetite and suggest a mafic or ultramafic source rock (*Ramdhor, 1980; Freeman, 1986*). This spinel series has the general formula of $\text{Fe}_{3-y}\text{Cr}_y\text{O}_4$ (*Schmidbauer, 1971*). From the weight ratio of $\text{Cr}_2\text{O}_3/\text{FeO}$ and using 52.0 as the atomic weight for Cr, it can be shown that

$$y = \frac{215.4 \frac{\text{Cr}_2\text{O}_3}{\text{FeO}}}{136 + 71.8 \frac{\text{Cr}_2\text{O}_3}{\text{FeO}}} \quad (3.2).$$

Table 3.1 shows that the average y for selected grains in site 606 is 0.357. Although spinels with y of this magnitude will not show a Verwey transition (*Schmidbauer, 1971*), they have a saturation magnetization of about $70 \text{ Am}^2/\text{kg}$ at room temperature comparable to the $90\text{-}92 \text{ Am}^2/\text{kg}$ for pure magnetite (*Robbins et al., 1971*). Spinel with this value of y should have a Curie point of about 427°C (*Robbins et al., 1971*).

Five specimens from site 606 were measured for magnetic susceptibility and SIRM as a function of temperature. Figure 3.11.a shows magnetic susceptibility as a function of high temperature for specimen 606-15-1-85 (128.15 mbsf), which is typical of all five specimens. The susceptibilities of specimens from site 606 are very weak making the Kappabridge readings noisy. On heating, the dominant magnetite mineral shows a Curie point of $\sim 580^\circ\text{C}$ suggesting pure magnetite. A Curie point of about 650°C is also present

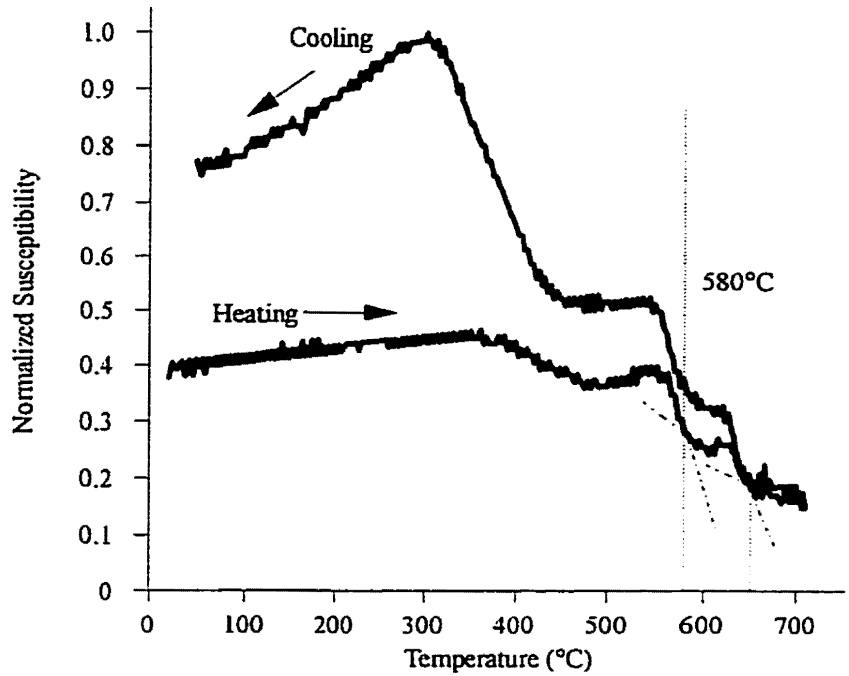
suggesting hematite. There is also a suggestion of a $\sim 440^{\circ}\text{C}$ Curie point which may be due to chromian spinel.

Figure 3.11.b shows SIRM as a function of low temperature for specimen 606-15-1-85. The curve is similar to that of surface oxidized magnetites. A small peak indicating the Verwey transition for magnetite is observed on the $d\text{SIRM}/dT$ curve. In conclusion, magnetite is likely responsible for most of the magnetic properties although hematite and chromian spinel may also contribute.

Figure 3.12 shows the results of hysteresis loop analysis for 33 specimens of site 606. The data points for the upper 60 m all fall in the pseudo-single-domain region, but are not as clustered as at other sites. Data from the lower 60 m are even more scattered although this scatter may in part be caused by inaccuracy in measuring hysteresis in these specimens of very low magnetic mineral content.

606-15-1-85
128.15 mbsf

(a)



(b)

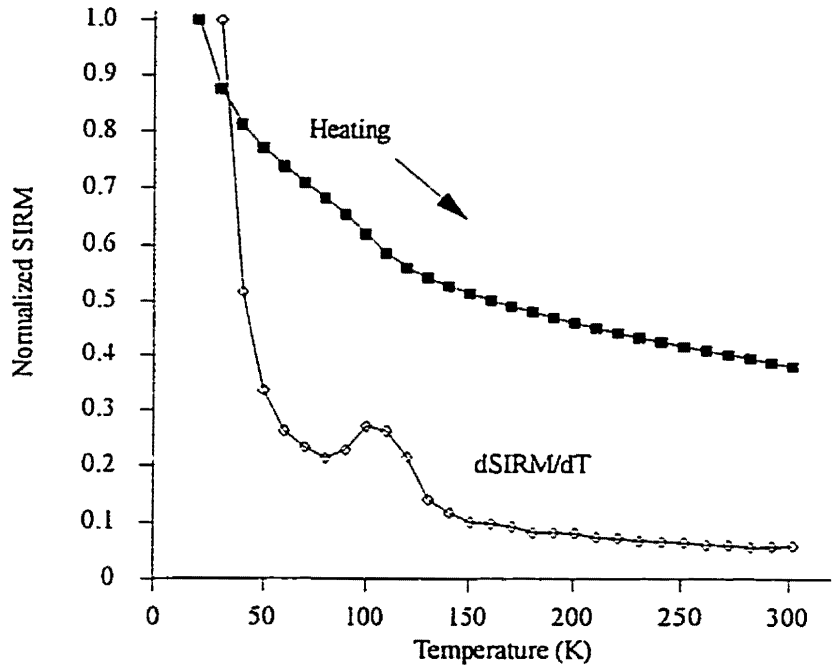


Figure 3.11 (a) Normalized susceptibility of a typical lime mud specimen from site 606 as a function of temperature. On heating, the dominant magnetic mineral shows a Curie point of about 580°C suggesting pure magnetite. Curie points of about 440°C and 650°C are also present suggesting chromian spinel and hematite respectively. (b) Normalized SIRM (solid squares) as a function of low temperature (20 to 300K). The Verwey transition is suppressed probably due to surface oxidation of magnetite but appears as a peak on the $dSIRM/dT$ curve (hollow diamonds).

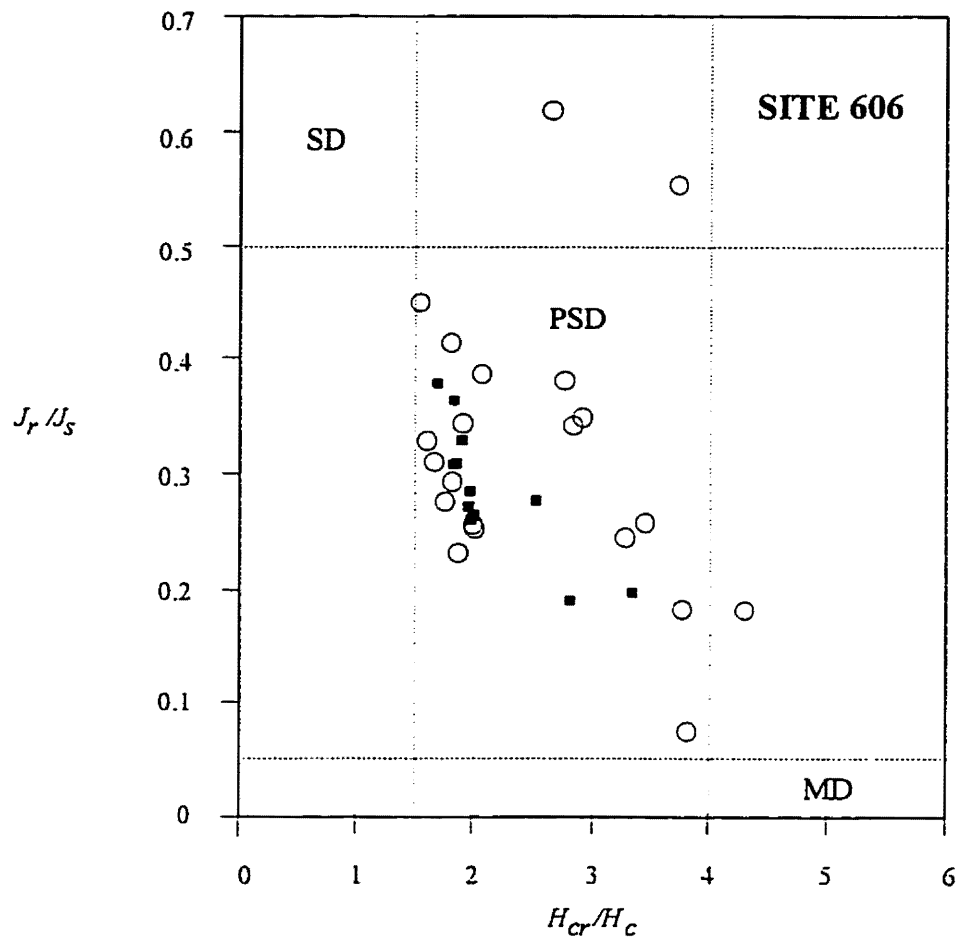


Figure 3.12 Parameters J_r/J_s vs H_{cr}/H_c from analysis of hysteresis loops for lime mud specimens of DSDP site 606. They are plotted on the diagram of *Day et al.* [1977]. Solid squares are for specimens from 0-60 m which generally have high NRM intensity, whereas open circles are for those from 60-165 m which have very weak and unstable NRMs.

CHAPTER 4

PALEOMAGNETIC MEASUREMENT

4.1 Methods

The natural remanence (NRM) of each specimen was measured and then monitored during stepwise alternating field (AF) demagnetization. Natural remanence can often be divided into what is called primary and secondary magnetizations. In sediments, the former is the magnetization acquired during or soon after deposition, while the latter refers to magnetization acquired during subsequent geological time. In the absence of diagenetic processes that alter the detrital ferromagnetic minerals, the primary component is magnetically more stable against demagnetization than the secondary component. Detailed stepwise demagnetization is required to isolate the primary remanence component so that its inclination (I_{obs}) can be determined. Also, the intensity decay curve produced by demagnetization may give clues about the stability of remanence as well as the magnetic mineralogy.

The natural remanence of most specimens was measured using a CTF superconducting magnetometer. For a few stronger specimens, however, the remanence was measured using a Schonstedt spinner magnetometer model SSM-1. To isolate its primary magnetization, each specimen was demagnetized by stepwise alternating field (AF) demagnetization using a Schonstedt demagnetizer model GDS-1. The demagnetization started with a peak alternating field of 5 mT followed by steps of 5 mT up to 40 mT; these

were followed by steps of 10 mT up to 100 mT or until the remanence decreased to less than 10% of its original intensity. Direction of the primary magnetization was determined using a computer program for principal component analysis based on *Kirschvink* [1980]. The inclination given by this program is termed the inclination of the observed remanence I_{obs} . The program also gives a parameter called maximum angular deviation (MAD) that indicates a quantitative measure of the precision with which the best-fit line is determined. Specimens whose MAD value exceeds 10° are considered unreliable.

4.2 Results

4.2.1 Clay-rich Turbidite Muds from the Scotian Rise

Of the 79 turbidite specimens collected, 37 specimens were from core 28, 22 from core 24, and 20 from core 13. All of the specimens were measured during stepwise AF demagnetization. Figure 4.1 shows the intensity decay curves and the vector projections of selected specimens typical for these turbidites. In most cases, the intensity of remanence was reduced to 10% or less after 80 mT. Most specimens have a stable, which is considered primary, magnetization. Two specimens from core 28 between the depth of 1084 to 1104 cm (specimens 28-1084 and 28-1104), have a strong secondary magnetization with opposite polarity to the primary magnetization (see Fig. 4.1.b) probably due to a magnetic polarity reversal or magnetic excursion. Obtaining more specimens for detailed study from this interval is difficult because it is very thin. No such interval was observed in the other two cores.

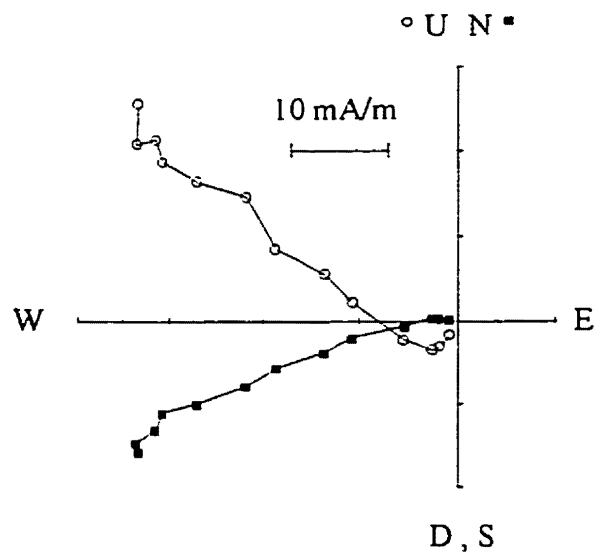
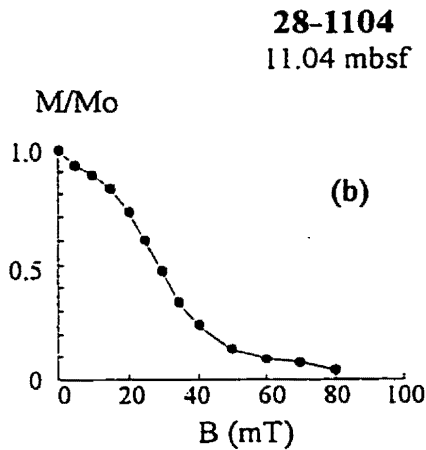
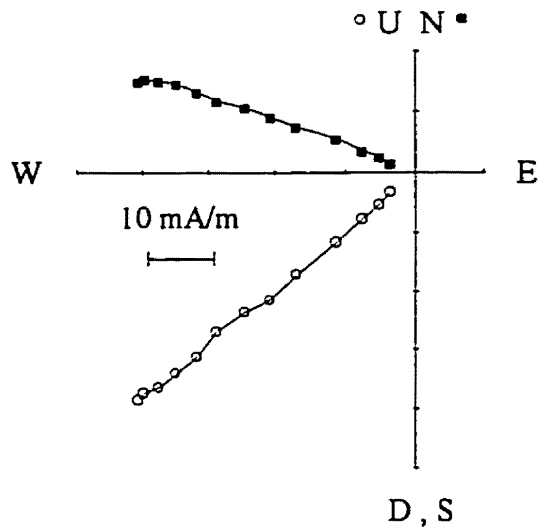
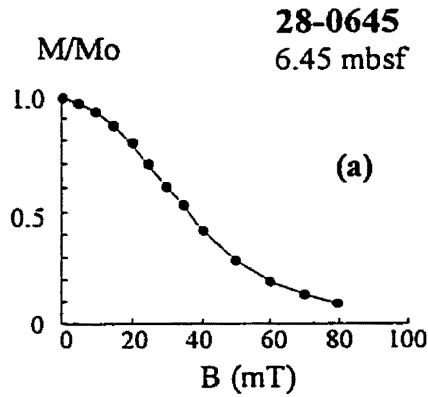
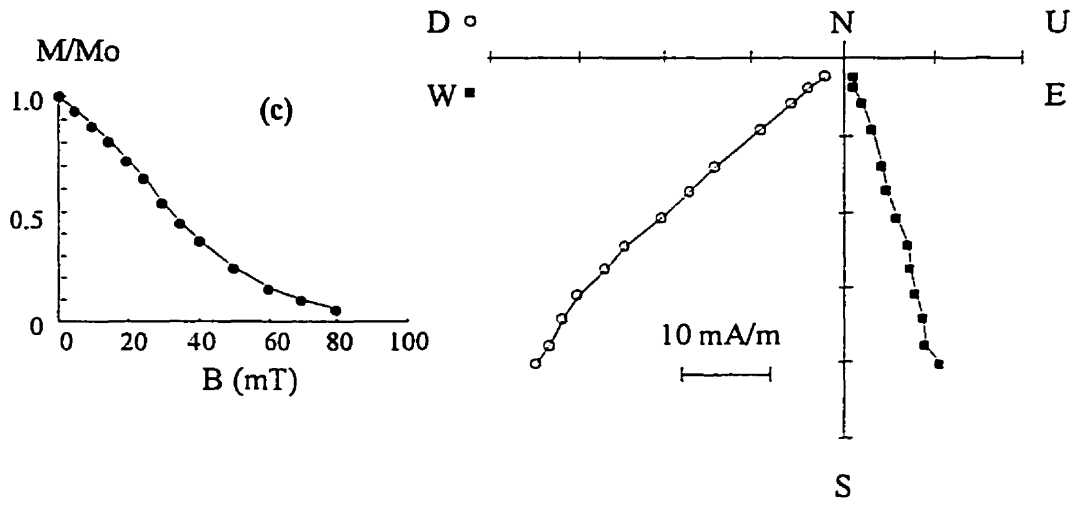


Figure 4.1 Typical intensity decay curves and the components of the natural remanence (NRM) during AF demagnetization for turbidite specimens of cores 28 (a and b), 24 (c) and 13 (d). Most specimens show a stable primary component that decay steadily with field. Specimen 28-1104 (see b) shows the presence of a secondary magnetization possibly due to a magnetic polarity excursion. This is observed in specimens from core 28 between the depth of 1085 to 1104 cm.

24-0656
6.56 mbsf



13-0623
6.23 mbsf

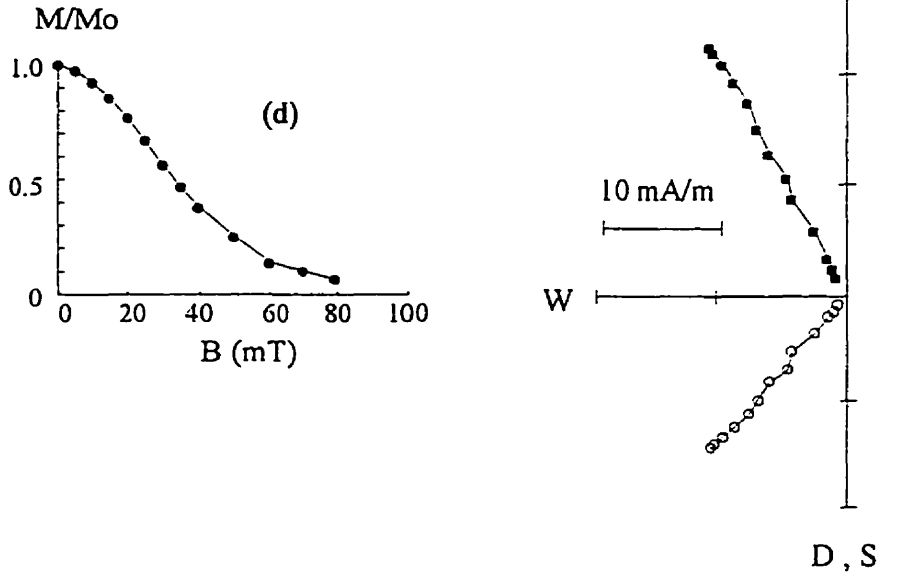


Figure 4.1 (Continued)

Figure 4.2 summarizes the paleomagnetic measurements. It shows that the NRM intensity in all core varies only slightly from one specimen to another. Except for specimens 28-1084 and 28-1104, the directions of remanence hardly change during AF demagnetization so that the inclination after AF cleaning is very similar to the NRM inclination. The MAD values for all specimens are less than 5°. The primary remanence inclination of most specimens is shallower than the expected 61° for the sites of these cores.

4.2.2 Pelagic Clay-rich Muds of DSDP Site 578

Eighty-seven specimens from site 578 were measured for natural remanence and demagnetized. Figure 4.3 shows the intensity decay curves and the vector projections of selected specimens that are typical for this site. The peak alternating field required to demagnetize the specimens from site 578 varies from 70 to 100 mT. During demagnetization the NRM intensity in most specimens decayed steadily, while the direction hardly changed suggesting a stable primary magnetization. The presence of an erratic intensity decay was observed only in a few specimens. Some specimens showed a viscous secondary component opposite to the primary direction (see Fig. 4.3.b, specimen 578-5-7-30).

Figure 4.4 shows the summary of the paleomagnetic measurements. Except for a few specimens, the NRM intensity varies only slightly from one specimen to another. AF demagnetization hardly changed the magnetic inclination. The primary inclination can be

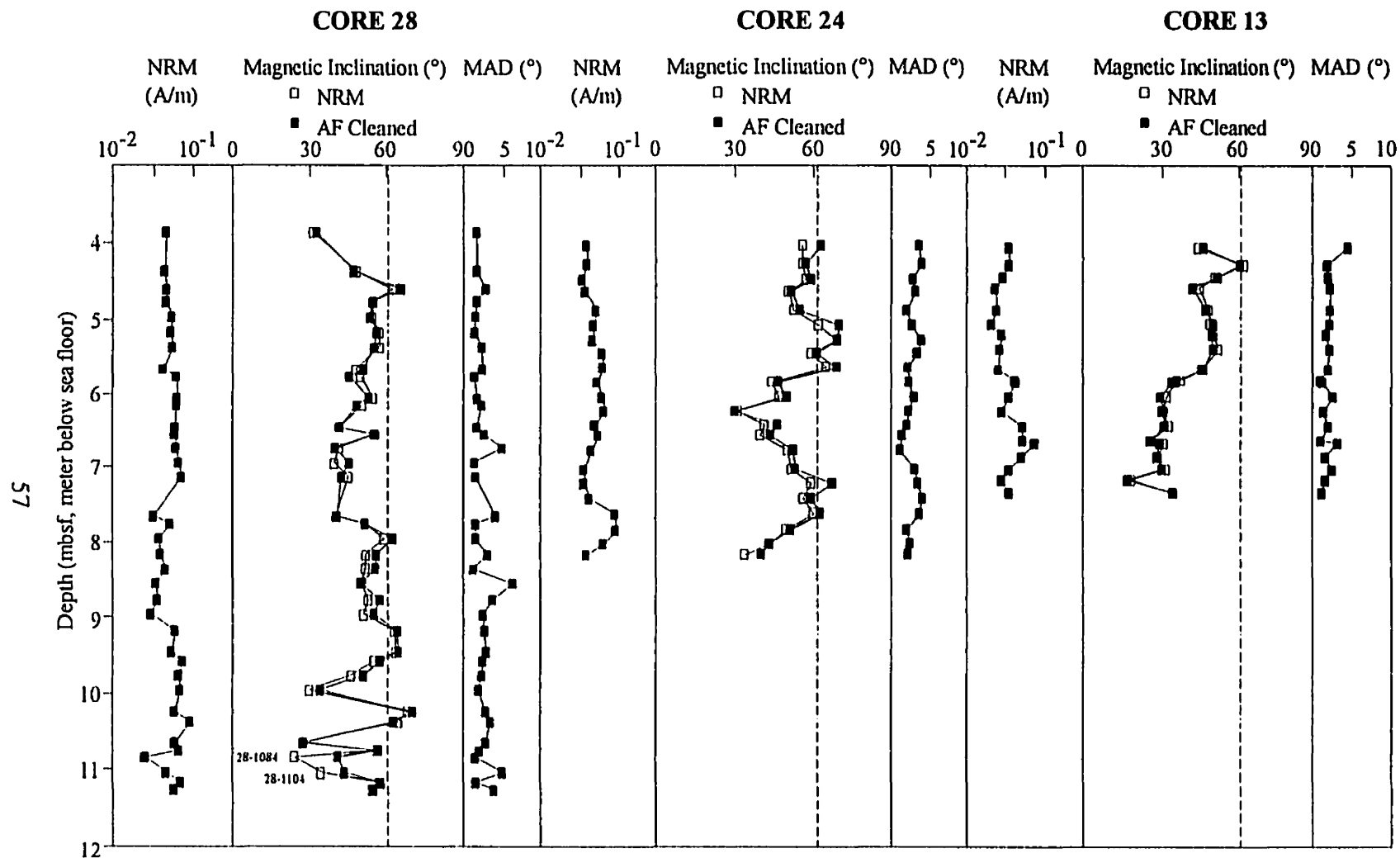
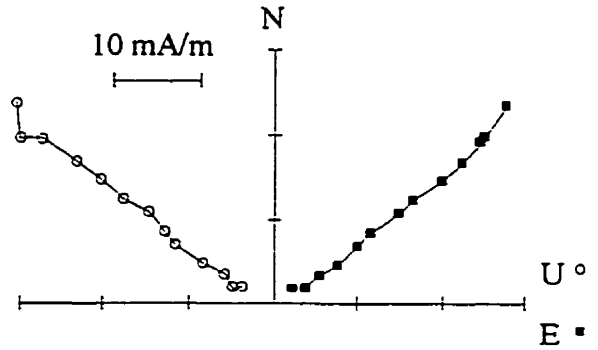
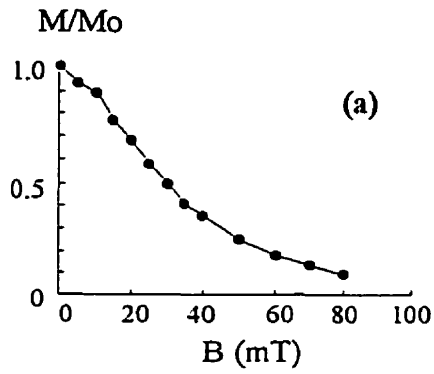


Figure 4.2 The summary of paleomagnetic measurements for turbidite specimens of cores 28, 24 and 13. All specimens have positive NRM inclination except for specimens 28-1084 and 28-1104 (see Fig. 4.1.b). The dashed lines on the magnetic inclination plots indicate the inclination at these sites according to the GAD model.

578-2-2-22
6.52 mbsf



578-5-7-30
42.60 mbsf

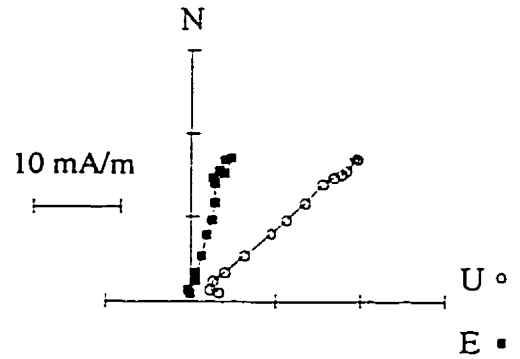
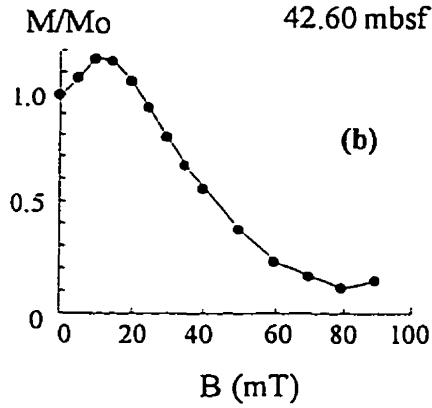
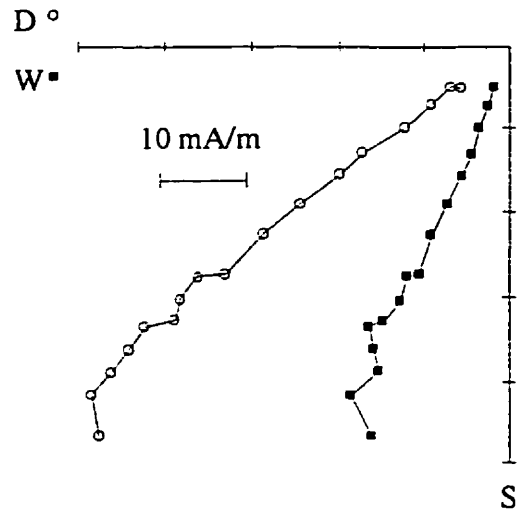
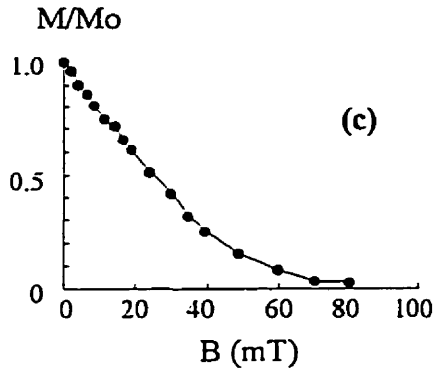


Figure 4.3 Typical intensity decay curves and the components of the natural remanence (NRM) during AF demagnetization for pelagic clay specimens of DSDP site 578.

578-10-2-78
83.08 mbsf



578-12-3-82
103.62 mbsf

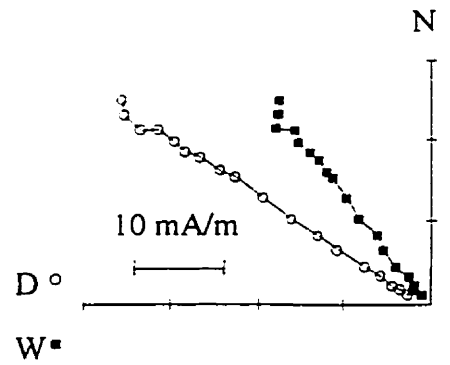
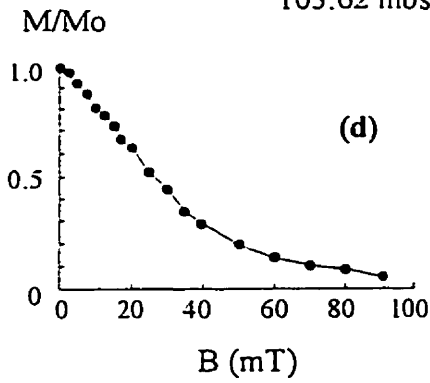


Figure 4.3 (Continued)

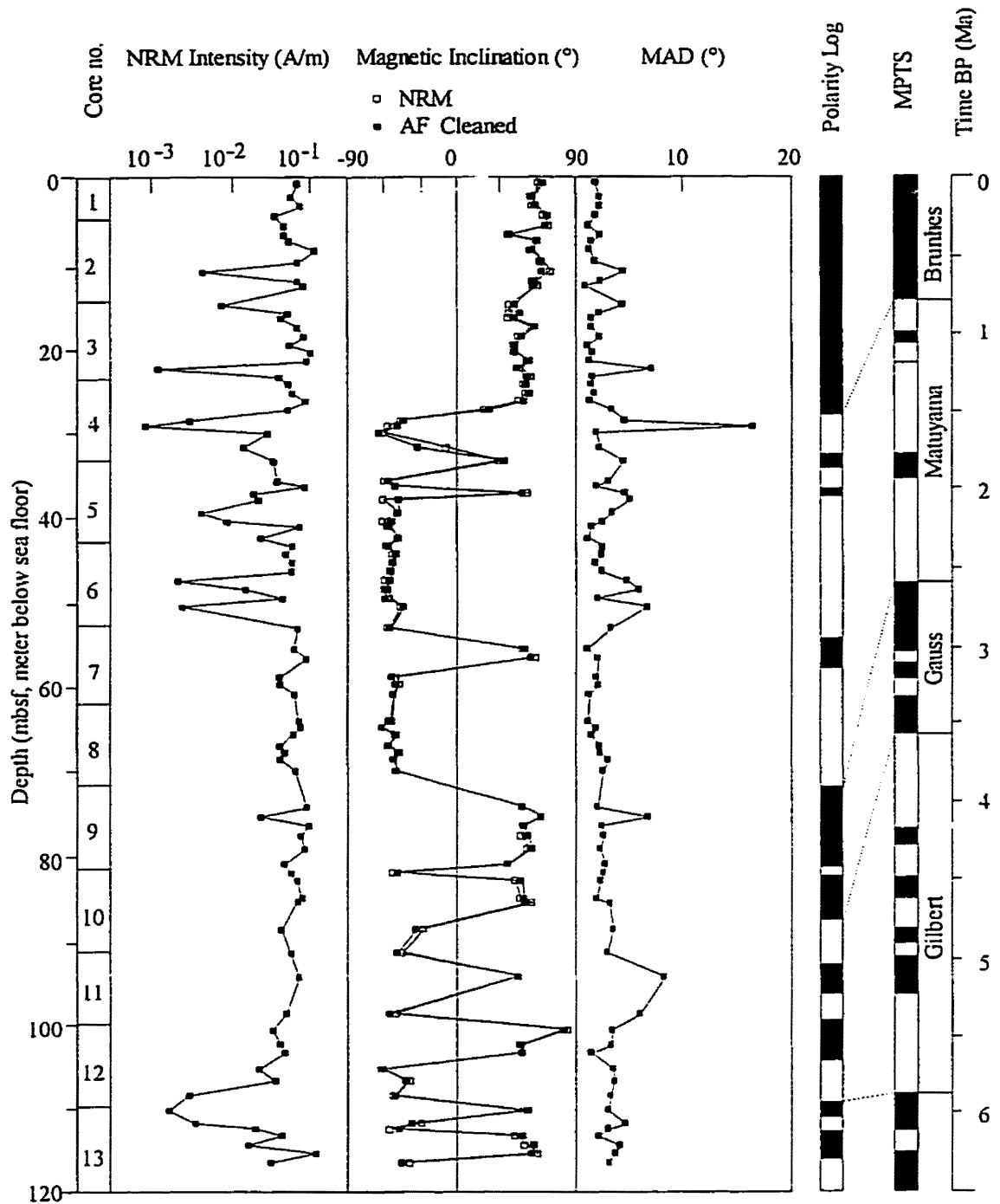


Figure 4.4 The summary of paleomagnetic measurements on pelagic clay specimens of DSDP site 578. MAD is the maximum angular deviation. MPTS is the magnetic polarity time scale based on *Ogg* [1995].

determined accurately as the MAD values are mostly less than 5°. Only one specimen was removed because its MAD value was more than 10° making its inclination unreliable. The magnetostratigraphy is similar to that of the earlier studies (*Heath et al.*, 1985; *Arason and Levi*, 1990a). However, the magnetic polarity time scale (MPTS) used in this study is slightly different from that of the earlier studies. It is based on more recent work by *Ogg* [1995] in which the magnetic polarity chrons within the Pleistocene and Pliocene epochs were dated with the aid of Milankovitch cycles.

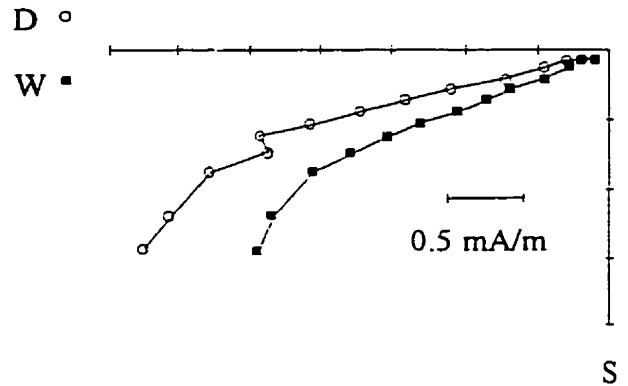
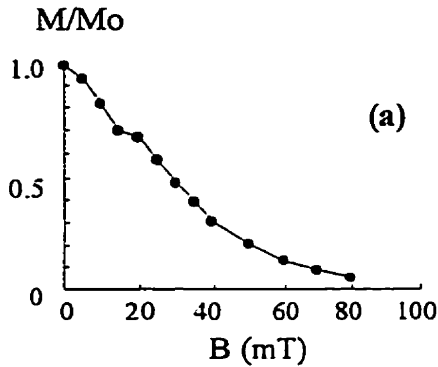
4.2.3 Pelagic Lime-Muds of DSDP Site 606

In total, 110 specimens from site 606 were sampled. The NRM's of some specimens were found to be too weak to be measured reliably even with the cryogenic magnetometer and were rejected from further discussions. Only 90 specimens were strong enough to be measured and demagnetized.

Figure 4.5 shows the intensity decay curves and the vector projections of typical specimens. Specimens from site 606 required a higher peak field to demagnetize than did specimens from site 578. In some cases, the maximum peak field of the demagnetizer (100 mT) was not sufficient to reduce NRM intensity to 10% of its original value. The presence of hematite (see Fig. 3.9.a) may explain why these specimens have a such high coercive force.

During demagnetization, the NRM intensity in some specimens shows an erratic decay, while its direction changes significantly. In most cases, the stable directions were

606-2-5-68
7.98 mbsf



606-6-6-132
50.02 mbsf

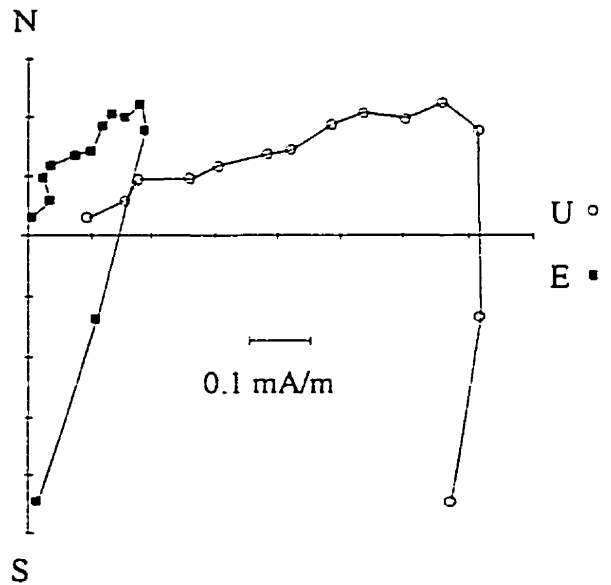
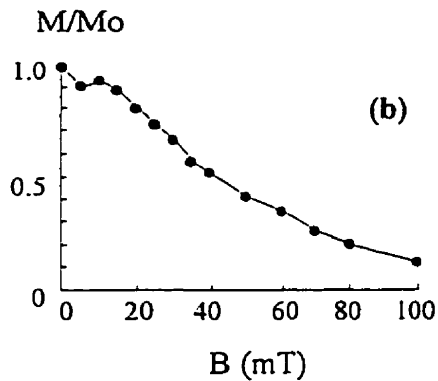


Figure 4.5 Typical intensity decay curves and the components of the natural remanence (NRM) during AF demagnetization for carbonate rich specimens of DSDP site 606. Most specimens show a weak secondary component that is erased at about 10-15 mT. Some specimens show erratic changes in their directions (see (c), 606-10-5-35). The primary directions for such specimens cannot be determined accurately as indicated by high MAD values.

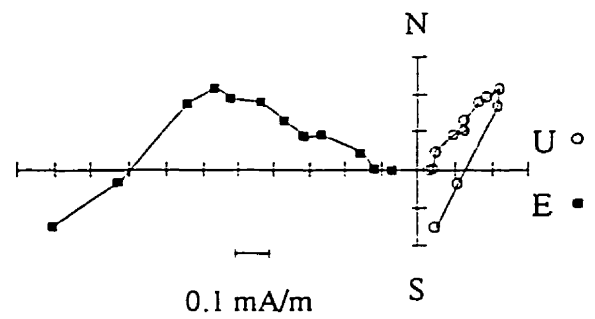
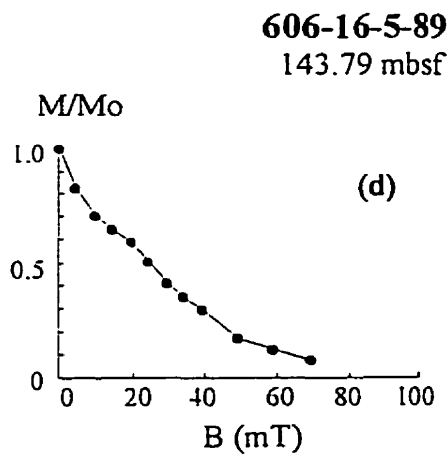
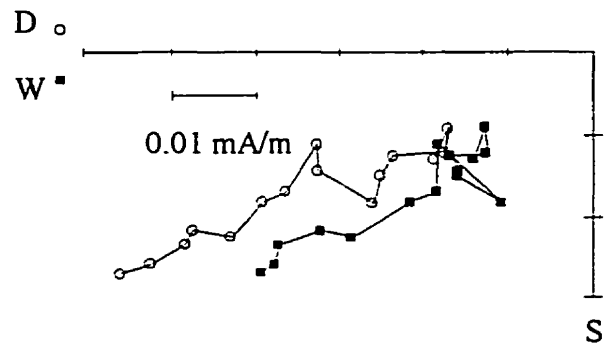
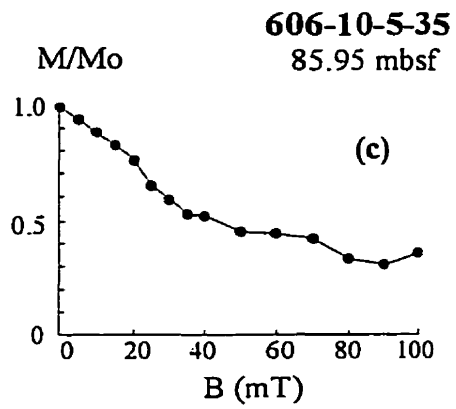


Figure 4.5 (Continued)

isolated once viscous secondary components were erased by AF fields of 10-15 mT. This stable direction will be considered primary magnetization.

Figure 4.6 summarizes the paleomagnetic measurements. It shows that the NRM intensity varies significantly (up to two orders of magnitude) from one horizon to another, dividing the core into high intensity and low-intensity intervals. The longest low-intensity interval is between 60 to 100 meters. The presence of secondary components and change in remanence direction during demagnetization create discrepancies between NRM inclinations and the calculated primary inclinations. For 18 of the specimens, the change in remanence direction was so severe that the MAD value exceeded 10° . These 18 specimens are removed from further discussion. The magnetostratigraphy the author has measured at this site is consistent with that of the earlier study (*Clement and Robinson, 1987*). The magnetic polarity time scale used in Fig. 4.6 is again based on *Ogg [1995]*.

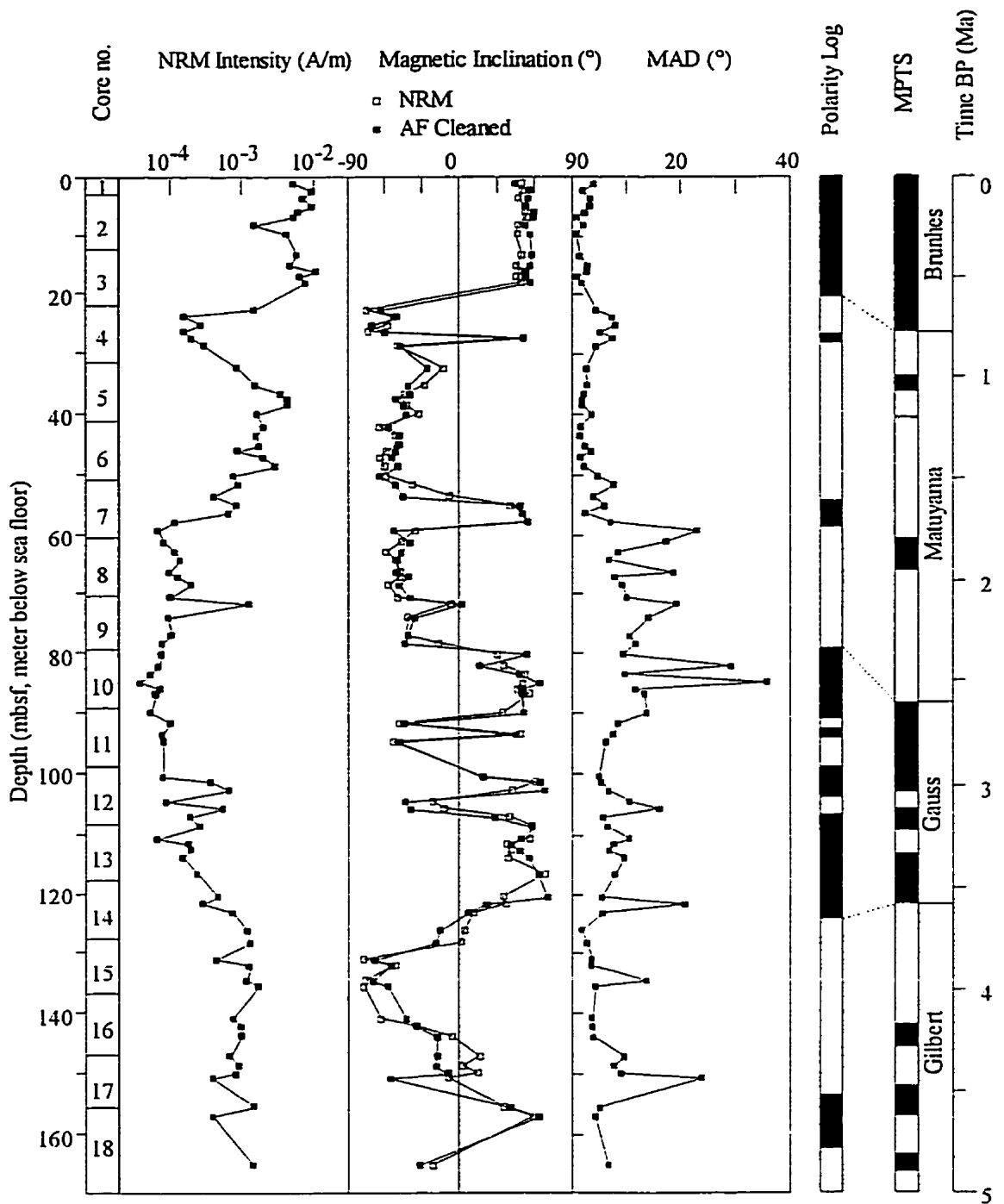


Figure 4.6 The summary of paleomagnetic measurements on carbonate rich specimens of DSDP site 606. MAD is the maximum angular deviation. MPTS is the magnetic polarity time scale based on Ogg [1995].

CHAPTER 5

MAGNETIC ANISOTROPY MEASUREMENTS

5.1 Introduction

In a magnetically anisotropic rock, the strength of various magnetic properties depends on the direction in which they are measured. The magnitude of anisotropy depends on the anisotropy of individual magnetic particles and on the degree of their alignment (*Tarling and Hrouda, 1993*). The anisotropy of the individual particles consists of two components, namely shape anisotropy and magnetocrystalline anisotropy (*Tarling and Hrouda, 1993*). Shape anisotropy is due to preferred orientation of non-spherical ferromagnetic grains. It is displayed only by magnetic minerals with high intrinsic susceptibility such as magnetite. It is easier to magnetize along the long axis of a magnetite grain because self demagnetizing fields are then weakest. Low susceptibility minerals such as hematite display only magnetocrystalline anisotropy. This type of anisotropy is due to magnetization along certain crystallographic axes being easier than along others. If the dominant magnetic mineral is magnetite as it is for the sediments of this study, then the magnetic anisotropy of the sediment should depend mainly on the shape and the orientation of the magnetite grains.

In this study, the magnetic anisotropy is measured in the form of ARM anisotropy and anisotropy of magnetic susceptibility (AMS). ARM anisotropy contains no contribution from paramagnetic and diamagnetic components in the specimen, so it

reflects the preferred orientation of the ferromagnetic particles more accurately than the anisotropy of magnetic susceptibility and should better correlate with inclination shallowing (*Hodych and Bijaksana*, 1993). Nevertheless, both AMS and ARM anisotropy of the sediments are measured to test for correlation with inclination data. The theoretical relationship between susceptibility and remanence ellipsoids has been discussed earlier by *Stephenson et al.* [1986] and tested using metamorphic rocks as well as artificial samples. Their theoretical relationship is tested for our sediments.

5.2 Methods of Magnetic Anisotropy Measurement

In this study, the procedure in ARM anisotropy measurements was similar to that of *McCabe et al.* [1985] modified by *Bijaksana* [1991]. After AF demagnetizing in at least 70 mT, the specimen was given an ARM by applying an alternating field of 70 mT peak strength, which was slowly reduced to zero, in the presence of a direct field of 0.2 mT. The direct field of 0.2 mT was generated by a current of 300 mA (from a 12 volt car battery) passed through an extra layer of turns of wire wound around the AF demagnetizer coil (Schonstedt model GSD-1). The remanence was then measured using the CTF superconducting magnetometer or the Schonstedt spinner magnetometer.

The specimen was given an ARM along the nine directions (N-S, E-W, D-U, NE-SW, ND-SU, ED-WU, NW-SE, NU-SD and EU-WD) proposed by *Girdler* [1961] and was subsequently measured. Each direction was given an ARM in the opposite sense as well and averaged to eliminate any small remanence left after AF demagnetization.

Treated as a second-rank tensor, the ARM anisotropy was then calculated from the nine measured values using the least squares method (details, including the computer program are in *Bijaksana, 1991*). The tensor is expressed in the form of three eigen-values (ARM_{max} , ARM_{int} , ARM_{min}) and three eigen-vectors representing the maximum, intermediate and minimum axes. Geometrically, they represent the principal axes of an ellipsoid.

The anisotropy of magnetic susceptibility (AMS) was measured using a model SI2B magnetic susceptibility meter (Sapphire Instruments) controlled by a personal computer. The instrument measures the magnetic susceptibility of a sample using an internal coil that operates at a frequency of about 19,000 Hz or an external coil at a frequency of about 800 Hz. Although the high frequency coil has a higher sensitivity it may not be suitable for wet samples. The high dielectric constant of water may affect the capacitance of the sample and cause a spurious change in the coil frequency unrelated to the magnetic susceptibility of the sample (*Sapphire Instruments, 1994*). This effect is negligible for the external 800 Hz coil. Since most of the specimens in this study were moist, the external coil was used.

The AMS was measured by inserting the specimen into the coil with the direction to be measured being placed parallel to the coil's axis. Six orientations were measured with two readings for each orientation. A computer program provided with the instrument calculates the magnitudes and directions of the three principal susceptibility axes. In this

study, magnetic susceptibility is expressed as the specific or mass susceptibility χ measured in unit of m^3/kg and the principal susceptibilities are termed χ_{max} , χ_{int} and χ_{min} .

The magnitude of anisotropy is expressed as percent anisotropy and defined as $h_A = 100 \times (ARM_{\text{max}} - ARM_{\text{min}})/ARM_{\text{int}}$ for ARM anisotropy and $h_\chi = 100 \times (\chi_{\text{max}} - \chi_{\text{min}})/\chi_{\text{int}}$ for AMS. The shape of the anisotropy ellipsoid is expressed as a shape parameter, T , defined as $(\ln F - \ln L)/(\ln F + \ln L)$, where $L = ARM_{\text{max}}/ARM_{\text{int}}$ and $F = ARM_{\text{int}}/ARM_{\text{min}}$ for ARM anisotropy and similarly $L = \chi_{\text{max}}/\chi_{\text{int}}$ and $F = \chi_{\text{int}}/\chi_{\text{min}}$ for AMS (Tarling and Hrouda, 1993). L and F are often called magnetic lineation and foliation, respectively. Positive values of T ($0 < T \leq 1$) indicate that magnetic foliation dominates (the ellipsoid is oblate or disk shaped) while negative values of T ($-1 \leq T < 0$) indicate that magnetic lineation dominates (the ellipsoid is prolate or rod shaped). $T = 0$ indicates that both foliation and lineation are equally developed. The intensity of ARM is represented by anhysteretic susceptibility, K_{ARVP} , a dimensionless parameter defined as mean ARM divided by the strength of the biasing field, where mean ARM = $(ARM_{\text{max}} + ARM_{\text{int}} + ARM_{\text{min}})/3$. The intensity of magnetic susceptibility is simply defined as $\chi = (\chi_{\text{max}} + \chi_{\text{int}} + \chi_{\text{min}})/3$.

Since AMS was measured after ARM anisotropy, it may be affected by field-impressed susceptibility anisotropy (Potter and Stephenson, 1990). To minimize this effect, all specimens were demagnetized using 3-axis tumble demagnetization with a peak field of 100 mT prior to AMS measurement.

The directions of the maximum and minimum axes are plotted on equal area stereographic projections. Although the azimuth of the cores from which the specimens

were obtained is unknown, the horizontal plane orientation of the principal axes of anisotropy can be estimated from the natural remanence direction. It was assumed that the primary declination produced by the principal component analysis of the demagnetization data for the NRM coincided with north. The orientation of the principal axes of anisotropy in the horizontal plane was adjusted accordingly.

Since the turbidite specimens were sampled at an interval of ~ 20 cm in each 1.5 m core section, the average primary declination for the 5 to 7 specimens from a core section was used as the "north" direction for that particular section. The specimens from DSDP site 578 and site 606, on the other hand, were sampled at approximately one specimen per section. Thus, each specimen was corrected individually. For example: the primary remanence of specimen 578-3-1-141 has a nominal declination of 186.6°. ARM anisotropy measurement shows that the maximum axis has a declination of 234.7°. Therefore the adjusted declination of the maximum axis is $(234.7 - 186.6)^\circ = 48.1^\circ$. A similar adjustment was also applied to the minimum axis.

5.3 Results

5.3.1 Clay-rich Turbidite Muds from the Scotian Rise

All 79 specimens were measured for ARM anisotropy and the results are summarized in Fig. 5.1. This figure shows that most specimens are very anisotropic with h_a averaging 17%. Eight specimens from core 28 that had already been mixed with deionized water and used in preliminary attempts to measure the particle anisotropy of

sediments (see Chapter 7) prior to AMS measurement. Thus, only 71 specimens were measured for AMS. The results are summarized in Fig. 5.2, which shows that most specimens are very anisotropic with h_z averaging 10%. In both ARM anisotropy and AMS, the values of shape parameter, T , for most specimens are positive, suggesting strong magnetic foliation. Figures 5.3 and 5.4 show the directional distribution of maximum and minimum axes for ARM anisotropy and AMS respectively. For most specimens, the maximum axes are parallel to bedding while the minimum axes are perpendicular to bedding.

5.3.2 Pelagic Clay-Rich Muds of DSDP Site 578

Of 86 specimens measured for natural remanence, 48 specimens were measured for ARM anisotropy (approximately one every two specimens). Figure 5.5 summarizes the results of ARM anisotropy measurements. It shows that most specimens have very low anisotropy ($h_z < 5\%$ in most cases). As in core 28, some specimens from this site were also used in the attempts to measure the particle anisotropy of sediments prior to AMS measurement. Thus, only 64 specimens were measured for AMS. The results are summarized in Fig. 5.6 which shows that most specimens have a very low anisotropy (h_z averages 2.6 %).

Low degree of anisotropy observed in both ARM anisotropy and AMS makes the directions of the principal axes as well as the shape parameter unreliable. The shape parameter, T , varies greatly from one specimen to another. Some specimens show

ARM ANISOTROPY IN THE TURBIDITES

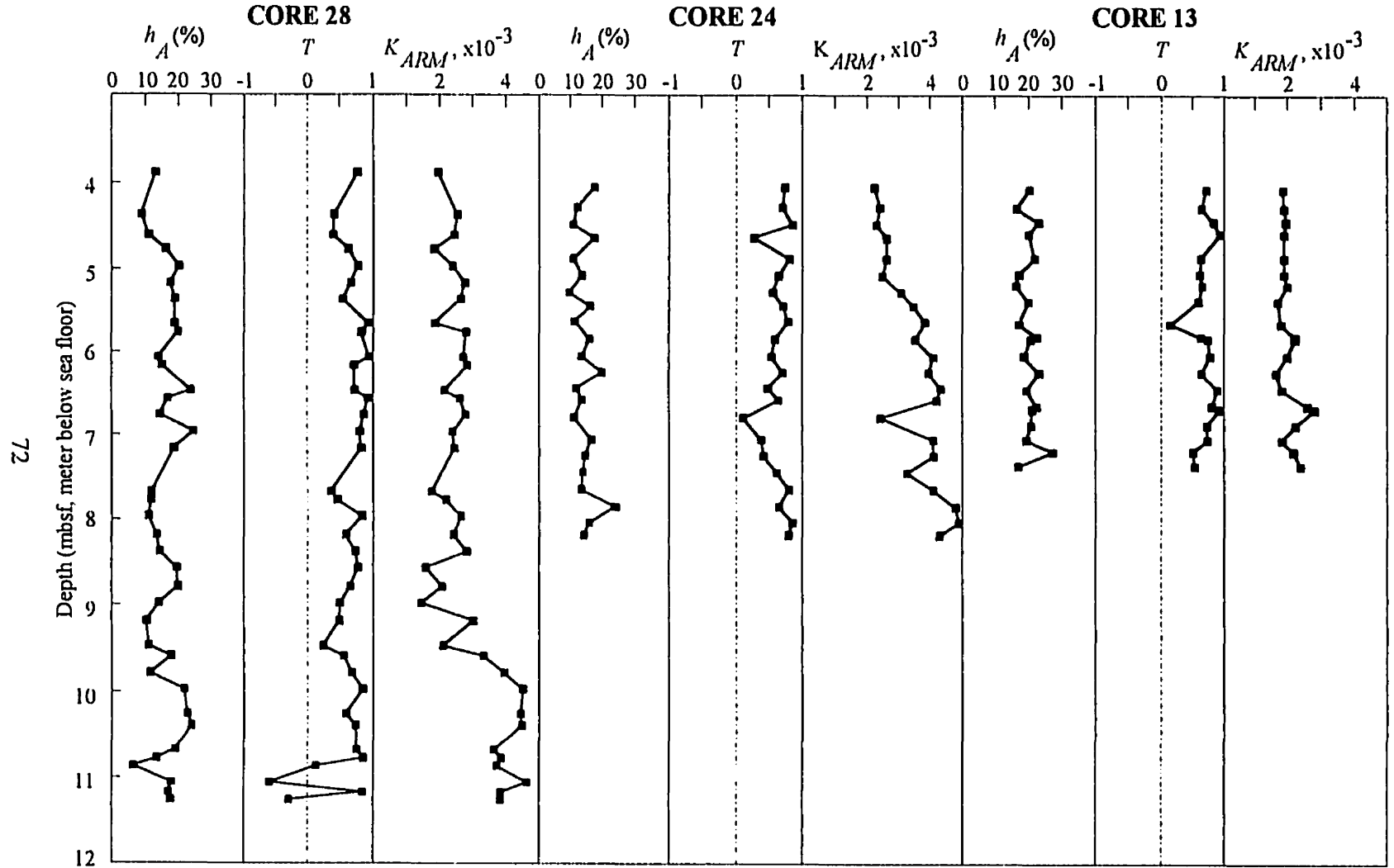


Figure 5.1 The summary of ARM anisotropy measurements for turbidite specimens of cores 28, 24 and 13. h_A indicates percent anisotropy, T the shape parameter and K_{ARM} the intensity of ARM.

SUSCEPTIBILITY ANISOTROPY IN THE TURBIDITES

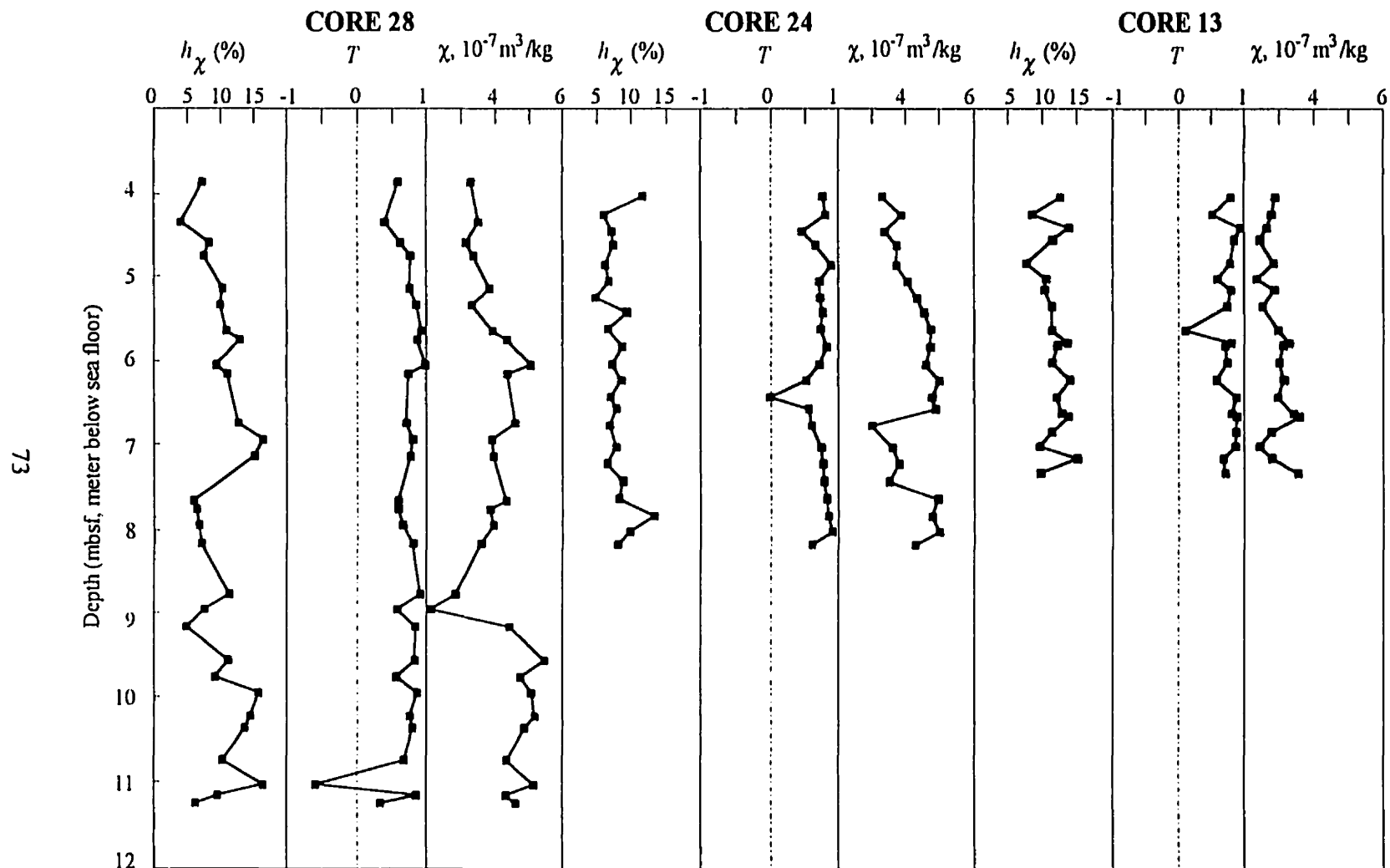
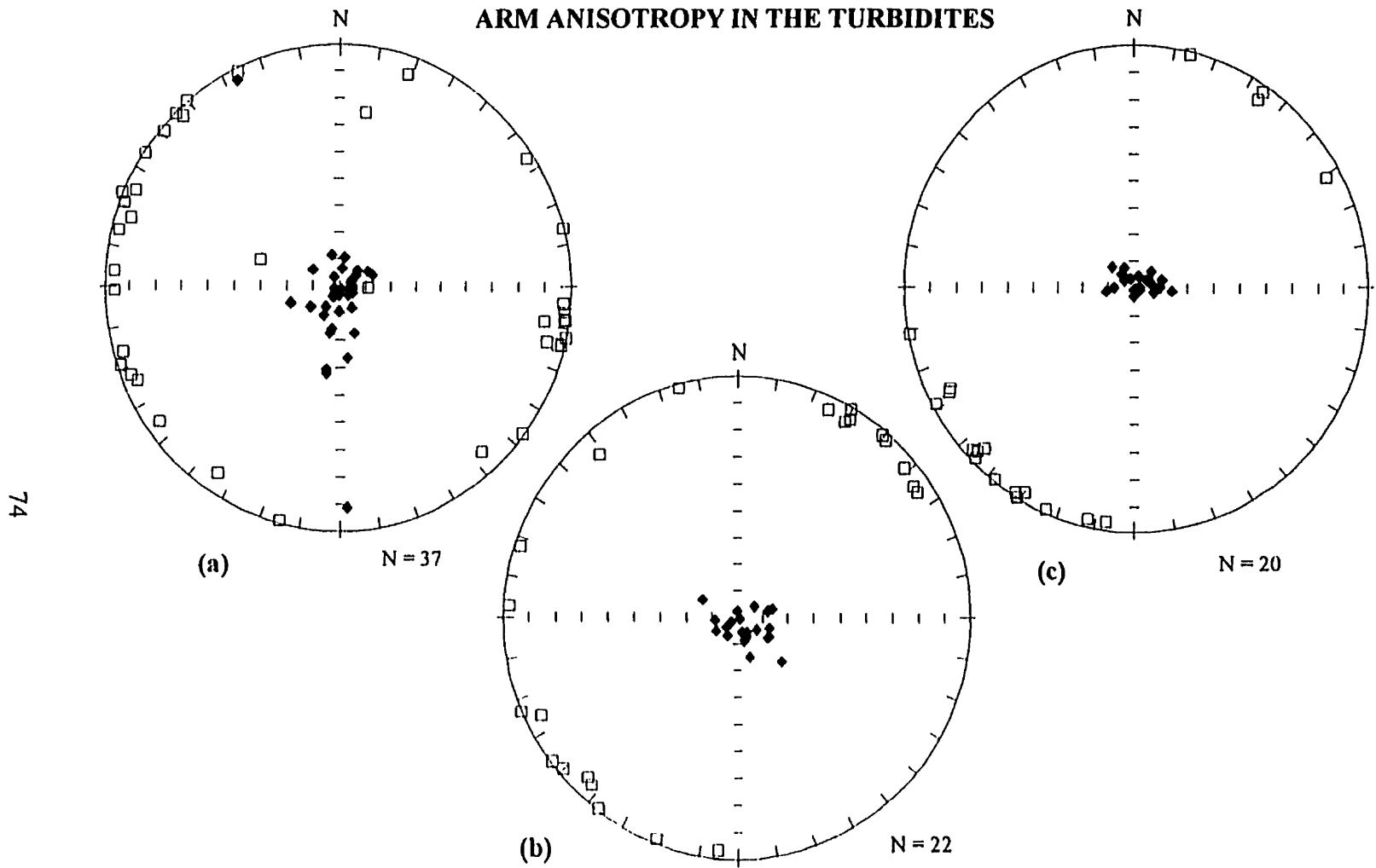


Figure 5.2 The summary of AMS measurements for turbidite specimens of cores 28, 24 and 13. h_χ indicates percent susceptibility anisotropy, T the shape parameter and χ the intensity of mass susceptibility.



74

Figure 5.3 Equal area projections of directions of ARM_{max} (open squares) and ARM_{min} (solid diamonds) axes in specimens of cores 28 (a), 24(b) and 13 (c). The azimuths have been estimated assuming that the primary remanence declination is north (Section 5.2).

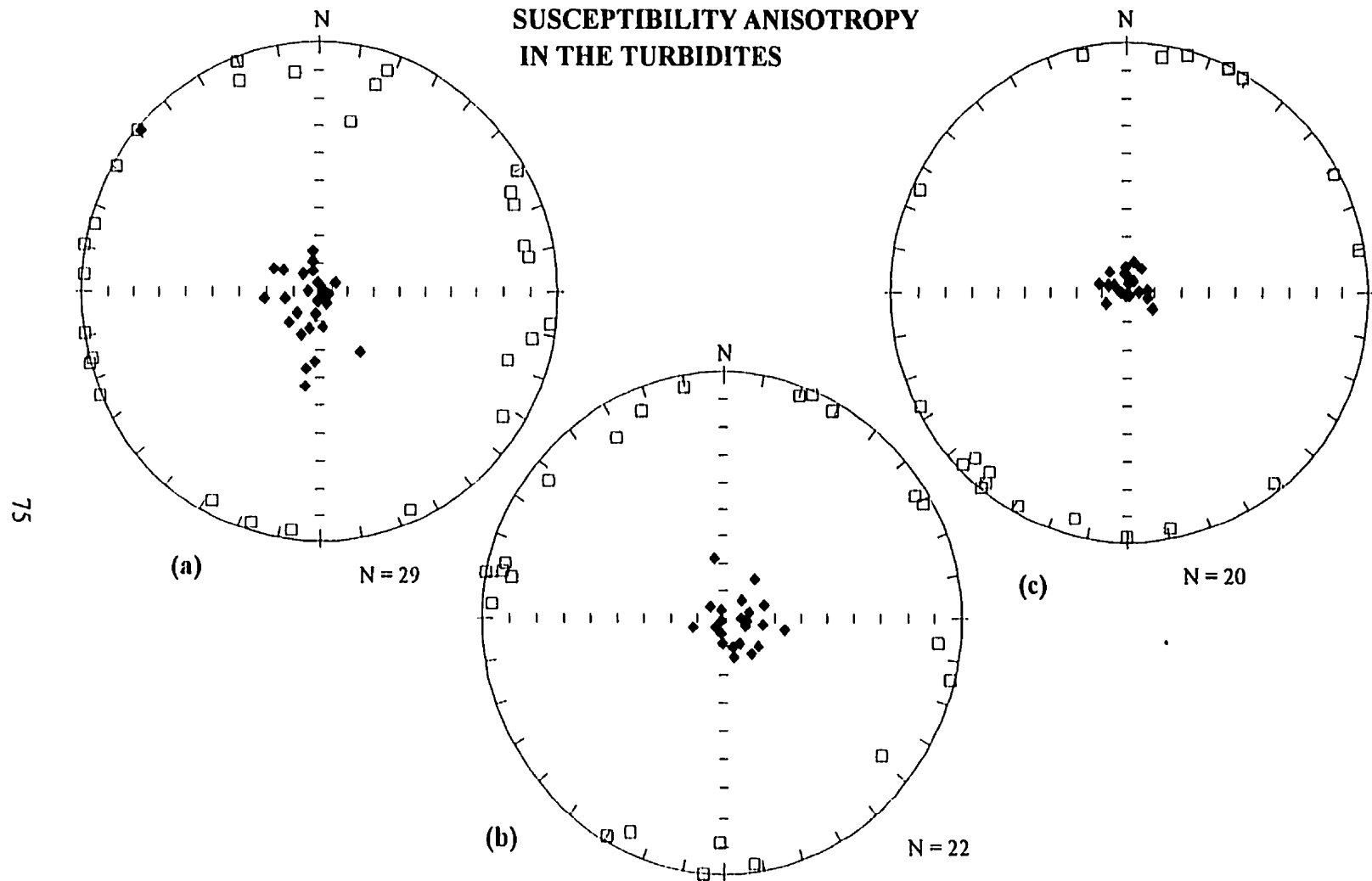


Figure 5.4 Equal area projections of directions of maximum (open squares) and minimum (solid diamonds) susceptibility axes in specimens of cores 28 (a), 24 (b) and 13 (c). The azimuths have been estimated assuming that the primary remanence declination is north (Section 5.2).

ARM ANISOTROPY OF THE PELAGIC CLAY-RICH MUDS

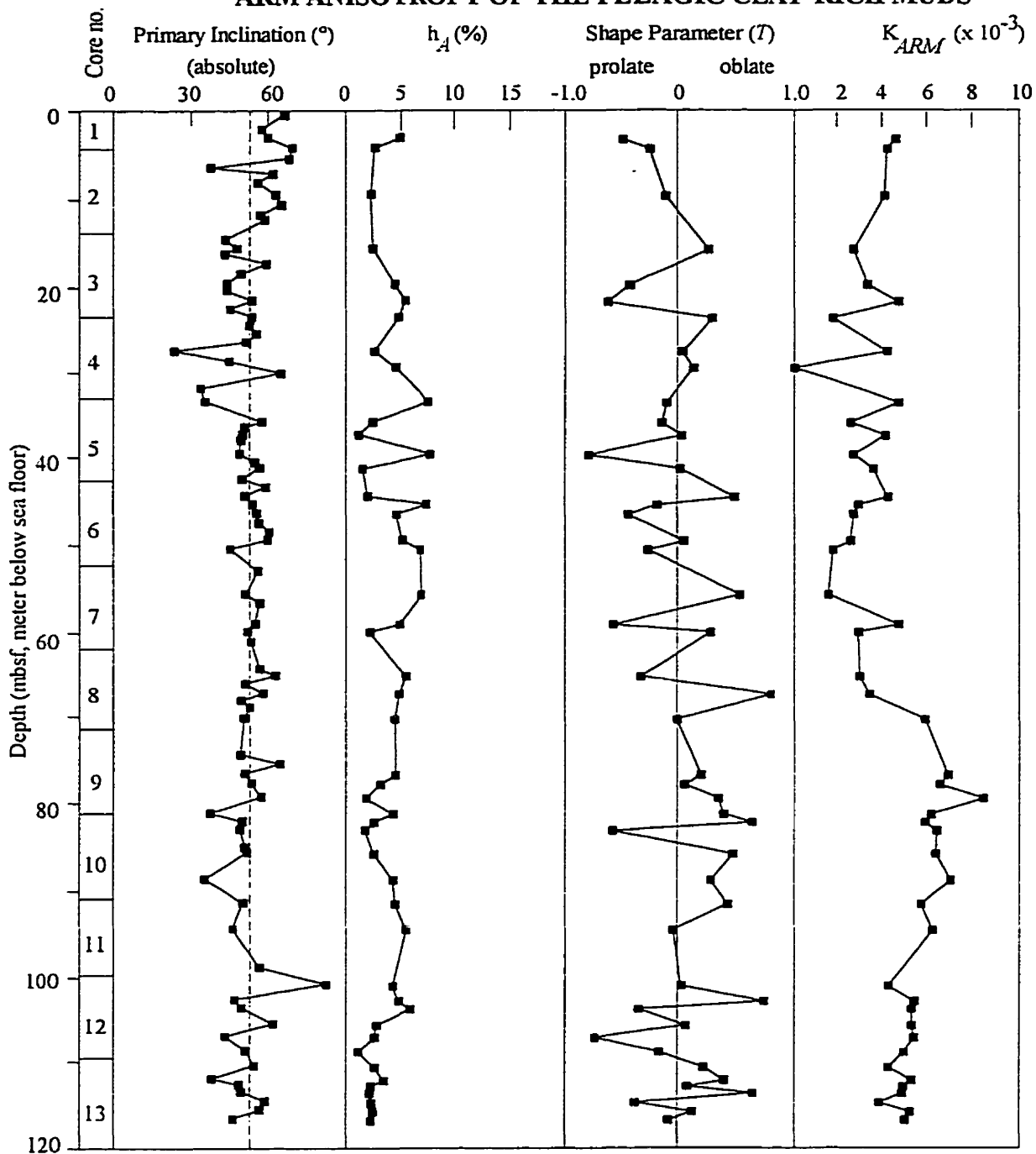


Figure 5.5 The absolute value of primary inclination for specimens whose MAD values are less than 10° and the summary of ARM anisotropy measurements for site 578. The dashed line on the primary inclination curve indicates 53.4° , which is the inclination at that site according to the GAD model. h_A indicates the percent anisotropy and K_{ARM} the intensity of ARM.

SUSCEPTIBILITY ANISOTROPY OF THE PELAGIC CLAY-RICH MUDS

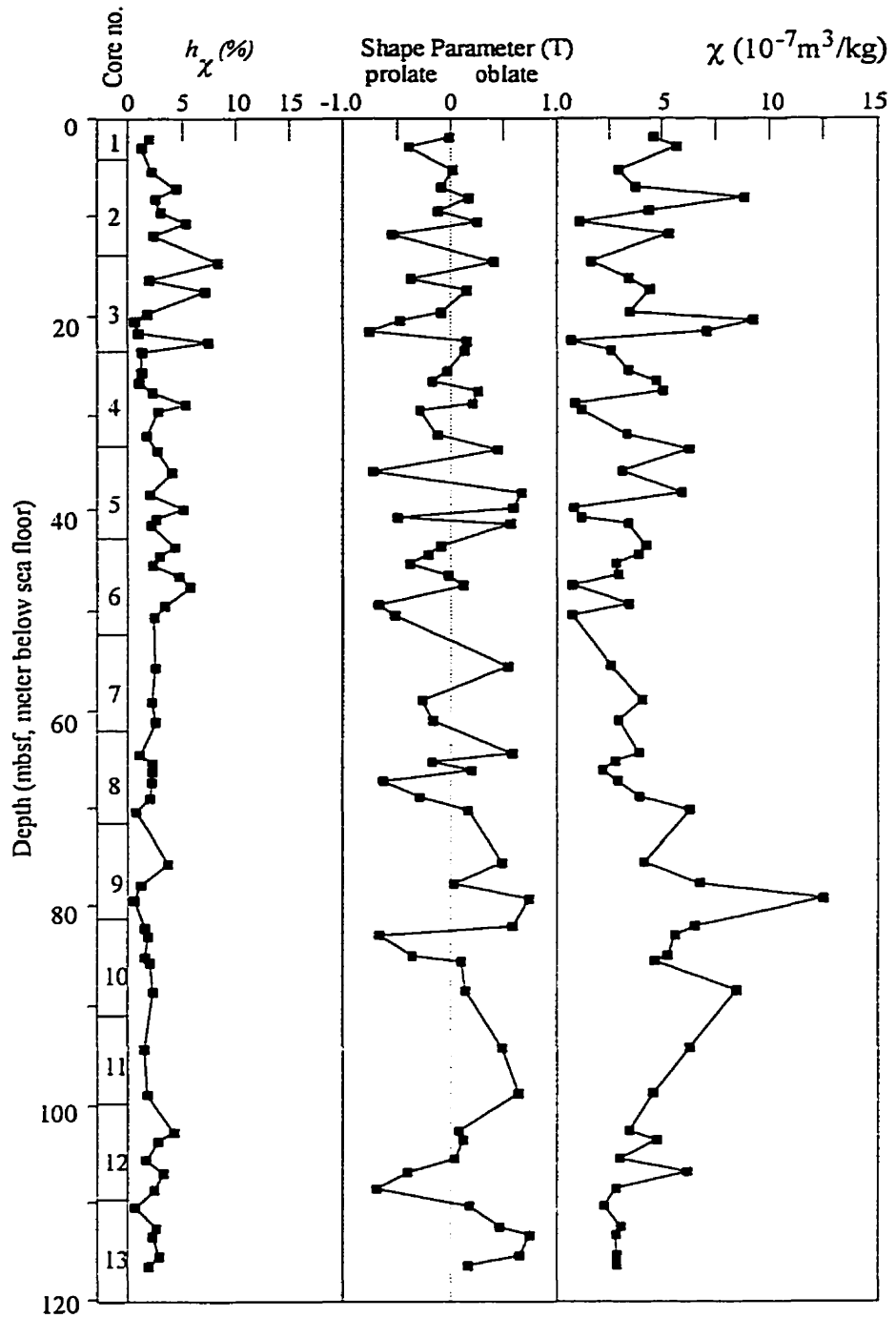


Figure 5.6 The summary of AMS measurements for pelagic clay specimens of DSDP site 578. h_{χ} indicates percent susceptibility anisotropy, T the shape parameter and χ the intensity of mass susceptibility.

SITE 578
PELAGIC CLAY-RICH MUDS

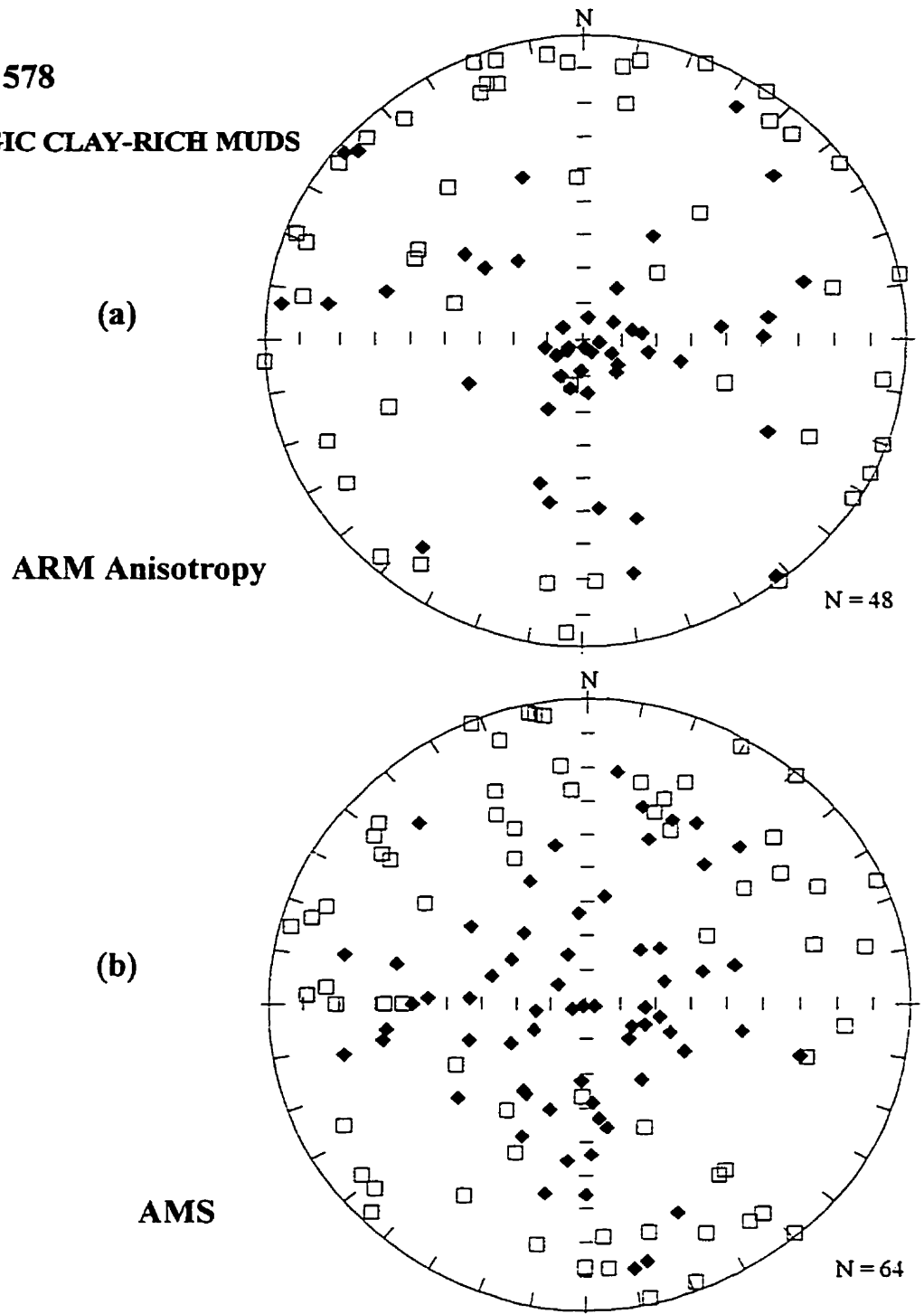


Figure 5.7 Equal area projections of directions of maximum (open squares) and minimum (solid diamonds) axes of ARM anisotropy (a) and AMS (b) in specimens of DSDP site 578. The azimuths have been estimated assuming that the primary remanence declination is north (Section 5.2).

magnetic foliation, while others show magnetic lineation. Figure 5.7 shows that the directions of maximum and minimum axes for both ARM anisotropy and AMS are very scattered.

5.3.3 Pelagic Lime-Muds of DSDP Site 606

Of 72 specimens with MAD values of less than 10° , 35 specimens were measured for ARM anisotropy. Figure 5.8 summarizes the ARM anisotropy measurements. Specimens from site 606, like those from site 578, possess low anisotropy ($h_A < 5\%$ in most cases) and the directions of their maximum and minimum axes are very scattered (Fig. 5.9). Figure 5.8 also shows that the shape parameter, T , varies greatly from one specimen to another, although much of this may be due to inaccuracy in measurement due to the low anisotropy. The values of K_{ARM} vary greatly in rough proportion to values of NRM intensity.

The magnetic susceptibilities of specimens from site 606 are too weak to be measured accurately with the current instrument, even with the high frequency coil. The AMS measurements for site 606 were terminated after finding that the 15 pilot specimens (including those from the high intensity zone) showed either negative or very low susceptibility (less than 1×10^{-5} SI approaching the 1×10^{-6} SI noise level of the sensor coil). This low or negative susceptibility is presumably due to the high content of calcite which is diamagnetic (Hunt *et al.*, 1995).

ARM ANISOTROPY OF THE PELAGIC LIME-MUDS

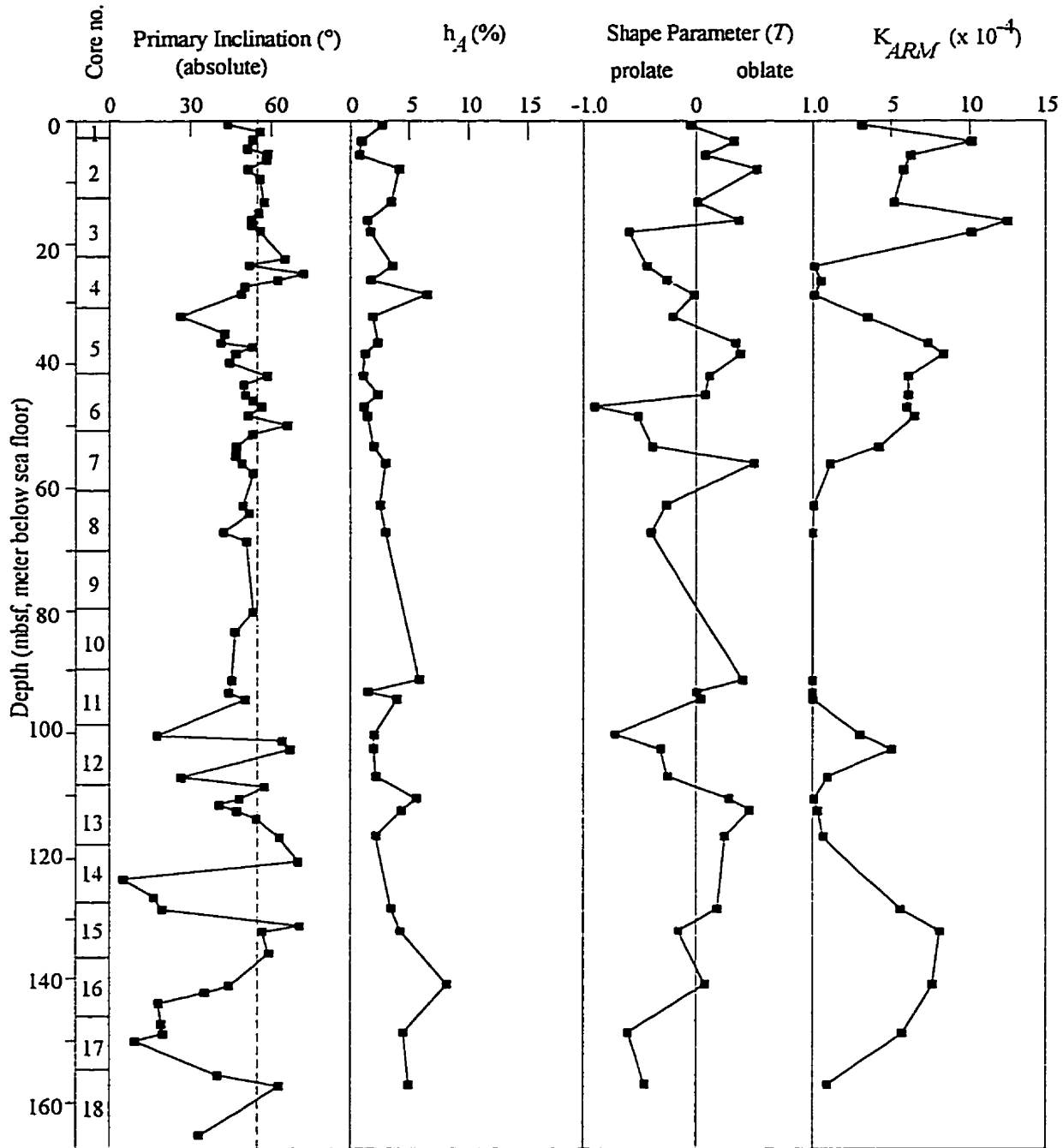


Figure 5.8 The absolute value of primary inclination for specimens whose MAD value are less than 10° and the summary of ARM anisotropy measurements for site 606. The dashed line on the primary inclination curve indicates 56.8° , which is the inclination at that site according to the GAD model. h_A indicates the percent anisotropy and K_{ARM} the intensity of ARM.

SITE 606

PELAGIC LIME-MUDS

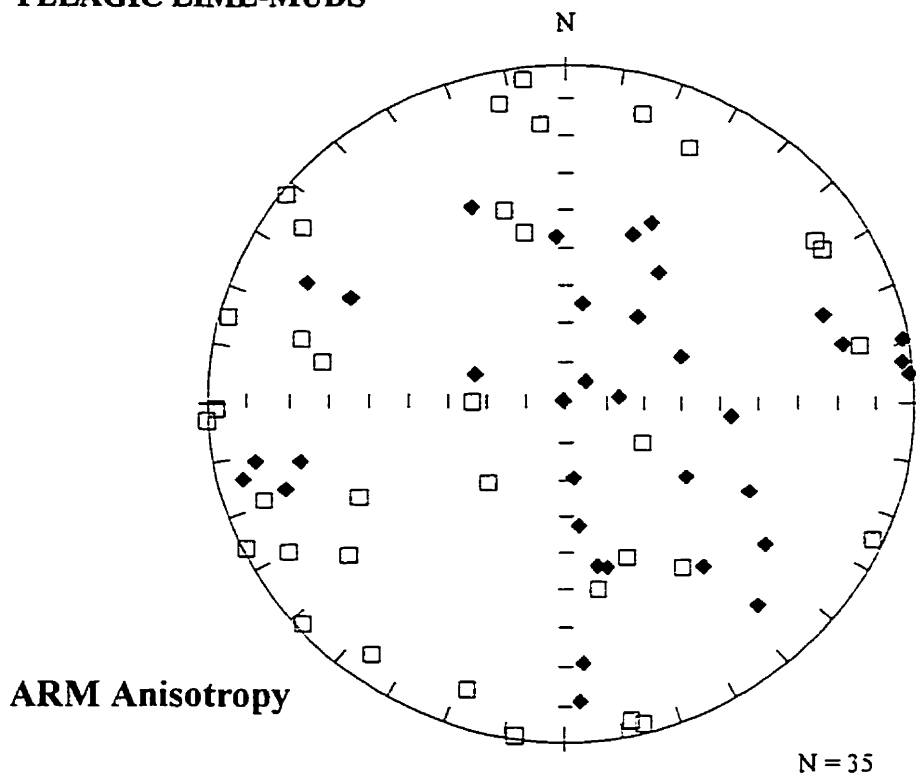


Figure 5.9 Equal area projections of directions of ARM_{max} (open squares) and ARM_{min} (solid diamonds) in specimens of DSDP site 606. The azimuths have been estimated assuming that the primary remanence declination is north (Section 5.2).

5.4 Magnetic Anisotropy of the Turbidites and the Pelagic Specimens Compared

Magnetic anisotropy measurements show that the turbidites from the Scotian Rise are strongly anisotropic while the pelagic clays of DSDP site 578 and the pelagic lime-muds of DSDP site 606 have very low anisotropy. The percent ARM anisotropy, h_a , in the turbidites is high, averaging $16.2\% \pm 4.5\%$ for core 28, $14.5\% \pm 3.3\%$ for core 24 and $20.3\% \pm 2.7\%$ for core 13. The percent susceptibility anisotropy, h_x , for these three cores is also high, averaging 10%. The percent ARM anisotropy, h_a , in the pelagic specimens is low, averaging $3.7\% \pm 1.7\%$ for site 578 and $3.0\% \pm 1.7\%$ for site 606 while the percent susceptibility anisotropy, h_x averages 2.6% for site 578. The magnetic susceptibilities of specimens from site 606 were too weak to be measured with the current instrument.

Except for a few specimens from core 28 (see Sect. 6.1), the maximum axes in the turbidite specimens are found to be parallel to bedding, while the minimum axes are perpendicular to bedding. These specimens are also magnetically foliated as indicated by their positive T values. In contrast, the principal axes of specimens from sites 578 and 606 are scattered in all directions (the minimum axes of ARM anisotropy in some specimens from site 578, however, are perpendicular to bedding). Besides, the directions of the principal axes, as well as the shape of the anisotropy ellipsoid, are meaningless in a nearly isotropic specimen. The possible causes for these differences in magnetic anisotropy between the turbidites and the pelagic sediments will be discussed in Chapter 7.

5.5 Comparing ARM Anisotropy and Susceptibility Anisotropy

Stephenson et al. [1986] showed that the susceptibility and remanence (including ARM) ellipsoids are related through

$$p_x = p_o + sq_x \quad (5.1)$$

where p_x is the normalized principal susceptibility along the x direction given by $\chi_x/(\chi_x + \chi_y + \chi_z)$ and q_x is the normalized principal ARM along the x direction given, as in Section 1.4, by $q_x = ARM_x/(ARM_x + ARM_y + ARM_z)$. Similar relations apply to p_y , p_z , q_y and q_z . The quantity p_o is defined by *Stephenson et al.* [1986] as

$$p_o = \frac{\gamma - \alpha}{(\alpha + 2)(\gamma - 1)} \quad (5.2),$$

where $\gamma = ARM_{//}/ARM_{\perp}$ is the ARM particle anisotropy (see Section 1.4) and α is the susceptibility equivalent of γ . Assuming that each magnetic particle has its anisotropy represented by an ellipsoid of revolution, α is defined as $\chi_{//}/\chi_{\perp}$, where $\chi_{//}$ and χ_{\perp} are the susceptibilities of the particle measured parallel and perpendicular to its axis of rotational symmetry respectively. The quantity s is defined as

$$s = \frac{(\alpha - 1)(\gamma + 2)}{(\alpha + 2)(\gamma - 1)} = 1 - 3p_o \quad (5.3).$$

In practice, α and γ are difficult to measure. However, parameters p_o and s can be calculated if one plots the normalized principal susceptibilities (p) against the normalized principal ARM's (q). Equation (5.1) predicts a straight line that passes through (1/3, 1/3) with slope s and intercept p_o . *Stephenson et al.* [1986] claim that p_o and s , whose values depend on whether the magnetic minerals are predominantly single-domain particles or multi-domain particles, can relate the individual particle characteristics to the anisotropy of the specimen.

Figure 5.10 shows the p versus q graphs for specimens from cores 28, 24 and 13. Both p and q are expressed in the directions of the principal (maximum, intermediate and minimum) axes. For each specimen, three data points were plotted (p_{max} , p_{int} , p_{min} against q_{max} , q_{int} , q_{min}). In all three cores, data points follow a straight line that passes closely through (1/3, 1/3). The values of p_o and s are determined using a least-squares fit line. The results are listed in Table 5.1. Although the values of s were determined independently from p_o , they agreed with $1 - 3p_o$ as predicted in Eq. (5.3). The values of the correlation coefficient, R , imply that the correlation between p and q is significant with 99.9% confidence.

Figure 5.10 also shows that the ARM ellipsoid of these turbidite specimens is more anisotropic than the susceptibility ellipsoid and that the maximum susceptibility axis corresponds with the maximum ARM axis. These results, and the values of p_o ranging from 0.12 to 0.15, are typical of multi-domain or pseudo-single-domain particles (*Stephenson et al.*, 1986).

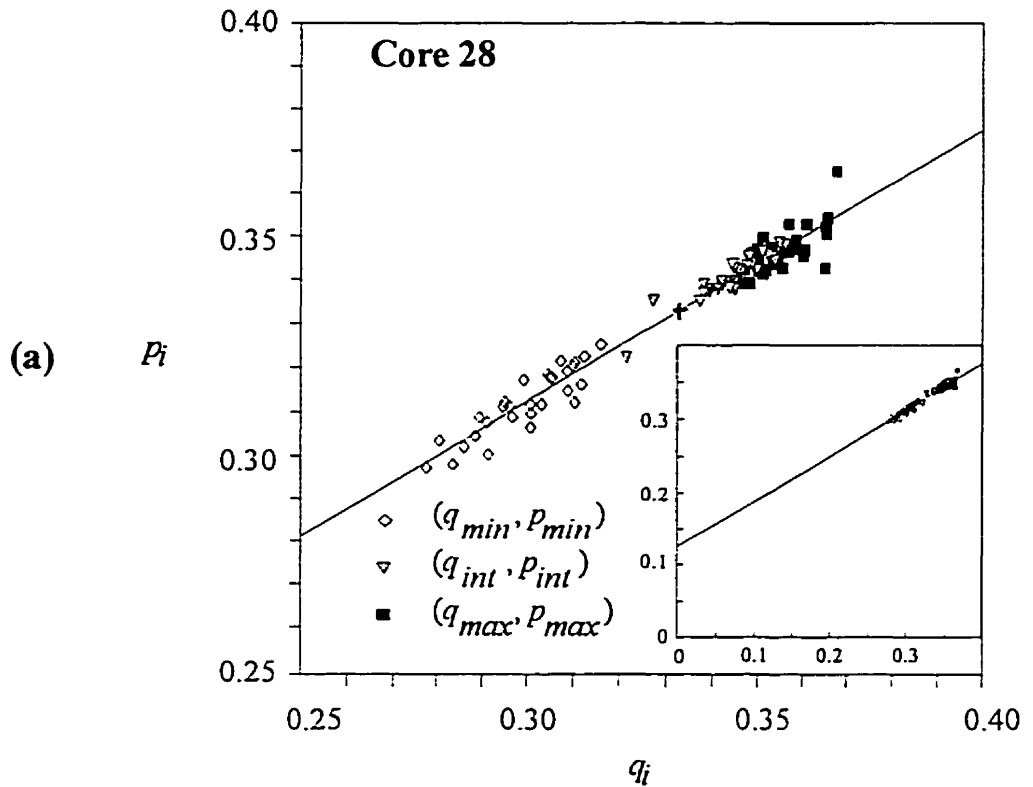


Figure 5.10 The normalized principal values of the susceptibility ellipsoid (p_i) and ARM ellipsoid (q_i) for turbidite specimens of cores 28 (a), 24 (b), and 13 (c). The cross is at $(1/3, 1/3)$. The straight line is the least-squares fit line for these data. The slope of the line is s and the intercept is p_o (see Table 5.1).

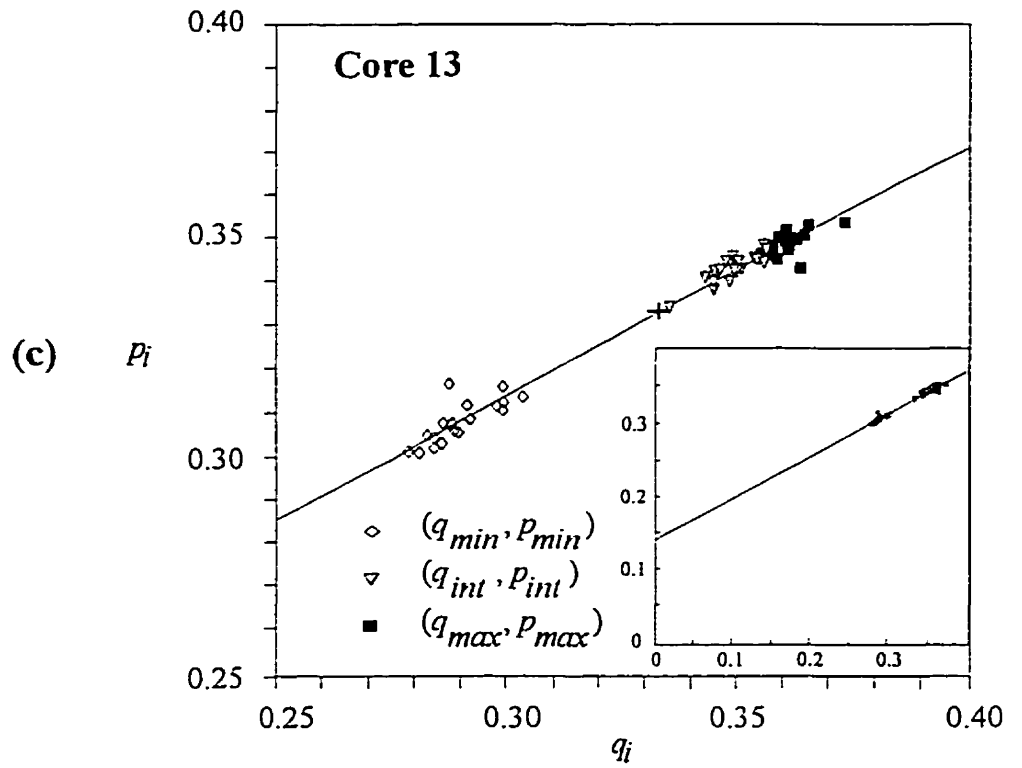
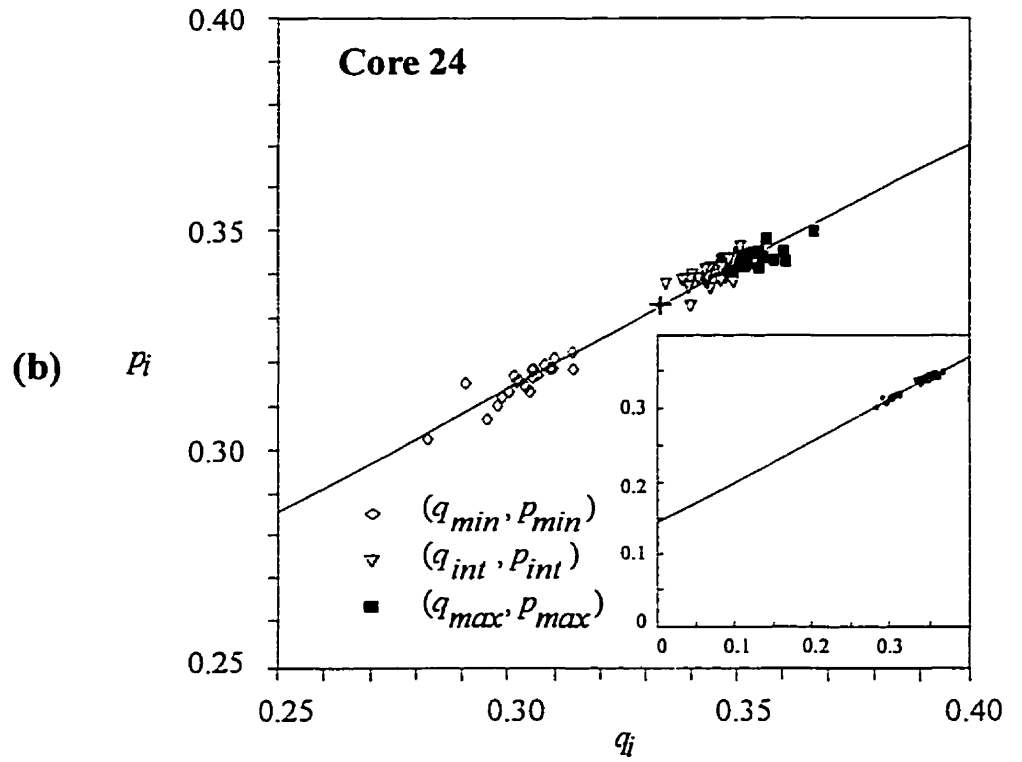


Figure 5.10 (Continued)

Table 5.1 Parameters p_o and s for the Turbidite Specimens

Core	No. of Spec.	p_o	Δp_o	s	Δs	R
28	29	0.126	0.003	0.621	0.013	0.981
24	22	0.148	0.002	0.557	0.012	0.984
13	20	0.144	0.002	0.569	0.011	0.992

The relationship between AMS and ARM anisotropy for the turbidite specimens in this study agrees well with the theory of *Stephenson et al.* [1986]. Also, it has been shown that the ellipsoids of AMS and ARM anisotropy have a similar shape and that the directions of their principal axes are quite similar. Although ARM anisotropy is expected to be superior to AMS in representing the fraction of magnetic particles carrying stable NRM, these results imply that AMS may also represent the stable fraction of magnetite reasonably well. Below, the possibility of using AMS in place of ARM anisotropy to detect inclination shallowing is explored. AMS has the advantage of speed of measurement and does not affect NRM.

Rewriting Eq. (5.1), it can be shown that

$$q_{\max} = \frac{p_{\max} - p_o}{s} \quad (5.4)$$

and that

$$q_{\min} = \frac{p_{\min} - p_o}{s} \quad (5.5).$$

Using ARM_{min}/ARM_{max} in place of q_{min}/q_{max} , one obtains

$$\frac{ARM_{min}}{ARM_{max}} = \frac{p_{min} - p_o}{p_{max} - p_o} \quad (5.6).$$

Assuming that $p_{int} = p_{max}$, one can then plot ARM_{min}/ARM_{max} versus χ_{min}/χ_{max} (which equals p_{min}/p_{max}) for different values of p_o . Figure 5.11 shows this relation for the observed range of χ_{min}/χ_{max} . It shows that for $p_o < 0.25$ the relation is approximately linear. Since p_o for the turbidites varies only from 0.126 (for core 28) to 0.148 (for core 24), χ_{min}/χ_{max} should be approximately linearly related to ARM_{min}/ARM_{max} . This is shown to be the case in Fig. 5.11.b.

Since the ellipsoid of susceptibility is generally less anisotropic than the ARM ellipsoid, AMS of a few percent is probably sufficient to warn of the presence of inclination shallowing. Data from the turbidites show that the average h_z of 10% corresponds to 12° of inclination shallowing. Hence, 5% AMS, which is often considered low enough for paleomagnetism, would give roughly 6° of inclination shallowing.

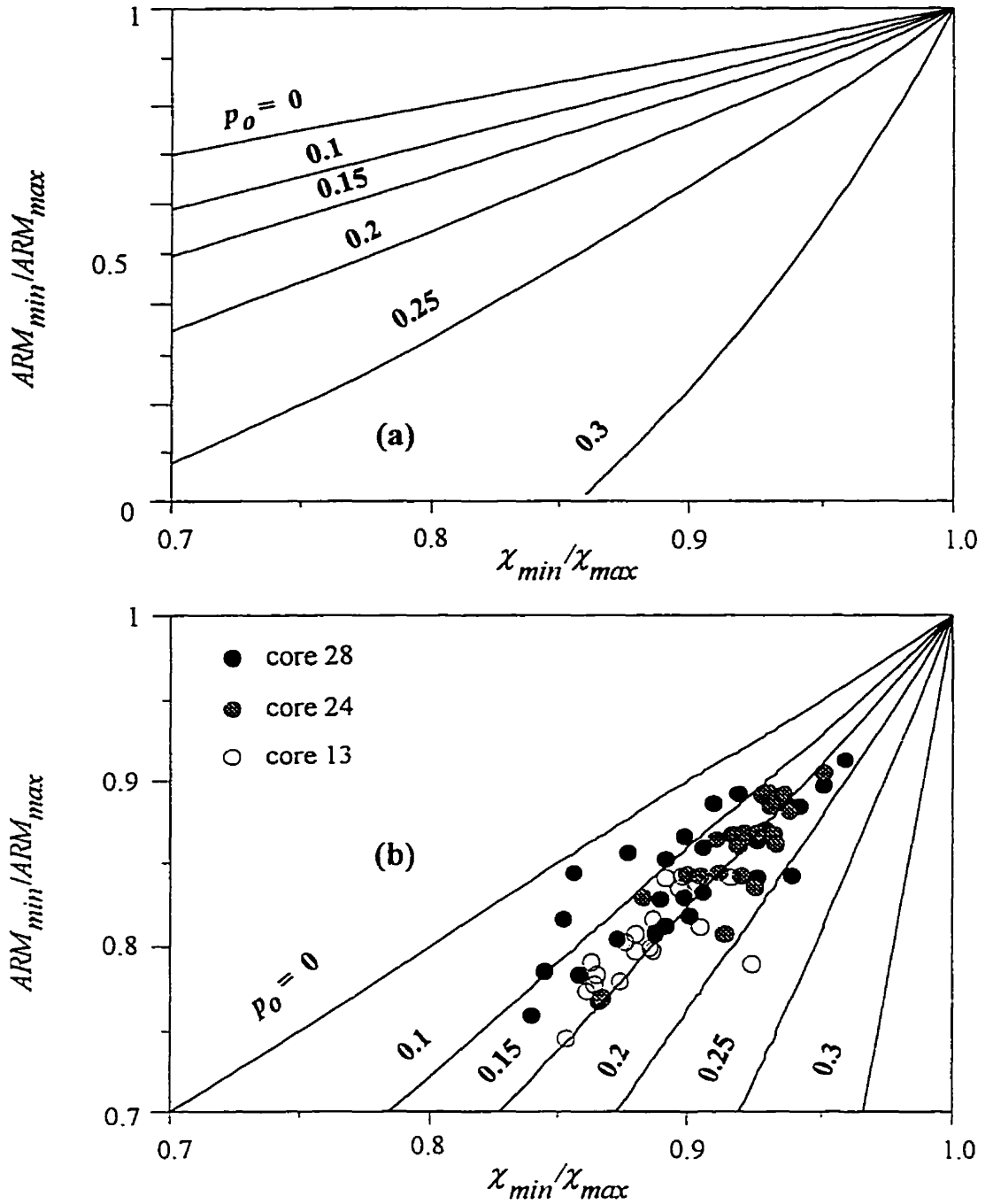


Figure 5.11 The relation between ARM anisotropy and susceptibility anisotropy predicted by Eq. (5.6) for various values of p_o in the observed range of χ_{min}/χ_{max} (a) and observed for the turbidite specimens (b).

CHAPTER 6

**CORRELATING REMANENCE INCLINATION AND MAGNETIC
ANISOTROPY AND PREDICTING PALEOMAGNETIC
INCLINATION SHALLOWING**

6.1 Correlation between Remanence Inclination and ARM anisotropy

It has been suggested (*Hodych and Bijaksana, 1993*) that ARM anisotropy can be used to test for the presence of magnetic inclination shallowing in a suite of sedimentary samples. The test requires that the minimum axis of ARM anisotropy of each sample be perpendicular to bedding and that the ARM anisotropy (ARM_{min}/ARM_{max}) (should) correlate significantly with the tangent of the inclination of the cleaned remanence.

The turbidite specimens are very suitable for this test. Their minimum axes of ARM anisotropy are perpendicular to bedding (except for a few specimens from core 28). They are also magnetically foliated as indicated by their positive T values. The percent ARM anisotropy is high, averaging $16.2\% \pm 4.5\%$ for core 28, $14.5\% \pm 3.3\%$ for core 24 and $20.3\% \pm 2.7\%$ for core 13.

The pelagic clay and the pelagic lime-mud specimens of DSDP sites 578 and 606 show their minimum axis of ARM anisotropy scattered at various angles to the bedding plane (Fig(s). 5.7 and 5.9) making them not very suitable for the above test. The scatter is likely due to the low values of percent ARM anisotropy which average only $3.7\% \pm 1.7\%$ for site 578 and $3.0\% \pm 1.7\%$ for site 606. Low anisotropy is likely also responsible for

the irregularity of the shape of the anisotropy ellipsoid as some specimens are magnetically foliated while the others are lineated. However, these results are compatible with theory in that this low ARM anisotropy is associated with a lack of significant inclination shallowing found in these pelagic specimens. The average primary inclination of the pelagic clay specimens measured in this study is $52^\circ \pm 9^\circ$, which does not differ significantly from the 53° calculated from the GAD model for this site. The primary inclination for the pelagic lime-muds of site 606 from 0 to 60 m averages $53^\circ \pm 8^\circ$, which does not differ significantly from the 57° calculated from the GAD model for this site. The inclination data below 60 m are unusable, their quality deteriorating in the low intensity zone from 60 to 100 m and becoming erratic from 100 m to the bottom (see Fig. 5.8).

Figure 6.1 shows $\tan I_{obs}$ plotted beside ARM_{min}/ARM_{max} as a function of depth in the three turbidite cores studied. The correlation between $\tan I_{obs}$ and ARM_{min}/ARM_{max} was tested for each core and the correlation coefficients are given in Fig. 6.1. In core 24, this correlation is significant with 90% confidence ($R = 0.378$, $N = 22$), while in core 13 it is significant with 95% confidence ($R = 0.530$, $N = 20$). There is no correlation in core 28 ($R = 0.058$, $N = 37$).

It is possible that the poor correlation between $\tan I_{obs}$ and ARM_{min}/ARM_{max} in core 28 arises from some of the specimens having been disturbed during coring. In strongly anisotropic sediments such as these turbidites, the ARM_{min} axis is expected to be perpendicular to the bedding. Disturbance such as that due to coring could change this orientation as well as distorting the remanence inclination. Thus, it should be possible to

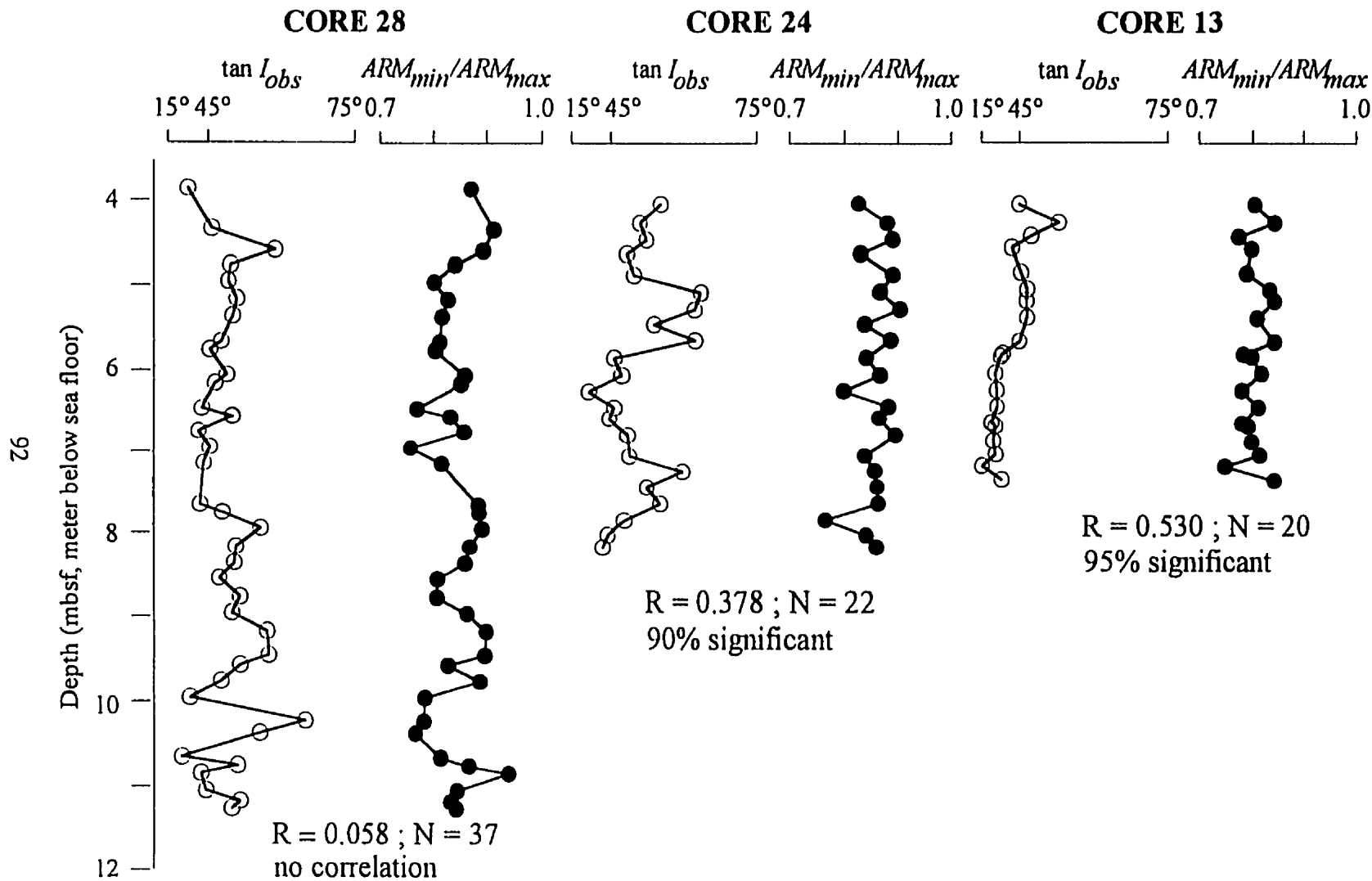


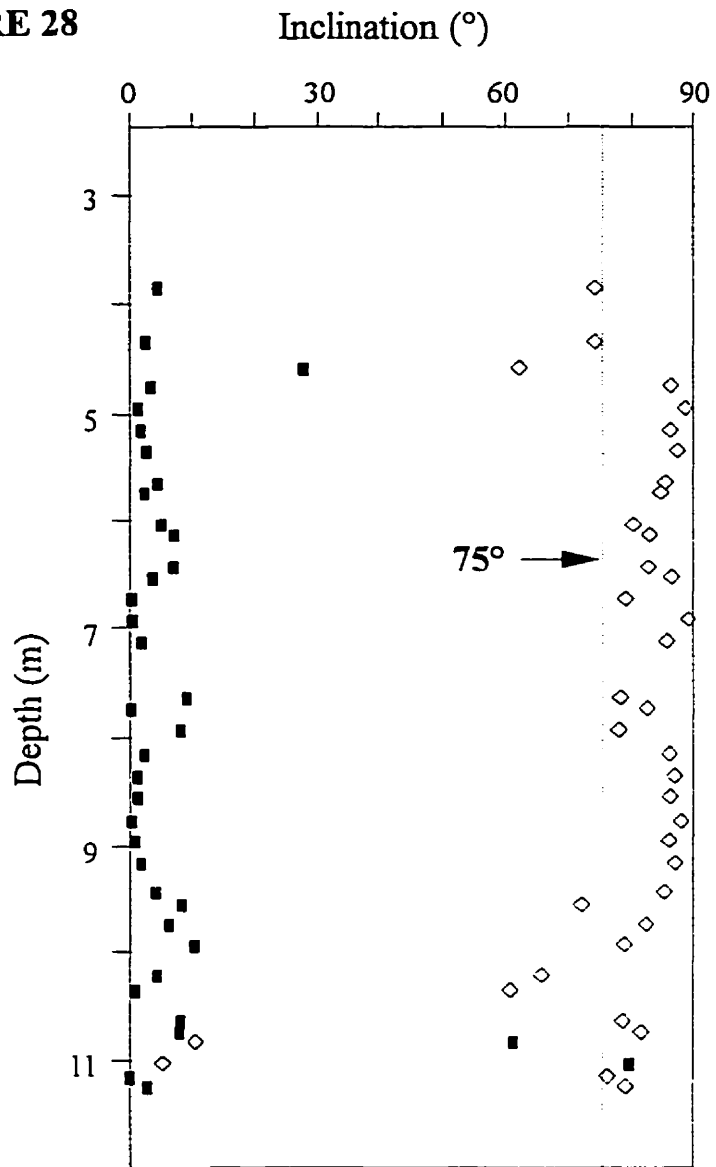
Figure 6.1 Tangent of the observed inclination $\tan I_{obs}$ and the inverse ARM anisotropy ARM_{min}/ARM_{max} for the three turbidite cores.

identify the disturbed specimens using the non-verticality of their ARM_{min} axes. Figure 6.2 shows that some of the specimens from core 28 have ARM_{min} axes that are tilted significantly from vertical. In this study, unreliable specimens will be defined as those whose ARM_{min} axes have inclinations of less than 75° . Among the 37 specimens of core 28, 8 are thus classified as unreliable and are excluded. The only other turbidite specimen classified as unreliable and excluded was a specimen from core 24 (24-0722).

To test the validity of this selection of unreliable specimens, all turbidite specimens from the three cores were photographed using a portable X-ray unit (Picker X-ray Corp.). The X-radiographs were scanned digitally into computer images and subsequently enlarged. Although most images did not reveal bedding, those that did (14 out of 33 specimens) all supported the selection process. Figure 6.3 shows the X-radiograph of 28-0459, which is a typical specimen selected as unreliable (inclination of ARM_{min} axis = 62.1°). It shows that the bedding plane has been tilted significantly. Figure 6.3 also shows the X-radiograph of 28-0877, which is a typical specimen selected as reliable (inclination of ARM_{min} axis = 87.8°). The bedding plane does appear undisturbed.

Figure 6.4 shows that when the 8 unreliable specimens are excluded, the correlation between $\tan I_{obs}$ and ARM_{min}/ARM_{max} in core 28 improves greatly and becomes significant with 99% confidence ($R = 0.540$, $N = 29$). Removal of the one other unreliable specimen (24-0722) has little effect on the results from core 24; the correlation remains significant at 90% confidence ($R = 0.393$, $N = 21$).

CORE 28



■ Inclination of ARM_{max} axis ◇ Inclination of ARM_{min} axis

Figure 6.2 The inclination of the ARM_{max} axis and the ARM_{min} axis of specimens as a function of depth in core 28. The specimens whose ARM_{min} axes are not vertical (inclination $< 75^\circ$) are considered disturbed and unreliable.

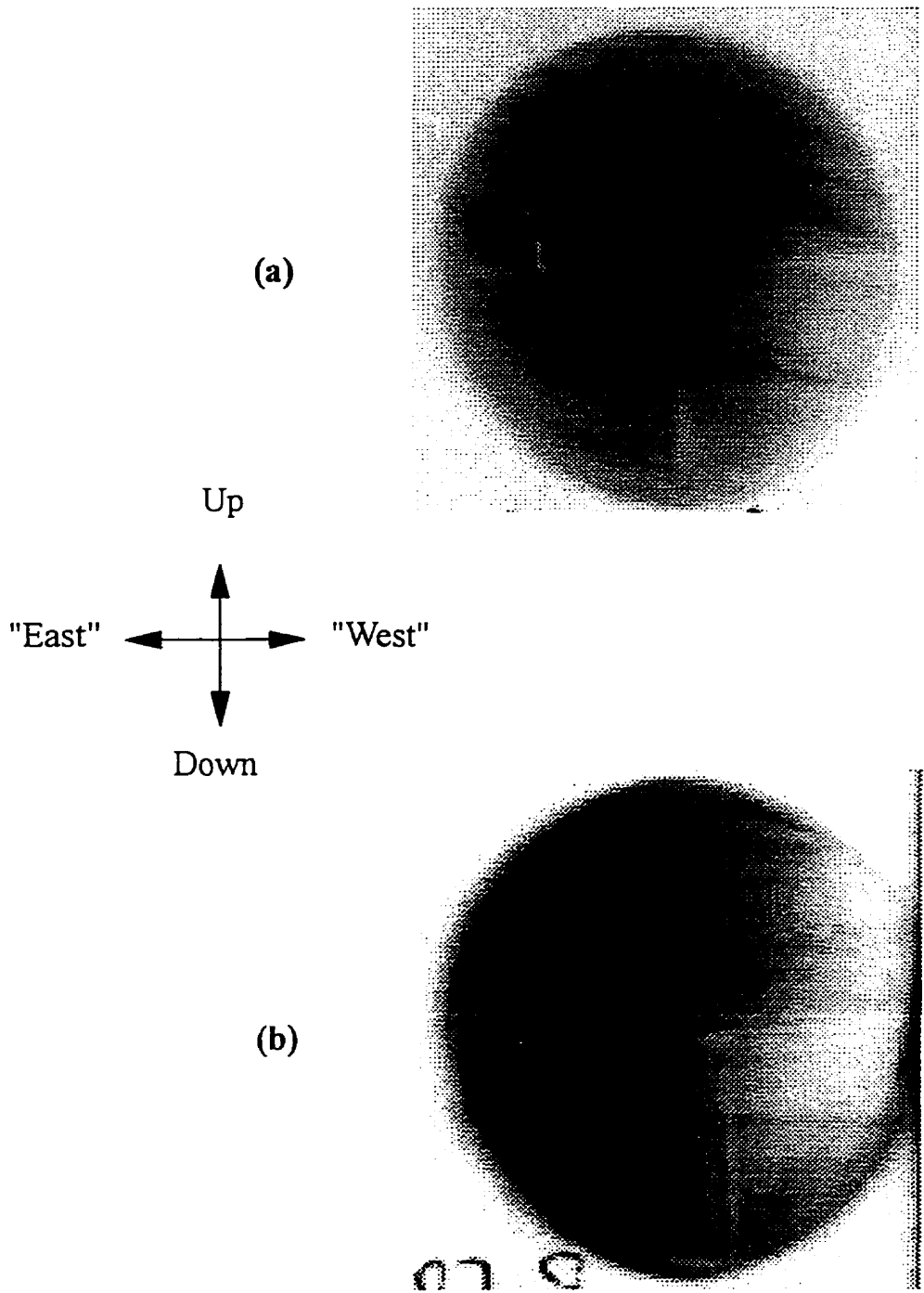


Figure 6.3 The X-radiographs of 28-0459 (a) and 28-0877(b) that represent typical disturbed and undisturbed turbidite specimens respectively.

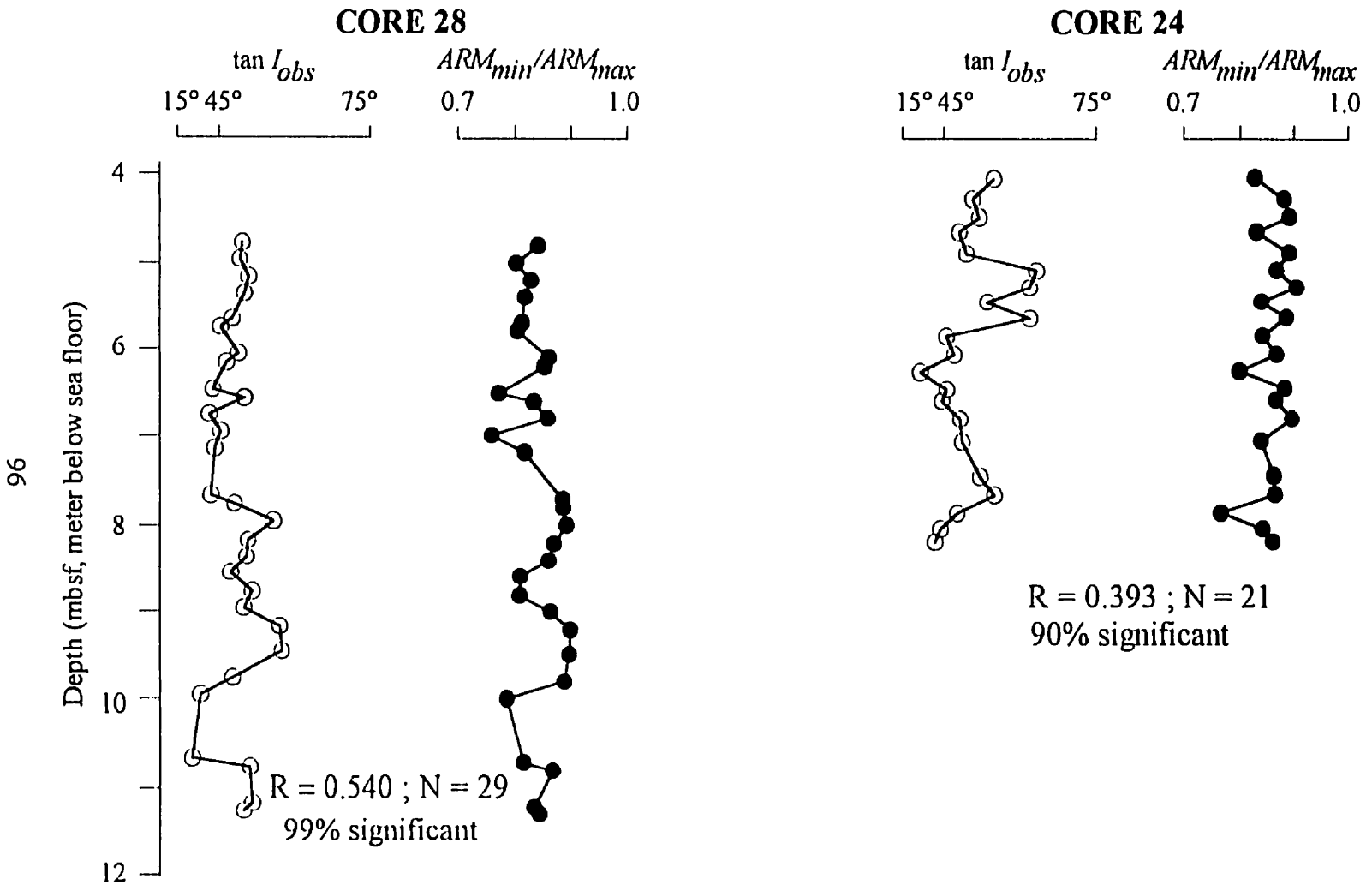


Figure 6.4 Tangent of the observed inclination $\tan I_{obs}$ and the ratio ARM_{min}/ARM_{max} for cores 28 and 24 after the exclusion of the specimens whose ARM_{min} axes are more than 15° from vertical. The correlation coefficient R for correlation between I_{obs} and ARM_{min}/ARM_{max} is shown and in core 28 is greatly improved by this exclusion.

6.2 Predicting Paleomagnetic Inclination Shallowing using the Correlation between Remanence Inclination and ARM Anisotropy

Hodych and Bijaksana [1993] suggested that the amount of inclination shallowing could be predicted if the ARM anisotropy is foliated in the bedding plane and if $\tan I_{obs}$ correlates significantly with ARM_{min}/ARM_{max} (see Chapter 1). The correlation line's prediction of $\tan I_{obs}$, when $ARM_{min}/ARM_{max} = 1$, will be an estimate of $\tan I_H$ where I_H is the inclination of the field in which I_{obs} was acquired.

Figure 6.5 shows this prediction method applied to the data for turbidite cores whose ARM anisotropy is foliated in the bedding plane. The value of $\tan I_{obs}$ for $ARM_{min}/ARM_{max} = 1$ was predicted using the regression modelling described in *McClave and Dietrich* [1992, pp. 523-529]. The predicted $\tan I_H$ and its 95% confidence interval is 2.20 ± 0.87 for core 28, 2.50 ± 1.64 for core 24 and 2.25 ± 1.30 for core 13. Thus, the predicted I_H is $66^\circ (+6^\circ/-13^\circ)$ for core 28, $68^\circ (+8^\circ/-27^\circ)$ for core 24 and $66^\circ (+8^\circ/-23^\circ)$ for core 13. Combining the data from the three cores (Fig. 6.5.d), the correlation between $\tan I_{obs}$ and ARM_{min}/ARM_{max} is significant with 99.9% confidence ($R = 0.613$, $N = 70$) and the value of $\tan I_{obs}$ for $ARM_{min}/ARM_{max} = 1$ and its 95 % confidence interval is 2.56 ± 0.92 which corresponds to a predicted I_H of $69^\circ (+5^\circ/-10^\circ)$. This interval includes the $I_H = 61^\circ$ expected from the GAD model.

If I_H predicted above is used to calculate $\tan I_{obs}/\tan I_H$ for each of the specimens, one can plot $\tan I_{obs}/\tan I_H$ versus ARM_{min}/ARM_{max} for the specimens from each core or all three cores combined as in Fig. 6.5. These plots can be compared with the theoretical

curves of Fig. 1.1 to predict the average value of $ARM_{\perp}/ARM_{\parallel}$ for the magnetic particles in the suite of specimens. The average value of $ARM_{\perp}/ARM_{\parallel}$ is predicted by inserting different values of $ARM_{\perp}/ARM_{\parallel}$ in Eq. (1.12) and calculating the sum of the squares of the differences between the observed and the theoretical $\tan I_{obs}/\tan I_H$ for given ARM_{min}/ARM_{max} values. The predicted average value of $ARM_{\perp}/ARM_{\parallel}$ is given by a value of $ARM_{\perp}/ARM_{\parallel}$ for which the sum is minimum and is shown in Fig. 6.6. It is 0.38 for core 28, 0.41 for core 24, 0.48 for core 13 and 0.47 for the data from all three cores combined. The standard error of this prediction, however, is quite complicated to calculate analytically due to the non-linearity of Eq. (1.12). In this study, therefore, the standard error is estimated graphically.

Consider that the ARM_{min}/ARM_{max} and $\tan I_{obs}/\tan I_H$ observations follow a linear model $y = \beta_0 + \beta_1 x$, where $y = \tan I_{obs}/\tan I_H$ and $x = ARM_{min}/ARM_{max}$. One can then obtain the least squares line (*i.e.*, the best estimate of β_0 and β_1) and its estimate of standard deviation ($= (\sum (y_i - \hat{y}_i)^2 / (N-2))^{1/2}$, where \hat{y} is the predicted value of y for a given x and N is the number of observation) for each core. In Fig. 6.6, the area within one standard deviation of the least squares line is shaded. The standard error of the average value of $ARM_{\perp}/ARM_{\parallel}$ for the magnetic particles in each core is then estimated from $ARM_{\perp}/ARM_{\parallel}$ for the two other theoretical curves that enclose all the data points within the shaded area. For example, the data points within the shaded area in core 28 (Fig. 6.6.a) are just enclosed between the theoretical curves for $ARM_{\perp}/ARM_{\parallel} = 0.22$ and for $ARM_{\perp}/ARM_{\parallel} = 0.54$. Therefore the predicted average $ARM_{\perp}/ARM_{\parallel}$ for the magnetic particles in

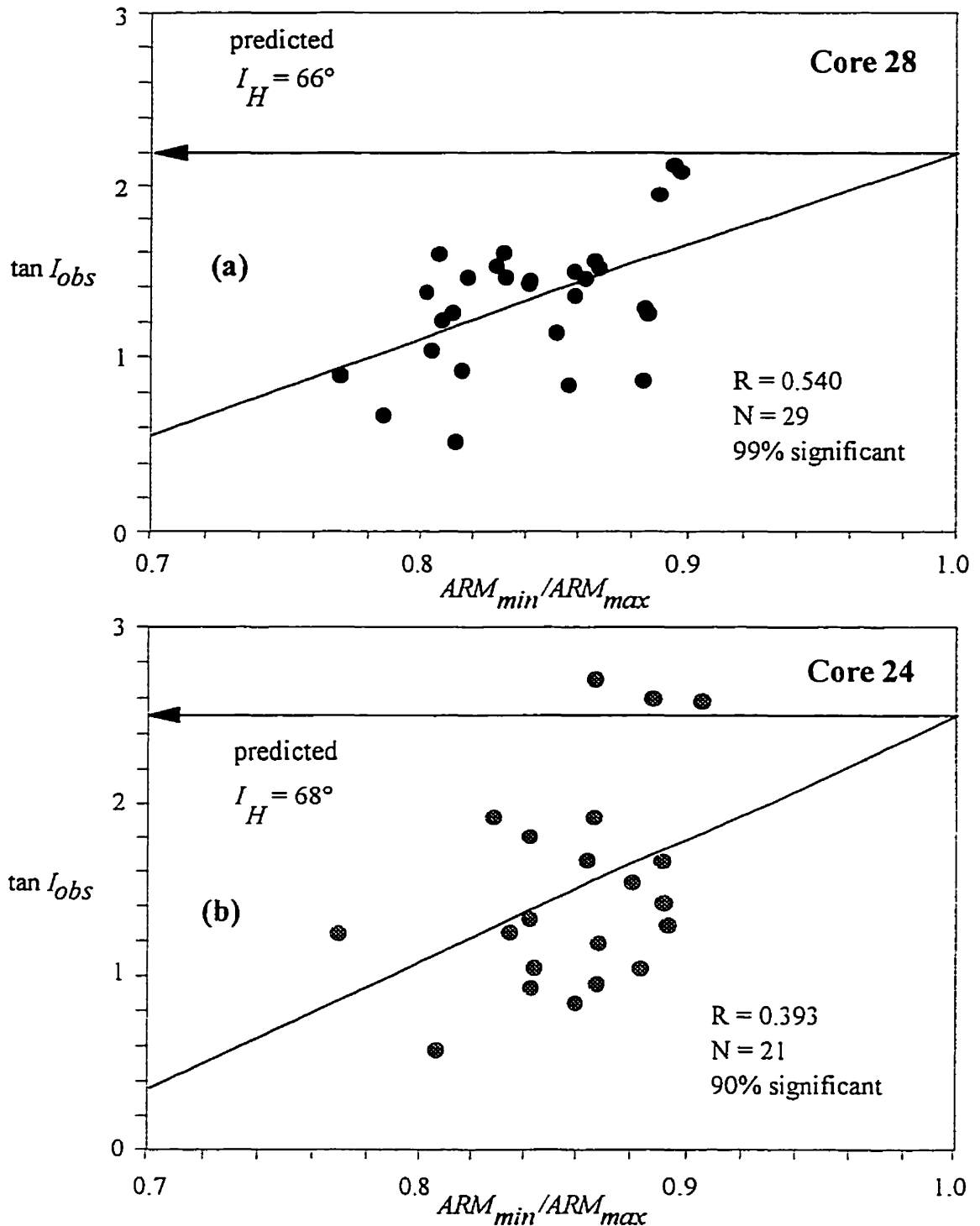


Figure 6.5 The correlation observed between $\tan I_{obs}$ and ARM_{min}/ARM_{max} for the turbidite cores 28 (a), 24 (b) and 13 (c). The combined data for all turbidite specimens are plotted in (d). For each core, the arrow points at $\tan I_{obs}$ for $ARM_{min}/ARM_{max} = 1$; the corresponding I_{obs} is the prediction of the field inclination I_H .

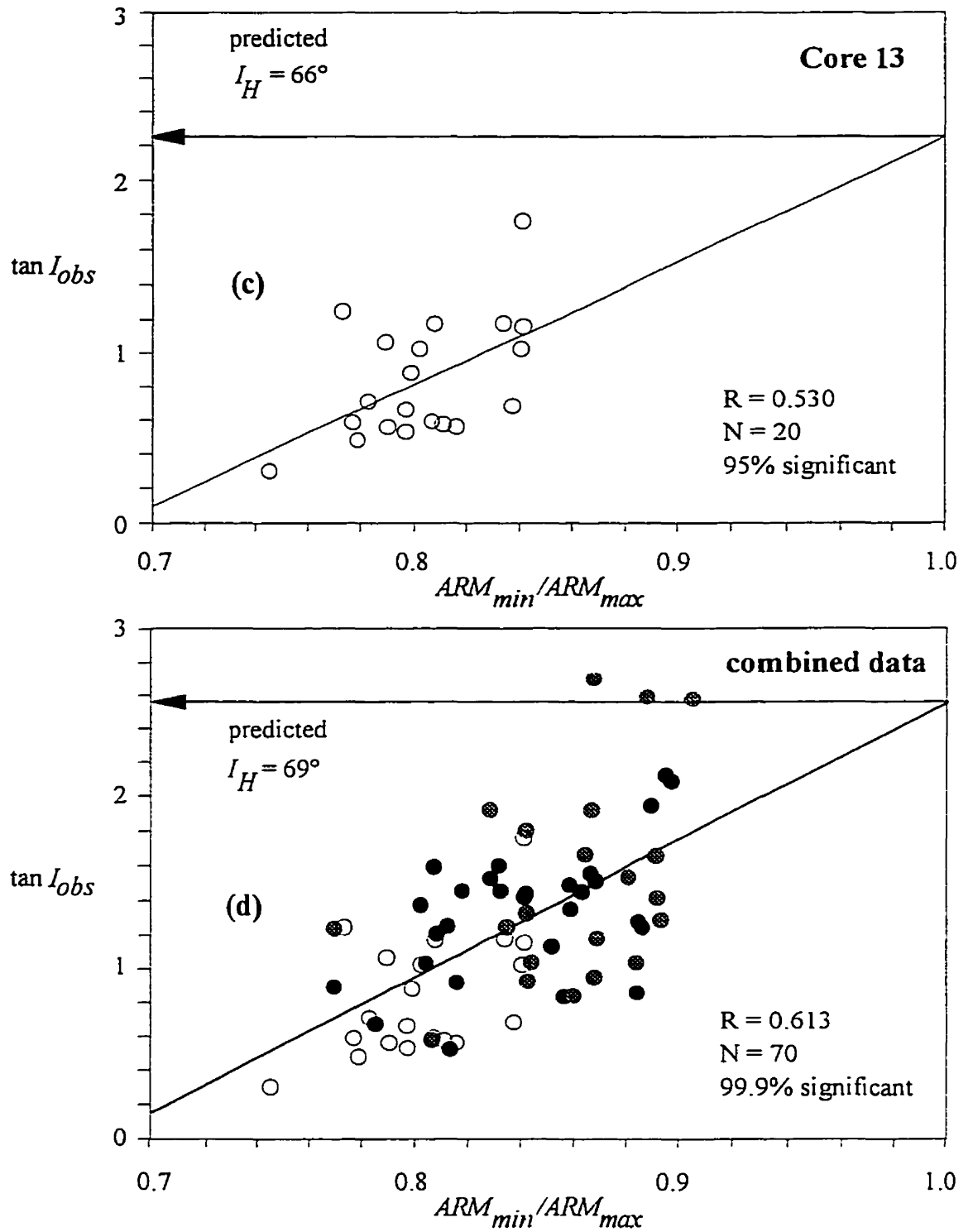


Figure 6.5 (Continued)

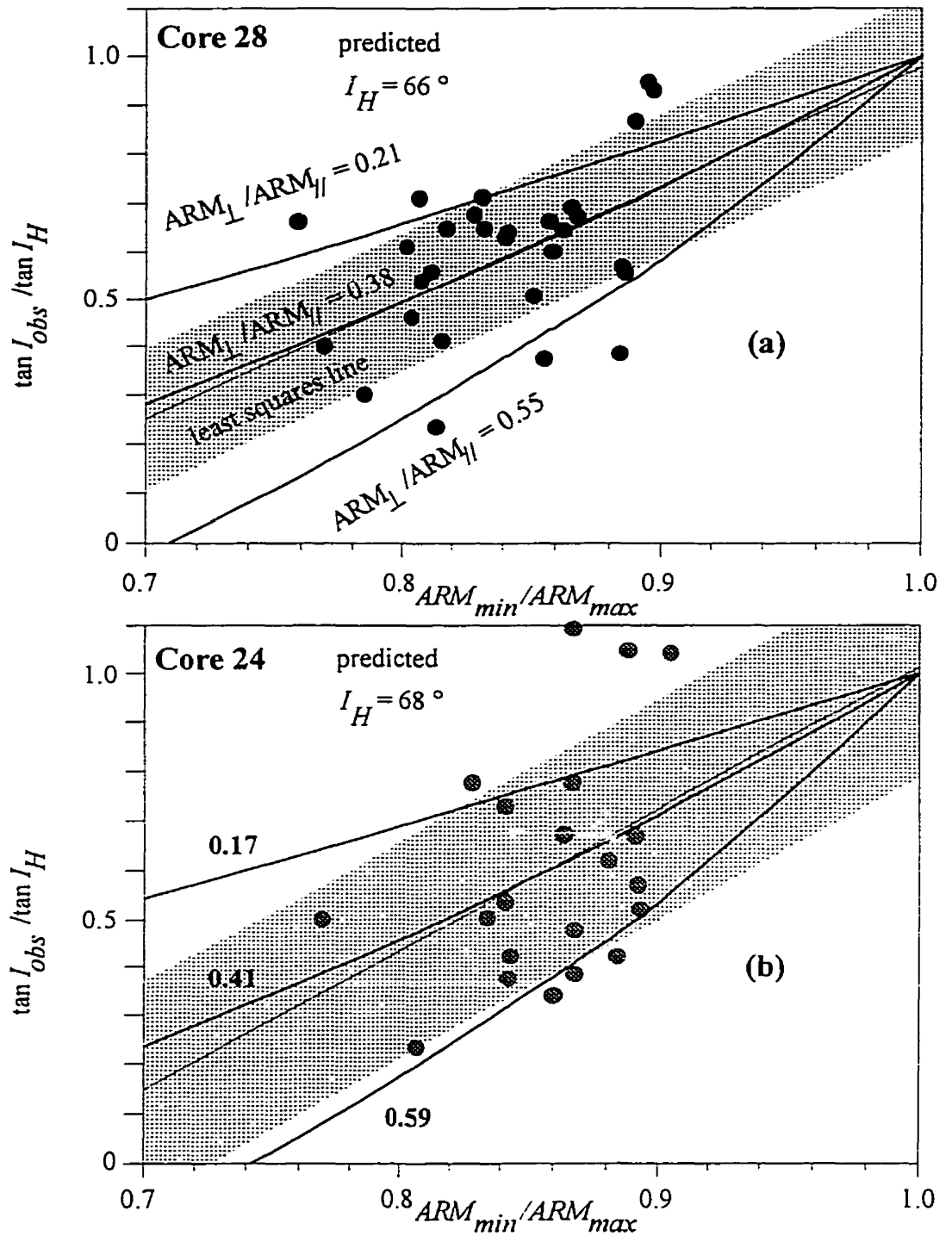


Figure 6.6 Plots of $\tan I_{obs} / \tan I_H$ versus ARM_{min} / ARM_{max} for a given predicted I_H in cores 28 (a), 24 (b), and 13 (c). The combined data for all turbidite specimens are plotted in (d). Thin solid lines and shaded areas indicate the least squares line and its standard deviation for data from each core. Thick solid lines are theoretical values based on Eq. (1.12) that represent the predicted average value of $ARM_{\perp} / ARM_{\parallel}$ and its uncertainty.

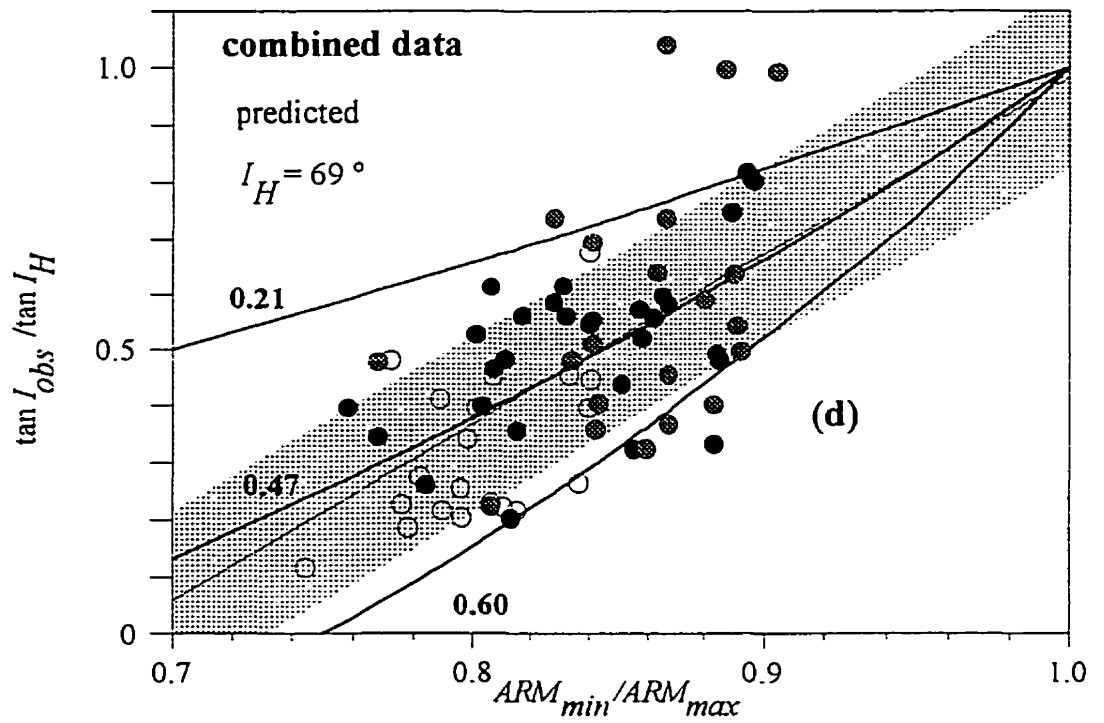
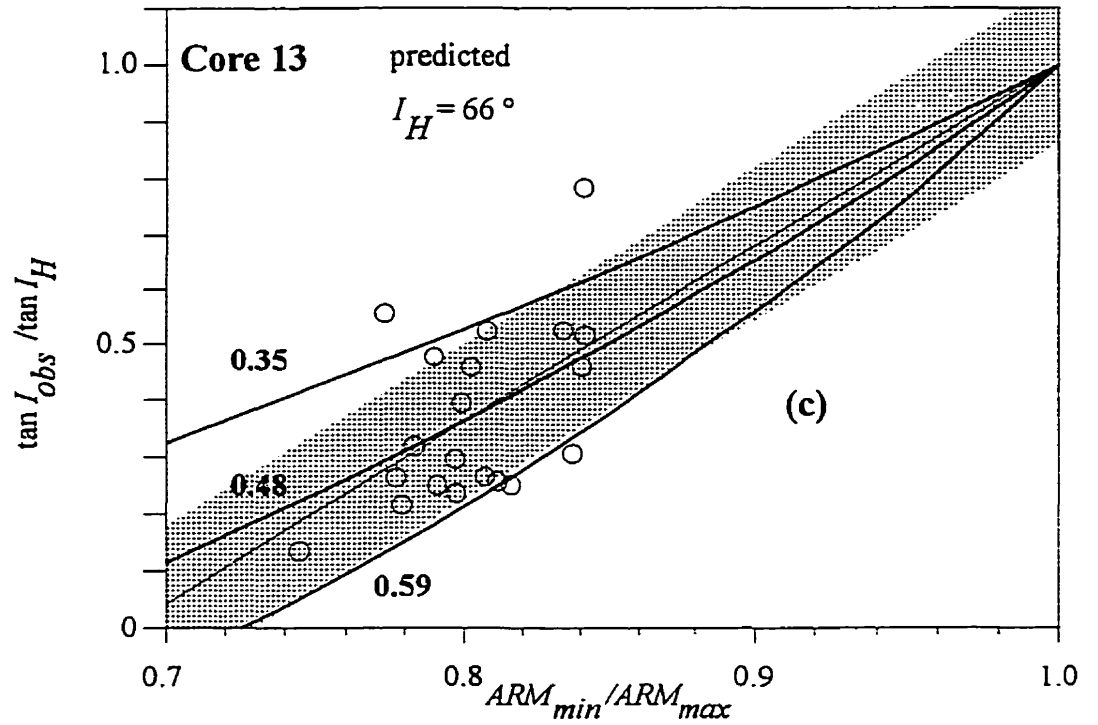


Figure 6.6 (Continued)

core 28 is 0.38 (+0.17/-0.17). Similarly, it is 0.41 (+0.18/-0.24) for core 24, 0.48 (+0.11/-0.13) for core 13 and 0.47 (+0.13/-0.26) for the data from all three cores combined.

Equation (1.12) and the inclination error prediction method of *Hodych and Bijaksana* [1993] can be tested further if the value of $ARM_{//}/ARM_{\perp}$ can be measured independently. In the following chapter, attempts to measure this ratio directly will be described.

6.3 Correlation between Remanence Inclination and Susceptibility Anisotropy

In Chapter 5, it was shown that for the turbidites χ_{min}/χ_{max} is approximately linearly related to ARM_{min}/ARM_{max} . Hence, a significant correlation between $\tan I_{obs}$ and χ_{min}/χ_{max} is also expected and would indicate the presence of inclination shallowing. Moreover, the fact that the value of $ARM_{min}/ARM_{max} = 1$ occurs only when $\chi_{min}/\chi_{max} = 1$ and vice versa implies that the correlation line's prediction of I_{obs} when $\chi_{min}/\chi_{max} = 1$ will also be an estimate of I_H .

Figure 6.7 shows $\tan I_{obs}$ alongside of χ_{min}/χ_{max} as a function of depth in the three turbidite cores studied. Three specimens (28-0896, 24-0486 and 24-0623) whose χ_{min} axis has an inclination of less than 75° (see Appendix C) were excluded. The correlation between $\tan I_{obs}$ and χ_{min}/χ_{max} was tested for each core and the correlation coefficients are given in Fig. 6.8. In core 28, this correlation is significant with 99% confidence ($R = 0.624$, $N = 21$), while in core 13 it is significant with 95% confidence ($R = 0.504$, $N = 20$).

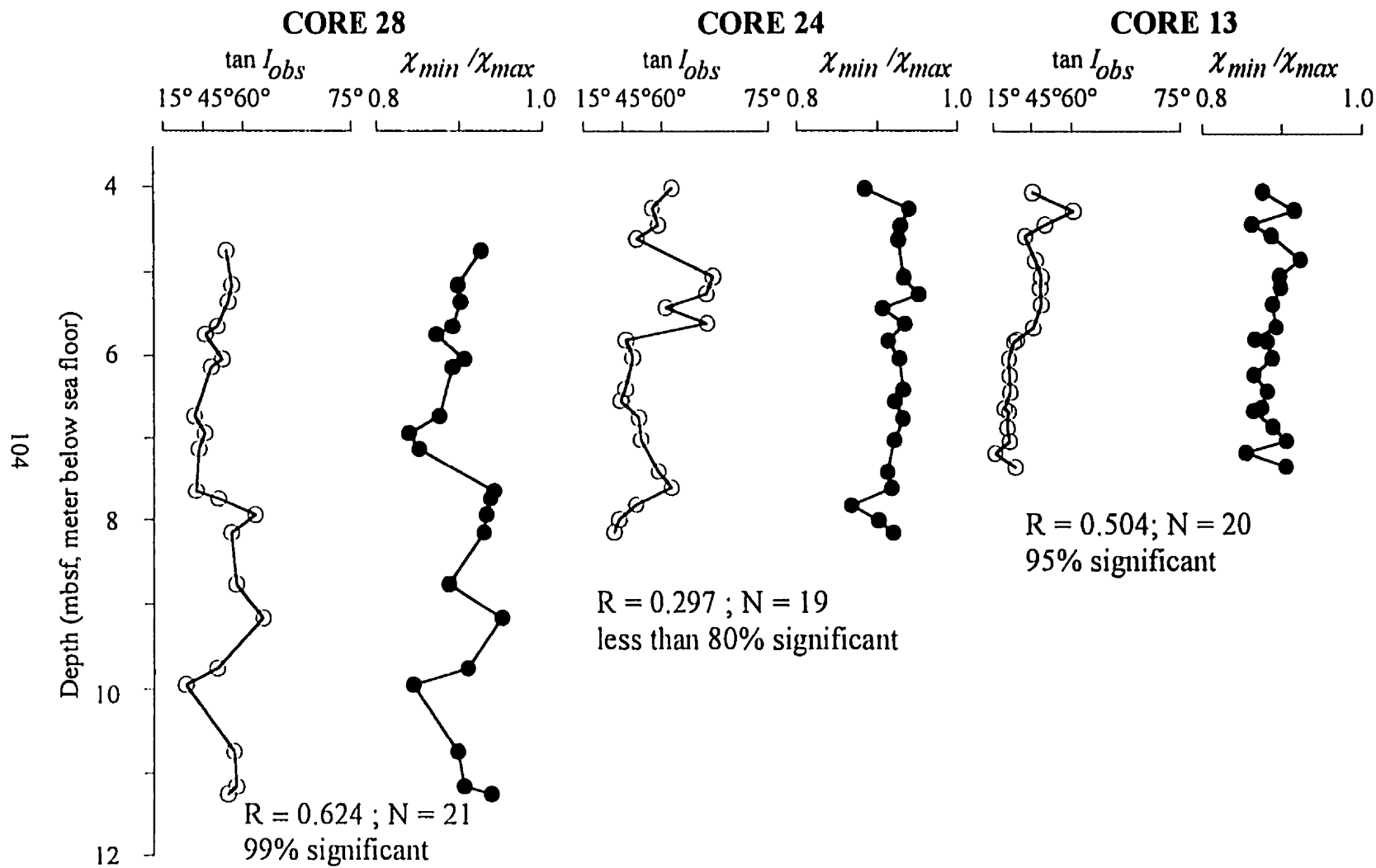


Figure 6.7 Tangent of the observed inclination $\tan I_{obs}$ and the ratio χ_{min}/χ_{max} for the three turbidite cores. The specimens whose χ_{min} axes are more than 15° from vertical are excluded.

The correlation is poorer in core 24 ($R = 0.297$, $N = 19$) where it is significant with less than 80% confidence.

The poor correlation in core 24 is probably due to the relatively lower anisotropy; h_x average only 7.6% compared to 10.0% and 11.7% in cores 28 and 13 respectively. The amount of inclination shallowing in core 24 is also the lowest among the three cores.

Since the AMS is also foliated in the bedding plane and since $\tan I_{obs}$ correlates significantly with χ_{min}/χ_{max} (at least in cores 28 and 13), then the correlation line's prediction of I_{obs} when $\chi_{min}/\chi_{max} = 1$ should predict I_H (Fig. 6.8). The predictions of $\tan I_{obs}$ for $\chi_{min}/\chi_{max} = 1$ and its 95% confidence interval were estimated as in the previous section. The results are 2.00 ± 0.74 for core 28, 2.27 ± 1.71 for core 24 and 1.94 ± 1.15 for core 13. The corresponding I_H is $63^\circ (+7^\circ/-11^\circ)$ for core 28, $66^\circ (+10^\circ/-37^\circ)$ for core 24 and $63^\circ (+9^\circ/-25^\circ)$ for core 13. Assuming that all specimens are from the same suite of sediments, the data from the three cores are combined in Fig. 6.8.d. The correlation between $\tan I_{obs}$ and χ_{min} / χ_{max} for these combined data is significant with 99.9% confidence ($R = 0.586$, $N = 60$) and the value of $\tan I_{obs}$ predicted for $\chi_{min} / \chi_{max} = 1$ is 2.33 ± 0.95 which corresponds to a predicted I_H of $67^\circ (+6^\circ/-13^\circ)$. As expected, these results agree well with $69^\circ (+5^\circ/-10^\circ)$ estimated from the correlation between remanence inclination and ARM anisotropy.

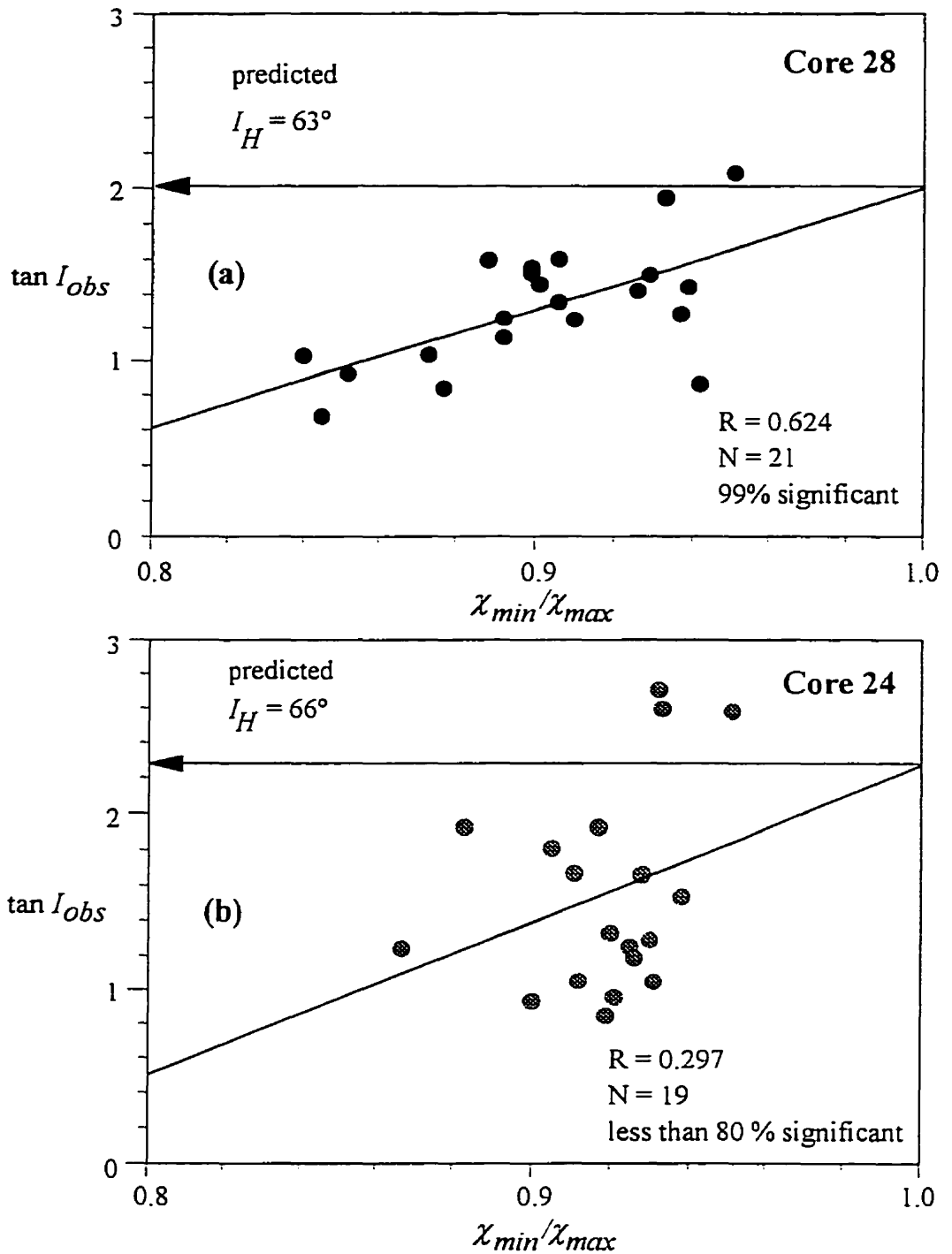


Figure 6.8 The correlations observed between $\tan I_{obs}$ and χ_{min}/χ_{max} for the turbidite cores 28 (a), 24 (b) and 13 (c). The combined data for all turbidite specimens are plotted in (d). For each core, the arrow points to $\tan I_{obs}$ predicted for $\chi_{min}/\chi_{max} = 1$; the corresponding I_{obs} is the prediction of the field inclination I_H .

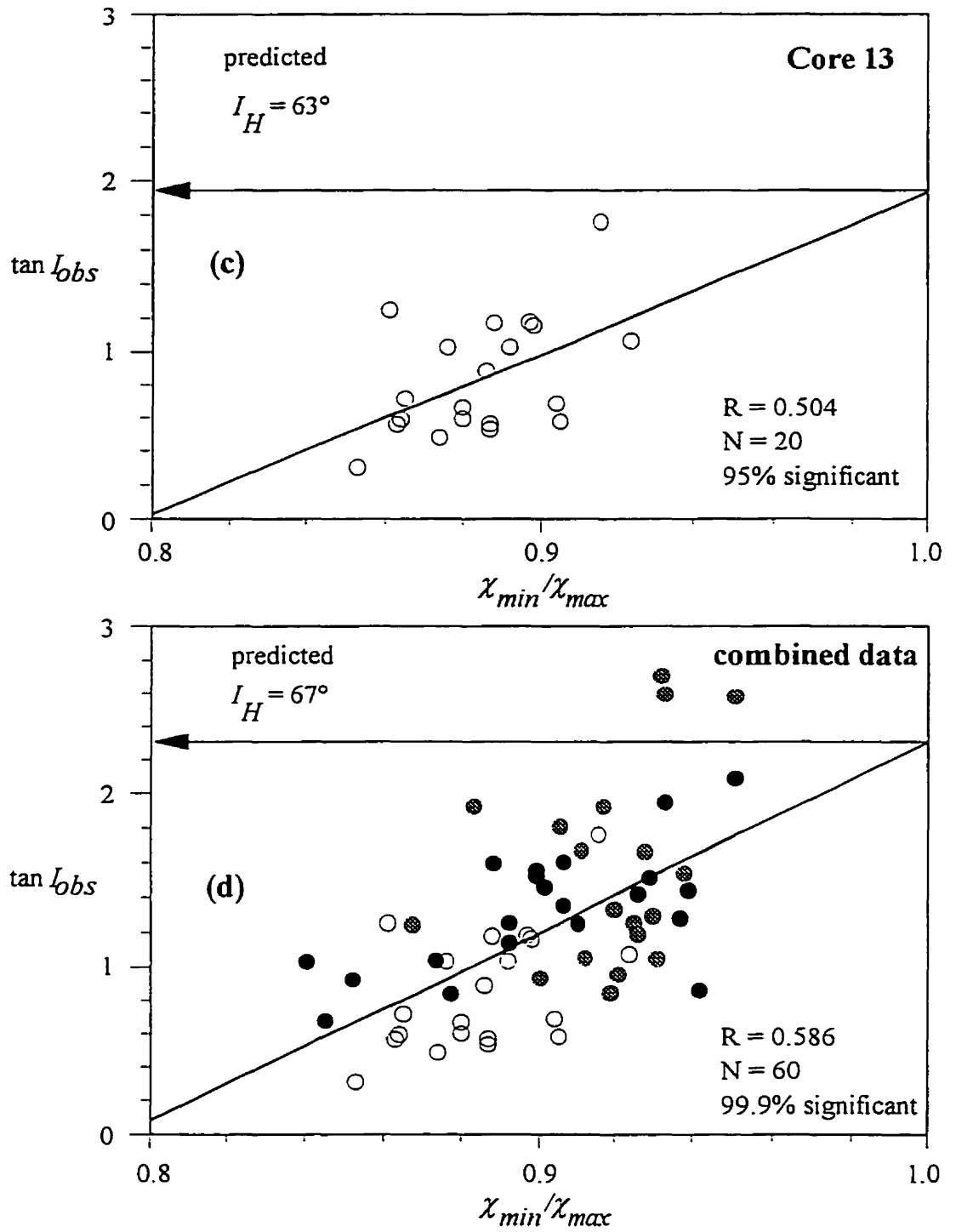


Figure 6.8 (Continued)

CHAPTER 7

PARTICLE ARM ANISOTROPY

7.1 Particle ARM Anisotropy Measurement

Demonstrating a correlation between $\tan I_{obs}$ and ARM_{min}/ARM_{max} as shown in Chapter 6 supports the theory of *Jackson et al.* [1991] reviewed in Chapter 1. Even if the theory were in error, demonstrating this correlation would provide an empirical method of estimating I_H without knowing the value of particle ARM anisotropy $\gamma = ARM_{//}/ARM_{\perp}$. To test the theory of *Jackson et al.* further, one wishes to measure γ to see if it agrees with the theoretically predicted value.

Jackson et al. [1991] estimated γ by mixing synthetic magnetite particles in epoxy and aligning their long axes with a strong magnetic field while the epoxy hardened. Then, $ARM_{//}$ and ARM_{\perp} were measured parallel and perpendicular to the aligning axis of the sample and their ratio gave an estimate of γ . Two samples were studied; one with acicular magnetite (axial ratio ≈ 4 , spherical equivalent diameter $\approx 0.45 \mu\text{m}$) and one with subequant ($0.75 \mu\text{m}$) magnetite. The sample with acicular magnetite was expected to have a higher γ than the one made with subequant magnetite. But the measurements yielded a γ estimate of only 1.2 for acicular magnetite sample and a γ estimate of ≈ 2.5 for the subequant magnetite sample. *Jackson et al.* [1991] suggested that this inconsistency was probably due to incomplete dispersion of the particles.

Hodych and Bijaksana [1993] modified this method by estimating γ as a function of magnetic grain concentration in the sample. Working with Cretaceous limestones, they dissolved the calcite with a buffered acetic acid solution that left iron oxides unaltered and mixed the remaining particles with warm liquid gelatine. The mixture was then stirred and placed in a horizontal 90 mT aligning field while the gelatine cooled and set. The mixture was then demagnetized and given an ARM along the grain alignment direction. The magnitude of this ARM was termed ARM_x . Similarly, ARMs were given in a horizontal and in a vertical direction perpendicular to the direction of the aligning field giving ARM_y and ARM_z respectively. This procedure was then repeated after taking half of the sample and diluting it with an equal volume of gelatine. *Hodych and Bijaksana* [1993] found that $2 ARM_x / (ARM_y + ARM_z)$ increased with dilution and repeated this procedure until it stopped increasing with dilution. The average $2 ARM_x / (ARM_y + ARM_z)$ that was stable to further dilution was used as an estimate of γ .

In this study, the above method was modified for two reasons. First, the turbidites are magnetically weak samples. Diluting them repeatedly reduced their ARM intensities close to the lowest end of the measuring range of the magnetometer before a stable $2 ARM_x / (ARM_y + ARM_z)$ was reached. Second, dilution may increase grain clustering or chaining as the grains become more mobile in a more dilute matrix of gelatine.

Instead of increasing dilution at constant field, dilution was kept constant and change in $2 ARM_x / (ARM_y + ARM_z)$ was measured as aligning field was increased. The

value of $2 ARM_x / (ARM_y + ARM_z)$ was expected to saturate as the intensity of the aligning field was increased and the saturated value could be used as an estimate of γ .

Four composite samples were made to represent each of the three turbidite cores and the pelagic clays of DSDP site 578. No sample was made for the pelagic lime muds of DSDP site 606 due to their low magnetic intensity. A composite sample was made by taking 2 to 3 g of each specimen (10 selected specimens in the case of site 578) and mixing them together. Deionized water was added to the mixture to form a thick slurry. The slurry was allowed to settle for at least 24 hours after which the head of clear water was removed by pipeting. About 7 to 8 cm³ of the slurry was then mixed with warm liquid gelatine in a small plastic cup about 12 cm³ in volume.

Each composite sample was stirred and placed in a near zero field environment while the gelatine cooled and set. Anhysteretic remanences, as in Section 5.2, were given and measured along the three axes and $2 ARM_x / (ARM_y + ARM_z)$ was calculated. As expected, the values did not differ significantly from unity.

Each sample was then warmed to liquefy the gelatine, stirred and placed in a horizontal 1.7 mT direct field until the gelatine cooled and set again. It was then demagnetized using alternating fields with a peak field of 100 mT. Anhysteretic remanences were again given and measured and $2 ARM_x / (ARM_y + ARM_z)$ was calculated. This process was repeated as the aligning direct field was increased in steps to 100 mT.

For all samples, $2 ARM_x / (ARM_y + ARM_z)$ increased as the aligning field was increased (Fig. 7.1). For the three turbidite cores, it approached 9 to 10 at an aligning field

of 33 mT and remained there at higher fields. These estimated values of $\gamma \approx 10$ in the turbidites give $ARM_{\perp} / ARM_{\parallel} \approx 0.1$, which does not agree with the predicted $ARM_{\perp} / ARM_{\parallel}$ of 0.38 (+0.17/-0.17) for core 28 and 0.48 (+0.11/-0.13) for core 13 (Fig. 6.6).

The high γ estimates observed in the turbidite samples might be caused by the presence of elongated particles. However, SEM photographs show that the grains are not elongated enough to account for $ARM_{\parallel} / ARM_{\perp} = 10$ (the required elongation of 2.6 to 1 will be calculated in the next section). Another possible cause for the high $ARM_{\parallel} / ARM_{\perp}$ values is that the grains attract each other as the field strength is increased and progressively form chains of particles linked up along the aligning field direction. Figure 3.2 shows an extreme example of a chain of magnetite particles oriented along the aligning field direction. Such chains were very common in the magnetic separates.

To test for the possibility of chaining, the measurements of $2 ARM_x / (ARM_y + ARM_z)$ as a function of aligning fields were repeated for the three turbidites samples. That is, the same samples used for the first set of measurements shown by open circles in Fig. 7.1 were demagnetized, warmed, stirred and allowed to cool again in increasing fields. If the grains were forming chains, stirring would probably not completely destroy the chains and low aligning fields would result in higher $2 ARM_x / (ARM_y + ARM_z)$ values the second time the sample was subjected to increasing fields, although the saturation values should be the same as the first time.

The results did support the chaining hypothesis. For the composite sample of core 28 (Fig. 7.1.a), the values of $2 ARM_x / (ARM_y + ARM_z)$ at low aligning fields are

significantly higher the second time the sample was subjected to increasing fields. Indeed, the initial curve seems to be approaching saturation at about 16.5 mT, but this is aborted, presumably by chaining. Both curves show similar saturation values at aligning fields above 50 mT. For composite samples of cores 24 and 13, the values of $2 ARM_x / (ARM_y + ARM_z)$ at low aligning fields are higher the second time the sample was subjected to increasing fields although the effect is not as pronounced as in core 28. These results imply that chaining probably is occurring in the turbidites. Apparently, this method of particle alignment, using DC fields, causes chaining of particles along the aligning field direction and hence overestimates the value of γ in the turbidites.

For comparison, a composite sample of the rather isotropic pelagic clay (DSDP site 578) was also measured. This sample showed a surprisingly high $2 ARM_x / (ARM_y + ARM_z)$ of about 3 at the maximum field of 100 mT (Fig. 7.1.d) which was presumably mostly due to chaining of roughly equidimensional magnetic particles.

The high estimates of γ may also be partly due to the IRM produced during particle alignment interfering with ARM acquisition. Particularly at higher aligning fields, the IRM could not be completely removed by the 100 mT peak alternating field used to demagnetize it. This residual IRM may lower the ARM intensity given perpendicular to it adding to the high $2 ARM_x / (ARM_y + ARM_z)$ observed.

Therefore a second set of experiments was tried. Composite samples from each core were prepared as in the first set of experiments. To eliminate the effect of residual IRM on ARM, an alternating field was used to align the grains without producing IRM.

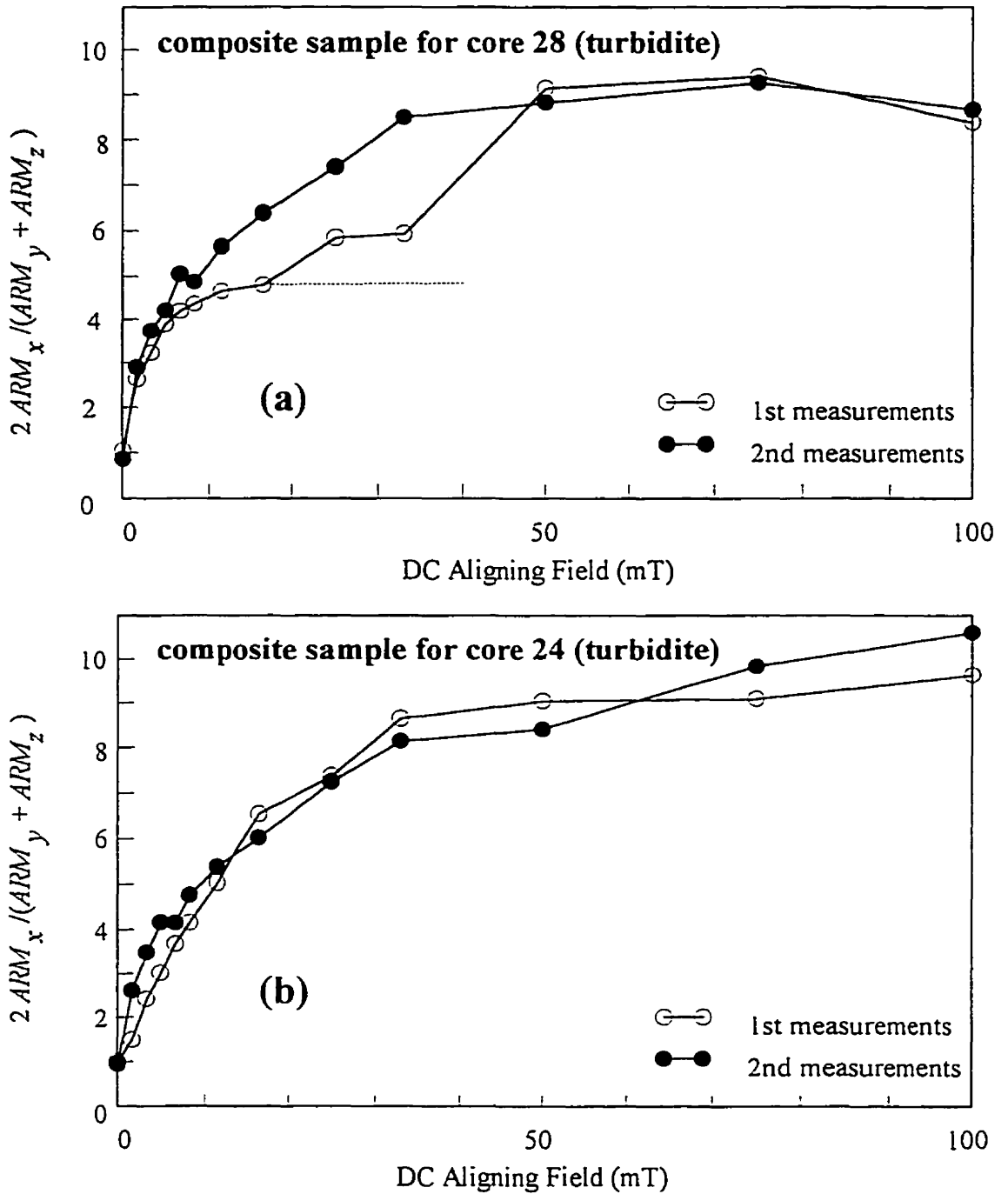


Figure 7.1 Results of particle ARM anisotropy measurement, in which magnetic grains from a composite sample for each core were aligned using a DC field. Hollow circles indicate results from the initial steps. Solid circles were from the repeat measurements. Dashed line in (a) indicate a possible aborted saturation.

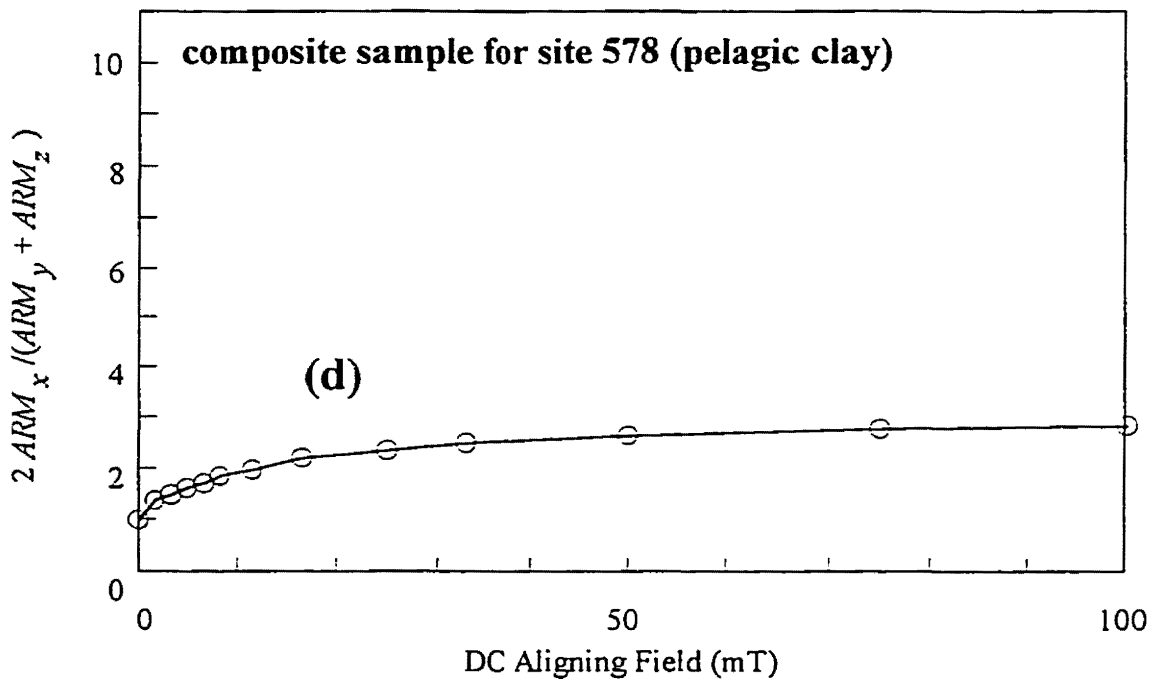
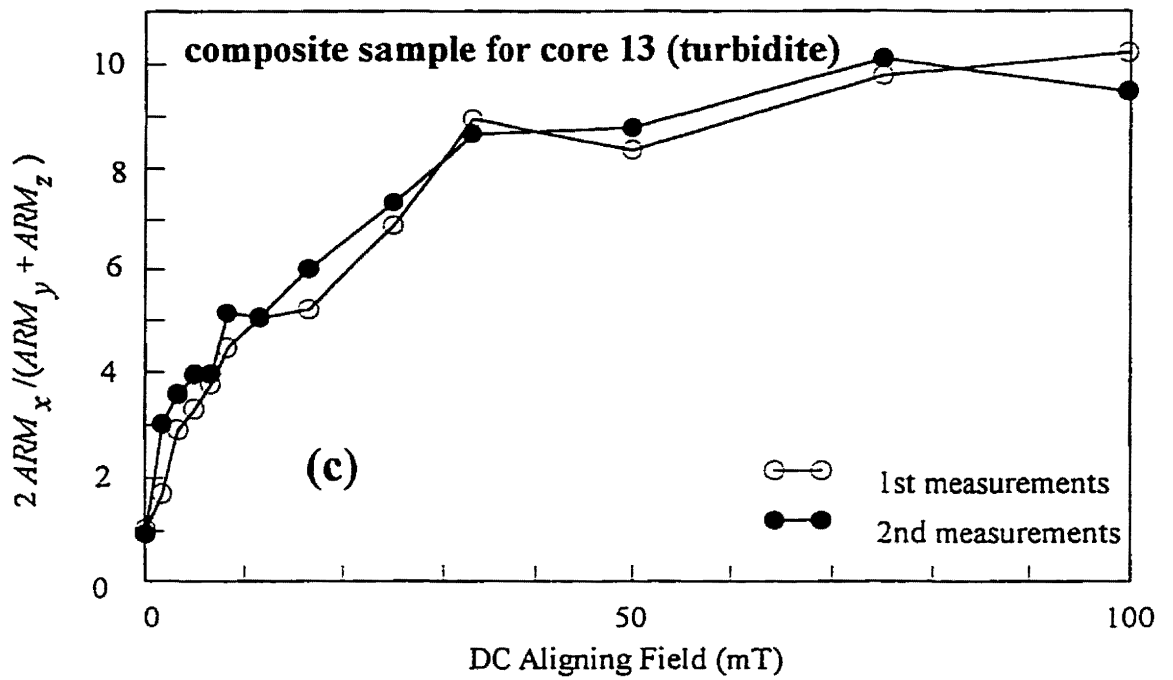


Figure 7.1 (Continued)

The alternating field was produced by an air-cored coil connected to a variable voltage source. The coil was placed in a field-free space produced by a set of Helmholtz coils. The starting field was 10 mT and was increased subsequently to 30, 50 and 70 mT after which it was increased in steps of 10 mT up to 200 mT. To detect chaining, the preceding step was repeated before going to a higher field. The sequence of alternating field applied was 0, 10, 30, 10, 50, 30, 70, 50, 80, 70, 90, ..., 190, 180, 200, 190 and 200 mT with $2 ARM_x / (ARM_y + ARM_z)$ being measured after each step.

Figure 7.2 shows the results for the three turbidite composite samples and the pelagic clay composite sample. As expected, the grains were randomly oriented ($2 ARM_x / (ARM_y + ARM_z) = 1$) at zero field. At low fields, the values of $2 ARM_x / (ARM_y + ARM_z)$ were < 1 suggesting that the grains had tried to align along the field direction, but many of them could not follow the cycles and were trapped when aligned perpendicular to the field direction. As the field increased, more grains were able to align along the field direction and increased the value of $2 ARM_x / (ARM_y + ARM_z)$. At very high fields, however, the value of $2 ARM_x / (ARM_y + ARM_z)$ fluctuated noisily. For the sample from site 578, however, the value of $2 ARM_x / (ARM_y + ARM_z)$ reached a peak at 130 mT and began to decrease in higher fields. The reason for this is unclear.

In all cases, the values of $2 ARM_x / (ARM_y + ARM_z)$ were repeatable at fields lower than 70 mT. That is, the same value was obtained if an alignment experiment was repeated (heating, stirring, aligning and remeasuring). For higher fields, repeating an alignment gave higher values of $2 ARM_x / (ARM_y + ARM_z)$ suggesting that the increase was due to chaining

of magnetic particles. Therefore, for a given field, $2 ARM_x / (ARM_y + ARM_z)$ was corrected for chaining by subtracting the cumulative differences between the initial and the repeat values of $2 ARM_x / (ARM_y + ARM_z)$. Denoting the initial and the repeat values of $2 ARM_x / (ARM_y + ARM_z)$ at X mT as $\gamma_{i,X}$ and $\gamma_{r,X}$ respectively, the corrected $2 ARM_x / (ARM_y + ARM_z)$ at 80 mT, for example, was equal to $\gamma_{i,80} - (\gamma_{r,70} - \gamma_{i,70}) - (\gamma_{r,50} - \gamma_{i,50}) - (\gamma_{r,30} - \gamma_{i,30}) - (\gamma_{r,10} - \gamma_{i,10})$.

For samples from core 28 and 13, the curve of corrected $2 ARM_x / (ARM_y + ARM_z)$ (shown as solid circles in Fig. 7.2) levels off as it approaches 1.8. The same curve for core 24 was erratic due to fluctuation in the measured values of $2 ARM_x / (ARM_y + ARM_z)$. Nevertheless, we could use 1.8 as an estimate of γ in the turbidites. This gives ARM_L / ARM_H of about 0.56, which is close to that predicted from the correlation between $\tan I_{obs}$ and ARM_{min} / ARM_{max} . This supports the theory of *Jackson et al.* [1991] but not decisively because of the large (and debatable) correction required for chaining. This method of measuring particle ARM anisotropy is also very time consuming and requires higher alternating fields than available in many laboratories.

7.2 Grain elongation and the Origin of Magnetic Anisotropy in the Turbidites

SEM photographs in Chapter 3 show that although their shapes are irregular, most of the magnetite grains in the turbidites are only slightly elongated. Are they elongated enough to yield $\gamma = 1.8$? An estimate of how much elongation is required can be obtained from the theory of *Stephenson et al.* [1986].

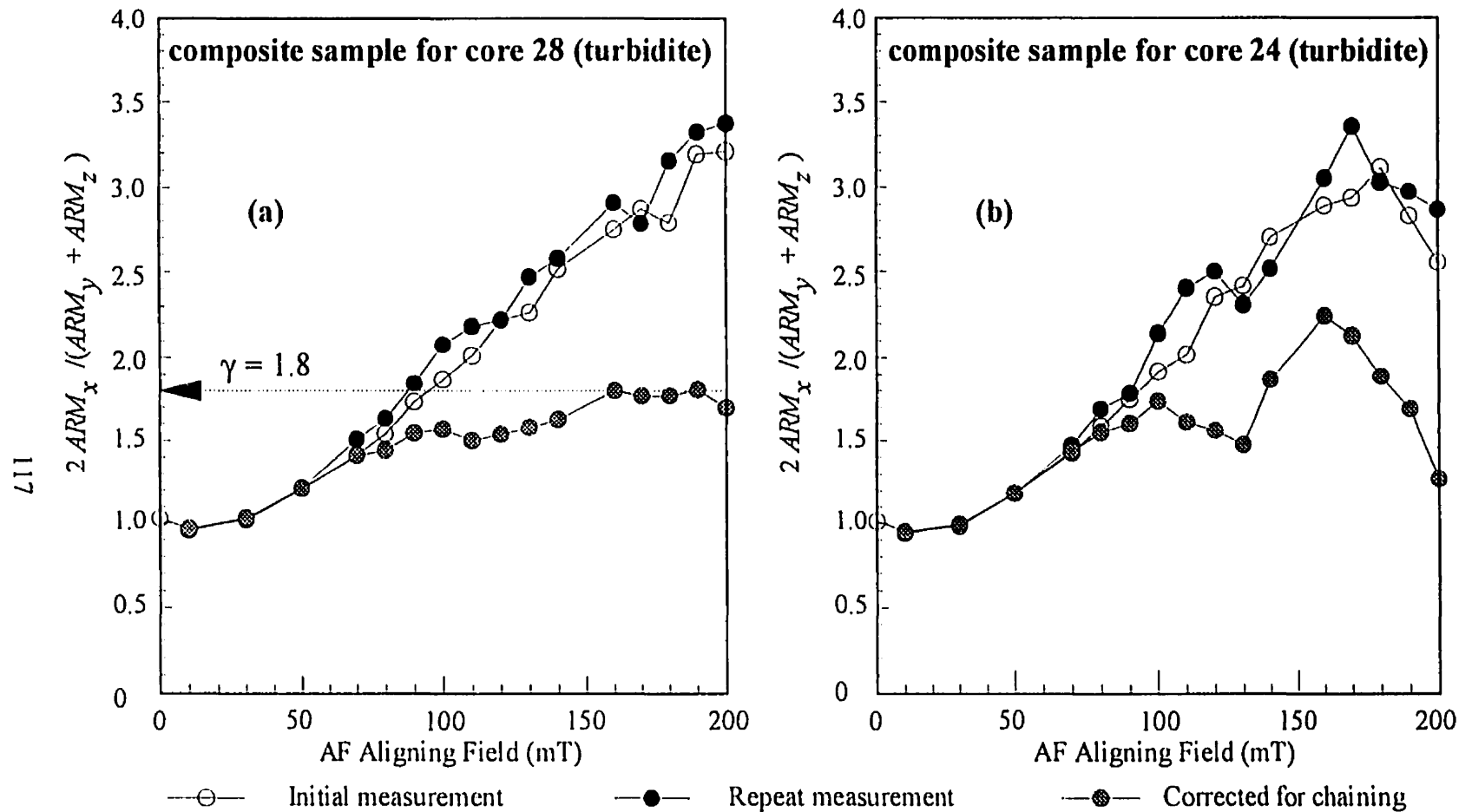
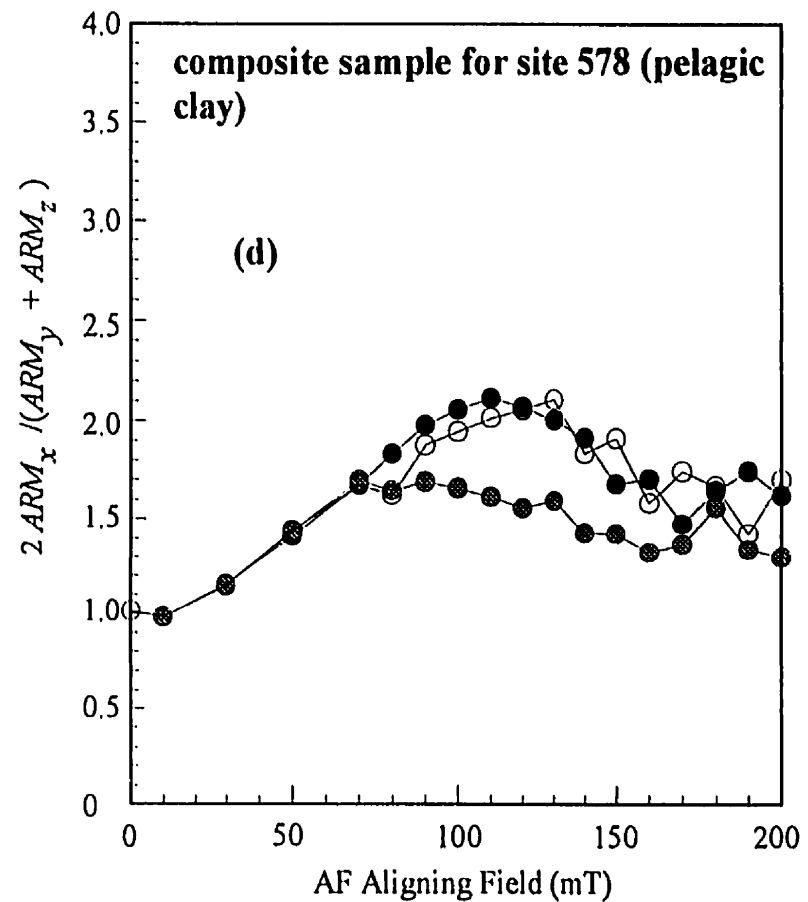
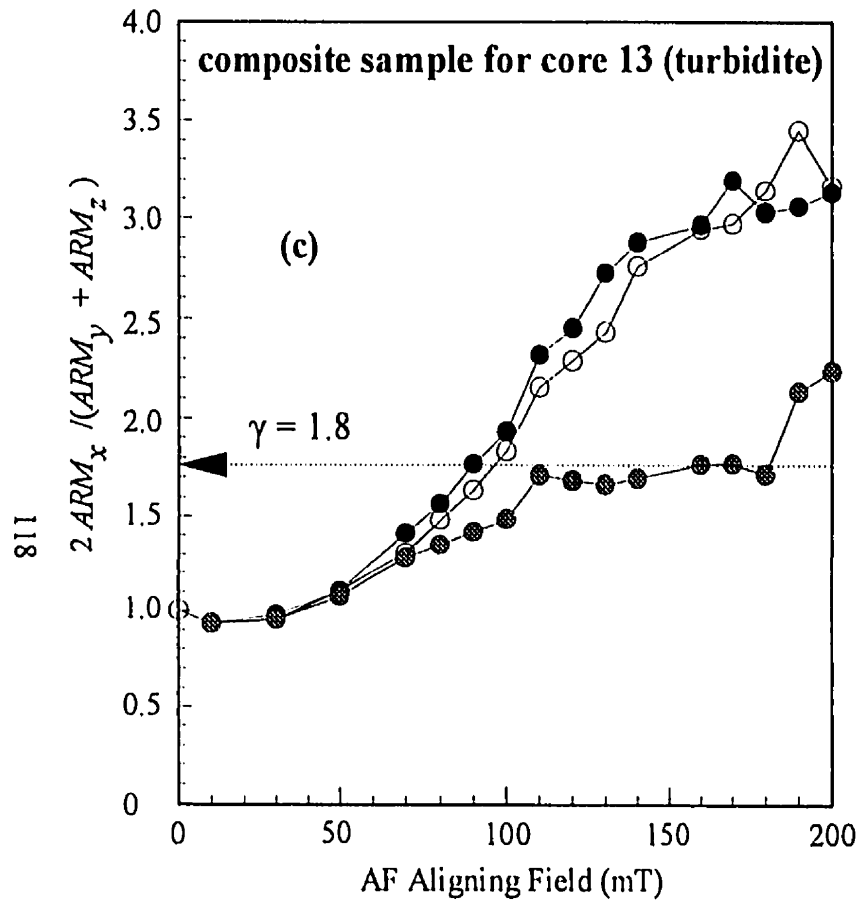


Figure 7.2 Results of particle ARM anisotropy measurement, in which magnetic grains from each composite sample were aligned using an alternating field. Hollow and solid circles indicate results from the initial and the repeat measurements in each step respectively. Shaded circles indicate the values corrected for chaining as explained in the text. The values of γ for cores 28 (a) and 13 (c) are estimated as the adjusted values approach saturation (dashed arrows). The results of core 24 (b) are too noisy for γ to be estimated reliably. The results of site 578 (d) are presented for comparison.



—○— Initial measurement —●— Repeat measurement —●— Corrected for chaining

Figure 7.2 (Continued)

Consider an ellipsoidal magnetite particle with a long axis a and two identical short axes b and c . From the relation $\chi = \chi_o / (1 + N\chi_o)$ (Néel, 1955), one can obtain

$$\frac{\chi_a}{\chi_b} = \frac{1 + N_b\chi_o}{1 + N_a\chi_o} \quad (7.1),$$

where χ_a and χ_b are the susceptibilities of the particle measured parallel and perpendicular to the long axis, N_a and N_b are the demagnetizing factors parallel and perpendicular to the long axis ($N_a + 2N_b = 1$) and χ_o is the intrinsic susceptibility. Assuming that magnetite has a large intrinsic susceptibility, Eq. (7.1) becomes

$$\frac{\chi_a}{\chi_b} = \frac{N_b}{N_a} \quad (7.2).$$

Using Eq(s). (5.1) to (5.3), it can be shown that

$$\frac{\chi_a}{\chi_b} = \frac{p_o(\gamma + 2) + s\gamma}{p_o(\gamma + 2) + s} \quad (7.3)$$

For $p_o = 0.14$, $s = 0.58$ (see Table 5.1) and $\gamma = 1.8$, $\chi_a/\chi_b = N_b/N_a = 1.4$. This ratio of N_b/N_a corresponds to a grain elongation of 1.3 to 1 (Stoner, 1945).

Therefore, $\gamma \approx 1.8$ as estimated using an alternating field and correcting for chaining could be caused by magnetite particles that are only slightly elongated, *i.e.* the long axis is only 30% longer than the shorter ones. SEM photographs in Chapter 3 show

that the magnetite grains in the turbidites readily satisfy this requirement. In contrast, γ of about 10, as estimated from the alignment using a DC field without correcting for chaining, would give $\chi_a/\chi_b = N_b/N_a = 3.3$ which corresponds to a grain elongation of 2.6 to 1. This is too high for the magnetic grains observed in the turbidites. Assigning a lower value of intrinsic susceptibility does not greatly affect these grain elongation estimates. For example, using $\chi_0 = 1.28 \pi$ (SI unit) (as measured by *Hodych* [1986] for the Matachewan dolerite) gives a grain elongation estimate of 1.65 to 1 to account for $\gamma \approx 1.8$, but an infinite grain elongation to account for $\gamma \approx 10$.

Magnetic anisotropy in the turbidites is most likely produced by the modest grain elongation visible in the magnetic concentrates. However, there may also be a contribution to magnetic anisotropy from magnetic interaction between the grains. The magnetic grains may interact with their closest magnetic neighbours forming a chain of two grains or a more complicated configuration. Such interactions produce what is termed distribution anisotropy (*Hargraves et al.*, 1991; *Stephenson*, 1994; *Gregoire et al.*, 1995) and result in magnetic grains appearing to be more elongated than they actually are. Although it was originally formulated for AMS, distribution anisotropy should have a similar effect on ARM anisotropy. The presence of distribution anisotropy may also explain the results of the earlier experimental study of *Jackson et al.* [1991], in which inclination shallowing and ARM anisotropy were observed in artificial samples made of equidimensional magnetite grains dispersed in clay.

Both individual elongated magnetic grains or interacting groups of magnetic grains would have shape anisotropy, *i.e.* they would be easier to magnetize along their longest axis. Compaction tends to rotate these grains, or groups of interacting grains, so that their longest axes lie preferentially in the bedding plane generating ARM anisotropy and AMS that are foliated in the bedding plane.

As mentioned earlier, the magnitude of magnetic anisotropy depends on the anisotropy of individual particles and the degree of their alignment. The latter is difficult to observe directly, but the former can be deduced, at least qualitatively, by looking at the mineralogy and the geometry (size and shape) of the magnetic particles. SEM images show that the size and shape of magnetic particles in the turbidites are similar to those in the pelagic clays and the pelagic lime-muds (Chapter 3). However, whereas the turbidites contain almost pure magnetite, the magnetite in the pelagic specimens contains Ti, suggesting that they may be cut by ilmenite lamellae which may reduce the magnetic anisotropy of the grains. Consider an elongated magnetite grain with principle axes a , b , and c ($a > b = c$). The growth of ilmenite lamellae reduces the magnetite in the grain to a volume fraction v_f which will then reduce the effective shape anisotropy of the grain from $(N_b - N_a)J_s$ to $(N_b - N_a) v_f J_s$, where N_a and N_b are the self-demagnetizing factors in a and b directions respectively. The value of v_f can be estimated from the weight ratio of TiO_2/FeO in Chapter 3. It can be shown that

$$v_f = \frac{1}{1 + \frac{31.7x}{44.2(1 - \frac{2}{3}x)}} \quad (7.4).$$

where x is defined in Eq. (3.1). For the pelagic clays, where x averages 0.37, v_f is 0.74. This should make the magnetite grains in the pelagic clays about 26% less anisotropic than those in the turbidites which is consistent with our measurements of particle anisotropy.

7.3 Estimating Particle ARM Anisotropy from Particle Shape

Measurements in Section 7.1 show that γ is quite difficult to measure reliably because of chaining of the magnetic grains. The approach in Section 7.2, in which the grain elongation required to give $\gamma = 1.8$ is estimated, can be reversed so that the value of γ can be estimated provided that the grain elongation is known. This could be important if one works with artificial samples where the dimension and mineralogy of the grains are known.

From Eq(s). (7.2) and (7.3), it can be shown that

$$\gamma = \frac{\frac{N_b}{N_a} - p_o \left(\frac{N_b}{N_a} + 2 \right)}{1 - p_o \left(\frac{N_b}{N_a} + 2 \right)} \quad (7.5).$$

Thus, to estimate γ from grain shape one needs to measure the ARM anisotropy and AMS to calculate the parameter p_o . The ratio of demagnetizing factors N_b/N_a can be obtained for the observed grain axial ratio from the table of *Stoner* [1945]. The relation between γ and the grain axial ratio for multi-domain or pseudo-single-domain magnetite as predicted by Eq. (7.5) is shown in Fig. (7.3) .

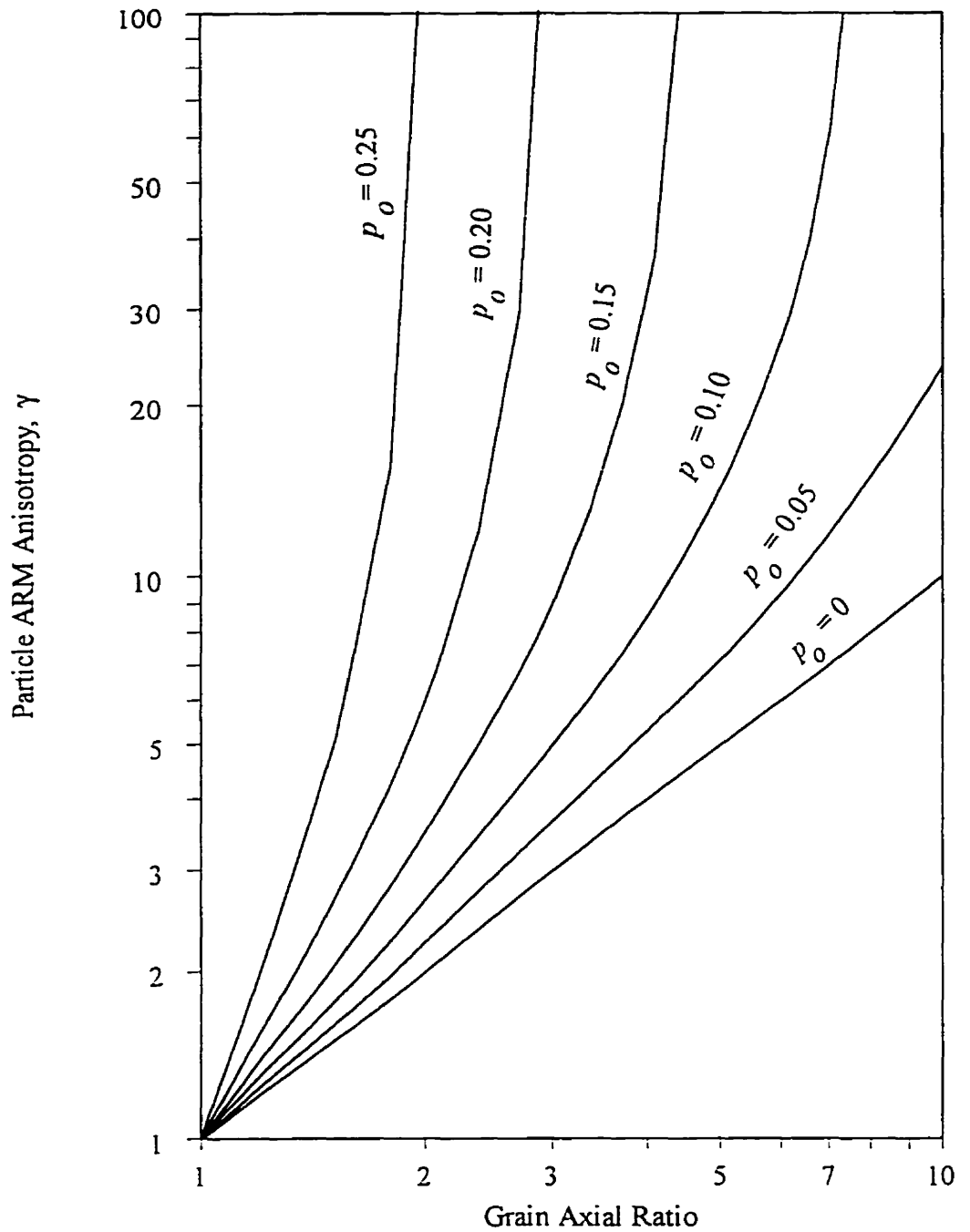


Figure 7.3 The relation between the particle ARM anisotropy γ and the grain axial ratio predicted by Eq. (7.5) for p_0 between 0 to 0.25 which is typical for multi-domain or pseudo-single-domain magnetite (Stephenson *et al.*, 1986).

CHAPTER 8

ARE THE OBSERVED INCLINATION SHALLOWING AND ARM ANISOTROPY COMPACTION-INDUCED?

The inclination shallowing and ARM anisotropy are much stronger in the turbidites than in the pelagic sediments. Therefore, this chapter will first consider the turbidites. We shall test whether the inclination shallowing and the ARM anisotropy in the turbidites are compaction-induced. This will be followed by discussion of whether the inclination shallowing in the pelagic sediments is also compaction-induced and why the inclination shallowing is so small.

8.1 Correlating the Degree of Compaction with Remanence Inclination and ARM Anisotropy in the Turbidites

The rock magnetic measurements of Chapter 3 show that the natural remanence in the turbidites is likely carried by pseudo-single-domain magnetite grains that are almost titanium free. Assuming that the grains behave like crushed, rather than hydrothermally grown magnetite, the ratio J/J_s of 0.1 to 0.2 (see Fig. 3.6) suggests a grain size of 0.5 to 1 μm (*Dunlop, 1995*). Because the turbidites likely have not been bioturbated (X-radiographs show that many specimens are laminated), the natural remanence could be a DRM with inclination shallowing originating during deposition. However, because of the fine grain size of the magnetite, one expects that the natural remanence is more likely a

pDRM (*Irving and Major, 1964*). If so, sediment compaction is the likely source of the observed inclination shallowing in the turbidites (*Hodych and Bijaksana, 1993*). It also becomes the likely source of the observed magnetic anisotropy, since inclination shallowing and magnetic anisotropy are correlated.

One way to test whether inclination shallowing and magnetic anisotropy in the turbidites are compaction-induced is to look for them to significantly correlate with the degree of compaction, ΔV . Such a test will not be attempted for the pelagic sediments because they have much smaller inclination shallowing and magnetic anisotropy and because the relationship between inclination shallowing and compaction in the pelagic sediments has already been addressed in earlier studies (*Arason and Levi, 1990a; Celaya and Clement, 1988*).

Density and water content data were available for turbidite cores 28 and 24, but not for core 13. The porosity, ϕ , was calculated for cores 28 and 24 from this data using the following formula suggested by the *Shipboard Scientific Party [1994]*.

$$\phi = \frac{\rho w}{(1 + w)\rho_w} \quad (8.1),$$

where ρ is the sample's bulk density, ρ_w is the pore fluid density and w is the volume fraction of water in the sample. For deep sea sediments, ρ_w is 1.05 g/cm³ (*Hamilton, 1976*). The degree of compaction, ΔV , was then calculated from ϕ using Eq. (1.7) and

assuming an initial porosity, ϕ_0 , of 0.72 ± 0.05 for terrigenous deep sea sediments (Hamilton, 1976).

If inclination shallowing is compaction-induced, a significant correlation between ΔV and $\tan I_{obs}$ is expected from Eq. (1.6) which predicts

$$\tan I_{obs} = \tan I_H - b \Delta V \tan I_H \quad (8.2).$$

Also, a significant correlation between ΔV and ARM_{min}/ARM_{max} is predicted when Eq(s). (1.6) and (1.12) are combined to obtain the equation

$$\frac{ARM_{min}}{ARM_{max}} = \frac{1 + 2 (ARM_{\perp}/ARM_{\parallel}) - b \Delta V}{1 + 2 (ARM_{\perp}/ARM_{\parallel}) - (ARM_{\perp}/ARM_{\parallel}) b \Delta V} \quad (8.3).$$

In an ARM_{min}/ARM_{max} versus ΔV diagram, Eq. (8.3) predicts a family of approximately linear curves for a given value of particle anisotropy (expressed as its inverse $ARM_{\perp}/ARM_{\parallel}$) and varying b . All curves intercept the ARM_{min}/ARM_{max} axis at (0,1), while their slopes depend on the values of b . Figure 8.1 shows these curves for the particle anisotropy of 1.8 ($ARM_{\perp}/ARM_{\parallel} = 0.56$) that was measured for the turbidites of cores 28 and 13 (Chapter 7).

Figure 8.2 plots $\tan I_{obs}$, ΔV and ARM_{min}/ARM_{max} versus depth for cores 28 and 24 respectively (excluding specimens whose ARM_{min} axis has an inclination of less than 75°). Correlation between ΔV and $\tan I_{obs}$ and between ΔV and ARM_{min}/ARM_{max} in core 28 are

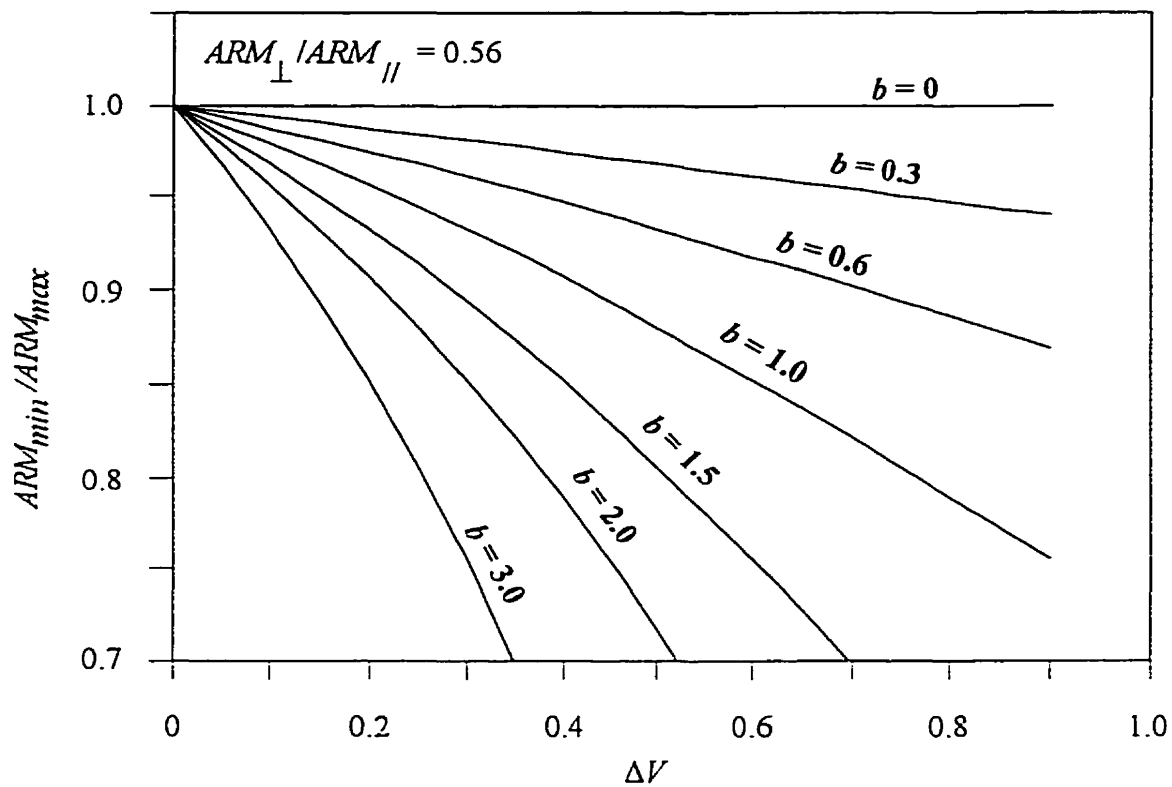


Figure 8.1 The relation between ARM_{min} / ARM_{max} and ΔV predicted by Eq. (8.3) for various values of b assuming $ARM_{\perp} / ARM_{\parallel} = 0.56$.

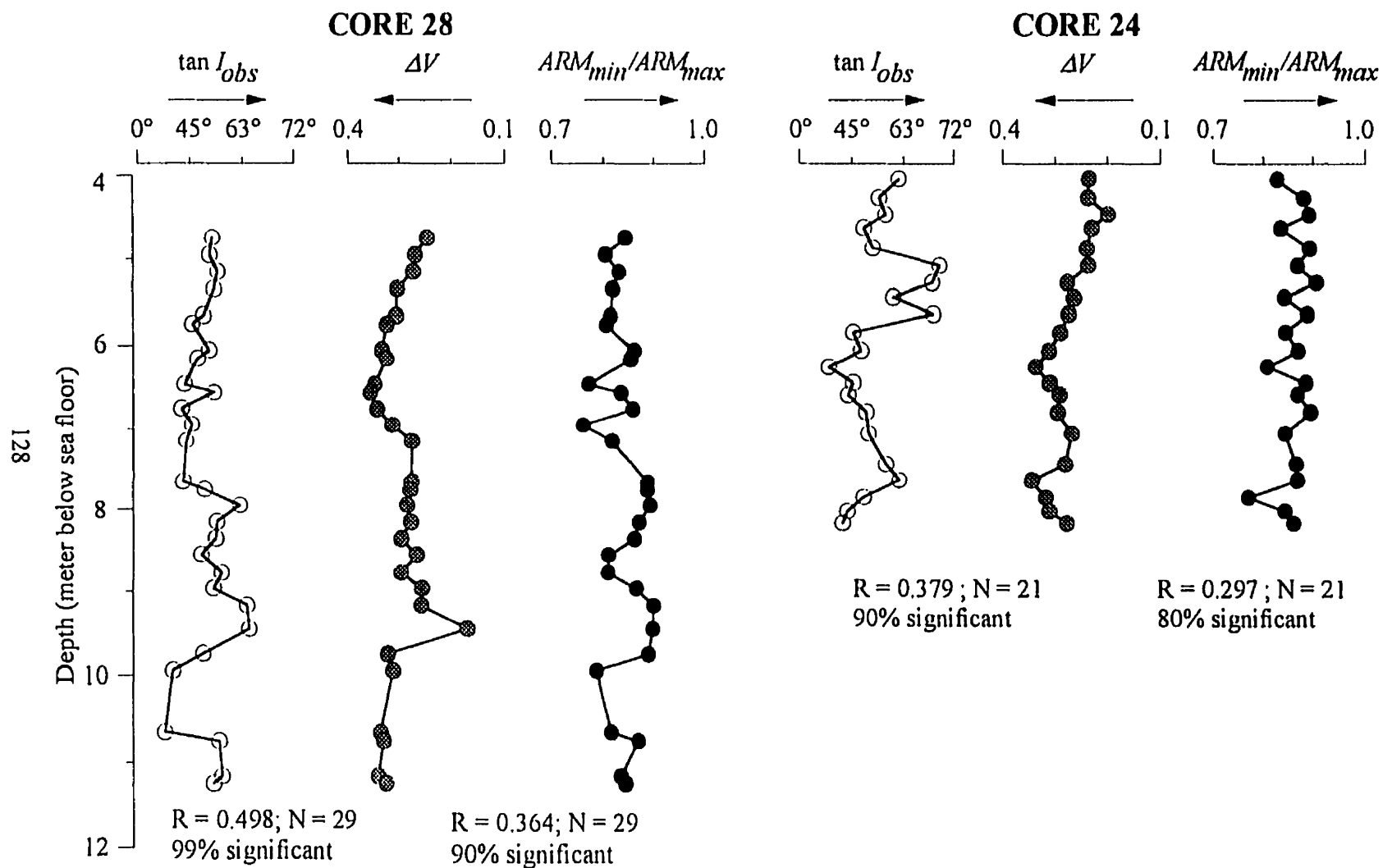


Figure 8.2 Tangent of the observed inclination $\tan I_{obs}$, the degree of compaction ΔV and the inverse ARM anisotropy ARM_{min}/ARM_{max} for cores 28 and 24. The quality of correlation between the degree of compaction and the other two parameters is indicated by the coefficient of correlation R .

significant with 99% and 90% confidence respectively ($R = 0.498$ and $R = 0.364$ respectively with $N = 29$). These correlations are less significant in core 24; correlation between ΔV and $\tan I_{obs}$ is significant with 90% confidence, whereas that between ΔV and ARM_{min}/ARM_{max} is significant with only 80% confidence ($R = 0.379$ and $R = 0.297$ respectively with $N = 21$). If the two sets of data are combined, correlation between ΔV and $\tan I_{obs}$ and between ΔV and ARM_{min}/ARM_{max} are both significant with 99% confidence ($R = 0.449$ and $R = 0.377$ respectively with $N = 50$). These results suggest that both the magnetic inclination shallowing and the ARM anisotropy were induced by compaction in the turbidites.

Since $\tan I_{obs}$ and ΔV correlate significantly in the turbidites, the least squares fit line on a $\tan I_{obs}$ versus ΔV plot can be used to estimate $\tan I_H$ and b . Eq. (8.2) predicts that the line's estimate of $\tan I_{obs}$ when $\Delta V = 0$ should be an estimate of $\tan I_H$, while the slope of the line divided by the estimated $\tan I_H$ should be an estimate of b . Figure 8.3 shows this prediction method applied to the turbidite data. As in Section 6.2, the value of $\tan I_{obs}$ for $\Delta V = 0$ was estimated using the regression modelling described in *McClave and Dietrich* [1992]. The predicted $\tan I_H$ and its 95% confidence interval are 2.76 ± 1.21 for core 28, 3.10 ± 2.23 for core 24 and 2.98 ± 1.28 for the combined data. Thus, the predicted I_H is $70^\circ (+6^\circ/-13^\circ)$ for core 28, $72^\circ (+7^\circ/-31^\circ)$ for core 24 and $71^\circ (+6^\circ/-12^\circ)$ for the combined data. This prediction's 95% confidence interval includes the $I_H = 61^\circ$ expected from the GAD model supporting the hypothesis that the inclination shallowing is

compaction-induced. The estimated value of b is 1.76 ± 0.59 for core 28, 1.85 ± 1.04 for core 24 and 1.84 ± 0.53 for the combined data.

Figure 8.4 plots ARM_{min}/ARM_{max} versus ΔV for the turbidite cores. The least squares fit lines are expected to pass through $ARM_{min}/ARM_{max} = 1$, $\Delta V = 0$. They pass below this point but not significantly considering that the estimated ARM_{min}/ARM_{max} for $\Delta V = 0$ and its 95% confidence interval are 0.94 ± 0.13 for core 28, 0.93 ± 0.13 for core 24 and 0.95 ± 0.10 for the combined data. Assuming $ARM_{1}/ARM_{//} \approx 0.56$ ($ARM_{//}/ARM_{1} \approx 1.8$ from the measurements of Chapter 7), the least squares fit lines of Fig. 8.4 agree reasonably well with the theoretical curves predicted by Eq. (8.3). The slope of the least squares fit line for core 28 is similar to the slope of the theoretical curve for $b = 1.5$ (Fig. 8.4.a) while that for core 24 is similar to the slope of the theoretical curve for $b = 1.2$ (Fig. 8.4.b). When the data for the two cores are combined, the slope of the least squares fit line is similar to that of the theoretical curve for $b = 1.5$ (Fig. 8.4.c). These estimates of b fall within the error limits of the b estimates made from plots of $\tan I_{obs}$ versus ΔV .

8.2 Compaction Experiments

The theoretical model of *Anson and Kodama* [1987] (see Eq. 1.6) suggests that compaction-induced inclination shallowing can be predicted if the degree of compaction and the value of b for a particular sediment are known. In the present study, compaction experiments were conducted to measure the value of b and to test this suggestion.

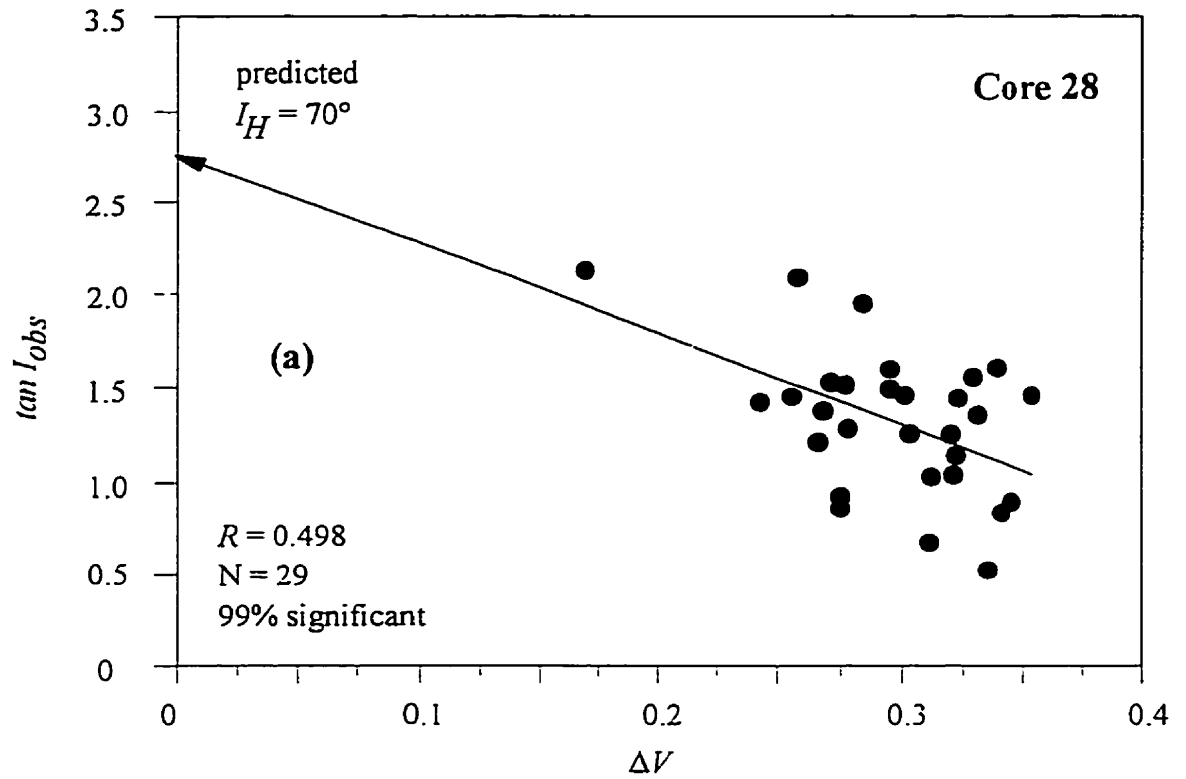


Figure 8.3 The correlation observed between $\tan I_{obs}$ and ΔV for the turbidite cores 28 (a) and 24 (b). The combined data are plotted in (c). For each core, the arrow points at $\tan I_{obs}$ predicted for $\Delta V = 0$; the corresponding I_{obs} is the prediction of the field inclination I_H .

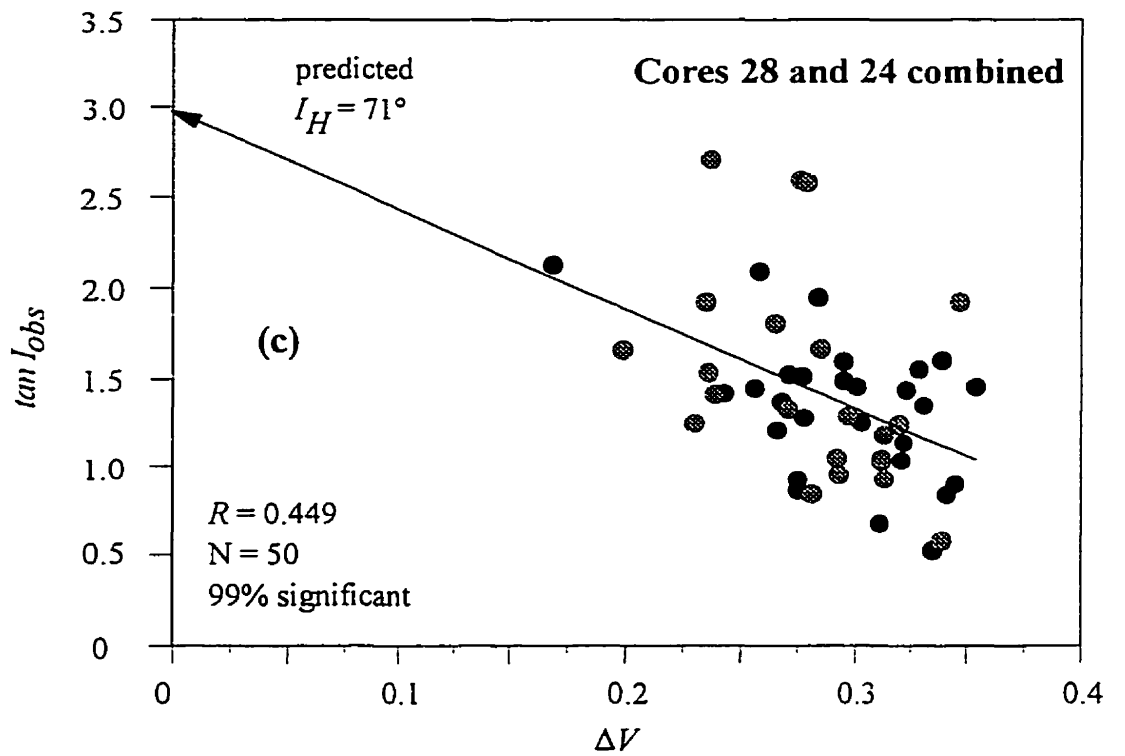
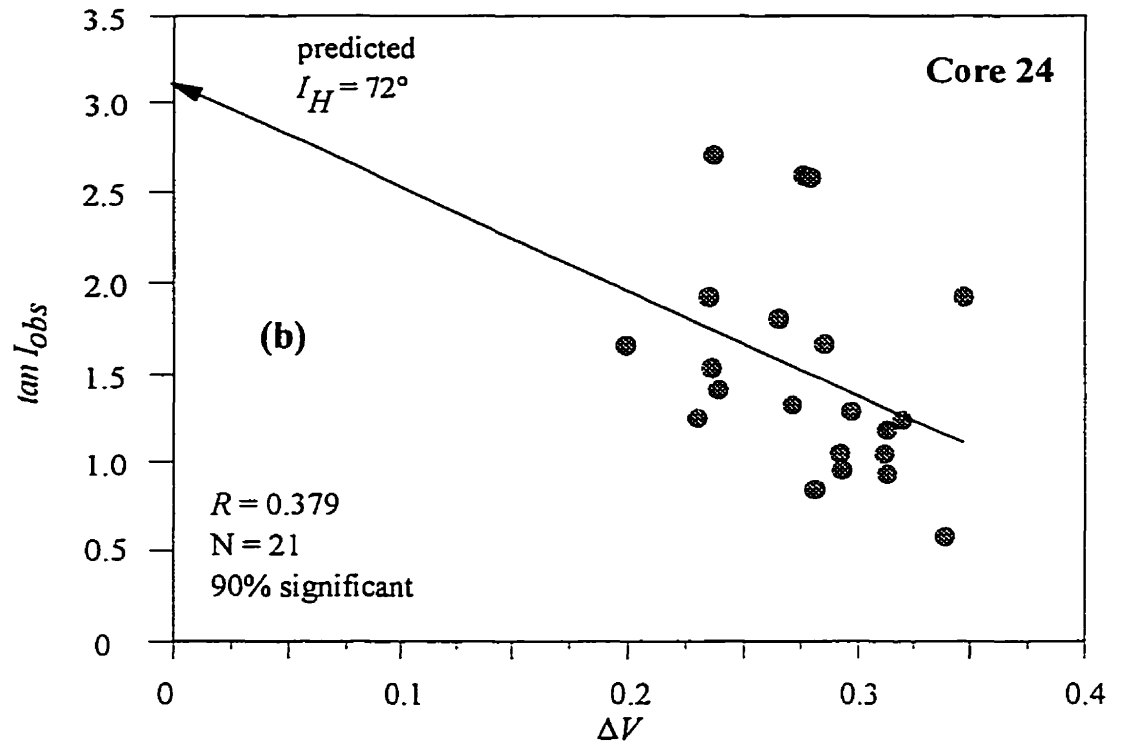


Figure 8.3 (Continued)

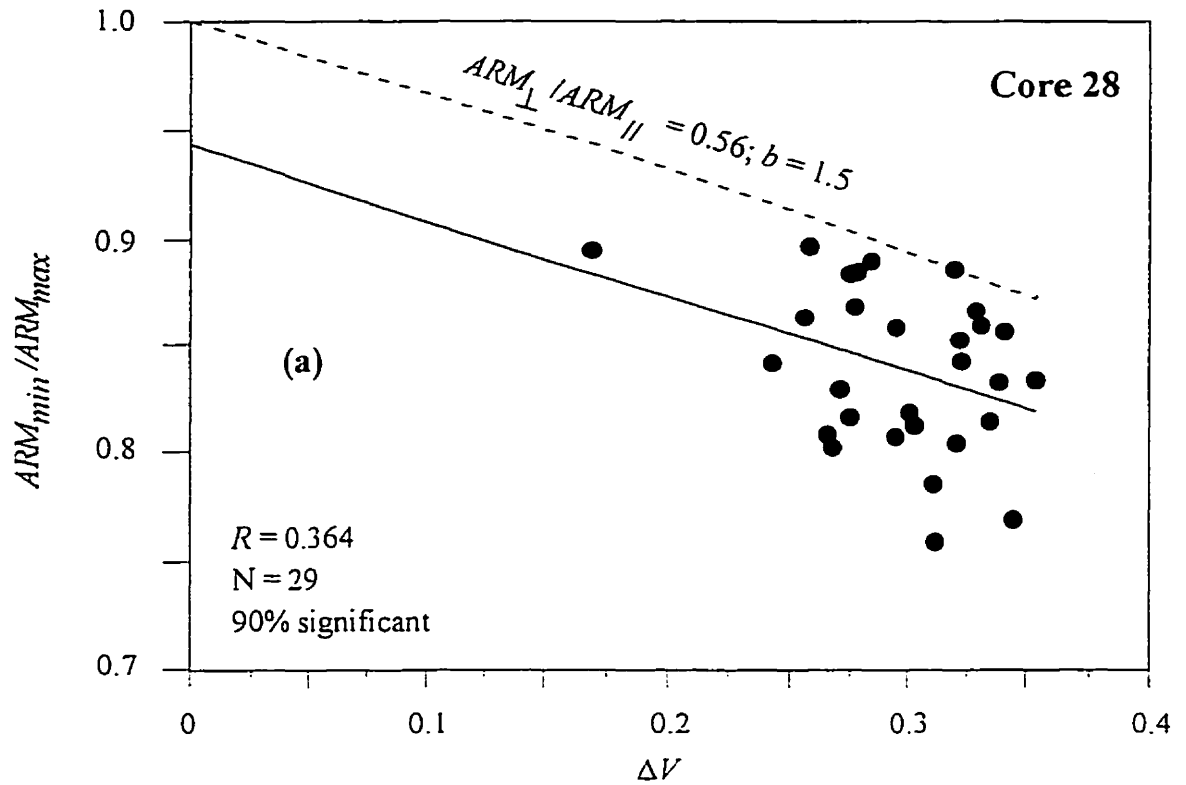


Figure 8.4 The correlation observed between ARM_{min} / ARM_{max} and ΔV for the turbidite cores 28 (a) and 24 (b). The combined data are plotted in (c). The solid line in each figure is the least squares fit line for the data while the dashed line is the theoretical line according to Eq. (8.3) for given values of $ARM_{\perp} / ARM_{\parallel}$ and b . Assuming that $ARM_{\perp} / ARM_{\parallel} = 0.56$, b is chosen so that the slope of the theoretical line approximates that of the least squares fit line.

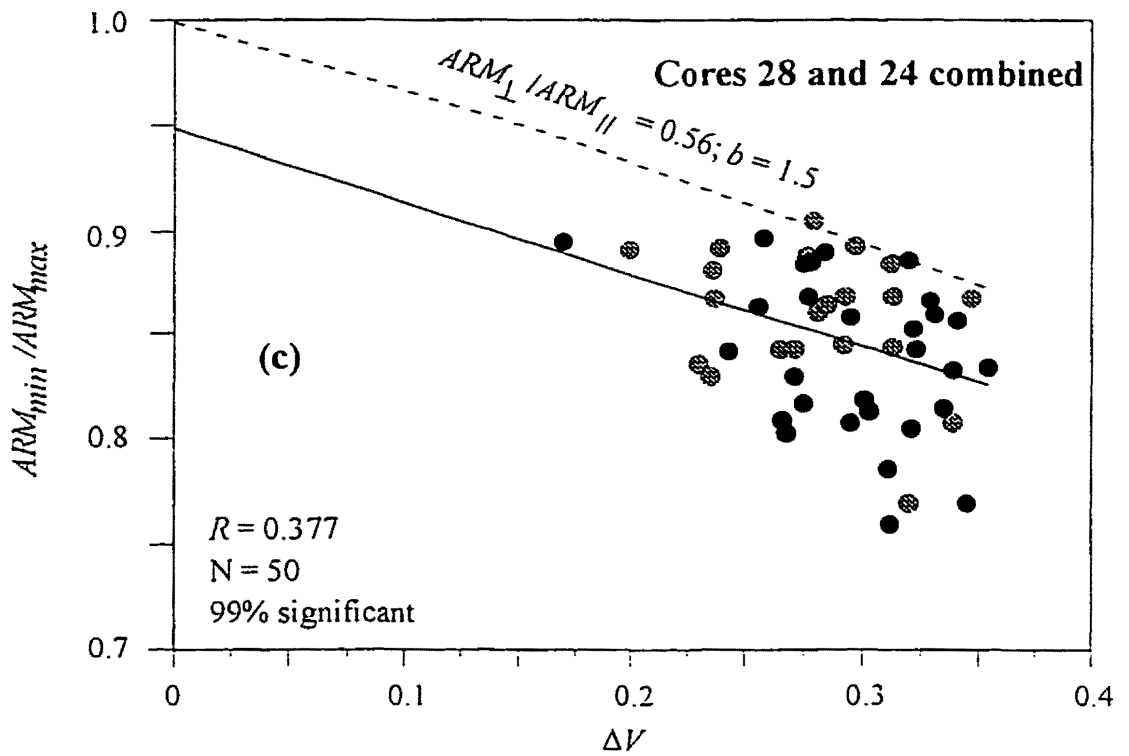
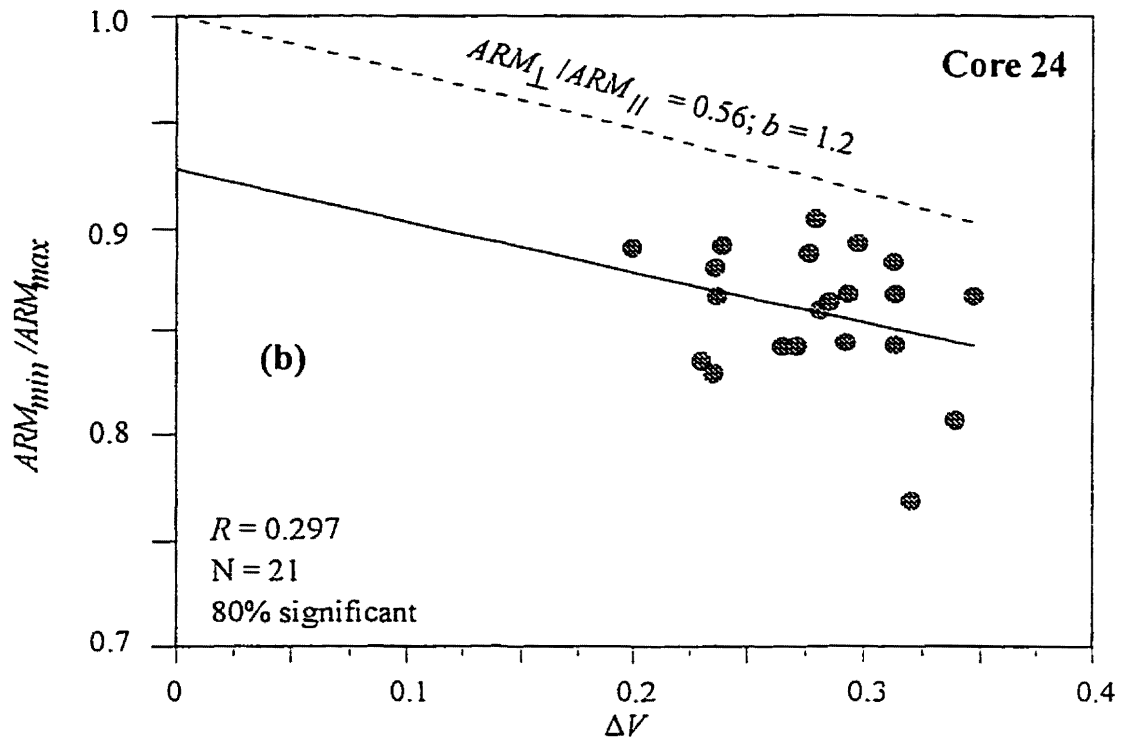


Figure 8.4 (Continued)

Compaction-induced ARM anisotropy was also measured. A compaction apparatus was built following the design of *Anson and Kodama* (1987) with a few modifications (Fig. 8.5).

Each sample in these experiments was made by mixing about 4 g of specimen with deionized water to form a slurry. The slurry was poured into a hollow cylindrical plastic tube of 2.2 cm internal diameter and 5.0 cm height with a snugly fitting porous disc at the bottom. (The porous disc was made of fine silica, was 2.4 mm thick and was manufactured by Kimble). The slurry was stirred and then was allowed to settle in a magnetic field of 45° inclination and 0.05 mT intensity maintained by two pairs of Helmholtz coils. After 24 hours, some clear water had escaped out the bottom through the porous disc and a head of clear water on top was removed by pipeting, reducing the sample's height to less than 2.5 cm. The detachable upper half of the plastic tube was then removed and a second snugly fitting porous disc was gently pressed down the remaining half of the tube onto the top of the sample. The height of the sample in the tube was then measured to determine the initial volume of the sample. The initial inclination of remanence of the sample in the tube was measured in a cryogenic magnetometer. Finally, the sample in its tube was returned to the 0.05 mT field of 45° inclination in the coils and compacted.

In the first compaction experiment, the sample was compacted by slowly (over about 30 minutes) filling the water tank with 500 ml of water (exerting a vertical pressure of 0.016 MPa on the sample). The sample remained inside the coils for another 2 hours to

ensure that its volume had stabilized. The sample in its tube was then removed and its volume and remanence inclination (I_{obs}) were measured again. This process was repeated several times. Each time the load was increased until the maximum load of 7500 ml (= 0.23 MPa) was reached.

Three turbidite specimens were measured and the results are plotted as $\tan I_{obs}$ versus ΔV diagrams in Fig. 8.6.a. The plots show that magnetic inclination decreases as the degree of compaction increases in all samples. Following Eq. (1.6), an estimate of $-b$ is given by the slope of the best fit line in these plots. However, a small load produces a large ΔV at the beginning of a compaction experiment resulting in few data points in the initial part of the plot. Hence, the accuracy of the estimate of b usually depends heavily on the initial value of the observed inclination at $\Delta V = 0$. The turbidite specimens 28-0645 and 28-0855 show a similar slope giving $b = 0.66$ (± 0.05 for 28-0645 and ± 0.02 for 28-0855) while the third specimen, 28-1065, gives $b = 0.84 \pm 0.02$. These b values are significantly lower than those estimated from plots of $\tan I_{obs}$ or ARM_{min}/ARM_{max} versus ΔV . However, this may be fortuitous and the experiment should be repeated with a composite sample that would better represent the turbidites.

In the second experiment, the sample was treated exactly as in the first experiment except that it was compacted in one step by slowly (over about 3 hours) and steadily filling the water tank to the maximum load of 7500 ml. As in the earlier experiment, the sample remained inside the coils for another 2 hours after reaching maximum load. The

sample's volume and then its ARM anisotropy were measured. Anhysteretic remanence was given along the vertical and the two horizontal axes. The ARM anisotropy is denoted by ARM_{hor}/ARM_{ver} , where ARM_{hor} is the average of the two horizontal ARMs and ARM_{ver} is the vertical ARM.

Two turbidite samples were measured and the results are presented in Fig. 8.6.b. The turbidites become very anisotropic with $ARM_{hor}/ARM_{ver} = 1.40$ (approximately 30% anisotropy) for specimen 28-0855 and 1.32 for specimen 28-0945. The degree of compaction is 0.75 in specimen 28-0855 and 0.70 in specimen 28-0945. Substituting these ARM_{ver}/ARM_{hor} measurements for ARM_{min}/ARM_{max} in Eq. (8.3) and assuming $ARM_{\perp}/ARM_{\parallel} = 0.56$ yields $b = 1.35$ for specimen 28-0855 and 1.27 for specimen 28-0945. These b values agree with b values estimated from plots of $\tan I_{obs}$ or ARM_{min}/ARM_{max} versus ΔV . However, this again may not be very definitive because the specimens may not represent the average turbidites and the experiment should be repeated with a composite sample. The limitedness of specimen volume (about 7 cm³ each) prevented us to make a composite sample for this experiment.

8.3 Difficulties in Measuring Parameter b

Although the amount of inclination shallowing in the turbidites can be predicted even without knowing the value of b , measuring this parameter with compaction experiments helps test the consistency of the theory. The b values so measured do support

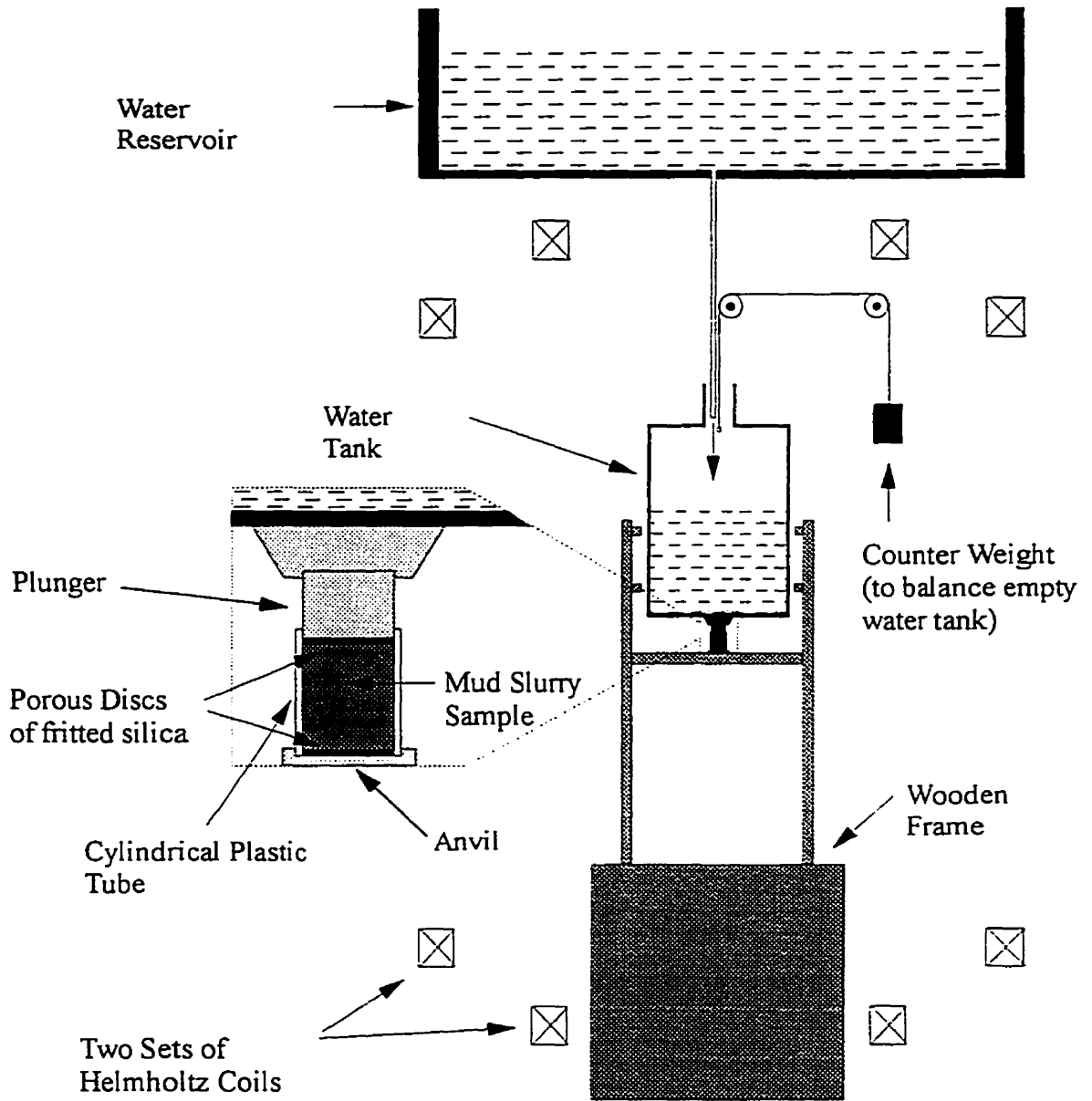


Figure 8.5 Schematic diagram of compaction apparatus used in this study. The intensity of magnetic field at the centre of the coils was set to 0.05 mT, while its inclination was 45°. Both the plunger and anvil had holes to allow water coming through the porous discs to escape from the compacting sample.

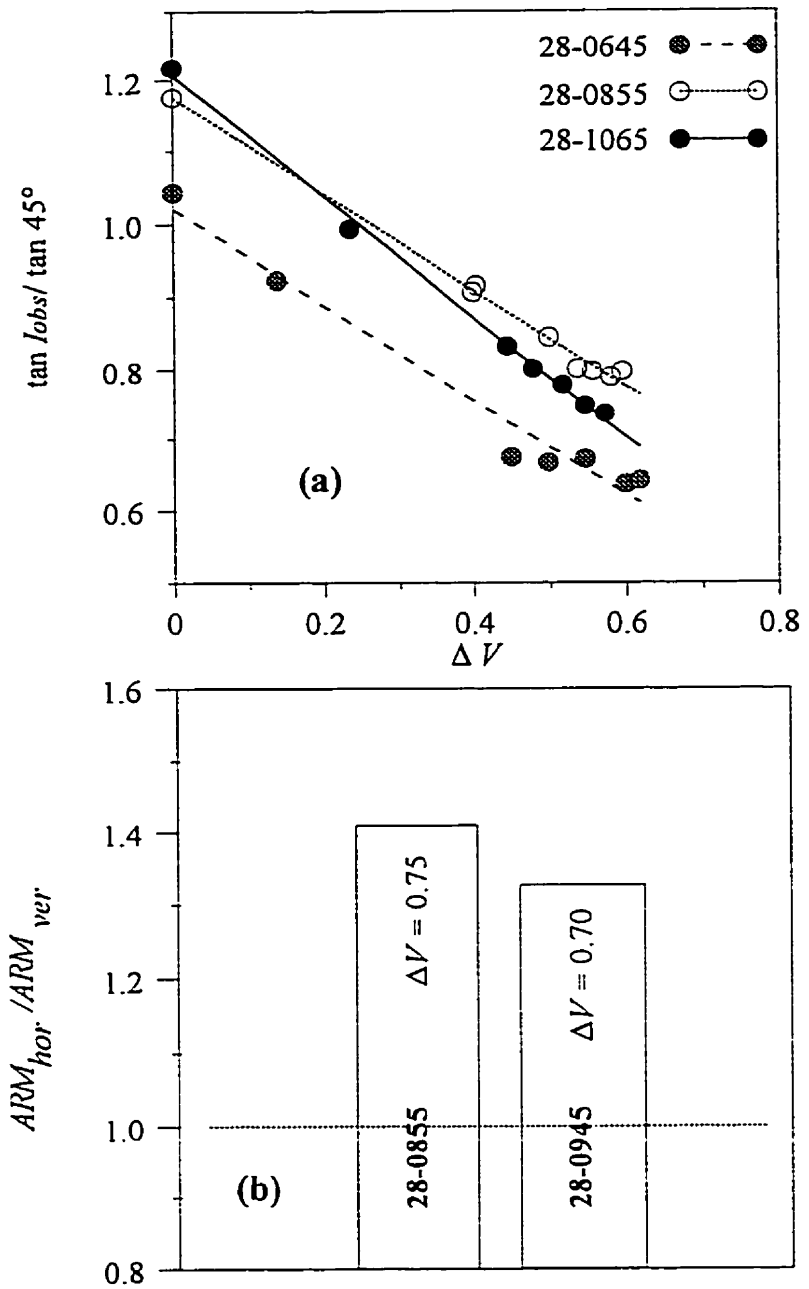


Figure 8.6 Results of compaction experiments. In (a), the three turbidite samples were compacted by increasing the load in steps. The inclination and the degree of compaction ΔV were measured after each step. Solid, dashed and dotted lines indicate the least squares fit for each specimen. The slope of the line estimates $-b$ for the specimen. Figure b shows ARM anisotropy denoted by ARM_{hor} / ARM_{ver} and the degree of compaction ΔV caused by applying the maximum load of 7500 ml of water for the two turbidite specimens measured.

the theory, although it would have been better to have used composite samples. There are other difficulties in measuring b with compaction experiments that should be mentioned.

The degree of compaction, ΔV , measured in the compaction experiments may differ from ΔV observed in natural sediments because the initial volume of specimen is measured differently. In our compaction experiments, the initial volume is determined when all clear water has either escaped out the bottom through the porous disc or been removed by pipeting after letting the slurry settle for 24 hours. For natural sediments, a certain value for the initial porosity, ϕ_0 , is assumed using the data of *Hamilton* [1976] for a very general type of sediments *i.e.* terrigenous deep sea sediments, which may not be very representative for the turbidites.

Randomization or disturbance of magnetic particles may occur during the early stage of compaction. For their clay-rich sediments, *Sun and Kodama* [1992] and *Kodama and Sun* [1992] suggest that, during the early phase of compaction, as clay particles move closer together, a preferential disturbance or randomization of magnetite grains with subvertical easy axes of magnetization occurs. This process, accompanied by a large decrease of volume, also causes a decrease of remanence intensity and a large inclination shallowing without the development of magnetic anisotropy. This does not seem to occur in our turbidite experiments (see Fig. 8.6). In nature, this effect may be erased by bioturbation or by the fine magnetite particles having time to realign along the Earth's field direction.

8.4 Low Inclination Shallowing in the Pelagic Sediments

The pelagic clays of DSDP site 578 and the pelagic lime-muds of DSDP site 606 were used in this study because they had been reported to show inclination shallowing (*Celaya and Clement, 1988; Arason and Levi, 1990a*). This study, however, shows that their inclination shallowing is small compared to that of the turbidites. Before we discuss why this is so, we shall discuss whether the inclination shallowing observed in the pelagic sediments is compaction-induced.

The presence of bioturbation in the pelagic sediments favours compaction-induced inclination shallowing. Evidence for bioturbation is common in the pelagic clays of site 578 (*Shipboard Scientific Party, 1985*) and occurs occasionally in the pelagic lime-muds of site 606 (*Shipboard Scientific Party, 1987*). The natural remanence of bioturbated sediments is likely a pDRM and therefore any inclination shallowing in them is likely compaction-induced (*Hodych and Bijaksana, 1993*).

A significant correlation between remanence inclination and the degree of compaction in the pelagic sediments also supports compaction-induced inclination shallowing. Measuring 563 closely spaced (one per 20 cm) pelagic clay specimens from site 578 and transforming the inclination from depth domain into time domain, *Arason and Levi [1990a]* found a significant correlation between inclination shallowing and compaction when the inclination and the porosity data were averaged over some time interval. (They argued that this averaging was necessary to eliminate high frequency components due to geomagnetic secular variation and other random noise in the case of

inclination data and due to climatic or lithological variation in the case of porosity data.) In the pelagic lime-muds, *Celaya and Clement* [1988] showed that the downcore decrease in inclination correlates with the downcore decrease in water content. They also averaged their inclination data so that each calculated mean represented one core (≈ 10 m) to allow for a more direct comparison with shipboard water content data.

Why is the inclination shallowing so much lower in the pelagic sediments than in the turbidites when it seems to be compaction-induced in both? One possibility is that compaction is lower in the pelagic sediments.

Consider the pelagic clays. *deMenocal et al.* [1990] pointed out that the structural strength of clays increases with decreasing sedimentation rate. Hence one would expect greater strength and less compaction in the pelagic clays which were deposited at a maximum rate of 4 cm per 10^3 years (*Arason and Levi*, 1990a) than in the turbidites which were deposited at an average rate of 34 cm per 10^3 years (6.8 m in core 13 represent 20 ka of deposition according to *Berry* [1992] and *Berry and Piper* [1993]). The value of ΔV for the individual pelagic clay specimens was estimated using Eq. (1.7) and assuming a constant initial porosity, ϕ_o , of 0.81 ± 0.05 for clay-rich deep sea sediments (*Hamilton*, 1976), while the porosity for each specimen was calculated by interpolating the porosity data of *Schultheiss* [1985]. The average ΔV for the pelagic clays is only 0.06 ± 0.11 compared to 0.29 ± 0.04 for the combined turbidite data from cores 28 and 24. Hence, low compaction may indeed be responsible for the low inclination shallowing observed in

the pelagic clays. However, this assumes that b is similar for the turbidites and the pelagic clays which is not proven. Also, many of the ΔV values for the pelagic clays are negative suggesting that ΔV may be too low because the assumed ϕ_0 is too high.

The degree of compaction in the pelagic lime-muds should be compared with the degree of compaction in another calcareous sediment that shows compaction-induced inclination shallowing. We use the Cretaceous limestones from the Pacific described by *Hodych and Bijaksana* [1993]. The value of ΔV for individual pelagic lime-mud specimens was estimated using Eq. (1.7) and assuming a constant initial porosity, ϕ_0 , of 0.72 ± 0.05 for calcareous deep sea sediments (*Hamilton, 1976*), while the porosity for each specimen was calculated by interpolating the porosity data of *Shipboard Scientific Party* [1987]. The average ΔV for the pelagic lime-muds is 0.27 ± 0.08 which is low compared to the 0.62 ± 0.10 reported for the Cretaceous limestones that show an average inclination shallowing of 17° (*Hodych and Bijaksana, 1993*). If we assume that the paleolatitudes of the pelagic lime-muds and the limestones were similar, *i.e.* $I_H = 57^\circ$, and that they had the same value of b (0.8 according to *Hodych and Bijaksana* [1993]), the pelagic lime-muds would be expected to show 7° of inclination shallowing compared to 19° in the limestones. Hence, it is possible that the low inclination in the pelagic lime-muds is also due to relatively low compaction.

CHAPTER 9

CONCLUSIONS

The Turbidites

The observed inclination (I_{obs}) of the natural remanence of 79 clay-rich turbidite specimens taken from cores 28, 24, and 13, from the Scotian Rise is, on average, 12° shallower than the 61° expected from the geocentric axial dipole model. The remanence in these specimens is carried primarily by slightly elongated magnetite grains with very low Ti content (judging from scanning electron microscope analysis of magnetic extracts, from Curie points and from the presence of the Verwey transition). Hysteresis loop analysis show that the magnetite is dominantly pseudo-single-domain and of small grain size (0.5 to $1 \mu\text{m}$).

The turbidite specimens were found to be strongly anisotropic. On average, the ratio of anhysteretic remanence given along the minimum axis to that along the maximum axis is 0.819. In most specimens, the minimum axis is perpendicular to the bedding plane and there is little difference in magnitude between the intermediate and the maximum axes. The few specimens whose minimum axis departed by 15° or more from vertical were considered unreliable and are excluded from further discussion.

A significant correlation between remanence inclination (represented by $\tan I_{obs}$) and ARM anisotropy (represented by anhysteretic remanence along the minimum axis to that along the maximum axis, ARM_{min}/ARM_{max}) was observed in all turbidite cores as

Hodych and Bijaksana [1993] showed was expected from the theory of *Jackson et al.* [1991]. The value of $\tan I_{obs}$ predicted by the correlation line for $ARM_{min}/ARM_{max} = 1$ then gives an estimate of the inclination of the field in which the remanence was acquired (denoted by I_H). For the combined turbidite data, the predicted field inclination I_H and its 95% confidence interval are $69^\circ (+5^\circ/-10^\circ)$. This agrees with the 61° expected from the geocentric axial dipole model. The correlation line also predicts that $ARM_{\perp}/ARM_{\parallel}$ should average approximately 0.47, where ARM_{\perp} and ARM_{\parallel} are ARM intensities given perpendicular and parallel to the long axis of the magnetite particles.

The parameter $ARM_{\perp}/ARM_{\parallel}$ of magnetite particles in the turbidites proved difficult to measure. A composite sample from each core was mixed with warm liquid gelatine and cooled in an aligning magnetic field and the ratio of ARM perpendicular and parallel to the aligning field direction was measured. This was repeated for higher and higher fields until the ARM ratio saturated which was then used as an estimate of $ARM_{\perp}/ARM_{\parallel}$. When a static field was used for the alignment, the $ARM_{\perp}/ARM_{\parallel}$ estimate was unreasonably low, probably due to chaining of magnetite particles along the field direction. Even when an alternating aligning field was used, it was found that there was still some chaining of the magnetite particles requiring large corrections to the ARM ratios. The estimate of $ARM_{\perp}/ARM_{\parallel}$ corrected for chaining was ≈ 0.56 . This is in satisfactory agreement with $ARM_{\perp}/ARM_{\parallel} \approx 0.47$ predicted from the correlation between $\tan I_{obs}$ and ARM_{min}/ARM_{max} . This result supports the theory of *Jackson et al.* [1991], but not conclusively because the correction for chaining is very large (and debatable).

If inclination shallowing is compaction-induced, a linear relationship between inclination and compaction is expected both theoretically (*Arason and Levi, 1990b*) and experimentally (*Anson and Kodama, 1987*). Estimating compaction ΔV from porosity data, a significant correlation between inclination (represented by $\tan I_{obs}$) and compaction ΔV was found. The correlation's estimate of $\tan I_{obs}$ when $\Delta V = 0$ predicts a field inclination $I_H = 71^\circ (+6^\circ/-12^\circ)$, which is similar to the result predicted from correlation between inclination and ARM anisotropy. A significant correlation was also found between ARM anisotropy and compaction suggesting that ARM anisotropy was mainly compaction-induced. Compaction experiments on redeposited turbidite samples gave less inclination shallowing than expected from the correlation observed in nature between $\tan I_{obs}$ and ΔV . However, the difference may not be significant.

The susceptibility anisotropy of the turbidites was similar to the ARM anisotropy, but of smaller magnitude. The ratio of susceptibility along the minimum axis (χ_{min}) to susceptibility along the maximum axis (χ_{max}) averaged 0.902. ARM anisotropy and susceptibility anisotropy were found to be related as predicted by the theory of *Stephenson et al. [1986]*. The parameter p_o that relates the ARM and susceptibility ellipsoids was found to be about 0.14 which is typical of multi-domain or pseudo-single-domain particles. It was shown that for $p_o < 0.25$, an approximately linear correlation is expected between χ_{min} / χ_{max} and ARM_{min} / ARM_{max} from the theory of *Stephenson et al. [1986]*. Such a correlation was found for the turbidites.

A significant correlation was also found between inclination (represented by $\tan I_{obs}$) and susceptibility anisotropy (represented by χ_{min}/χ_{max}) as expected since susceptibility anisotropy and ARM anisotropy are linearly correlated. This was used analogously to the correlation between inclination and ARM anisotropy to estimate the field inclination. For the combined turbidite data, the field inclination I_H and its 95% confidence interval are 67° ($+6^\circ/-13^\circ$). This agrees with the 61° expected from the geocentric axial dipole model and with the 69° ($+5^\circ/-10^\circ$) predicted by the correlation between inclination and ARM anisotropy. Susceptibility anisotropy has the advantage over ARM anisotropy of being much faster to measure and does not destroy natural remanence.

The Pelagic Clays

The observed inclination of the natural remanence of 87 pelagic clay specimens at DSDP site 578 in the northwest Pacific, which averaged 52° , does not significantly differ from the 53° expected from the geocentric axial dipole model. Curie points and evidence of a Verwey transition (partially suppressed, perhaps by oxidation) suggest that the remanence is carried by magnetite. Scanning electron microscope analysis of magnetic extracts shows a high Ti content suggesting that the magnetite is now intergrown with ilmenite. Hysteresis loop analysis suggest that the magnetite is predominantly pseudo-single-domain. The shape of the magnetite-ilmenite intergrown grains is similar to that in the turbidites judging by scanning electron microscope backscattered images of magnetic extracts.

The pelagic clays were found to be much less anisotropic than the turbidites. The average percent anisotropy is only 3.7% (for ARM anisotropy) and 2.6% (for susceptibility anisotropy). The directions of the principal ARM and susceptibility axes are scattered.

The low inclination shallowing and anisotropy are both probably due to relatively low compaction. The average compaction ΔV is 0.06 ± 0.11 compared to 0.29 ± 0.04 in the turbidites.

The Pelagic Lime-Muds

The natural remanence of 90 pelagic lime-mud specimens at DSDP site 606 located on the Mid-Atlantic Ridge were measured. Specimens from below 60 m were found to be unreliable. During AF demagnetization, some specimens were too weak to be measured reliably, while the others show an erratic intensity decay or directional changes. The average observed inclination of 53° does not differ significantly from the 57° expected from the geocentric axial dipole model. Curie points and evidence of a Verwey transition (partially suppressed, perhaps by oxidation) suggest that the remanence is dominantly carried by magnetite. Scanning electron microscope analysis of magnetic extracts from the upper 60 m of core shows the presence of nearly pure magnetite, titanomagnetite, and iron-rich chromian spinels. The hysteresis loop analysis suggest that the magnetite is predominantly pseudo-single-domain. Judging by scanning electron microscope

backscattered images of magnetic extracts, the particles are generally smaller and less abundant than in the turbidites and pelagic clays.

The pelagic lime-muds were found to be less anisotropic than the turbidites with the percent ARM anisotropy averaging 3.0%. The directions of the principal axes are scattered. The susceptibility anisotropies of the pelagic lime-muds were too weak to be measured with our instrument.

The low inclination shallowing and anisotropy are probably at least partly due to low compaction. The average ΔV for the pelagic lime-muds is 0.27 ± 0.08 , which is low compared to the 0.62 ± 0.10 reported for the Cretaceous limestones from the Pacific (*Hodych and Bijaksana, 1993*), which show 17° inclination shallowing.

REFERENCES

- Anson, G. L., and K. P. Kodama, Compaction-induced inclination shallowing of the post depositional remanent magnetization in a synthetic sediment, *Geophys. J. R. Astron. Soc.*, 88, 673-692, 1987.
- Arason, P., and S. Levi, Compaction and inclination shallowing in deep-sea sediments from the Pacific Ocean, *J. Geophys. Res.*, 95, 4,501-4,510, 1990a.
- Arason, P., and S. Levi, Models of inclination shallowing during sediment compaction, *J. Geophys. Res.*, 95, 4,481-4,499, 1990b.
- Arason, P., *Paleomagnetic inclination shallowing in deep-sea sediments*, Ph.D. thesis, 363 pp., Oregon State University, Corvallis, 1991.
- Baldauf, J. G., E. Thomas, B. Clement *et al.*, Magnetostratigraphic and biostratigraphic synthesis, deep sea drilling project leg 94, in *Initial Reports of the Deep Sea Drilling Project, vol. XCIV part 2*, pp. 1,159-1,205, U.S. Government Printing Office, Washington, D.C., 1987.
- Berry, J. A., *A detailed study of a debris flow on the Scotian Rise*, M.Sc. thesis, 202 pp., Dalhousie University, Halifax, 1992.
- Berry, J. A., and D. J. W. Piper, Seismic stratigraphy of the central Scotian Rise: A record of continental margin glaciation, *Geo-Mar. Lett.*, 13, 197-206, 1993.
- Bijaksana, S., Magnetic anisotropy of Cretaceous deep sea sedimentary rocks from the Pacific plate, M.Sc. thesis, 162 pp., Memorial University of Newfoundland, St. John's, 1991.
- Bloemendal, J., and P. deMenocal, Evidence for a change in the periodicity of tropical climate cycles at 2.4 Myr from whole-core magnetic susceptibility measurements, *Nature*, 342, 897-900, 1989.
- Blow, R. A., and N. Hamilton, Effect of compaction on the acquisition of a detrital remanent magnetization in fine-grained sediments, *Geophys. J. R. Astron. Soc.*, 52, 13-23, 1978.
- Buddington, A.F., and D.H. Lindsley, Iron-titanium oxide minerals and synthetic equivalents, *J. Petrology*, 5, 310-357, 1964.

- Butler, R. F., *Paleomagnetism*, 319 pp., Blackwell, Oxford, 1992.
- Celaya, M. A., and B. M. Clement, Inclination shallowing in deep-sea sediments from the North Atlantic, *Geophys. Res. Lett.*, *15*, 52-55, 1988.
- Chang, M. A., and J. L. Kirschvink, Magnetofossils, the magnetization of sediments, and the evolution of magnetite biomineralization, *Ann. Rev. Earth Planet. Sci.*, *17*, 166-195, 1989.
- Clement, B. M., and F. Robinson, The magnetostratigraphy of leg 94 sediments, in *Initial Reports of the Deep Sea Drilling Project, vol. XCIV part 2*, pp. 635-650, U.S. Government Printing Office, Washington, D.C., 1987.
- Collombat, H., P. Rochette, and M. J. Jackson, Possible correction of the inclination error in deep sea sediments using the anisotropy of anhysteretic remanence (abstract), *Eos Trans. AGU*, *71*, 1,288, 1990.
- Collombat, H., P. Rochette, and D. V. Kent, Detection and correction of inclination shallowing in deep sea sediments using the anisotropy of anhysteretic remanence, *Bull. Soc. géol. France*, *164*, 103-111, 1993.
- Day, R., M. Fuller, and V. A. Schmidt, Hysteresis properties of titanomagnetites: grain-size and compositional dependence, *Phys. Earth Planet. Inter.*, *13*, 260-267, 1977.
- Dearmer, G. A., and K. P. Kodama, Compaction-induced inclination shallowing in synthetic and natural clay-rich sediments, *J. Geophys. Res.*, *95*, 4,511-4,529, 1990.
- deMenocal, P. B., W. F. Ruddiman, and D. V. Kent, Depth of post-depositional remanence acquisition in deep-sea sediments: A case study of the Brunhes-Matuyama reversal and oxygen isotopic stage 19.1, *Earth Planet. Sci. Lett.*, *99*, 1-13, 1990.
- Dunlop, D. J., Magnetism in rocks, *J. Geophys. Res.*, *100*, 2,161-2,174, 1995.
- Foster, J. H., and N. D. Opdyke, Upper Miocene to Recent magnetic stratigraphy in deep-sea sediments, *J. Geophys. Res.*, *75*, 4,465-4,473, 1970.
- Freeman, R., Magnetic mineralogy of pelagic limestones, *Geophys. J. R. Astron. Soc.*, *85*, 433-452, 1986.
- Girdler, R. W., The measurement and computation of anisotropy of magnetic susceptibility of rocks, *Geophys. J. R. Astron. Soc.*, *5*, 34-44, 1961.

- Gordon, R. G., Test for bias in paleomagnetically determined palaeolatitudes from Pacific plate Deep Sea Drilling Project sediments, *J. Geophys. Res.*, 95, 8,397-8,404, 1990.
- Grégoire, V., M. de Saint Blanquat, A. Nédélec, and J. Bouchez, Shape anisotropy versus magnetic interactions of magnetic grains: experiments and application to AMS in granitic rocks, *Geophys. Res. Lett.*, 22, 2,765-2,768, 1995.
- Griffith D. H., R. F. King, A. I. Rees, and A. E. Wright, Remanent magnetism of some recent varved sediments, *Proc. Roy. Soc. London, Ser. A*, 256, 359-383, 1960.
- Hamilton, E. L., Variations of density and porosity with depth in deep-sea sediments, *J. Sediment. Petrol.*, 46, 280-300, 1976.
- Hargraves, R. B., D. Johnson, and C. Y. Chan, Distribution anisotropy: the cause of AMS in igneous rocks?, *Geophys. Res. Lett.*, 18, 2,193-2,196, 1991.
- Heath, G. R., D. H. Rea, and S. Levi, Paleomagnetism and accumulation rates of sediments at sites 576 and 578, deep sea drilling project leg 86, western North Pacific, in *Initial Reports of the Deep Sea Drilling Project, vol. LXXXVI*, pp. 459-502, U.S. Government Printing Office, Washington, D.C., 1985.
- Henshaw, P. C., and R. T. Merrill, Magnetic and chemical changes in marine sediments, *Rev. Geophys. Space Phys.*, 18, 483-504, 1980.
- Hodych, J. P., Determination of self-demagnetizing factor N for multidomain magnetite grains in rock, *Phys. Earth Planet. Inter.*, 41, 283-291, 1986.
- Hodych, J. P., Low temperature demagnetization of saturation remanence in rocks bearing multidomain magnetite, *Phys. Earth Planet. Inter.*, 66, 144-152, 1991.
- Hodych, J. P., and S. Bijaksana, Can remanence anisotropy detect paleomagnetic inclination shallowing due to compaction? A case study using Cretaceous deep-sea limestones, *J. Geophys. Res.*, 98, 22,429-22,441, 1993.
- Hunt, C. P, B. M. Moskowitz, and S. K. Banerjee, Magnetic properties of rocks and minerals, in *Rock Physics & Phase Relation, A Handbook of Physical Constants, AGU Reference Shelf 3*, T. J. Ahrens ed., pp. 189-204, American Geophysical Union, Washington D.C., 1995.
- Irving, E., and A. Major, Post-depositional detrital remanent magnetization in a synthetic sediment, *Sedimentology*, 3, 135-143, 1964.

- Jackson, M. J., S. K. Banerjee, J. A. Marvin, R. Lu, and W. Gruber, Detrital remanence, inclination errors and anhysteretic remanence anisotropy: Quantitative model and experimental results, *Geophys. J. Int.*, 104, 95-103, 1991.
- Janecek, T. R., Eolian sedimentation in the northwest Pacific Ocean: a preliminary examination of the data from deep sea drilling sites 576 and 578, in *Initial Reports of the Deep Sea Drilling Project*, vol. LXXXVI, pp. 589-603, U.S. Government Printing Office, Washington, D.C., 1985.
- Johnson, E. A., T. Murphy, and O. W. Torreson, Pre-history of the Earth's magnetic field, *Terr. Magn. Atmos. Elec.*, 53, 349-372, 1948.
- Karlin, R., and S. Levi, Geochemical and sedimentological control of the magnetic properties of hemipelagic sediments, *J. Geophys. Res.*, 90, 10,373-10,392, 1985.
- Kent, D.V., and D. Spariosu, Magnetostratigraphy of Caribbean site 502 hydraulic piston cores, in *Initial Reports of the Deep Sea Drilling Project*, vol. LXVIII, 419-434, U.S. Government Printing Office, Washington, D.C., 1982.
- King, R. F., Remanent magnetism of artificially deposited sediments, *Monthly Notices Roy. Astron. Soc. Geophys. Suppl.*, 7, 115-134, 1955.
- Kirschvink, J. L., The least squares line and plane and the analysis of paleomagnetic data, *Geophys. J. R. Astron. Soc.*, 62, 699-718, 1980.
- Kodama, K. P., and W. W. Sun, SEM and magnetic fabric study of a compacting sediment, *Geophys. Res. Lett.*, 17, 795-798, 1990.
- Kodama, K. P., and W. W. Sun, Magnetic anisotropy as a correction for compaction caused paleomagnetic inclination shallowing, *Geophys. J. Int.*, 111, 465-469, 1992.
- Ku, T. L., J. R. Southon, J. S. Vogel *et al.*, ¹⁰Be distributions in deep sea drilling project site 576 and site 578 sediments studied by accelerator mass spectrometry, in *Initial Reports of the Deep Sea Drilling Project*, vol. LXXXVI, pp. 539-546, U.S. Government Printing Office, Washington, D.C., 1985.
- Lenôtre, N., H. Chamley, and M. Hoffert, Clay stratigraphy at deep sea drilling project sites 576 and 578, leg 86 (western North Pacific), in *Initial Reports of the Deep Sea Drilling Project*, vol. LXXXVI, pp. 571-579, U.S. Government Printing Office, Washington, D.C., 1985.

- Lu, R., S. K. Banerjee, and J. Marvin, The effects of clay mineralogy and the electrical conductivity of water on the acquisition of DRM in sediments, *J. Geophys. Res.*, 95, 4,531-4,538, 1990.
- McCabe, C., M. Jackson, and B. B. Ellwood, Magnetic anisotropy in the Trenton Limestone: Results of a new technique, anisotropy of anhysteretic susceptibility, *Geophys. Res. Lett.*, 12, 333-336, 1985.
- McClave, J. T., and F. D. Dietrich II, *A first course in statistics*, 4th ed., 583 pp., Macmillan, New York, 1992.
- Nagata, T., *Rock Magnetism*, 350 pp., Maruzen, Tokyo, 1961.
- Néel, L., Some theoretical aspects of rock magnetism, *Adv. Phys.*, 4, 191-243, 1955.
- Ogg, J. G., Magnetic polarity time scale of the Phanerozoic, in *Global Earth Physics, A Handbook of Physical Constants, AGU Reference Shelf 1*, T. J. Ahrens ed., pp. 240-270, American Geophysical Union, Washington D.C., 1995.
- Opdyke, N. D., and J. D. Phillips, Paleomagnetic stratigraphy of sites 1-7 (leg 1) preliminary report, in *Initial Reports of the Deep Sea Drilling Project, vol. I*, pp. 501-517, U.S. Government Printing Office, Washington, D.C., 1969.
- Opdyke, N.D., and K.W. Henry, A test of dipole hypothesis, *Earth Planet. Sci. Lett.*, 6, 138-151, 1969.
- Opdyke, N. D, L. H. Buckle, and A. Todd, The extension of the magnetic time scale in sediments of the Central Pacific Ocean, *Earth Planet. Sci. Lett.*, 22, 300-306, 1974.
- Özdemir, Ö., D. J. Dunlop, and B. M. Moskowitz, The effect of oxidation on the Verwey transition in magnetite, *Geophys. Res. Lett.*, 20, 1,671-1,674, 1993.
- Potter, D. K., and A. Stephenson, Field-impressed anisotropies of magnetic susceptibility and remanence in minerals, *J. Geophys. Res.*, 95, 15,573-15,588, 1990.
- Rea, D. K., The paleoclimatic record provided by eolian deposition in the deep sea: the geologic history of wind, *Rev. Geophys.*, 32, 159-195, 1994.
- Ramdhor, P., *The ore minerals and their intergrowths, vol. 2*, 2nd. ed., 1207 pp., Pergamon Press, Oxford, 1980.

- Robbins, M., G. K. Wertheim, R. C. Sherwood, and D. N. E. Buchanan, Magnetic properties and site distributions in the system $\text{FeCr}_2\text{O}_4\text{-Fe}_3\text{O}_4(\text{Fe}^{2+}\text{Cr}_{2-x}\text{Fe}_x^{3+}\text{O}_4)$, *J. Phys. Chem. Solids*, 32, 717-729, 1971.
- Sapphire Instruments, *SI2B magnetic susceptibility and anisotropy meter manual*, 33 pp., Sapphire Instruments, Ruthven, 1994.
- Schmidbauer, E., Magnetization of Fe-Cr spinels and its application for the identification of such ferrites in rocks, *Z. Geophys.*, 37, 421-424, 1971.
- Schoonmaker, J., F. T. Mackenzie, M. Manghnani *et al.*, Mineralogy and diagenesis: their effect on acoustic and electrical properties of pelagic clays, deep sea drilling project leg 86, in *Initial Reports of the Deep Sea Drilling Project*, vol. LXXXVI, pp. 549-570, U.S. Government Printing Office, Washington, D.C., 1985.
- Schultheiss, P. J., Physical and geotechnical properties of sediments from the northwest Pacific: deep sea drilling project leg 86, in *Initial Reports of the Deep Sea Drilling Project*, vol. LXXXVI, pp. 701-722, U.S. Government Printing Office, Washington, D.C., 1985.
- Slater, J. G., and A. Cox, Palaeolatitudes from JOIDES deep-sea sediment cores, *Nature*, 226, 934-935, 1970.
- Shipboard Scientific Party (Heath, G. R., L. H. Burckle, *et al.*), Site 578, in *Initial Reports of the Deep Sea Drilling Project*, vol. LXXXVI, pp. 139-173, U.S. Government Printing Office, Washington, D.C., 1985.
- Shipboard Scientific Party (Ruddiman, W. F., R. B. Kidd, *et al.*), Site 606, in *Initial Reports of the Deep Sea Drilling Project*, vol. XCIV, pp. 21-74, U.S. Government Printing Office, Washington, D.C., 1987.
- Shipboard Scientific Party (Westbrook, G. K, B. Carson, *et al.*), Explanatory notes, in *Proc. ODP, Init. Repts.*, 146 (Pt.1), pp. 15-48, Ocean Drilling Program, College Station, TX, 1994.
- Stephenson, A., S. Sadikun, and D. K. Potter, A theoretical and experimental comparison of the anisotropies of magnetic susceptibility and remanence in rocks and minerals, *Geophys. J. R. Astron. Soc.*, 84, 185-200, 1986.
- Stephenson, A., Distribution anisotropy: two simple models for magnetic lineation and foliation, *Phys. Earth Planet. Inter.*, 82, 49-53, 1994.

- Stolz, J. F., D. R. Lovley, and S. E. Haggerty, Biogenic magnetite and the magnetization of sediments, *J. Geophys. Res.*, *95*, 4,355-4,361, 1990.
- Stoner, E. C., The demagnetizing factors for ellipsoids, *Phil. Mag.*, *7* (36), 803-821, 1945.
- Strangway, D. W., E. E. Larson, and M. Goldstein, A possible cause of high magnetic stability on volcanic rocks, *J. Geophys. Res.*, *73*, 3,787-3,795, 1968.
- Sun, W. W., and K. P. Kodama, Magnetic anisotropy, scanning electron microscopy, and X ray pole figure goniometry study of inclination shallowing in a compacting clay-rich sediment, *J. Geophys. Res.*, *97*, 19,599-19,615, 1994.
- Syono, Y., Magnetocrystalline anisotropy and magnetostriction of Fe_3O_4 - Fe_2TiO_4 series with special application to rock magnetism, *Japan. J. Geophys.*, *4*, 71-143, 1965.
- Tarduno, J. A., Absolute inclination value from deep sea sediments: A reexamination of the Cretaceous Pacific record, *Geophys. Res. Lett.*, *17*, 101-104, 1990.
- Tarling, D. H., and F. Hrouda, *The magnetic anisotropy of rocks*, 217 pp., Chapman and Hall, London, 1993.
- Verosub, K. L., Depositional and postdepositional processes in the magnetization of sediments, *Rev. Geophys. Space Phys.*, *15*, 129-143, 1977.
- Verosub, K. L., and A. P. Roberts, Environmental magnetism: past, present, and future, *J. Geophys. Res.*, *100*, 2,175-2,192, 1995.

APPENDIX A

DETAILED PALEOMAGNETIC DATA

The following tables present the detailed paleomagnetic data of this study. The second column gives the identification of the specimens as explained in Chapter 2. The third column gives the depth. The fourth column gives the intensity NRM. The fifth and sixth columns give the inclination and the nominal declination of remanence. The seventh and eight columns give the inclination and the nominal declination of the primary (or characteristic) magnetization. This inclination is considered as the inclination of the observed remanence I_{obs} . The characteristic declination is assumed to coincide with north and used to adjust the declination of the principal axes of the anisotropy (see Chapter 5). The ninth column gives the value of maximum angular deviation (MAD) calculated from the vector component analysis program (Chapter 2). The tenth column gives the ratio of H_{σ}/H_c and the eleventh the ratio of J_r/J_s (Chapter 3). The last column gives the degree of compaction ΔV (Chapter 8).

No.	Sample ID	Depth (m)	NRM			Primary		MAD (°)	H_c/JH_c	J/J_s	ΔV
			Intensity (A/m)	Inc. (°)	Dec. (°)	Inc. (°)	Dec. (°)				
1	28-0386	3.86	4.531E-02	31.2	187.4	32.5	186.5	1.5	3.455	0.121	0.25
2	28-0435	4.35	4.326E-02	48.4	218.4	47.4	222.8	1.5	3.086	0.149	0.25
3	28-0459	4.59	4.516E-02	62.8	278.3	65.8	274.7	2.7	3.069	0.136	0.25
4	28-0475	4.75	4.463E-02	55.4	279.2	54.8	280.0	1.5	3.044	0.135	0.24
5	28-0495	4.95	5.340E-02	54.7	286.1	53.9	289.7	1.4	3.109	0.131	0.27
6	28-0515	5.15	5.146E-02	57.4	265.0	56.7	265.0	1.3	3.141	0.124	0.27
7	28-0535	5.35	5.416E-02	57.7	312.2	55.5	315.0	2.2	2.833	0.147	0.30
8	28-0565	5.65	4.128E-02	48.3	304.4	51.4	305.4	2.3	3.062	0.126	0.30
9	28-0575	5.75	5.943E-02	50.3	296.6	46.0	298.6	1.2	3.125	0.120	0.32
10	28-0605	6.05	6.222E-02	55.2	292.4	53.5	295.9	1.7	3.410	0.112	0.33
11	28-0615	6.15	6.039E-02	51.0	273.5	48.7	278.1	2.2	3.297	0.114	0.32
12	28-0645	6.45	5.852E-02	41.8	290.2	41.9	291.9	1.6	3.083	0.122	0.34
13	28-0655	6.55	5.768E-02	55.8	277.6	55.5	282.8	2.5	3.227	0.117	0.35
14	28-0674	6.74	5.981E-02	41.8	266.5	40.0	266.3	4.8	3.388	0.107	0.34
15	28-0694	6.94	6.499E-02	39.7	262.2	45.8	265.3	1.2	3.237	0.112	0.31
16	28-0714	7.14	7.000E-02	45.4	266.8	42.7	269.5	1.4	3.200	0.122	0.27
17	28-0765	7.65	3.087E-02	40.5	253.9	40.8	253.3	4.0	4.721	0.064	0.28
18	28-0775	7.75	5.032E-02	52.1	242.4	52.0	246.6	1.4	2.863	0.134	0.28
19	28-0794	7.94	3.616E-02	59.4	198.5	62.8	197.1	1.4	2.977	0.126	0.28
20	28-0816	8.16	3.792E-02	52.4	207.4	56.5	208.2	2.9	2.942	0.132	0.28
21	28-0836	8.36	4.408E-02	52.2	214.7	56.1	216.0	1.1	2.789	0.130	0.29
22	28-0855	8.55	3.305E-02	50.8	228.2	50.4	226.5	6.2	2.929	0.140	0.27
23	28-0877	8.77	3.445E-02	53.3	213.8	57.9	213.7	3.6	3.007	0.126	0.29
24	28-0896	8.96	2.869E-02	51.8	209.9	55.4	209.2	2.4	3.413	0.126	0.26
25	28-0917	9.17	5.814E-02	63.5	255.1	64.4	265.0	2.5	3.372	0.101	0.26
26	28-0945	9.45	5.265E-02	63.8	200.1	64.8	200.7	2.8	3.144	0.125	0.17
27	28-0957	9.57	7.175E-02	55.6	183.6	57.9	186.1	2.3	3.033	0.116	0.31
28	28-0976	9.76	6.449E-02	46.5	213.9	51.3	216.5	2.2	2.912	0.122	0.32
29	28-0995	9.95	6.710E-02	29.9	235.4	34.0	241.1	1.8	2.976	0.122	0.31
30	28-1023	10.23	5.720E-02	68.4	238.8	70.4	249.0	2.7	2.863	0.121	0.32
31	28-1037	10.37	9.018E-02	64.8	238.9	63.0	251.4	3.3	2.819	0.125	0.34
32	28-1065	10.65	5.767E-02	27.3	263.3	27.6	263.8	2.7	3.066	0.111	0.34
33	28-1075	10.75	6.496E-02	56.7	265.2	57.2	271.2	1.9	2.774	0.132	0.33
34	28-1084	10.84	2.435E-02	-23.9	253.4	-41.2	261.0	1.4	3.036	0.124	0.34
35	28-1104	11.04	4.546E-02	-34.5	244.8	43.9	273.7	4.9	2.803	0.126	0.34
36	28-1116	11.16	6.798E-02	57.5	266.6	58.0	270.6	1.4	2.634	0.139	0.34
37	28-1125	11.25	5.584E-02	54.7	251.6	55.2	256.7	3.7	2.891	0.121	0.32

No.	Sample ID	Depth (m)	NRM			Primary		MAD (°)	H_a/H_c	J/J_s	ΔV
			Intensity (A/m)	Inc. (°)	Dec. (°)	Inc. (°)	Dec. (°)				
1	24-0403	4.03	3.807E-02	55.6	119.3	62.5	114.9	3.5	3.156	0.124	0.24
2	24-0426	4.26	3.841E-02	55.7	113.8	56.9	106.4	3.9	3.115	0.121	0.24
3	24-0446	4.46	3.376E-02	56.9	122.5	58.9	114.9	2.7	3.350	0.113	0.20
4	24-0462	4.62	3.689E-02	50.5	111.9	51.3	104.9	3.1	3.217	0.116	0.23
5	24-0486	4.86	5.123E-02	52.5	136.8	54.7	135.3	1.9	N/A	N/A	0.24
6	24-0506	5.06	4.742E-02	61.9	113.4	69.7	110.4	2.6	3.595	0.098	0.24
7	24-0526	5.26	4.629E-02	68.9	129.8	68.8	116.1	3.9	2.913	0.128	0.28
8	24-0543	5.43	6.104E-02	59.1	130.2	61.0	123.5	3.3	2.882	0.130	0.27
9	24-0562	5.62	6.256E-02	64.8	128.6	68.9	124.1	2.1	2.887	0.128	0.28
10	24-0583	5.83	5.234E-02	43.9	137.7	46.3	134.5	2.2	2.737	0.133	0.29
11	24-0604	6.04	6.144E-02	46.9	142.3	49.8	137.1	2.9	2.805	0.127	0.31
12	24-0623	6.23	6.497E-02	31.1	140.7	30.0	135.9	2.2	2.771	0.129	0.34
13	24-0642	6.42	4.953E-02	41.3	171.9	46.2	171.3	2.0	2.848	0.125	0.31
14	24-0656	6.56	5.502E-02	39.6	165.0	43.6	166.0	1.3	2.967	0.118	0.29
15	24-0677	6.77	4.432E-02	50.1	169.5	52.2	171.7	1.1	2.979	0.134	0.30
16	24-0703	7.03	3.528E-02	51.3	145.9	53.0	134.4	3.0	2.620	0.147	0.27
17	24-0722	7.22	3.562E-02	59.1	155.1	67.0	141.1	3.4	2.623	0.144	0.27
18	24-0742	7.42	4.189E-02	56.0	139.7	59.0	133.6	4.0	2.970	0.129	0.28
19	24-0762	7.62	9.226E-02	60.1	143.0	62.5	138.1	3.6	2.808	0.124	0.35
20	24-0783	7.83	9.330E-02	49.4	153.3	51.1	147.5	1.9	2.880	0.118	0.32
21	24-0801	8.01	6.392E-02	43.4	147.6	42.9	147.7	2.4	2.780	0.128	0.31
22	24-0816	8.16	3.837E-02	33.8	131.1	40.1	126.7	2.1	2.729	0.134	0.28

No.	Sample ID	Depth (m)	NRM			Primary		MAD (°)	H_d/H_c	J/J_s	ΔV
			Intensity (A/m)	Inc. (°)	Dec. (°)	Inc. (°)	Dec. (°)				
1	13-0405	4.05	3.559E-02	43.6	297.8	45.8	304.8	4.4	3.093	0.138	N/A
2	13-0427	4.27	3.563E-02	61.9	321.9	60.4	324.7	1.8	3.077	0.139	N/A
3	13-0443	4.43	2.989E-02	50.4	307.6	51.3	311.9	1.9	3.132	0.161	N/A
4	13-0457	4.57	2.376E-02	44.2	309.6	41.5	315.0	2.2	3.139	0.149	N/A
5	13-0485	4.85	2.483E-02	47.8	319.4	46.9	319.5	2.2	2.944	0.142	N/A
6	13-0504	5.04	2.124E-02	48.3	327.2	49.7	326.2	2.1	3.278	0.153	N/A
7	13-0517	5.17	2.888E-02	49.7	323.2	49.2	319.7	1.6	2.966	0.175	N/A
8	13-0537	5.37	2.751E-02	51.7	322.6	49.6	322.8	2.1	3.092	0.140	N/A
9	13-0565	5.65	2.629E-02	45.3	331.5	45.8	330.2	1.9	3.170	0.146	N/A
10	13-0580	5.80	4.224E-02	37.0	318.1	35.5	319.2	0.8	3.209	0.122	N/A
11	13-0583	5.83	4.387E-02	35.0	329.1	33.5	331.3	1.2	3.051	0.142	N/A
12	13-0603	6.03	3.530E-02	31.6	332.8	29.3	330.8	2.5	3.040	0.138	N/A
13	13-0623	6.23	2.920E-02	29.9	335.1	30.5	335.2	1.3	3.371	0.112	N/A
14	13-0643	6.43	5.327E-02	32.6	334.3	30.7	333.0	1.9	3.139	0.135	N/A
15	13-0663	6.63	5.314E-02	25.3	331.2	25.7	331.5	1.0	2.959	0.136	N/A
16	13-0667	6.67	7.627E-02	30.5	324.4	29.2	324.3	3.1	3.007	0.135	N/A
17	13-0686	6.86	5.225E-02	28.2	321.2	27.9	323.1	1.5	2.934	0.149	N/A
18	13-0703	7.03	3.552E-02	31.2	313.5	29.9	313.8	2.4	2.949	0.166	N/A
19	13-0717	7.17	2.874E-02	18.1	297.2	16.8	298.6	1.5	2.980	0.149	N/A
20	13-0734	7.34	3.619E-02	33.9	326.9	34.4	326.7	1.1	2.986	0.139	N/A

DSDP SITE 578

No. Sample ID	Depth (m)	NRM			Primary		MAD (°)	H_c/H_e	J_r/J_s	ΔV
		Intensity (A/m)	Inc. (°)	Dec. (°)	Inc. (°)	Dec. (°)				
1 578-1-1-47	0.47	6.963E-02	62.4	326.7	65.9	328.4	1.8	2.495	0.239	0.11
2 578-1-2-61	2.11	5.711E-02	56.8	271.8	57.2	271.8	2.3	N/A	N/A	0.08
3 578-1-3-10	3.10	7.749E-02	58.4	286.8	59.6	283.1	2.3	2.416	0.235	0.05
4 578-1-3-121	4.21	3.460E-02	66.1	267.3	69.0	290.7	1.9	N/A	N/A	0.01
5 578-2-1-69	5.49	4.703E-02	70.4	67.8	67.8	54.1	1.2	N/A	N/A	-0.04
6 578-2-2-22	6.52	4.711E-02	39.4	49.5	37.3	52.7	2.4	2.403	0.224	-0.08
7 578-2-2-91	7.21	5.401E-02	61.0	102.0	61.5	88.3	1.5	N/A	N/A	-0.11
8 578-2-3-47	8.27	1.178E-01	57.0	39.6	55.7	34.8	1.3	N/A	N/A	-0.17
9 578-2-4-29	9.59	6.970E-02	65.5	343.6	62.6	344.5	1.9	2.652	0.204	-0.05
10 578-2-4-140	10.70	4.317E-03	72.1	351.7	64.8	349.6	4.6	N/A	N/A	0.00
11 578-2-5-109	11.89	7.128E-02	59.6	356.3	56.6	2.8	2.4	N/A	N/A	-0.04
12 578-2-6-20	12.50	8.312E-02	62.0	11.0	58.3	10.0	0.9	2.214	0.279	-0.05
13 578-3-1-42	14.72	7.360E-03	38.7	190.5	43.0	191.1	4.6	N/A	N/A	-0.12
14 578-3-1-141	15.71	5.208E-02	38.7	186.4	47.7	186.6	2.3	2.492	0.201	-0.14
15 578-3-2-53	16.33	4.171E-02	37.6	191.0	42.9	192.0	1.5	N/A	N/A	-0.16
16 578-3-3-18	17.48	7.010E-02	57.8	200.8	59.0	199.4	1.5	N/A	N/A	-0.07
17 578-3-3-129	18.59	8.465E-02	46.6	222.9	49.2	219.3	2.3	2.429	0.201	0.03
18 578-3-4-93	19.73	5.463E-02	42.0	218.2	43.5	219.6	1.1	N/A	N/A	0.06
19 578-3-5-18	20.48	1.029E-01	42.9	240.8	43.5	241.2	1.6	N/A	N/A	0.06
20 578-3-5-133	21.63	9.053E-02	54.5	240.6	53.5	248.1	1.3	2.680	0.217	0.06
21 578-3-6-75	22.55	1.232E-03	47.8	250.3	44.9	244.6	7.2	N/A	N/A	0.06
22 578-3-7-21	23.51	3.975E-02	56.4	260.1	53.3	254.0	1.6	N/A	N/A	0.49
23 578-4-1-70	24.50	5.202E-02	50.6	158.4	52.5	158.5	1.5	2.761	0.196	0.31
24 578-4-2-19	25.49	5.895E-02	51.9	153.5	55.1	153.2	1.8	N/A	N/A	0.13
25 578-4-2-122	26.52	8.714E-02	46.9	159.6	51.0	158.5	1.4	N/A	N/A	0.12
26 578-4-3-76	27.56	5.142E-02	19.5	146.6	23.2	143.3	3.5	2.302	0.216	0.21
27 578-4-4-53	28.83	2.997E-03	-47.2	233.2	-44.5	250.3	4.7	N/A	N/A	0.15
28 578-4-4-119	29.49	8.402E-04	-57.2	218.5	-49.4	239.8	16.5	N/A	N/A	0.12
29 578-4-5-45	30.25	2.760E-02	-60.0	238.5	-64.6	251.6	2.0	2.618	0.188	0.07
30 578-4-6-72	32.02	1.369E-02	-10.5	167.5	-33.3	163.1	2.3	N/A	N/A	0.10
31 578-5-1-30	33.60	3.368E-02	31.2	126.2	35.1	122.3	4.6	2.359	0.226	0.14
32 578-5-2-112	35.92	3.757E-02	-59.5	326.0	-57.3	331.4	3.2	N/A	N/A	0.15
33 578-5-3-31	36.61	8.586E-02	-51.1	344.5	-50.6	350.2	2.0	2.388	0.220	0.12
34 578-5-3-114	37.44	1.852E-02	54.4	178.9	49.8	173.2	4.7	N/A	N/A	0.11
35 578-5-4-36	38.16	2.150E-02	-61.1	13.5	-49.2	13.3	5.2	N/A	N/A	0.12
36 578-5-5-40	39.70	4.008E-03	-48.9	6.0	-48.7	5.1	3.5	3.498	0.253	0.14

37	578-5-5-138	40.68	8.697E-03	-61.4	8.7	-54.4	10.8	2.6	N/A	N/A	0.06
38	578-5-6-53	41.33	7.255E-02	-57.5	11.9	-56.3	12.7	1.5	N/A	N/A	0.06
39	578-5-7-30	42.60	2.274E-02	-48.9	10.8	-49.6	14.9	1.2	2.406	0.220	0.06
40	578-6-1-77	43.57	5.805E-02	-57.2	225.7	-58.9	222.4	2.6	N/A	N/A	0.06
41	578-6-2-22	44.52	4.797E-02	-53.6	220.6	-50.7	223.1	2.5	N/A	N/A	0.06
42	578-6-2-112	45.42	5.823E-02	-53.2	236.8	-53.6	240.8	1.9	2.313	0.216	0.04
43	578-6-3-76	46.56	5.710E-02	-54.8	253.6	-55.2	251.5	2.5	N/A	N/A	-0.02
44	578-6-4-29	47.59	2.108E-03	-59.4	219.5	-56.0	232.4	4.9	N/A	N/A	-0.08
45	578-6-4-131	48.61	1.464E-02	-57.3	258.4	-60.2	252.0	6.0	2.408	0.211	-0.11
46	578-6-5-73	49.53	4.364E-02	-56.2	247.1	-59.4	250.7	2.1	N/A	N/A	-0.11
47	578-6-6-27	50.57	2.307E-03	-46.7	243.2	-44.9	243.6	6.8	3.836	0.219	-0.11
48	578-7-1-79	53.09	6.996E-02	-56.5	127.1	-55.7	127.2	3.4	2.374	0.223	-0.07
49	578-7-3-37	55.67	6.038E-02	49.3	291.0	50.9	291.4	1.1	N/A	N/A	-0.07
50	578-7-3-139	56.69	9.089E-02	59.3	309.7	56.3	316.4	2.2	2.509	0.213	-0.09
51	578-7-5-75	59.05	4.020E-02	-50.4	151.3	-54.7	153.0	2.0	2.317	0.230	-0.08
52	578-7-6-14	59.94	4.039E-02	-47.5	128.6	-51.6	124.7	2.2	N/A	N/A	-0.06
53	578-7-6-134	61.14	6.308E-02	-52.9	123.8	-53.0	123.7	1.3	N/A	N/A	-0.04
54	578-8-2-110	64.40	7.013E-02	-53.9	244.9	-56.5	247.0	1.2	N/A	N/A	0.02
55	578-8-3-41	65.21	7.463E-02	-62.5	239.9	-62.5	243.4	2.0	2.277	0.216	0.07
56	578-8-3-136	66.16	5.494E-02	-51.7	245.8	-50.8	252.4	1.6	N/A	N/A	0.13
57	578-8-4-98	67.28	4.198E-02	-57.1	242.4	-57.7	241.1	2.3	N/A	N/A	0.20
58	578-8-5-36	68.16	4.696E-02	-47.5	251.2	-49.5	255.2	2.4	2.317	0.217	0.25
59	578-8-5-114	68.94	4.147E-02	-52.1	258.7	-52.7	262.4	3.2	N/A	N/A	0.30
60	578-8-6-98	70.28	6.427E-02	-51.0	230.1	-50.3	233.2	2.6	N/A	N/A	0.33
61	578-9-3-22	74.52	9.110E-02	49.4	297.9	49.1	301.7	2.1	2.597	0.271	0.06
62	578-9-3-136	75.66	2.302E-02	64.0	307.7	64.2	321.9	6.9	N/A	N/A	0.06
63	578-9-4-91	76.71	9.586E-02	50.0	154.7	50.6	152.3	2.5	N/A	N/A	0.06
64	578-9-5-56	77.86	7.607E-02	48.5	147.2	53.2	148.9	2.7	2.326	0.241	0.07
65	578-9-6-60	79.40	8.537E-02	54.1	156.0	56.9	156.9	2.4	N/A	N/A	0.10
66	578-10-1-40	81.20	4.536E-02	37.9	216.6	37.0	201.9	2.9	N/A	N/A	0.13
67	578-10-1-135	82.15	5.480E-02	-53.0	41.5	-49.6	43.0	2.7	N/A	N/A	0.14
68	578-10-2-78	83.08	6.843E-02	43.6	199.2	48.8	201.5	2.4	2.382	0.248	0.11
69	578-10-3-134	85.14	7.769E-02	47.7	174.4	50.6	179.5	2.0	N/A	N/A	0.05
70	578-10-4-42	85.72	6.496E-02	57.6	141.2	51.5	135.3	3.3	2.253	0.273	0.03
71	578-10-6-34	88.64	4.300E-02	-28.5	232.7	-34.9	245.1	3.7	2.534	0.235	0.05
72	578-11-1-111	91.41	5.489E-02	-45.4	17.6	-50.0	17.9	3.1	N/A	N/A	0.06
73	578-11-3-101	94.31	7.251E-02	45.7	197.3	45.9	199.0	8.4	2.491	0.205	0.06
74	578-11-6-102	98.82	4.882E-02	-50.6	40.2	-56.1	39.3	6.1	N/A	N/A	0.20
75	578-12-1-104	100.84	3.308E-02	85.2	13.3	82.1	20.6	3.6	N/A	N/A	0.40
76	578-12-2-134	102.64	4.175E-02	49.2	308.4	46.7	309.8	3.5	N/A	N/A	0.11
77	578-12-3-82	103.62	4.679E-02	49.1	324.3	49.4	323.6	1.5	2.453	0.263	0.11
78	578-12-4-123	105.53	2.163E-02	-62.6	112.9	-61.5	126.9	3.7	N/A	N/A	0.11
79	578-12-5-116	106.96	3.558E-02	-39.7	140.5	-42.8	131.2	3.8	2.842	0.206	0.10

80	578-12-6-137	108.67	2.819E-03	-52.4	93.1	-50.9	100.0	3.4	N/A	N/A	0.07
81	578-13-1-117	110.47	1.586E-03	50.8	346.7	54.0	341.7	3.2	N/A	N/A	0.04
82	578-13-2-117	111.97	3.330E-03	-30.1	175.7	-37.7	175.3	4.8	N/A	N/A	0.01
83	578-13-3-33	112.63	1.942E-02	55.8	166.2	-48.4	166.9	3.2	2.426	0.258	0.02
84	578-13-3-115	113.45	4.240E-02	44.0	8.1	49.2	9.8	2.2	N/A	N/A	0.04
85	578-13-4-74	114.54	1.565E-02	51.5	28.3	58.5	37.8	4.3	N/A	N/A	0.05
86	578-13-5-23	115.53	1.195E-01	61.9	42.7	56.1	39.7	3.9	2.337	0.269	0.09
87	578-13-5-128	116.58	3.131E-02	-38.9	202.6	-46.0	208.7	3.2	N/A	N/A	0.15

DSDP SITE 606

No. Sample ID	Depth (m)	NRM			Primary		MAD (°)	H_c/H_c	J/J_s	ΔV
		Intensity (A/m)	Inc. (°)	Dec. (°)	Inc. (°)	Dec. (°)				
1 606-1-1-85	0.85	5.303E-03	53.8	285.5	43.8	286.6	4.1	2.525	0.277	0.24
2 606-1-2-52	2.02	9.721E-03	54.1	266.8	56.0	270.3	2.1	N/A	N/A	0.24
3 606-2-1-56	3.36	7.270E-03	51.1	274.0	53.3	279.3	3.2	N/A	N/A	0.24
4 606-2-2-129	4.63	9.766E-03	56.0	295.8	51.1	302.6	3.2	1.977	0.285	0.24
5 606-2-2129	5.59	6.266E-03	55.9	95.4	59.0	91.2	2.4	N/A	N/A	0.24
6 606-2-3-67	6.47	5.440E-03	57.6	164.6	58.5	158.0	0.8	N/A	N/A	0.18
7 606-2-4-68	7.98	1.546E-03	51.0	238.2	51.4	240.7	2.0	2.806	0.191	0.05
8 606-2-5-68	9.48	4.298E-03	48.7	239.1	56.0	248.2	0.8	N/A	N/A	0.03
9 606-3-1-78	13.18	6.024E-03	54.0	165.8	57.6	158.7	1.6	N/A	N/A	0.16
10 606-3-2-112	15.02	4.723E-03	49.2	205.1	55.5	207.6	2.8	N/A	N/A	0.22
11 606-3-3-70	16.10	1.094E-02	54.0	225.3	52.9	228.1	2.6	1.965	0.272	0.20
12 606-3-4-9	16.99	6.603E-03	49.2	229.0	53.0	232.3	0.9	N/A	N/A	0.18
13 606-3-4-111	18.01	7.980E-03	53.2	223.2	56.1	239.1	1.8	N/A	N/A	0.15
14 606-4-1-62	22.62	1.549E-03	-73.3	96.6	-65.2	40.8	4.5	N/A	N/A	0.16
15 606-4-2-25	23.75	1.544E-04	-50.5	395.6	-51.9	33.7	7.5	N/A	N/A	0.17
16 606-4-3-16	25.16	2.772E-04	-56.6	179.8	-72.2	0.9	8.1	N/A	N/A	0.17
17 606-4-3-128	26.28	1.534E-04	-71.6	296.3	-62.7	16.4	5.2	N/A	N/A	0.17
18 606-4-4-87	27.37	1.986E-04	54.9	211.9	50.2	209.0	7.7	N/A	N/A	0.18
19 606-4-5-60	28.60	3.033E-04	-47.4	168.9	-49.1	170.8	4.5	3.331	0.198	0.18
20 606-5-1-75	32.35	8.986E-04	-9.9	202.5	-26.7	212.5	2.6	1.697	0.378	0.22
21 606-5-3-59	35.19	1.606E-03	-25.3	210.5	-42.9	230.3	2.9	N/A	N/A	0.24
22 606-5-4-57	36.67	3.624E-03	-42.2	226.6	-41.6	235.4	2.3	1.990	0.261	0.23
23 606-5-4-128	37.38	4.388E-03	-44.3	213.0	-53.2	228.2	1.8	N/A	N/A	0.23
24 606-5-5-86	38.46	4.511E-03	-40.0	215.9	-47.0	233.6	1.9	N/A	N/A	0.22
25 606-5-6-87	39.97	1.682E-03	-29.8	210.9	-44.6	219.3	3.6	1.909	0.329	0.21
26 606-6-1-86	42.06	2.063E-03	-62.1	51.9	-59.0	48.6	1.5	N/A	N/A	0.19
27 606-6-2-73	43.43	1.600E-03	-49.6	89.1	-50.0	76.2	1.4	N/A	N/A	0.18
28 606-6-3-85	45.05	1.820E-03	-47.0	91.5	-50.3	86.8	2.5	1.837	0.308	0.17
29 606-6-4-28	45.98	9.017E-04	-56.8	95.2	-53.4	48.9	3.6	N/A	N/A	0.18
30 606-6-4-130	47.00	2.045E-03	-61.9	88.3	-56.8	41.7	1.6	N/A	N/A	0.20
31 606-6-5-129	48.49	3.034E-03	-58.4	41.1	-51.6	36.4	2.2	2.010	0.265	0.22
32 606-6-6-132	50.02	8.103E-04	-56.7	177.9	-66.4	43.8	4.8	N/A	N/A	0.25
33 606-7-1-64	51.44	9.255E-04	-34.7	239.0	-53.2	283.7	7.9	1.865	0.309	0.27
34 606-7-2-108	53.38	4.127E-04	-5.1	220.1	-47.1	297.4	4.1	N/A	N/A	0.30
35 606-7-3-105	54.85	8.813E-04	44.5	143.7	46.9	91.6	6.0	N/A	N/A	0.32
36 606-7-4-84	56.14	6.879E-04	53.8	97.5	49.3	70.0	2.5	1.842	0.363	0.32

37	606-7-5-84	57.64	1.171E-04	58.9	65.8	53.5	67.0	7.2	N/A	N/A	0.32
38	606-7-6-75	59.05	6.798E-05	-32.9	200.6	-54.9	240.8	23.3	N/A	N/A	0.32
39	606-8-1-64	61.04	8.265E-05	-44.1	290.5	-41.5	270.7	17.6	N/A	N/A	0.32
40	606-8-2-86	62.76	1.177E-04	-57.0	243.9	-49.7	261.9	8.5	N/A	N/A	0.32
41	606-8-3-65	64.05	1.368E-04	-48.9	284.0	-51.9	284.7	6.9	2.759	0.380	0.32
42	606-8-4-134	66.24	9.665E-05	-45.2	228.5	-52.2	267.1	19.0	N/A	N/A	0.32
43	606-8-5-63	67.03	1.289E-04	-45.2	246.1	-42.5	255.6	7.9	N/A	N/A	0.31
44	606-8-6-56	68.46	1.935E-04	-55.0	224.8	-51.0	238.9	9.4	2.914	0.348	0.31
45	606-9-1-56	70.56	1.006E-04	-47.3	139.2	-40.8	135.9	10.3	N/A	N/A	0.30
46	606-9-2-26	71.76	1.287E-03	-4.2	101.1	1.1	268.5	19.6	3.445	0.258	0.30
47	606-9-3-104	74.04	9.376E-05	-38.9	158.9	-37.8	141.4	14.5	N/A	N/A	0.31
48	606-9-5-113	77.13	1.074E-04	-39.4	141.6	-43.2	138.9	10.8	3.269	0.245	0.32
49	606-9-6-84	78.34	7.816E-05	-13.2	167.7	-46.4	149.9	12.0	N/A	N/A	0.32
50	606-10-1-65	80.25	7.681E-05	33.1	104.1	53.5	99.3	9.6	2.833	0.341	0.33
51	606-10-2-105	82.15	7.681E-05	39.2	209.3	15.1	191.6	29.5	N/A	N/A	0.34
52	606-10-3-85	83.45	5.398E-05	56.0	66.4	46.8	77.3	9.8	N/A	N/A	0.34
53	606-10-4-85	84.95	3.946E-05	54.7	49.1	64.0	11.0	35.9	1.819	0.413	0.35
54	606-10-5-35	85.95	7.336E-05	49.6	235.5	49.3	241.8	11.8	N/A	N/A	0.34
55	606-10-5-107	86.67	6.531E-05	59.8	206.8	49.7	219.6	13.7	N/A	N/A	0.34
56	606-11-1-67	89.87	5.542E-05	38.3	351.9	50.6	21.6	14.1	2.655	0.618	0.33
57	606-11-2-81	91.51	1.010E-04	-46.2	344.8	-45.6	345.2	8.6	N/A	N/A	0.32
58	606-11-3-125	93.45	7.896E-05	51.9	349.9	44.5	348.5	7.8	N/A	N/A	0.31
59	606-11-4-84	94.54	8.028E-05	-51.4	10.2	-50.3	10.1	6.2	N/A	N/A	0.31
60	606-12-2-13	100.33	8.047E-05	21.7	193.8	17.9	192.1	5.0	1.546	0.449	0.30
61	606-12-2-106	101.26	3.831E-04	64.6	191.5	64.4	335.1	5.5	N/A	N/A	0.30
62	606-12-3-85	102.55	6.963E-04	46.3	209.5	67.2	325.3	6.9	N/A	N/A	0.30
63	606-12-4-115	104.35	8.726E-05	-18.6	174.5	-45.5	158.6	10.9	3.775	0.183	0.30
64	606-12-5-86	105.56	5.626E-04	-8.9	197.2	-40.4	246.0	16.5	N/A	N/A	0.30
65	606-12-6-76	106.96	1.840E-04	44.1	298.9	27.0	324.1	5.8	N/A	N/A	0.31
66	606-13-1-25	108.45	2.593E-04	61.9	215.2	57.9	300.2	6.6	3.736	0.554	0.31
67	606-13-2-70	110.40	6.720E-05	59.8	94.4	48.1	48.8	10.7	N/A	N/A	0.31
68	606-13-3-11	111.31	1.805E-04	41.4	155.0	40.7	120.2	7.8	N/A	N/A	0.31
69	606-13-3-115	112.35	1.922E-04	44.0	139.2	47.3	105.3	6.9	2.079	0.386	0.31
70	606-13-4-85	113.55	1.508E-04	42.6	155.4	54.8	123.9	9.8	N/A	N/A	0.32
71	606-13-6-71	116.41	2.420E-04	72.2	91.0	63.4	82.7	8.1	4.306	0.182	0.32
72	606-14-2-109	120.29	4.783E-04	38.5	208.6	70.2	328.4	5.4	1.770	0.276	0.33
73	606-14-3-84	121.54	2.894E-04	40.4	190.9	20.6	234.1	21.1	N/A	N/A	0.33
74	606-14-4-86	123.06	7.918E-04	14.4	207.2	5.5	228.4	5.7	N/A	N/A	0.33
75	606-14-6-85	126.05	1.218E-03	6.8	203.6	-16.7	226.3	1.9	N/A	N/A	0.33
76	606-15-1-85	128.15	1.343E-03	4.1	231.6	-19.8	253.1	2.8	1.877	0.232	0.33
77	606-15-3-67	130.97	4.552E-04	-75.1	254.6	-70.6	321.4	3.7	N/A	N/A	0.34
78	606-15-4-15	131.95	1.346E-03	-50.0	325.9	-56.9	337.5	3.5	2.019	0.253	0.34
79	606-15-5-126	134.56	1.225E-03	-73.8	332.7	-71.3	25.4	14.0	N/A	N/A	0.36

80	606-15-6-66	135.46	1.772E-03	-74.9	24.5	-59.5	15.6	4.4	2.006	0.256	0.37
81	606-16-3-87	140.77	7.804E-04	-61.6	262.1	-44.5	326.1	3.7	1.828	0.293	0.40
82	606-16-4-66	142.06	1.009E-03	-32.0	283.5	-35.5	289.1	3.8	N/A	N/A	0.40
83	606-16-5-89	143.79	1.010E-03	-3.0	261.2	-18.4	295.6	4.0	1.674	0.310	0.40
84	606-17-1-56	147.06	7.167E-04	19.1	202.8	-19.6	239.4	9.8	N/A	N/A	0.40
85	606-17-2-67	148.67	9.483E-04	5.7	207.0	-20.1	244.8	7.9	1.611	0.328	0.39
86	606-17-3-33	149.83	8.450E-04	17.9	203.1	-9.8	210.5	9.3	N/A	N/A	0.39
87	606-17-3-116	150.66	4.020E-04	-5.7	183.0	-57.4	194.7	24.2	N/A	N/A	0.39
88	606-17-6-134	155.34	1.547E-03	38.4	211.0	40.2	219.2	5.2	N/A	N/A	0.37
89	606-18-1-86	156.96	4.117E-04	63.3	11.5	63.1	293.0	4.3	1.918	0.343	0.37
90	606-18-6-130	164.90	1.474E-03	-17.8	206.8	-33.5	202.6	6.7	3.819	0.074	0.34

APPENDIX B

DETAILED ARM ANISOTROPY DATA

The following table presents the detailed ARM anisotropy data of this study. The second column gives the identification of the samples as explained in Chapter 2. The third intensity of ARM along the maximum axis. The fourth and fifth column give the magnetic lineation and foliation respectively. Columns numbered six to nine give the declination and the inclination of maximum and minimum axes. The tenth column gives the percent anisotropy. The last column gives the anhysteretic susceptibility, a dimensionless parameter defined as mean ARM divided by the strength of the biasing field.

No.	Sample ID	ARM_{max} (A/m)	L	F	Max. Axis		Min. Axis		h_d (%)	K_{ARM}
					Dec. (°)	Inc. (°)	Dec. (°)	Inc. (°)		
1	28-0386	3.280E-01	1.016	1.132	268.8	4.5	162.7	74.1	13.2	1.961E-03
2	28-0435	4.221E-01	1.027	1.067	93.8	2.6	192.9	74.0	9.0	2.551E-03
3	28-0459	4.099E-01	1.034	1.084	9.2	27.9	190.1	62.1	11.2	2.454E-03
4	28-0475	3.162E-01	1.031	1.152	291.2	3.5	136.9	86.2	16.3	1.861E-03
5	28-0495	4.127E-01	1.024	1.217	103.8	1.4	255.9	88.4	20.3	2.401E-03
6	28-0515	4.729E-01	1.031	1.170	97.6	1.8	215.3	86.0	17.6	2.771E-03
7	28-0535	4.548E-01	1.045	1.170	57.4	2.7	222.3	87.2	19.0	2.643E-03
8	28-0565	3.170E-01	1.007	1.223	254.1	4.6	61.8	85.3	18.9	1.862E-03
9	28-0575	4.793E-01	1.018	1.221	251.1	2.4	7.2	84.5	19.9	2.796E-03
10	28-0605	4.574E-01	1.004	1.160	248.0	5.1	9.3	80.2	14.2	2.734E-03
11	28-0615	4.797E-01	1.022	1.149	233.8	7.2	57.3	82.7	15.2	2.842E-03
12	28-0645	3.794E-01	1.035	1.256	246.4	7.1	47.9	82.5	23.9	2.173E-03
13	28-0655	4.420E-01	1.006	1.194	283.8	3.8	101.5	86.2	16.8	2.616E-03
14	28-0674	4.686E-01	1.010	1.156	76.4	0.4	344.1	79.1	14.5	2.792E-03
15	28-0694	4.202E-01	1.027	1.284	292.6	0.5	168.1	89.1	24.8	2.405E-03
16	28-0714	4.187E-01	1.017	1.205	311.1	2.0	68.0	85.6	18.7	2.454E-03
17	28-0765	2.978E-01	1.039	1.089	214.2	9.3	73.3	78.2	12.0	1.775E-03
18	28-0775	3.694E-01	1.032	1.095	126.6	0.2	218.2	82.3	11.9	2.207E-03
19	28-0794	4.392E-01	1.009	1.114	103.9	8.3	237.1	77.9	11.1	2.649E-03
20	28-0816	4.094E-01	1.029	1.120	96.0	2.5	327.3	86.1	13.6	2.435E-03
21	28-0836	4.755E-01	1.020	1.142	303.6	1.2	191.4	86.7	14.4	2.827E-03
22	28-0855	2.725E-01	1.022	1.210	194.9	1.3	85.8	86.0	19.6	1.590E-03
23	28-0877	3.597E-01	1.036	1.196	320.5	0.3	221.9	87.8	20.0	2.088E-03
24	28-0896	2.462E-01	1.037	1.118	316.0	0.9	212.8	85.9	14.2	1.457E-03
25	28-0917	5.030E-01	1.027	1.085	333.6	2.0	102.8	86.9	10.5	3.024E-03
26	28-0945	3.547E-01	1.042	1.072	316.9	4.3	111.8	85.2	11.0	2.120E-03
27	28-0957	5.731E-01	1.041	1.160	136.7	8.5	253.3	72.1	17.9	3.346E-03
28	28-0976	6.589E-01	1.019	1.108	295.4	6.4	150.2	82.3	11.6	3.956E-03
29	28-0995	7.820E-01	1.017	1.252	99.5	10.6	299.7	78.7	21.8	4.533E-03
30	28-1023	7.776E-01	1.049	1.218	274.3	4.5	174.3	65.7	22.8	4.454E-03
31	28-1037	7.844E-01	1.034	1.260	98.1	0.9	189.7	60.7	24.0	4.491E-03
32	28-1065	6.261E-01	1.025	1.200	287.7	8.3	64.3	78.6	19.1	3.657E-03
33	28-1075	6.452E-01	1.010	1.143	19.1	8.1	184.3	81.6	13.5	3.859E-03
34	28-1084	6.124E-01	1.027	1.037	288.1	61.4	178.3	10.5	6.3	3.734E-03
35	28-1104	8.166E-01	1.144	1.035	91.6	79.8	332.7	5.0	17.8	4.648E-03
36	28-1116	6.531E-01	1.013	1.186	101.9	0.1	192.2	76.2	17.0	3.854E-03
37	28-1125	6.719E-01	1.060	1.116	104.0	3.0	210.0	79.1	12.0	3.851E-03

No.	Sample ID	ARM_{max} (A/m)	L	F	Max. Axis		Min. Axis		h_A (%)	K_{ARM}
					Dec. (°)	Inc. (°)	Dec. (°)	Inc. (°)		
1	24-0403	3.816E-01	1.023	1.179	233.4	0.7	106.2	88.8	17.5	2.242E-03
2	24-0426	4.023E-01	1.018	1.115	272.8	3.4	153.7	83.1	12.1	2.412E-03
3	24-0446	3.817E-01	1.007	1.113	344.9	2.3	240.1	81.2	10.9	2.305E-03
4	24-0462	4.510E-01	1.067	1.123	201.2	2.0	358.7	87.8	17.6	2.618E-03
5	24-0486	4.336E-01	1.010	1.109	184.5	3.9	76.7	77.4	10.9	2.616E-03
6	24-0506	4.169E-01	1.025	1.125	30.9	4.9	230.7	84.8	13.6	2.482E-03
7	24-0526	5.091E-01	1.022	1.081	221.7	7.1	57.9	82.6	9.7	3.074E-03
8	24-0543	5.876E-01	1.024	1.160	30.5	6.6	211.2	83.4	16.2	3.468E-03
9	24-0562	6.387E-01	1.012	1.113	49.1	5.1	160.6	76.2	11.3	3.846E-03
10	24-0583	6.025E-01	1.034	1.146	41.5	3.3	236.4	86.6	16.1	3.547E-03
11	24-0604	6.918E-01	1.032	1.116	54.1	6.6	263.9	82.4	13.6	4.110E-03
12	24-0623	6.814E-01	1.032	1.202	55.9	7.2	295.1	76.2	19.9	3.961E-03
13	24-0642	7.266E-01	1.031	1.097	319.2	10.6	108.5	77.8	12.0	4.342E-03
14	24-0656	7.084E-01	1.025	1.125	224.2	9.4	79.1	78.6	13.6	4.218E-03
15	24-0677	4.058E-01	1.051	1.065	39.8	1.7	145.2	83.6	11.2	2.417E-03
16	24-0703	7.027E-01	1.053	1.127	216.8	0.6	122.3	82.2	16.6	4.107E-03
17	24-0722	6.964E-01	1.044	1.113	230.0	3.0	132.5	67.7	14.6	4.109E-03
18	24-0742	5.491E-01	1.027	1.126	244.0	7.6	120.2	76.5	13.9	3.263E-03
19	24-0762	6.869E-01	1.014	1.138	247.3	0.1	156.9	83.1	13.5	4.103E-03
20	24-0783	8.409E-01	1.046	1.242	30.3	0.5	122.6	77.5	24.1	4.798E-03
21	24-0801	8.266E-01	1.011	1.173	25.5	5.9	161.1	81.7	15.9	4.900E-03
22	24-0816	7.210E-01	1.015	1.146	287.7	3.2	161.9	84.6	14.2	4.295E-03

No.	Sample ID	ARM_{max} (A/m)	L	F	<u>Max. Axis</u>		<u>Min. Axis</u>		h_A (%)	K_{ARM}
					Dec. (°)	Inc. (°)	Dec. (°)	Inc. (°)		
1	13-0405	3.222E-01	1.031	1.209	225.2	2.2	334.5	83.2	20.4	1.871E-03
2	13-0427	3.236E-01	1.031	1.153	33.8	3.0	182.8	86.5	16.4	1.905E-03
3	13-0443	3.393E-01	1.020	1.268	258.9	0.8	106.9	89.1	23.1	1.956E-03
4	13-0457	3.238E-01	1.006	1.244	186.6	3.8	319.6	84.4	20.2	1.893E-03
5	13-0485	3.296E-01	1.044	1.213	211.8	2.1	314.3	80.4	22.0	1.896E-03
6	13-0504	3.248E-01	1.035	1.158	211.4	0.2	305.1	86.4	17.2	1.904E-03
7	13-0517	3.392E-01	1.030	1.154	13.6	0.8	186.5	89.2	16.3	1.997E-03
8	13-0537	2.950E-01	1.044	1.186	224.8	8.0	47.8	82.0	20.1	1.708E-03
9	13-0565	3.129E-01	1.076	1.106	218.5	0.7	111.4	87.5	17.1	1.815E-03
10	13-0580	3.923E-01	1.045	1.223	34.0	6.9	262.7	79.6	22.7	2.251E-03
11	13-0583	3.844E-01	1.028	1.220	202.6	2.3	333.5	86.6	20.9	2.229E-03
12	13-0603	3.413E-01	1.022	1.200	241.6	9.7	77.4	79.9	18.8	1.997E-03
13	13-0623	2.886E-01	1.045	1.232	191.6	4.1	24.3	85.8	23.3	1.652E-03
14	13-0643	3.148E-01	1.010	1.227	240.7	1.8	91.7	87.9	19.5	1.844E-03
15	13-0663	4.505E-01	1.023	1.255	243.3	10.8	95.2	77.4	22.6	2.600E-03
16	13-0667	4.824E-01	1.008	1.255	60.6	6.5	269.8	82.6	21.1	2.811E-03
17	13-0686	3.865E-01	1.031	1.217	210.4	4.1	58.8	85.3	20.9	2.239E-03
18	13-0703	3.160E-01	1.027	1.200	226.5	3.6	105.4	83.1	19.4	1.842E-03
19	13-0717	3.896E-01	1.075	1.249	225.6	5.1	78.6	83.9	27.4	2.183E-03
20	13-0734	4.091E-01	1.041	1.147	209.8	4.4	89.0	81.4	16.9	2.397E-03

DSDP Site 578

No.	Sample ID	ARM_{max} (A/m)	L	F	Max. Axis		Min. Axis		h_A (%)	K_{ARM}
					Dec. (°)	Inc. (°)	Dec. (°)	Inc. (°)		
1	578-1-3-10	7.445E-01	1.036	1.013	78.0	0.1	168.0	23.1	4.8	4.550E-03
2	578-1-3-121	6.770E-01	1.016	1.010	299.0	40.2	48.1	21.2	2.6	4.194E-03
3	578-2-4-29	6.540E-01	1.013	1.010	342.3	11.7	82.7	41.0	2.3	4.060E-03
4	578-3-1-141	4.327E-01	1.009	1.015	48.1	63.9	142.0	1.9	2.4	2.688E-03
5	578-3-4-93	5.406E-01	1.032	1.013	192.6	77.7	310.6	5.8	4.4	3.312E-03
6	578-3-5-133	7.726E-01	1.043	1.010	290.8	4.1	103.2	85.9	5.4	4.703E-03
7	578-3-7-21	2.887E-01	1.017	1.031	286.5	55.3	31.7	10.3	4.7	1.775E-03
8	578-4-3-76	6.746E-01	1.012	1.013	42.3	43.6	309.2	3.2	2.5	4.185E-03
9	578-4-4-119	2.037E-02	1.020	1.025	10.4	22.4	117.0	34.7	4.4	1.253E-04
10	578-5-1-30	7.816E-01	1.043	1.034	44.1	7.4	241.2	82.3	7.5	4.724E-03
11	578-5-2-112	4.127E-01	1.014	1.010	113.5	24.2	249.2	57.8	2.4	2.560E-03
12	578-5-3-114	6.576E-01	1.006	1.006	319.0	34.7	88.5	42.5	1.1	4.108E-03
13	578-5-5-40	4.482E-01	1.069	1.008	176.7	21.8	305.9	57.7	7.7	2.686E-03
14	578-5-6-53	5.743E-01	1.007	1.007	266.2	0.0	175.4	76.5	1.5	3.581E-03
15	578-6-2-22	6.797E-01	1.005	1.015	250.6	35.1	85.5	53.9	2.0	4.235E-03
16	578-6-2-112	4.820E-01	1.045	1.030	121.6	1.9	240.0	86.1	7.4	2.913E-03
17	578-6-3-76	4.398E-01	1.033	1.013	290.2	8.3	33.3	57.3	4.5	2.693E-03
18	578-6-5-73	4.170E-01	1.025	1.027	106.5	51.3	217.2	15.8	5.1	2.555E-03
19	578-6-6-27	2.954E-01	1.043	1.025	116.3	1.2	212.3	79.1	6.8	1.790E-03
20	578-7-3-37	2.609E-01	1.017	1.054	337.5	13.2	75.3	30.2	6.8	1.593E-03
21	578-7-5-75	7.725E-01	1.038	1.010	23.4	0.5	117.2	82.4	4.8	4.719E-03
22	578-7-6-14	4.660E-01	1.008	1.014	237.8	13.1	340.4	43.1	2.1	2.899E-03
23	578-8-3-41	4.866E-01	1.036	1.018	321.6	8.2	84.0	74.9	5.4	2.968E-03
24	578-8-4-98	5.510E-01	1.005	1.045	77.5	21.6	191.1	45.3	4.8	3.401E-03
25	578-8-6-98	9.606E-01	1.022	1.022	357.7	46.3	175.0	43.7	4.3	5.904E-03
26	578-9-4-91	1.122E+00	1.018	1.027	296.3	39.8	163.5	39.2	4.4	6.904E-03
27	578-9-5-56	1.058E+00	1.015	1.016	222.2	4.5	321.3	63.3	3.1	6.545E-03
28	578-9-6-60	1.359E+00	1.006	1.012	214.9	10.6	102.7	63.6	1.8	8.469E-03
29	578-10-1-40	9.983E-01	1.013	1.030	177.3	21.7	283.8	35.6	4.2	6.157E-03
30	578-10-1-135	9.491E-01	1.005	1.021	53.8	2.3	301.2	84.1	2.5	5.904E-03
31	578-10-2-78	1.032E+00	1.013	1.004	188.5	20.7	306.2	50.9	1.7	6.146E-03
32	578-10-4-42	1.025E+00	1.007	1.018	39.4	7.8	258.8	80.0	2.5	6.371E-03
33	578-10-6-34	1.139E+00	1.016	1.027	35.5	0.3	126.8	79.1	4.2	7.018E-03
34	578-11-1-111	9.256E-01	1.013	1.032	110.1	0.8	12.9	83.8	4.4	5.705E-03
35	578-11-3-101	1.020E+00	1.029	1.026	338.7	1.9	163.6	88.1	5.4	6.237E-03
36	578-12-1-104	6.884E-01	1.021	1.021	352.8	5.7	101.0	73.3	4.2	4.235E-03
37	578-12-2-134	8.766E-01	1.006	1.042	141.5	0.3	235.4	84.9	4.7	5.409E-03

38	578-12-3-82	8.680E-01	1.039	1.019	98.0	6.6	195.9	50.1	5.7	5.284E-03
39	578-12-4-123	8.521E-01	1.013	1.014	342.7	3.6	149.5	86.3	2.7	5.282E-03
40	578-12-5-116	8.712E-01	1.022	1.003	7.9	9.9	277.0	4.5	2.5	5.388E-03
41	578-12-6-137	7.874E-01	1.006	1.004	10.7	7.2	278.1	19.7	1.1	4.917E-03
42	578-13-1-117	6.837E-01	1.010	1.016	307.3	3.8	206.9	69.6	2.5	4.244E-03
43	578-13-2-117	8.529E-01	1.010	1.024	313.5	5.2	184.4	81.8	3.4	5.280E-03
44	578-13-3-33	7.859E-01	1.010	1.012	357.4	9.3	135.9	77.7	2.2	4.885E-03
45	578-13-3-115	7.783E-01	1.004	1.017	278.9	12.3	79.3	77.0	2.1	4.849E-03
46	578-13-4-74	6.188E-01	1.016	1.007	183.0	4.7	61.2	81.2	2.2	3.839E-03
47	578-13-5-23	8.392E-01	1.011	1.013	248.1	13.5	33.3	73.7	2.4	5.211E-03
48	578-13-5-128	7.992E-01	1.012	1.010	339.6	10.9	194.5	76.8	2.2	4.964E-03

DSDP Site 606

No. Sample ID	ARM_{max} (A/m)	L	F	<u>Max. Axis</u>		<u>Min. Axis</u>		h_A (%)	K_{ARM}
				Dec. (°)	Inc. (°)	Dec. (°)	Inc. (°)		
1 606-1-1-85	5.227E-02	1.015	1.013	222.0	63.8	70.7	23.3	2.8	3.238E-04
2 606-2-1-56	1.610E-01	1.003	1.007	167.5	5.1	258.7	13.3	1.0	1.007E-03
3 606-2-2129	9.921E-02	1.004	1.005	352.7	4.1	82.9	2.8	0.9	6.206E-04
4 606-2-4-68	9.375E-02	1.009	1.031	268.8	2.9	173.7	60.3	3.9	5.795E-04
5 606-3-1-78	8.412E-02	1.017	1.018	285.3	3.4	43.4	82.9	3.5	5.193E-04
6 606-3-3-70	1.982E-01	1.005	1.010	233.4	25.0	356.6	49.5	1.5	1.237E-03
7 606-3-4-111	1.621E-01	1.014	1.003	165.9	3.2	257.4	25.0	1.7	1.008E-03
8 606-4-2-25	2.739E-03	1.025	1.010	267.0	0.3	176.9	12.6	3.5	1.687E-05
9 606-4-3-128	9.674E-03	1.011	1.007	56.6	14.5	287.6	67.6	1.8	6.018E-05
10 606-4-5-60	2.712E-03	1.033	1.032	187.5	0.9	324.0	88.8	6.4	1.650E-05
11 606-5-1-75	5.711E-02	1.012	1.008	239.6	12.2	140.3	36.6	2.0	3.550E-04
12 606-5-4-57	1.170E-01	1.008	1.016	15.1	13.3	116.5	40.0	2.4	7.275E-04
13 606-5-5-86	1.323E-01	1.004	1.009	343.3	40.9	168.9	48.9	1.3	8.262E-04
14 606-6-1-86	9.773E-02	1.005	1.007	25.6	18.0	126.0	29.1	1.2	6.104E-04
15 606-6-3-85	9.826E-02	1.011	1.013	347.5	10.9	256.1	7.5	2.4	6.101E-04
16 606-6-4-130	9.608E-02	1.010	1.001	59.0	14.9	166.0	47.6	1.1	5.993E-04
17 606-6-5-129	1.035E-01	1.011	1.004	227.9	1.9	137.3	18.9	1.5	6.446E-04
18 606-7-2-108	6.839E-02	1.014	1.006	169.7	43.0	25.9	40.8	2.0	4.248E-04
19 606-7-4-84	1.997E-02	1.007	1.022	117.0	69.1	295.8	20.9	2.9	1.240E-04
20 606-8-2-86	2.138E-03	1.016	1.009	283.6	24.8	67.7	60.3	2.6	1.324E-05
21 606-8-5-63	1.511E-03	1.021	1.009	270.8	69.3	78.2	20.2	3.0	9.333E-06
22 606-11-2-81	1.133E-03	1.018	1.043	243.8	1.4	334.8	36.5	5.9	6.937E-06
23 606-11-3-125	1.404E-03	1.008	1.008	244.0	35.8	35.8	50.7	1.6	8.748E-06
24 606-11-4-84	1.681E-03	1.019	1.022	279.7	31.9	120.9	56.3	4.1	1.035E-05
25 606-12-2-13	5.095E-02	1.018	1.003	79.2	15.1	176.0	23.6	2.2	3.158E-04
26 606-12-3-85	8.160E-02	1.014	1.007	114.8	3.1	21.6	45.9	2.1	5.066E-04
27 606-12-6-76	1.734E-02	1.014	1.009	307.9	1.9	41.5	63.0	2.3	1.076E-04
28 606-13-2-70	2.734E-03	1.020	1.038	157.5	49.4	297.0	33.0	5.7	1.674E-05
29 606-13-3-115	7.024E-03	1.012	1.034	145.2	39.8	252.3	19.4	4.5	4.330E-05
30 606-13-6-71	1.235E-02	1.008	1.014	347.1	47.8	78.9	1.7	2.3	7.681E-05
31 606-15-1-85	9.071E-02	1.014	1.021	354.9	19.2	85.1	0.5	3.5	5.604E-04
32 606-15-4-15	1.317E-01	1.025	1.019	197.6	11.7	93.5	49.7	4.4	8.084E-04
33 606-16-3-87	1.257E-01	1.039	1.046	216.1	9.3	82.2	76.7	8.3	7.586E-04
34 606-17-2-67	9.361E-02	1.037	1.009	304.7	12.4	173.7	71.5	4.6	5.722E-04
35 606-18-1-86	1.726E-02	1.037	1.014	251.4	12.4	10.4	65.5	5.0	1.054E-04

APPENDIX C

DETAILED AMS DATA

The following table presents the detailed AMS data of this study. The second column gives the identification of the samples as explained in Chapter 2. The third column gives magnetic susceptibility along the maximum axis. The fourth and fifth column give the magnetic lineation and foliation respectively. Columns numbered six to nine give the declination and the inclination of maximum and minimum susceptibility axes. The tenth column gives the percent susceptibility anisotropy. The last column gives the intensity of magnetic susceptibility $\chi = (\chi_{max} + \chi_{int} + \chi_{min})/3$.

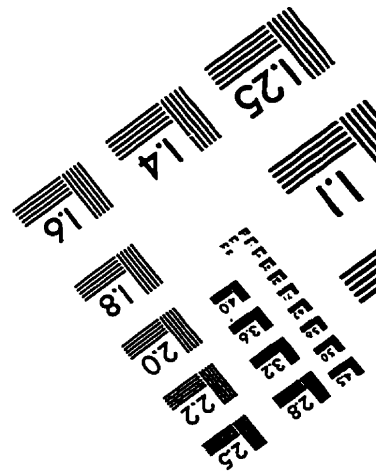
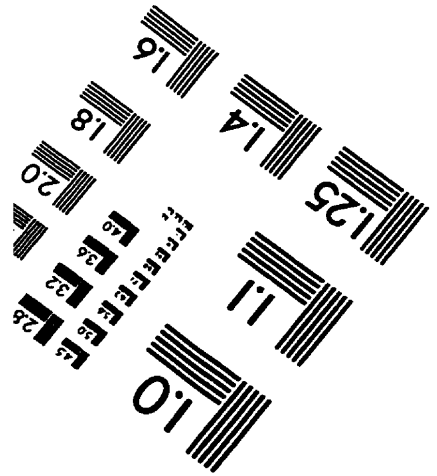
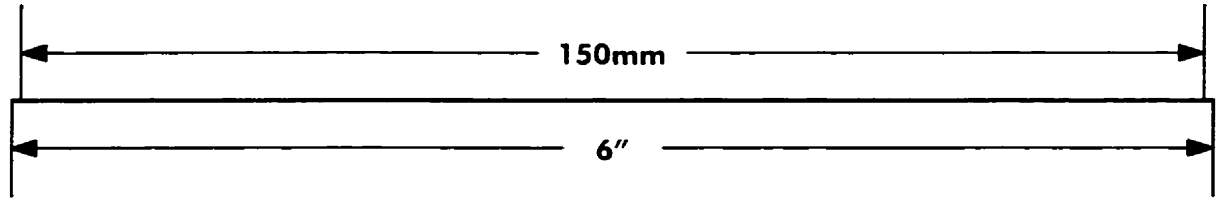
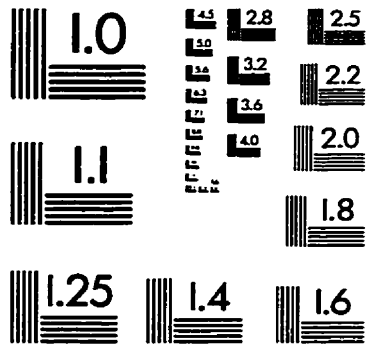
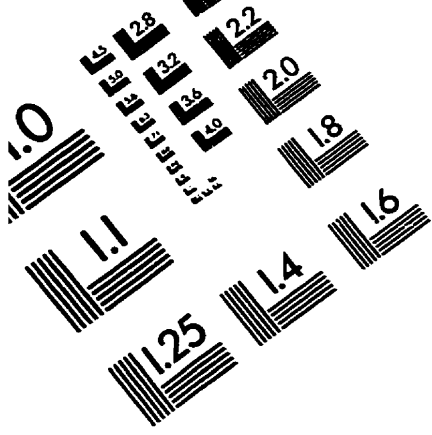
No. Sample ID	χ_{max} (m ³ /kg)	L	F	Max. Axis		Min. Axis		h_{χ} (%)	χ (m ³ /kg)
				Dec. (°)	Inc. (°)	Dec. (°)	Inc. (°)		
1 28-0386	3.385E-07	1.015	1.061	16.1	14.3	143.6	67.3	7.3	3.288E-07
2 28-0435	3.567E-07	1.013	1.030	18.1	7.3	193.6	82.7	4.1	3.504E-07
3 28-0459	3.253E-07	1.016	1.071	10.8	31.2	189.8	58.8	8.3	3.147E-07
4 28-0475	3.449E-07	1.009	1.070	353.6	11.5	175.6	78.5	7.5	3.353E-07
5 28-0515	3.975E-07	1.013	1.098	260.6	1.3	81.6	88.7	10.3	3.824E-07
6 28-0535	3.430E-07	1.008	1.101	60.2	3.3	273.0	86.1	9.9	3.308E-07
7 28-0565	4.074E-07	1.004	1.116	311.0	0.8	130.0	89.2	10.9	3.921E-07
8 28-0575	4.541E-07	1.009	1.135	207.6	7.2	345.6	80.4	12.8	4.335E-07
9 28-0605	5.219E-07	1.001	1.102	121.7	8.6	349.6	77.3	9.4	5.055E-07
10 28-0615	4.531E-07	1.015	1.105	197.1	4.1	60.7	84.4	11.0	4.345E-07
11 28-0674	4.809E-07	1.019	1.119	186.8	5.1	313.5	81.6	12.6	4.581E-07
12 28-0694	4.151E-07	1.018	1.171	281.0	0.3	38.7	89.4	16.3	3.905E-07
13 28-0714	4.182E-07	1.018	1.152	255.2	2.2	105.7	87.4	15.1	3.951E-07
14 28-0765	4.421E-07	1.013	1.049	340.2	2.4	196.3	87.0	5.9	4.317E-07
15 28-0775	3.944E-07	1.014	1.053	339.0	10.3	206.1	75.1	6.4	3.844E-07
16 28-0794	4.055E-07	1.012	1.059	77.7	11.7	259.7	78.3	6.8	3.948E-07
17 28-0816	3.668E-07	1.007	1.068	253.6	0.2	348.1	87.0	7.1	3.573E-07
18 28-0877	2.948E-07	1.005	1.121	301.0	2.0	110.9	88.0	11.3	2.832E-07
19 28-0896	2.192E-07	1.016	1.063	108.0	16.5	294.7	73.4	7.5	2.126E-07
20 28-0917	4.496E-07	1.004	1.047	245.7	0.3	338.2	83.2	4.9	4.417E-07
21 28-0957	5.690E-07	1.010	1.112	156.4	5.9	263.9	70.9	11.1	5.463E-07
22 28-0976	4.917E-07	1.021	1.076	273.8	2.3	152.2	85.7	9.2	4.736E-07
23 28-0995	5.354E-07	1.011	1.170	80.5	10.8	300.3	76.1	15.6	5.058E-07
24 28-1023	5.447E-07	1.019	1.143	67.0	10.6	184.7	68.1	14.4	5.156E-07
25 28-1037	5.094E-07	1.015	1.138	286.2	2.6	190.7	64.6	13.6	4.843E-07
26 28-1075	4.519E-07	1.017	1.094	64.1	10.1	229.5	79.6	10.3	4.340E-07
27 28-1104	5.633E-07	1.133	1.032	76.8	86.7	310.5	2.0	16.4	5.142E-07
28 28-1116	4.464E-07	1.007	1.096	97.3	2.1	197.0	77.7	9.5	4.312E-07
29 28-1125	4.739E-07	1.021	1.043	100.7	8.6	229.1	76.3	6.2	4.609E-07

No. Sample ID	χ_{max} (m ³ /kg)	L	F	Max. Axis		Min. Axis		h_{χ} (%)	χ (m ³ /kg)
				Dec. (°)	Inc. (°)	Dec. (°)	Inc. (°)		
1 24-0403	3.515E-07	1.014	1.117	209.9	2.8	90.6	84.4	11.9	3.362E-07
2 24-0426	4.026E-07	1.006	1.060	57.9	4.9	183.3	81.7	6.2	3.935E-07
3 24-0446	3.534E-07	1.020	1.057	22.8	1.3	219.3	88.6	7.4	3.426E-07
4 24-0462	3.908E-07	1.013	1.067	104.1	1.5	344.7	86.9	7.6	3.794E-07
5 24-0486	3.863E-07	1.003	1.065	181.1	13.5	39.6	72.9	6.4	3.777E-07
6 24-0506	4.211E-07	1.010	1.063	280.9	0.3	188.0	84.8	6.9	4.102E-07
7 24-0526	4.470E-07	1.007	1.045	96.3	10.1	255.2	79.2	5.0	4.386E-07
8 24-0543	4.774E-07	1.011	1.092	60.9	4.0	225.0	85.8	9.6	4.606E-07
9 24-0562	4.931E-07	1.009	1.062	274.0	4.7	162.7	77.2	6.7	4.807E-07
10 24-0583	4.944E-07	1.007	1.088	205.0	8.7	46.4	80.6	8.9	4.787E-07
11 24-0604	4.796E-07	1.010	1.069	171.9	4.3	310.8	84.3	7.4	4.661E-07
12 24-0623	5.228E-07	1.021	1.071	128.5	14.8	350.9	70.3	8.8	5.042E-07
13 24-0642	5.008E-07	1.036	1.037	308.0	8.5	72.9	75.4	7.2	4.834E-07
14 24-0656	5.111E-07	1.018	1.067	281.5	8.2	75.6	80.9	8.1	4.946E-07
15 24-0677	3.120E-07	1.014	1.060	184.6	0.0	94.7	81.8	7.0	3.034E-07
16 24-0703	3.771E-07	1.010	1.076	28.6	4.3	144.1	80.1	8.1	3.658E-07
17 24-0722	3.957E-07	1.008	1.063	328.9	15.0	100.4	68.0	6.7	3.859E-07
18 24-0742	3.674E-07	1.009	1.087	283.7	8.3	107.4	81.7	9.0	3.554E-07
19 24-0762	5.163E-07	1.007	1.083	280.5	11.6	139.0	75.4	8.4	5.008E-07
20 24-0783	5.086E-07	1.010	1.143	19.9	4.2	125.6	74.9	13.5	4.843E-07
21 24-0801	5.231E-07	1.004	1.106	338.2	10.1	161.6	79.9	10.0	5.050E-07
22 24-0816	4.476E-07	1.016	1.071	350.1	4.9	99.4	75.5	8.2	4.330E-07

No. Sample ID	χ_{max} (m ³ /kg)	L	F	<u>Max. Axis</u>		<u>Min. Axis</u>		h_x (%)	χ (m ³ /kg)
				Dec. (°)	Inc. (°)	Dec. (°)	Inc. (°)		
1 13-0405	3.027E-07	1.014	1.126	242.5	2.0	351.1	83.7	12.6	2.888E-07
2 13-0427	2.889E-07	1.021	1.069	60.9	2.2	297.0	86.0	8.6	2.788E-07
3 13-0443	2.786E-07	1.004	1.156	225.7	3.1	85.3	86.0	13.9	2.654E-07
4 13-0457	2.546E-07	1.010	1.118	193.5	7.9	357.9	81.8	11.5	2.442E-07
5 13-0485	2.925E-07	1.009	1.073	140.8	4.4	300.0	85.2	7.7	2.842E-07
6 13-0504	2.454E-07	1.023	1.091	219.4	4.2	28.0	85.7	10.6	2.352E-07
7 13-0517	2.975E-07	1.011	1.102	15.1	0.5	140.8	89.2	10.3	2.863E-07
8 13-0537	2.627E-07	1.016	1.109	8.5	4.5	244.7	82.0	11.4	2.516E-07
9 13-0565	3.142E-07	1.053	1.065	28.8	1.4	195.5	88.6	11.3	2.976E-07
10 13-0580	3.462E-07	1.014	1.139	294.7	3.5	285.5	79.5	13.7	3.291E-07
11 13-0583	3.264E-07	1.019	1.115	25.1	0.4	292.1	82.8	12.2	3.114E-07
12 13-0603	3.152E-07	1.015	1.110	225.1	8.9	13.9	79.6	11.5	3.018E-07
13 13-0623	3.325E-07	1.031	1.123	180.2	3.4	7.7	86.6	14.1	3.141E-07
14 13-0643	3.097E-07	1.007	1.128	80.2	2.4	269.7	87.5	12.1	2.966E-07
15 13-0663	3.579E-07	1.013	1.130	219.6	8.9	32.1	81.0	12.8	3.413E-07
16 13-0667	3.759E-07	1.008	1.149	219.3	1.2	316.4	80.6	13.8	3.578E-07
17 13-0686	2.894E-07	1.008	1.118	168.7	5.2	3.9	84.6	11.4	2.778E-07
18 13-0703	2.523E-07	1.007	1.098	349.0	2.7	102.5	83.3	9.6	2.437E-07
19 13-0717	2.967E-07	1.026	1.143	209.1	4.3	82.1	82.8	15.1	2.797E-07
20 13-0734	3.682E-07	1.014	1.090	25.0	0.9	119.8	79.5	9.7	3.546E-07

No. Sample ID	χ_{max} (m ³ /kg)	L	F	Max. Axis		Min. Axis		h_x (%)	χ (m ³ /kg)
				Dec. (°)	Inc. (°)	Dec. (°)	Inc. (°)		
1 578-1-2-61	4.592E-07	1.009	1.009	270.1	22.2	108.7	66.6	1.8	4.550E-07
2 578-1-3-10	5.648E-07	1.008	1.003	182.5	65.6	6.5	24.3	1.1	5.612E-07
3 578-2-1-69	2.919E-07	1.010	1.010	356.0	29.5	173.8	60.4	2.1	2.890E-07
4 578-2-2-91	3.794E-07	1.024	1.020	24.8	36.5	177.8	50.2	4.4	3.710E-07
5 578-2-3-47	8.869E-07	1.010	1.014	287.7	10.0	24.4	33.5	2.4	8.768E-07
6 578-2-4-29	4.395E-07	1.017	1.013	159.2	3.2	263.3	76.6	2.9	4.328E-07
7 578-2-4-140	1.005E-07	1.021	1.034	270.4	40.5	166.9	15.1	5.3	9.810E-08
8 578-2-5-109	5.343E-07	1.017	1.005	140.7	12.7	43.2	30.0	2.2	5.274E-07
9 578-3-1-42	1.578E-07	1.026	1.061	335.1	32.3	170.9	56.6	8.3	1.522E-07
10 578-3-2-53	3.425E-07	1.013	1.006	60.4	54.3	169.5	13.2	1.9	3.389E-07
11 578-3-3-18	4.535E-07	1.031	1.042	307.3	20.1	74.2	58.5	7.1	4.386E-07
12 578-3-4-93	3.466E-07	1.009	1.007	291.4	12.9	191.5	37.0	1.6	3.437E-07
13 578-3-5-18	9.220E-07	1.004	1.001	55.1	26.8	214.0	61.5	0.5	9.191E-07
14 578-3-5-133	7.053E-07	1.007	1.001	309.3	14.3	128.8	75.6	0.8	7.016E-07
15 578-3-6-75	5.803E-08	1.033	1.043	242.7	15.1	348.9	46.0	7.4	5.603E-08
16 578-3-7-21	2.516E-07	1.005	1.006	75.1	27.8	205.6	50.9	1.1	2.503E-07
17 578-4-2-19	3.382E-07	1.006	1.005	143.6	13.1	339.1	76.3	1.1	3.363E-07
18 578-4-2-122	4.692E-07	1.005	1.004	353.7	21.6	216.2	61.7	0.9	4.669E-07
19 578-4-3-76	5.038E-07	1.008	1.014	227.7	10.8	116.2	62.4	2.2	4.988E-07
20 578-4-4-53	7.492E-08	1.022	1.032	349.2	2.5	258.2	22.5	5.3	7.309E-08
21 578-4-4-119	1.053E-07	1.017	1.009	53.0	37.7	180.1	37.9	2.7	1.037E-07
22 578-4-6-72	3.302E-07	1.009	1.007	212.3	26.7	9.2	61.2	1.6	3.275E-07
23 578-5-1-30	6.272E-07	1.007	1.019	47.3	21.4	242.9	67.7	2.6	6.204E-07
24 578-5-2-112	3.150E-07	1.035	1.005	175.4	13.9	52.2	65.5	4.0	3.074E-07
25 578-5-4-36	5.919E-07	1.003	1.016	95.2	20.5	300.9	67.4	1.9	5.875E-07
26 578-5-5-40	7.306E-08	1.011	1.042	270.2	35.9	39.0	40.8	5.1	7.157E-08
27 578-5-5-138	1.088E-07	1.019	1.006	225.4	4.4	115.8	76.9	2.5	1.072E-07
28 578-5-6-53	3.388E-07	1.005	1.016	245.2	52.1	29.5	32.2	2.0	3.360E-07
29 578-6-1-77	4.300E-07	1.024	1.019	77.7	12.6	319.3	64.7	4.3	4.207E-07
30 578-6-2-22	3.932E-07	1.018	1.011	334.2	46.0	104.0	31.6	2.9	3.872E-07
31 578-6-2-112	2.800E-07	1.015	1.007	179.6	14.6	281.5	38.2	2.2	2.765E-07
32 578-6-3-76	2.947E-07	1.025	1.023	142.7	30.7	20.4	41.9	4.7	2.879E-07
33 578-6-4-29	6.445E-08	1.026	1.032	155.3	54.2	281.6	23.1	5.7	6.271E-08
34 578-6-5-73	3.450E-07	1.028	1.005	231.6	10.6	336.4	53.6	3.4	3.381E-07
35 578-6-6-27	6.337E-08	1.018	1.005	205.0	45.6	318.0	20.8	2.3	6.253E-08
36 578-7-3-37	2.524E-07	1.006	1.019	61.5	19.5	286.0	63.5	2.4	2.499E-07

37	578-7-5-75	4.077E-07	1.014	1.008	22.6	21.9	269.8	43.9	2.1	4.030E-07
38	578-7-6-134	2.928E-07	1.015	1.010	274.3	18.9	100.0	70.9	2.5	2.891E-07
39	578-8-2-110	3.907E-07	1.002	1.008	65.9	1.8	156.8	26.5	1.0	3.892E-07
40	578-8-3-41	2.756E-07	1.013	1.009	341.5	10.0	110.4	74.2	2.2	2.725E-07
41	578-8-3-136	2.140E-07	1.009	1.013	153.2	16.5	272.9	59.0	2.1	2.119E-07
42	578-8-4-98	2.881E-07	1.017	1.004	19.3	34.2	260.3	35.4	2.1	2.844E-07
43	578-8-5-114	3.954E-07	1.013	1.007	337.5	1.0	102.0	88.0	1.9	3.912E-07
44	578-8-6-98	6.254E-07	1.003	1.004	338.2	38.4	186.9	47.8	0.6	6.235E-07
45	578-9-3-136	4.190E-07	1.010	1.027	20.4	28.8	199.2	61.1	3.6	4.126E-07
46	578-9-5-56	6.734E-07	1.005	1.005	140.6	31.0	271.8	47.5	1.1	6.698E-07
47	578-9-6-60	1.248E-06	1.001	1.004	284.8	3.7	184.1	70.3	0.5	1.245E-06
48	578-10-1-135	6.527E-07	1.003	1.011	312.3	11.8	93.2	74.8	1.4	6.489E-07
49	578-10-2-78	5.614E-07	1.015	1.003	307.4	22.7	144.1	66.3	1.7	5.555E-07
50	578-10-3-134	5.259E-07	1.010	1.004	349.8	4.1	244.1	74.9	1.4	5.217E-07
51	578-10-4-42	4.655E-07	1.009	1.010	40.6	0.5	307.1	80.8	1.9	4.613E-07
52	578-10-6-34	8.509E-07	1.010	1.012	272.1	13.3	43.8	70.2	2.2	8.420E-07
53	578-11-3-101	6.273E-07	1.004	1.010	30.2	3.1	253.5	85.7	1.4	6.236E-07
54	578-11-6-102	4.564E-07	1.003	1.013	165.3	23.6	355.0	66.0	1.6	4.534E-07
55	578-12-2-134	3.483E-07	1.020	1.022	176.4	24.8	303.5	52.5	4.2	3.412E-07
56	578-12-3-82	4.756E-07	1.012	1.015	337.2	24.6	176.5	64.0	2.7	4.695E-07
57	578-12-4-123	2.971E-07	1.008	1.008	168.0	2.0	72.6	69.3	1.6	2.948E-07
58	578-12-5-116	6.242E-07	1.023	1.009	12.9	25.6	262.8	35.6	3.2	6.131E-07
59	578-12-6-137	2.790E-07	1.020	1.003	191.1	20.6	74.9	49.5	2.3	2.751E-07
60	578-13-1-117	2.163E-07	1.002	1.003	301.7	39.0	100.3	48.9	0.6	2.158E-07
61	578-13-3-33	3.026E-07	1.007	1.018	351.6	5.2	253.0	58.2	2.5	2.994E-07
62	578-13-3-115	2.766E-07	1.003	1.019	217.4	55.2	15.2	32.7	2.2	2.743E-07
63	578-13-5-23	2.810E-07	1.005	1.023	104.5	29.8	234.2	48.0	2.8	2.779E-07
64	578-13-5-128	2.820E-07	1.008	1.010	138.8	0.7	257.6	88.5	1.8	2.797E-07



APPLIED IMAGE . Inc
1653 East Main Street
Rochester, NY 14609 USA
Phone: 716/482-0300
Fax: 716/288-5989

© 1993, Applied Image, Inc., All Rights Reserved

